Imperial College London

Imperial College London

Department of Mathematics

Phase Space Approximations for Non-Hermitian Quantum Systems

Wasim Rehman

November 27, 2025

Submitted in part fulfilment of the requirements for the degree of Doctor of Philosophy in Mathematics of Imperial College London and the Diploma of Imperial College London.

Declaration of Originality

I, Wasim Rehman, declare that the work in this thesis is my own. The work of others has been appropriately referenced. A full list of references is given in the bibliography.

Copyright

The copyright of this thesis rests with the author. Unless otherwise indicated, its contents are licensed under a Creative Commons Attribution-NonCommercial 4.0 International Licence (CC BY-NC).

Under this licence, you may copy and redistribute the material in any medium or format. You may also create and distribute modified versions of the work. This is on the condition that: you credit the author and do not use it, or any derivative works, for a commercial purpose. When reusing or sharing this work, ensure you make the licence terms clear to others by naming the licence and linking to the licence text. Where a work has been adapted, you should indicate that the work has been changed and describe those changes.

Please seek permission from the copyright holder for uses of this work that are not included in this licence or permitted under UK Copyright Law.

Abstract

In this thesis, we study phase-space approximations to quantum dynamics for both Hermitian and non-Hermitian quantum systems, motivated by the need to efficiently describe quantum effects in models that are analytically intractable but admit classical analogues offering insight into their complex behaviour. Such systems arise in diverse areas, include but are not limited to quantum optics, condensed matter, open quantum systems, and quantum technologies.

We begin by exploring phase-space approximations for quantum systems governed by the Heisenberg-Weyl algebra. Building on established coherent-state methods, we develop a semiclassical Husimi approximation for non-Hermitian Hamiltonians. This approach reveals that the resulting dynamics comprise the transport of initial Husimi distributions along classical trajectories, overlaid with a time-dependent norm landscape reflecting non-unitary evolution. We demonstrate the effectiveness of this method through several examples, including damped Kerr oscillators and PT-symmetric models, providing a superior approximation for observables compared to standard coherent-state techniques.

To generalise these ideas, we develop a unified framework for phase-space approximations that applies across a wide range of algebraic structures. By identifying a set of general criteria, we enable systematic application of the approximation scheme to any quantum system satisfying these conditions. This provides a cohesive theoretical foundation that connects previously distinct results under a common approach.

We then apply this framework to both the $\mathfrak{su}_2$ algebra and non-Lie algebraic bosonic conversion systems. For $\mathfrak{su}_2$, we analyse two-mode Bose-Hubbard models with various Hamiltonians, demonstrating quantum-classical correspondence and exploring the effects of PT-symmetry. For bosonic conversion systems, we propose coherent states for these non-Lie algebraic structures and derive their associated phase-space geometry, characterised as quantum Kummer shapes with classical counterparts as orbifolds.

Our results advance the understanding of quantum-classical correspondence in multi-boson systems beyond traditional Hermitian frameworks and offer practical tools for simulating quantum dynamics in experimentally relevant models.

Acknowledgements

This doctoral thesis has been a passion project in the truest sense. After leaving academia at bachelor's level to pursue career aspirations and fulfill financial responsibilities, I made a promise to myself that I would one day return to mathematics and complete the journey I had started. Fulfilling this promise part-time, alongside other commitments, has been a profound challenge. I could only undertake it thanks to the enduring inspiration of my father, Fazal Rehman, who pursued his own passion project under circumstances far more difficult than mine.

I owe deep gratitude to my supervisor, Eva-Maria Graefe, for her support, intellectual generosity, and encouragement. What began with a master's level module grew into a master's dissertation, and ultimately this doctoral thesis. Her guidance has been instrumental throughout.

I am especially thankful to Simon Malzard and Rishi Melanthuru. Though younger than me in years, they have been invaluable mentors, offering both technical insight and moral support, especially during the final stages of this work. I am also grateful to Florian Mintert and Modesto Orozco-Ruiz, who gave me the opportunity to collaborate on a fascinating project during this journey.

I would like to thank the following who have offered conversation, company and laughs over the last few years during what was often a quite solitary project: Raheel Altaf, Shareen Rehman Ellahi, Salma Rehman Ijaz, Sonia Rehman, Nick Lawson, Sejal Sachdev, Leigh Shlomovich and Christine Burroughs. I must also offer a light-hearted note of thanks to Lana Del Rey for the countless hours of musical company during the writing process.

To my parents, I offer heartfelt thanks for instilling in me a deep appreciation for education and for giving me the platform to thrive. I also remember my maternal grandfather, whose belief in me at such a young age before his passing remains a lasting source of strength, and from whom I suspect my mathematical instincts were inherited.

Above all, I dedicate this thesis to my children, Ehsan, Sana, and Safi. I hope they pursue education not out of obligation, but for the joy and wonder it brings. May they always be guided by curiosity and a love of learning.

Contents

1 Introduction **4**

2 Coherent State Methods for Heisenberg-Weyl Systems **9**

2.1 Glauber Coherent States 10
2.2 Coherent-State Approximation 16
2.3 Semiclassical Husimi Approximation 19
2.4 Kerr Hamiltonian 20
2.5 Non-Hermitian Quantum Dynamics 23
2.5.1 Non-Hermitian Harmonic Oscillator 28
2.6 Coherent-State Approximations for Non-Hermitian Hamiltonians 30
2.7 Semiclassical Husimi Approximation for non-Hermitian Hamiltonians 32
2.8 Examples 33
2.8.1 Damped Kerr Hamiltonian 34
2.8.2 Damped Tilted Mexican Hat Hamiltonian 38
2.8.3 PT Symmetric Kerr Hamiltonian 40

3 A Generalised Approach for Phase-Space Approximations of Quantum Systems **47**

3.1 Coherent-State Approximations for General Quantum Systems 48
3.1.1 General Coherent-State Approximation Criteria for Hermitian Systems . 50
3.1.2 Factorisation Property using $\mathcal{D}$-Algebra 51
3.1.3 General Coherent-State Approximation Criteria for Hermitian Systems . 53
3.1.4 General Coherent-State Approximation Criteria for non-Hermitian Systems 56
3.2 Generalised Semiclassical Husimi Dynamics 60

4 Applications of Phase-Space Approximations to $\mathfrak{su}_2$ Spin Systems **62**

4.1 Examples 71
4.1.1 Linear Hermitian Hamiltonian 72
4.1.2 Linear Non-Hermitian Hamiltonian 74
4.1.3 Hermitian Two-Mode Bose–Hubbard Hamiltonian 77
4.1.4 Non-Hermitian Two-Mode Bose-Hubbard Hamiltonian 85

5 Bosonic Conversion Algebra: A Deformed $\mathfrak{su}_2$ and Applications of Phase-Space Approximations **98**

5.1 Bosonic Conversion Algebra 99
5.2 Phase-Space Approximations 102
5.2.1 Coherent States 102
5.2.2 Quantum Phase Space 105
5.2.3 $\mathcal{D}$-Algebra 107
5.2.4 Classical Phase Space 111
5.3 Phase-space approximation for the $(2,1)$ Bosonic Conversion System 116
5.3.1 Linear Hermitian Hamiltonian 118
5.3.2 Linear non-Hermitian Hamiltonian 122
5.3.3 $(2,1)$ 2-mode Bose-Hubbard Model Hamiltonian 124
5.3.4 $(2,1)$ 2-mode non-Hermitian Bose-Hubbard Hamiltonian 131
5.4 Generalised Multi-Mode Bosonic Conversion Systems 135

6 Conclusions **137**
6.1 Summary 138
6.2 Future Work 140

References **151**

Chapter 1

Introduction

In this thesis, we develop classical and semiclassical methods to approximate quantum dynamics in phase space for both Hermitian and non-Hermitian systems. While such methods are well established for certain classes of Hermitian systems [1–6], their extension to more general systems, particularly those governed by non-Hermitian Hamiltonians, remains relatively underdeveloped. This work contributes to the formulation of a more general framework for phase-space approximations, enabling their application to a broader class of quantum systems, including those without an underlying Lie algebraic structure.

The question of quantum-classical correspondence has attracted interest since the early development of quantum mechanics. Initial investigations centred on whether quantum theory could recover classical physics in an appropriate limit, ensuring compatibility with well-established classical phenomena and scientific intuition.

With the advent of group-theoretic methods in the 1970s, a more formal connection between quantum and classical mechanics was established through coherent states. Gilmore and Perelomov independently developed constructions for Lie group–based coherent states [7, 8], where classical phase spaces emerge naturally as coadjoint orbits, endowed with symplectic structures via the Kirillov–Kostant–Souriau (KKS) framework [9–11]. This geometric perspective is particularly effective for semi-simple Lie groups and the Heisenberg–Weyl group, provided suitable representations and stability subgroups exist.

In systems where the Hamiltonian lies within the associated Lie algebra, quantum–classical correspondence is exact. More generally, coherent states provide a systematic approach for constructing classical analogues of quantum systems whose dynamics may involve nonlinear functions of algebra generators. In such cases, they enable approximate, but often highly accurate classical descriptions of quantum evolution [12–15].

In standard quantum mechanics, systems are described by Hermitian Hamiltonians, which ensure unitary evolution, probability conservation, and real energy spectra. This framework is well suited for closed and isolated systems. However, many physical systems, such as those involving dissipation, decay, or continuous measurement, are commonly modelled using either non-Hermitian

Hamiltonians [16] or Lindblad master equations [17], two well-established approaches for open quantum system dynamics. Non-Hermitian Hamiltonians are typically used for effective system dynamics and gain/loss processes, while Lindblad dynamics is employed when complete mixed-state evolution and rigorous treatment of decoherence are required. In such cases, the imaginary parts of complex eigenvalues represent loss and gain [18–21]. A particularly significant development in this area was the discovery by Bender et al. that certain non-Hermitian Hamiltonians can possess entirely real spectra if they exhibit PT-symmetry, that is, invariance under the combined operations of parity (P) and time-reversal (T) [22, 23]. Parity transformation typically reflects spatial coordinates ($x \to -x$), while time reversal reverses the direction of momentum and complex conjugates the wavefunction. Remarkably, even though these Hamiltonians are not Hermitian, they can generate real eigenvalues as long as the PT symmetry remains unbroken. This has opened new directions of research and found applications in diverse areas such as optics [24–27], photonics [28, 29], and quantum electronics [30, 31].

Despite these advances, non-Hermitian quantum mechanics remains a relatively young and evolving field, with many fundamental questions still unresolved. In particular, the extension of classical and semiclassical approximation techniques, well developed for Hermitian systems, to more general non-Hermitian contexts is still in its early stages.

Since most quantum systems do not admit exact analytical solutions, a wide variety of approximation techniques have been developed to study their dynamics. These include perturbation theory [32, 33], variational methods [34, 35], path integral formulations [36–38], and numerical techniques such as Monte Carlo simulations [39] and grid-based time-dependent methods [40, 41]. Each of these approaches has proven useful in different contexts, depending on the system, the observables of interest, and the computational constraints.

In this thesis, we focus on approximation techniques rooted in classical and semiclassical frameworks that exploit connections with classical phase space. Classical approximations explore the relationship between the evolution of quantum mechanical expectation values and the dynamics of the corresponding classical variables in phase space [42–44]. Although these approaches are well understood and widely applied in Hermitian systems, and to a limited extent in certain non-Hermitian systems such as those based on the Heisenberg-Weyl algebra [45], they remain largely underdeveloped for more general non-Hermitian Hamiltonians.

A central tool in classical approximations for Hermitian systems is the use of coherent states, quantum states that provide a natural connection between quantum and classical descriptions. Coherent states are highly localised wave packets that exhibit the most classical-like behaviour among quantum states: they follow classical trajectories under appropriate Hamiltonians, minimise quantum fluctuations in observables relevant to the classical limit, and maintain their localisation properties under time evolution. When constructed with respect to a Lie group structure, coherent states also provide a natural phase space and a bridge to the underlying classical dynamics [12, 46]. However, their extension to more general non-Hermitian systems and to systems lacking an underlying Lie algebra remains a challenging and largely open problem.

Furthermore, Lie algebras describe only a subset of quantum systems. Many physically relevant

systems are associated with algebras that do not conform to a Lie structure [47–49]. Klauder's original approach [50, 51] offers great flexibility for such systems, requiring only continuity, normalisation, and resolution of identity for coherent state construction. Later, Gazeau and Klauder extended this approach by adding temporal stability as an additional requirement, providing a framework particularly suited to systems with well-defined action-angle variables [52]. While these approaches extend the applicability of coherent state methods beyond traditional Lie algebra-based systems, standard techniques for constructing phase-space approximations that rely on group symmetries cannot be directly applied. This makes establishing a meaningful quantum-classical correspondence and approximating quantum systems significantly more challenging. This has led to a growing interest in developing alternative methods that can accommodate more general algebraic structures [49, 53, 54].

Semiclassical methods are particularly valuable as they refine classical descriptions by incorporating wave packet effects while maintaining computational tractability. Rather than reducing quantum states to single classical trajectories, semiclassical methods use distributions, ensembles of paths, or quantum corrections to capture aspects of quantum wave evolution. Foundational tools in this category include the WKB approximation [5, 55], semiclassical propagators, quantisation conditions, and path integral formulations [36, 56]. In this thesis, we focus on a particular semiclassical method that approximates the dynamics of phase-space representations of quantum states by evolving classical distributions [57–61]. These distribution-based approaches capture quantum spreading and flow effects while remaining more amenable to analytical treatment and providing intuitive insights into quantum dynamics.

Several representations of quantum states in phase space are commonly used. The Wigner function [62] is perhaps the most well-known; it preserves all information about the quantum state and enables exact reconstruction of observables, but it is not a true probability distribution, as it can take on negative values. The Glauber-Sudarshan P-representation [63, 64] expresses the density matrix as a weighted sum over coherent states and is particularly useful in quantum optics. However, it often becomes highly singular for non-classical states, limiting its practical utility. The Husimi Q-function [65], on the other hand, is a smoothed, non-negative representation of the quantum state, obtained by projecting onto coherent states. While it sacrifices some detail due to its coarse-graining nature, it provides a regular and interpretable phase-space picture of quantum dynamics.

In this work, we adopt the Husimi representation as the foundation for our semiclassical approach. Since coherent states form the basis of our classical approximations, it is natural to use Husimi distributions due to their direct connection with coherent states. Its regularity and positivity make it especially well suited for developing approximation schemes that remain stable under time evolution, even in the presence of non-Hermitian effects. For Hermitian Hamiltonians, the evolution of the Husimi function has been successfully used to construct semiclassical Husimi approximations [66]. A closely related method in the Wigner representation is the Truncated Wigner Approximation (TWA) [67, 68], which similarly truncates the Moyal expansion to obtain classical transport of a phase-space distribution. While both yield the same leading-order classical dynamics, the Husimi formulation offers a positive and smoothed phase-space density and, as

developed in this thesis, extends naturally to non-Hermitian settings through a coherent-state geometric framework. However, extending this methodology to non-Hermitian systems remains an open and largely unexplored challenge, one that we aim to address in this thesis.

Motivated by this gap, the present work develops two phase-space approximation schemes for the dynamics of quantum states governed by nonlinear, non-Hermitian Hamiltonians. We begin by considering the time evolution of an initial coherent state and introduce a classical approximation based on the assumption that the state remains coherent throughout its evolution. This leads to what we call the coherent-state approximation, which captures the classical limit of the system's dynamics.

Building on this foundation, we formulate a semiclassical Husimi approximation, in which the dynamics of an initial phase-space distribution are approximated by applying the coherent-state approximation locally to each point in phase space. The full evolution is then inferred by following the flow generated by these pointwise approximations, providing a tractable semiclassical description of the system's behaviour under non-Hermitian evolution.

The thesis is organised as follows. Chapter 2 explores phase-space approximations for systems governed by the Heisenberg-Weyl algebra. We introduce coherent states and semiclassical Husimi approximations for both Hermitian and non-Hermitian Hamiltonians, followed by an application of these approximations to three representative non-Hermitian systems. This work has been published in Physical Review Letters [69].

Chapter 3 presents a general framework for constructing classical and semiclassical phase-space approximations, building upon the Gazeau–Klauder approach to generalised coherent states. Rather than focusing on a specific algebraic structure, we identify a set of sufficient (though not necessary) conditions under which the approximation scheme is valid, thereby enabling a unified treatment across a broad class of systems.

Chapter 4 applies this general framework to systems governed by the $\mathfrak{su}_2$ algebra, using the two-mode Bose-Hubbard model as a primary example. Both Hermitian and non-Hermitian cases are explored, and the results are currently being prepared for publication.

Chapter 5 extends the method to bosonic conversion systems governed by polynomially deformed algebras. We construct coherent states for these non-Lie algebraic systems, analyse their phase-space dynamics, and compare them to conventional two-mode models. This work addresses open questions from recent literature [70] and will be prepared for publication.

Appendix A contains an independent research project on Generally Noise-Resilient Quantum Gates for Trapped Ions [71]. This work addresses nonlinear Hamiltonian dynamics for trapped ion systems modelled using Glauber coherent states, providing a complementary perspective to the coherent state methods developed in the main thesis. While distinct from the core theoretical framework presented here, the noise-resilient gate protocols and generalised coherent state techniques developed in this thesis may be integrated into future extensions using the concept of product coherent states [72].

Appendix C introduces the Jacobi algebra underlying Gaussian wave packet dynamics. By treating Gaussian states as coherent states of the Jacobi group, we interpret the symplectic-geometric method of Ohsawa and Leok [14] through our coherent state framework. While we do not explore detailed dynamical examples, this theoretical introduction provides a novel perspective on Gaussian wave packet evolution.

Chapter 2

Coherent State Methods for Heisenberg-Weyl Systems

In this chapter, we study quantum-classical correspondence using Glauber coherent states, which arise naturally in systems governed by the Heisenberg-Weyl algebra. First introduced by Glauber in the context of quantum optics [63], these states are distinguished by their classical-like behaviour; they are the eigenstates of the annihilation operator, exhibit minimum uncertainty, and evolve classically under linear Hamiltonians.

We begin by reviewing the key properties of Glauber coherent states and show how they naturally lead to a coherent-state approximation to quantum dynamics, which provides a bridge to classical mechanics in the limit $\hbar \to 0$. Building on this, we construct a semiclassical Husimi approximation that uses phase-space distributions derived from coherent states to approximate the evolution of quantum systems. This framework is closely related to the approach developed by Milburn [66], who demonstrated how Husimi functions can be evolved semiclassically by accounting for classical transport and local deformation.

In the second part of the chapter, we extend these ideas to non-Hermitian systems, where conventional unitary evolution breaks down. We introduce the structure of non-Hermitian Hamiltonians and describe the extension of the coherent-state approximation developed by Graefe, Höning, and Korsch [45], which adapts methods to systems with gain, loss, and decay. This extension enables semiclassical analysis of non-Hermitian Heisenberg–Weyl systems within the coherent-state framework.

We conclude the chapter with a semiclassical method for non-Hermitian dynamics that, while inspired by Milburn's treatment of Hermitian systems [66], introduces a structurally distinct extension appropriate for complex-valued Hamiltonian evolution [69]. This development provides a new perspective on phase-space methods in non-Hermitian quantum systems and lays the groundwork for the techniques used in the following chapters.

2.1 Glauber Coherent States

Coherent states are a key concept in quantum mechanics, particularly in the study of quantum-classical correspondence. The conceptual foundation was laid by Schrödinger in 1926, who investigated minimum uncertainty wave packets that follow classical trajectories in the harmonic oscillator [73]. The modern formulation, however, began to take shape in the early 1960s with the pioneering work of Glauber and Sudarshan [63, 64], whose studies in quantum optics established both the terminology and mathematical structure of coherent states as they are widely used today. Glauber formalised their role as quasi-classical states of the electromagnetic field, highlighting their minimum uncertainty and Poissonian statistics.

In the 1970s, Gilmore and Perelomov independently developed group-theoretic approaches to coherent states based on Lie groups and their unitary representations [7, 8]. Their construction interprets coherent states as points in a homogeneous space associated with the action of a Lie group on a reference state, allowing for systematic generalisation beyond the Heisenberg-Weyl case. This framework applies to Lie groups that admit square-integrable irreducible unitary representations, which includes compact semisimple Lie groups, certain non-compact semisimple groups, and nilpotent groups like the Heisenberg-Weyl group.

The one-dimensional Heisenberg-Weyl algebra $\mathfrak{h}_1$ is generated by the annihilation operator $\hat{a}$, the creation operator $\hat{a}^\dagger$, number operator $\hat{n} = \hat{a}^\dagger\hat{a}$ and the identity operator $\hat{I}$, satisfying the fundamental commutation relation

$$[\hat{a}, \hat{a}^\dagger] = \hat{I}, \qquad [\hat{n}, \hat{a}] = -\hat{a}, \qquad [\hat{n}, \hat{a}^\dagger] = \hat{a}^\dagger, \qquad [\hat{n}, \hat{I}] = 0. \tag{2.1}$$

Note that the Heisenberg-Weyl algebra differs from the ordinary Heisenberg algebra $\mathfrak{h}_1^0$ in that it includes the number operator $\hat{n}$ as a generator.

This algebra describes two principal physical contexts. In single-particle quantum mechanics, the position and momentum operators are given by

$$\hat{q} = \sqrt{\frac{\hbar}{2}}(\hat{a} + \hat{a}^\dagger), \qquad \hat{p} = \mathrm{i}\sqrt{\frac{\hbar}{2}}(\hat{a}^\dagger - \hat{a}), \tag{2.2}$$

satisfying the canonical commutation relation

$$[\hat{q}, \hat{p}] = \mathrm{i}\hbar \tag{2.3}$$

and in many-body physics, $\hat{a}$ and $\hat{a}^\dagger$ correspond to bosonic annihilation and creation operators, respectively, in the second-quantised formalism [74].

The harmonic oscillator Hamiltonian is

$$\hat{\mathcal{H}} = \hbar\omega\left(\hat{a}^\dagger\hat{a} + \frac{1}{2}\hat{I}\right), \tag{2.4}$$

with eigenstates $\{|n\rangle\}_{n=0}^{\infty}$ forming an orthonormal basis of the Hilbert space $\mathcal{H}$.

To construct coherent states, the Gilmore approach, which we follow here, considers a unitary representation $U : G \to \mathcal{U}(\mathbf{H})$ acting on a Hilbert space $\mathbf{H}$, and defines coherent states as the orbit of a reference state $|E\rangle \in \mathbf{H}$ under the group action induced by this representation. The construction considers the stability (isotropy) subgroup $I \subset G$ that leaves the state $|E\rangle$ invariant up to a phase, such that $U(k)\,|E\rangle = e^{\mathrm{i}\omega(k)}\,|E\rangle$ for $k \in I$.

Under this construction, each element of the coset space G/I is associated with a coherent state $|\psi\rangle$, which is naturally an element of the projective Hilbert space $\mathbb{P}\mathbf{H}$ since states differing by a phase factor are physically equivalent. The coherent states are then defined as $|x\rangle = U(g)\,|E\rangle$, where $x \in G/I$ and g is a representative of the coset x.

From a physical perspective, this coset space G/I can be interpreted as the classical phase space of the system, carrying a natural symplectic structure inherited from the group action, thus providing a direct connection between the quantum coherent states and classical geometry [9].

In the case of the quantum harmonic oscillator, the relevant group is the Heisenberg-Weyl group, which we denote as the group corresponding to the Heisenberg-Weyl algebra $\mathfrak{h}_1$. Group elements are parametrised as

$$U(\alpha, \theta, \phi) = \exp\left(\alpha\hat{a}^\dagger - \alpha^*\hat{a} + \mathrm{i}\theta\hat{I} + \mathrm{i}\phi\hat{n}\right), \tag{2.5}$$

where $\alpha \in \mathbb{C}$ and $\theta, \phi \in [0, 2\pi)$. The stability subgroup $\mathrm{U}(1) \times \mathrm{U}(1)$ is generated by $\hat{n}$ and $\hat{I}$, since these operators leave the vacuum state $|0\rangle$ invariant up to a phase.

Since the phase factors associated with $\hat{I}$ and $\hat{n}$ do not change the physical state in the projective Hilbert space, the coherent state orbit is obtained solely via the displacement operator, which contains only the creation and annihilation operators

$$D(\alpha) = e^{(\alpha\hat{a}^\dagger - \alpha^*\hat{a})}. \tag{2.6}$$

To express coherent states in the number basis, we separate the creation and annihilation operators using the Baker-Campbell-Hausdorff formula [75]. For operators with commutator $[\hat{A}, \hat{B}] = \hat{C}$ that commutes with both $\hat{A}$ and $\hat{B}$, we have $e^{\hat{A}+\hat{B}} = e^{\hat{A}}e^{\hat{B}}e^{-\frac{1}{2}[\hat{A},\hat{B}]}$. Applying this to equation (2.6)

$$D(\alpha) = e^{-\frac{1}{2}|\alpha|^2}e^{\alpha\hat{a}^\dagger}e^{-\alpha^*\hat{a}}. \tag{2.7}$$

Following the group-theoretic formulation, we choose the vacuum state $|0\rangle$ as our extremal state since it is annihilated by $\hat{a}$ and is an eigenstate of the number operator $\hat{n}$. Applying the displacement operator to this extremal state generates the coherent states

$$\begin{aligned} |\alpha\rangle &= e^{(\alpha\hat{a}^\dagger - \alpha^*\hat{a})}\,|0\rangle\,, \\ &= e^{-\frac{1}{2}|\alpha|^2}e^{\alpha\hat{a}^\dagger}e^{-\alpha^*\hat{a}}\,|0\rangle\,. \end{aligned} \tag{2.8}$$

Since $\hat{a}\,|0\rangle = 0$, the term $e^{-\alpha^*\hat{a}}\,|0\rangle = |0\rangle$ simplifies, leaving us with

$$\begin{aligned} |\alpha\rangle &= e^{-\frac{1}{2}|\alpha|^2} e^{\alpha\hat{a}^\dagger}\,|0\rangle \\ &= e^{-\frac{1}{2}|\alpha|^2} \sum_{n=0}^{\infty} \frac{\alpha^n}{n!} (\hat{a}^\dagger)^n\,|0\rangle \\ &= e^{-\frac{1}{2}|\alpha|^2} \sum_{n=0}^{\infty} \frac{\alpha^n}{\sqrt{n!}}\,|n\rangle\,. \end{aligned} \tag{2.9}$$

It is often convenient to work with non-normalised coherent states for certain applications, as they simplify algebraic manipulations, particularly in generating functions and operator calculus. The absence of the normalisation factor avoids unnecessary complications in intermediate steps, and normalisation can be restored when computing physical quantities such as probabilities or expectation values. These are defined as

$$||\alpha\rangle = e^{\alpha\hat{a}^\dagger}\,|0\rangle = \sum_{n=0}^{\infty} \frac{\alpha^n}{\sqrt{n!}}\,|n\rangle\,, \tag{2.10}$$

which relate to the normalised states via $|\alpha\rangle = e^{-\frac{1}{2}|\alpha|^2}||\alpha\rangle$. The normalisation function for these non-normalised states is defined as

$$\mathcal{M}(\alpha) = \langle\alpha||\alpha\rangle = e^{|\alpha|^2}, \tag{2.11}$$

For Glauber coherent states, the phase space is naturally associated with the complex plane, with each point $\alpha \in \mathbb{C}$ representing a unique coherent state. The complex amplitude α encodes the expectation values of the canonical operators $\hat{q}, \hat{p}$ in the coherent state as

$$\alpha = \frac{\langle\hat{q}\rangle + \mathrm{i}\,\langle\hat{p}\rangle}{\sqrt{2\hbar}}. \tag{2.12}$$

To obtain a well-defined classical limit as $\hbar \to 0$, it is convenient to introduce a rescaled phase-space coordinate

$$z = \frac{1}{\sqrt{2}}(q + ip), \quad \text{where} \quad q = \langle\hat{q}\rangle\,, \quad p = \langle\hat{p}\rangle\,. \tag{2.13}$$

This rescaling allows us to label coherent states independently of $\hbar$, and ensures that phase-space trajectories remain finite in the semiclassical limit [76, 77].

Glauber coherent states possess a number of important properties that make them central to both semiclassical and quantum optical analyses. They are the eigenstates of the annihilation operator, satisfying $\hat{a}\,|\alpha\rangle = \alpha\,|\alpha\rangle$. These states are not mutually orthogonal, with inner product

$$\langle\alpha_1|\alpha_2\rangle = e^{-\frac{1}{2}|\alpha_1|^2 - \frac{1}{2}|\alpha_2|^2 + \alpha_1^*\alpha_2}. \tag{2.14}$$

They form an overcomplete basis of the Hilbert space and satisfy the resolution of the identity,

$$\int |\alpha\rangle \langle\alpha| \frac{\mathrm{d}^2\alpha}{\pi} = \hat{I}, \tag{2.15}$$

allowing any state in the Hilbert space to be expanded as a continuous superposition of coherent states.

One particularly useful feature of coherent states is their ability to map quantum operators to functions on classical phase space [8, 78]. Given an operator $\hat{F}$, its coherent-state symbol is defined as the expectation value $f(\alpha) = \langle\alpha| \hat{F} |\alpha\rangle$. This function provides a phase-space representation of the operator and plays a central role in constructing approximations. For systems built from the Heisenberg-Weyl algebra, the coherent-state symbols provide an exact correspondence between the commutators of the algebra elements and the Poisson brackets of their corresponding symbols. Specifically, one finds that

$$\langle[\hat{a}, \hat{a}^\dagger]\rangle = \mathrm{i}\{\alpha, \alpha^*\} = 1, \tag{2.16}$$

$$\langle[\hat{a}, \hat{n}]\rangle = \mathrm{i}\{\alpha, \alpha\alpha^*\} = \alpha, \tag{2.17}$$

$$\langle[\hat{a}^\dagger, \hat{n}]\rangle = \mathrm{i}\{\alpha^*, \alpha\alpha^*\} = -\alpha^*, \tag{2.18}$$

$$\langle[\hat{q}, \hat{p}]\rangle = \mathrm{i}\hbar\{q, p\} = \mathrm{i}\hbar \tag{2.19}$$

where the Poisson bracket is defined by

$$\{u, v\} = \frac{\partial u}{\partial q}\frac{\partial v}{\partial p} - \frac{\partial u}{\partial p}\frac{\partial v}{\partial q}. \tag{2.20}$$

These relations show that, when evaluated in coherent states, the expectation values of quantum commutators reproduce the structure of classical Poisson brackets. This correspondence reflects how the underlying symplectic geometry of classical phase space emerges naturally from quantum mechanics in the semiclassical limit.

In the context of non-Hermitian quantum systems, it will become useful to define an additional structure alongside the Poisson bracket. To this end, we introduce the metric bracket, defined analogously as

$$\{\!\{u, v\}\!\} = \frac{\partial u}{\partial q}\frac{\partial v}{\partial p} + \frac{\partial u}{\partial p}\frac{\partial v}{\partial q}. \tag{2.21}$$

While the Poisson bracket corresponds to the antisymmetric part of operator dynamics and is naturally associated with the quantum commutator, the metric bracket captures the symmetric part, reflecting the structure of the quantum anti-commutator. This distinction becomes particularly important for non-Hermitian evolution, where both unitary and non-unitary components play a role. The metric bracket thus encodes dissipative or amplifying effects that arise from the imaginary part of the Hamiltonian, while the Poisson bracket continues to represent the conservative (Hamiltonian) flow. Together, these brackets provide a complete phase-space representation of non-Hermitian dynamics [45].

Another key property of coherent states is that, under time evolution governed by a Hamiltonian linear in the generators of the Heisenberg-Weyl algebra (e.g., $\hat{\mathcal{H}} = \omega\hat{a}^\dagger\hat{a} + c\hat{a} + d\hat{a}^\dagger$), an initial coherent state $|\alpha_0\rangle$ remains a coherent state at all times. That is, the time-evolved state takes the form

$$|\psi(t)\rangle = e^{-\mathrm{i}\hat{\mathcal{H}}t/\hbar}\,|\alpha_0\rangle = |\alpha(t)\rangle\,, \tag{2.22}$$

where $\alpha(t)$ evolves along a classical trajectory in phase space. This preservation of coherence reflects the group-theoretic structure of coherent states: both the time-evolution operator and the displacement operator are elements of the Heisenberg-Weyl group, and their product yields another valid group element. Thus, the evolved state remains within the coherent-state manifold.

The trajectory $\alpha(t)$ can be obtained from the Heisenberg equations of motion. For example, one finds

$$\frac{\mathrm{d}\alpha}{\mathrm{d}t} = \langle\alpha|\,[\hat{a}, \hat{\mathcal{H}}]\,|\alpha\rangle = \{\alpha, h\}, \tag{2.23}$$

where $h = \langle\alpha|\,\hat{\mathcal{H}}\,|\alpha\rangle$ is the classical Hamiltonian. This shows that the evolution of the coherent state follows classical dynamics in phase space, governed by h and the associated Poisson bracket structure.

While coherent states preserve their form under time evolution generated by Hamiltonians that are linear in the generators of the Heisenberg-Weyl algebra, this stability is lost when the Hamiltonian contains nonlinear terms from the universal enveloping algebra of $\mathfrak{h}_1$. For Hamiltonians that lie entirely within the Lie algebra, the time evolution operator $e^{-i\hat{H}t/\hbar}$ can be expressed as a group element of the Heisenberg-Weyl group using the Baker-Campbell-Hausdorff formula. However, when the Hamiltonian includes nonlinear terms such as $\hat{a}^\dagger\hat{a}^\dagger\hat{a}\hat{a}$ in the Kerr Hamiltonian $\hat{H} = \hat{a}^\dagger\hat{a} + \beta\hat{a}^\dagger\hat{a}^\dagger\hat{a}\hat{a}$, it belongs to the universal enveloping algebra but not to the Lie algebra itself. In this case, $e^{-i\hat{H}t/\hbar}$ is no longer a group element and cannot be decomposed using the group structure. Consequently, an initial coherent state typically evolves into a general quantum state that no longer maintains the simple classical correspondence characteristic of coherent states. Without an exact classical counterpart, one can use classical and semiclassical approximation methods to analyse and approximate the system's behaviour.

To analyse these more complex dynamics, we must move beyond the exact preservation of coherent states and adopt phase-space methods that remain applicable even when the Lie group structure is no longer available. Coherent states still play a crucial role in this context by enabling the construction of Husimi function, a smooth, non-negative phase-space representation of quantum states. This function offers an intuitive bridge between quantum and classical descriptions. Given a quantum state $|\phi\rangle$, the Husimi function is defined as

$$Q(\alpha) = |\langle\alpha|\phi\rangle|^2, \tag{2.24}$$

where $|\alpha\rangle$ is a coherent state centred at the complex phase-space point α.

For example, a coherent state centred at α_c yields a Gaussian Husimi distribution,

$$Q(\alpha) = e^{-|\alpha-\alpha_c|^2}, \tag{2.25}$$

whereas a Fock state $|n\rangle$ leads to a ring-like distribution,

$$Q(\alpha) = \frac{|\alpha-\alpha_c|^{2n}}{n!} e^{-|\alpha-\alpha_c|^2}. \tag{2.26}$$

These expressions highlight how the Husimi distribution captures classical-like localisation in the case of coherent states and more quantum-like features in Fock states. Figure 2.1 shows examples of both, centred at the same phase-space point for comparison.

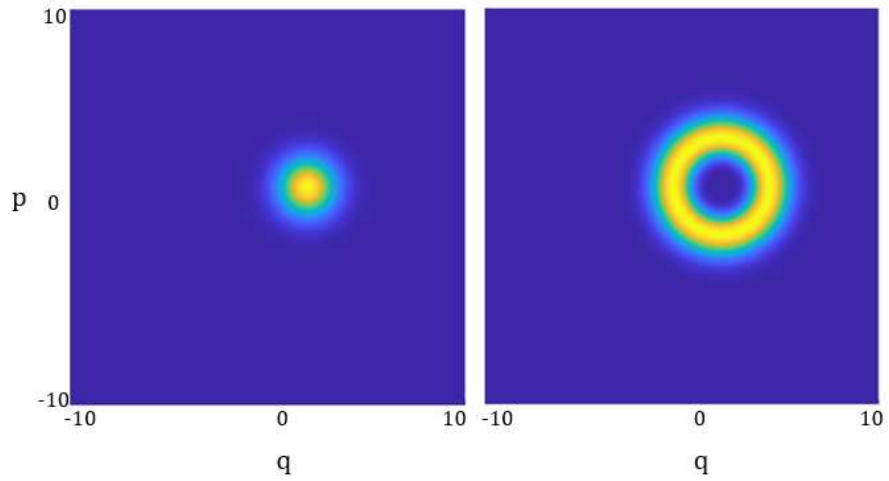


Figure 2.1: Husimi distributions for harmonic oscillator states, each centred at the phase-space point $(q, p) = (2, 1)$. Left: A coherent state, showing Gaussian localisation. Right: The Fock state $|3\rangle$, illustrating a ring-like structure characteristic of non-coherent states. The choice of $|3\rangle$ is arbitrary and serves to highlight qualitative differences between classical-like and non-classical states.

Coherent states allow operators to be represented as differential operators through the $\mathcal{D}$-algebra formalism [76, 79]. Specifically, for a non-normalised coherent state $||\alpha\rangle$, each operator $\hat{X}_i$ admits a differential operator representation, $\mathcal{D}_{X_i}(\alpha)$, such that

$$\hat{X}_i||\alpha\rangle = \mathcal{D}_{X_i}(\alpha)||\alpha\rangle\,, \quad \hat{X}_i\hat{X}_j||\alpha\rangle = \mathcal{D}_{X_i}(\alpha)\mathcal{D}_{X_j}(\alpha)||\alpha\rangle\,. \tag{2.27}$$

This formalism maps operators in the universal enveloping algebra to differential operators that can act both on coherent state vectors and on phase-space functions, enabling efficient calculation of expectation values and classical limits.

As an example for the Heisenberg-Weyl algebra, the differential operation of the annihilation and creation operators is particularly simple

$$\mathcal{D}_a(\alpha) = \alpha, \qquad \mathcal{D}_{a^\dagger}(\alpha) = \frac{\partial}{\partial\alpha}. \tag{2.28}$$

This follows directly from the definition of the non-normalised coherent state as $||\alpha\rangle = e^{\alpha\hat{a}^\dagger}|0\rangle$,

and the fact that differentiating with respect to α pulls down a factor of $\hat{a}^\dagger$.

For $\hat{X}_i \in \mathfrak{h}_1$, we often need to compute $\langle\alpha|\, \hat{X}_1\hat{X}_2\cdots\hat{X}_n\, |\alpha\rangle$ in the context of nonlinear Hamiltonians and in the resulting dynamical equations. These expressions typically arise when computing expectation values of polynomial terms in the Hamiltonian, especially when moving beyond the linear regime. The $\mathcal{D}$-algebra formalism provides a systematic approach to handling such terms within coherent states. This is achieved via repeated application of the identity [80, 81]

$$\langle\alpha|\, \hat{F}\hat{X}_i\, |\alpha\rangle = \frac{1}{\mathcal{M}}\mathcal{D}_{X_i}\left(\mathcal{M}f\right), \tag{2.29}$$

where $f(\alpha) = \langle\alpha|\, \hat{F}\, |\alpha\rangle$ and $\mathcal{M}(\alpha)$ is the normalisation factor of the non-normalised state.

This recursive relation enables expectation values of arbitrary operator products to be built up step-by-step, with each operator replaced by its corresponding differential action.

For the Heisenberg-Weyl algebra, the results simplify to [82]

$$\langle\alpha|\, \hat{F}\hat{a}\, |\alpha\rangle = \alpha f, \tag{2.30}$$

$$\langle\alpha|\, \hat{F}\hat{a}^\dagger\, |\alpha\rangle = e^{-|\alpha|^2}\frac{\partial}{\partial\alpha}\left(e^{|\alpha|^2}f\right). \tag{2.31}$$

These expressions are particularly useful for constructing classical approximations, where operator expectation values are replaced by functions on phase space.

In the following work, we note that a point in phase space can equivalently be labelled by either α or z, where α is the conventional complex coordinate used in Glauber coherent states and $z = \alpha/\sqrt{\hbar}$ is the rescaled coordinate that remains finite as $\hbar \to 0$. For calculations involving classical limits, it proves advantageous to work with coherent states labelled as $|z\rangle$, due to the explicit $\hbar$-independence of z.

Having established the mathematical foundations of coherent states and their representation in phase space, we now turn to their practical application in developing approximations that connect quantum systems to their classical counterparts. In the following section, we will demonstrate how the properties of coherent states developed above allow us to derive classical equations of motion from quantum dynamics in a systematic manner.

2.2 Coherent-State Approximation

The coherent-state approximation provides a method for connecting quantum dynamics with classical equations of motion. This well-known technique relies on evaluating the expectation values of Heisenberg's equations of motion for operators in coherent states in the limit $\hbar \to 0$ [46], a process often referred to as taking the classical limit. In this section, we review the derivation of the classical counterpart to the Hamiltonian and the associated classical equations of motion for approximating quantum dynamics in systems governed by the Heisenberg-Weyl algebra.

We begin by considering a Hamiltonian that is analytic in the canonical operators $\hat{q}$ and $\hat{p}$, expressed

as

$$\hat{\mathcal{H}} = \sum_{m,n} a_{mn} \hat{q}^m \hat{p}^n + \text{H.c.}, \tag{2.32}$$

where $a_{mn} \in \mathbb{C}$ and H.c. denotes the Hermitian conjugate.

It is known (and will be justified below) that to leading order in $\hbar$, the dynamics of the corresponding classical phase-space variables are governed by the classical Hamiltonian

$$h = \lim_{\hbar \to 0} \langle z | \hat{\mathcal{H}} | z \rangle , \tag{2.33}$$

given by the coherent-state expectation value of the quantum Hamiltonian. This limiting procedure defines the classical Hamiltonian function on phase space, often referred to as the classical limit of the quantum system.

The corresponding equations of motion are given by the classical Hamiltonian flow

$$\frac{\mathrm{d}q}{\mathrm{d}t} = \{q, h\}, \tag{2.34}$$

$$\frac{\mathrm{d}p}{\mathrm{d}t} = \{p, h\}. \tag{2.35}$$

We now outline the derivation of these classical equations of motion. Starting from the Heisenberg equation of motion for the operator $\hat{q}$,

$$\frac{\mathrm{d}}{\mathrm{d}t} \langle \hat{q} \rangle = -\frac{\mathrm{i}}{\hbar} \langle [\hat{q}, \hat{\mathcal{H}}] \rangle , \tag{2.36}$$

and substituting the analytic form of the Hamiltonian from the equation (2.32), we have

$$\frac{\mathrm{d} \langle \hat{q} \rangle}{\mathrm{d}t} = -\frac{\mathrm{i}}{\hbar} \sum_{m,n} a_{mn} \langle \hat{q}^m [\hat{q}, \hat{p}^n] \rangle + H.c. \tag{2.37}$$

To evaluate this expression, it is useful to consider each monomial term in equation (2.32) separately. A key step is to show that

$$-\frac{\mathrm{i}}{\hbar} \langle [\hat{q}, \hat{p}^n] \rangle = \{q, p^n\} + O(\hbar), \tag{2.38}$$

with equality in the semiclassical limit $\hbar \to 0$.

This identity can be proven by induction. For $n = 1$, the canonical commutation relation in (2.3) gives

$$-\frac{\mathrm{i}}{\hbar} \langle [\hat{q}, \hat{p}] \rangle = \{q, p\}, \tag{2.39}$$

which serves as the base case.

For illustrative purposes, we consider the case $n = 2$,

$$\begin{aligned} -\frac{\mathrm{i}}{\hbar}\langle[\hat{q},\hat{p}^2]\rangle &= -\frac{\mathrm{i}}{\hbar}(\langle\hat{p}[\hat{q},\hat{p}]\rangle + \langle[\hat{q},\hat{p}]\hat{p}\rangle) \\ &= 2\langle\hat{p}\rangle = 2p, \end{aligned} \tag{2.40}$$

and confirm by direct calculation that this equals the right-hand side

$$\{q, p^2\} = 2p\{q, p\} = 2p. \tag{2.41}$$

To complete the induction step, we first establish a key property of coherent-state expectation values using the $\mathcal{D}$-algebra identity from equation (2.30). Let $\hat{F}$ be an arbitrary analytic function of $\hat{q}$ and $\hat{p}$, and let $f = \langle\alpha|\,\hat{F}\,|\alpha\rangle$ denote its coherent-state expectation value.

If f is independent of $\hbar$, as is often the case by construction in semiclassical approximations, then we can express

$$\begin{aligned} \langle\hat{q}\hat{F}\rangle &= \sqrt{\frac{\hbar}{2}}\langle(\hat{a}+\hat{a}^\dagger)\hat{F}\rangle \\ &= \sqrt{\frac{\hbar}{2}}\left(e^{-|\alpha|^2}\frac{\partial}{\partial\alpha^*}\left(e^{|\alpha|^2}f\right) + \alpha^* f\right) \\ &= qf + \frac{\hbar}{2}\left(\frac{\partial f}{\partial q} + \mathrm{i}\frac{\partial f}{\partial p}\right), \end{aligned} \tag{2.42}$$

where the chain rule has been applied via

$$\frac{\partial f}{\partial\alpha^*} = \frac{\partial f}{\partial q}\frac{\partial q}{\partial\alpha^*} + \frac{\partial f}{\partial p}\frac{\partial p}{\partial\alpha^*}, \tag{2.43}$$

$$\text{with} \quad \frac{\partial q}{\partial\alpha^*} = \sqrt{\frac{\hbar}{2}}, \quad \frac{\partial p}{\partial\alpha^*} = \mathrm{i}\sqrt{\frac{\hbar}{2}}. \tag{2.44}$$

Since f has no $\hbar$ dependence, it follows that

$$\langle\hat{q}\hat{F}\rangle = qf + O(\hbar). \tag{2.45}$$

This factorisation property is central to establishing quantum-classical correspondence [12], and it allows us to proceed with the induction step. Assuming that equation (2.38) holds for some integer $n \geq 1$, we consider the case for $n+1$

$$\begin{aligned} -\frac{\mathrm{i}}{\hbar}\langle[\hat{q},\hat{p}^{n+1}]\rangle &= -\frac{\mathrm{i}}{\hbar}(\langle\hat{p}[\hat{q},\hat{p}^n]\rangle + \langle[\hat{q},\hat{p}^n]\hat{p}\rangle) \\ &= -2\frac{\mathrm{i}}{\hbar}(\langle\hat{p}\rangle\langle[\hat{q},\hat{p}^n]\rangle + O(\hbar) \\ &= 2p\{q,p^n\} + O(\hbar) \\ &= \{q,p^{n+1}\} + O(\hbar), \end{aligned} \tag{2.46}$$

and thus by induction we have shown that equation (2.38) holds.

Finally, returning to the Heisenberg equation of motion,

$$\frac{\mathrm{d}}{\mathrm{d}t}\langle\hat{q}\rangle = -\frac{\mathrm{i}}{\hbar}\langle[\hat{q},\hat{\mathcal{H}}]\rangle\,, \tag{2.47}$$

and using the above results we obtain

$$\frac{\mathrm{d}\langle\hat{q}\rangle}{\mathrm{d}t} = \{q,h\} + O(\hbar), \tag{2.48}$$

which implies that in the classical limit,

$$\frac{\mathrm{d}q}{\mathrm{d}t} = \{q,h\}. \tag{2.49}$$

The same reasoning applies to $\frac{\mathrm{d}p}{\mathrm{d}t}$, completing the derivation of the classical equations of motion.

In summary, the evolution of expectation values for position and momentum for an initial coherent state follows the corresponding classical dynamics to leading order in $\hbar$, in accordance with the Ehrenfest theorem [83]. This result establishes the coherent-state approximation as a classical limit of quantum dynamics. Building on this, one can extend the approximation from the dynamics of a single point in phase space to the evolution of an entire distribution. In particular, using the Husimi distribution, we obtain a phase-space representation that enables a more global semiclassical description of quantum state evolution.

2.3 Semiclassical Husimi Approximation

To extend the coherent-state approximation beyond the evolution of a single phase-space point, we consider the time evolution of the entire Husimi distribution associated with the arbitrary initial state $|\psi_0\rangle$. The Husimi function at time t is given by

$$Q_{\psi_0}(z,t) = |\langle z|\,\hat{U}(t)\,|\psi_0\rangle|^2, \tag{2.50}$$

where $\hat{U}(t) = e^{-\mathrm{i}\hat{\mathcal{H}}t/\hbar}$ is the time-evolution operator for a time-independent Hamiltonian $\hat{\mathcal{H}}$.

While the conventional approach would be to apply $\hat{U}(t)$ to the initial state $|\psi_0\rangle$, we instead apply the time evolution operator to the left. That is, we evolve the coherent state $|z\rangle$ using the adjoint operator

$$|\epsilon(t)\rangle = \hat{U}^\dagger(t)\,|z\rangle\,. \tag{2.51}$$

Since $\hat{U}(t) = e^{-\mathrm{i}\hat{\mathcal{H}}t/\hbar}$, it follows that $\hat{U}^\dagger(t) = e^{\mathrm{i}\hat{\mathcal{H}}t/\hbar} = e^{-\mathrm{i}(-\hat{\mathcal{H}})t/\hbar}$, which corresponds to evolution under the time-reversed Hamiltonian $-\hat{\mathcal{H}}$. The state $|\epsilon(t)\rangle$ can therefore be interpreted as the coherent state $|z\rangle$ evolved backward in time under $-\hat{\mathcal{H}}$.

In general, the state $|\epsilon(t)\rangle$ is not a coherent state. However, under the coherent-state approximation,

we approximate $|\epsilon(t)\rangle$ with a time-dependent coherent state $|\tilde{z}(t)\rangle$ where

$$\tilde{z}(t) = \frac{\tilde{q}(t) + \mathrm{i}\tilde{p}(t)}{\sqrt{2}}, \tag{2.52}$$

and $\tilde{q}(t)$ and $\tilde{p}(t)$ is the point obtained by evolving the initial point (q, p) under the Hamiltonian flow generated by the negative classical Hamiltonian h.

Since the Husimi distribution depends only on the modulus of the overlap and not on the relative phase, we can neglect the overall phase evolution of $|\epsilon(t)\rangle$ in this approximation therefore the time-evolved Husimi distribution is then given by

$$Q(z, t) = |\langle\tilde{z}(t)|\psi_0\rangle|^2. \tag{2.53}$$

To find an expression for the Husimi function at a given phase space point z and time t, we must determine which initial condition at $t = 0$ evolved to reach this point under the classical flow. This requires mapping each phase space coordinate z back to its corresponding initial point using the backward Hamiltonian flow of h.

Denoting this backward flow by $\Phi_{-t}(z)$, we obtain

$$Q(z, t) = |\langle\tilde{z}(t)|\psi_0\rangle|^2 = Q_{\psi_0}(\Phi_{-t}(z)). \tag{2.54}$$

This equation reveals that the time evolution of the Husimi distribution corresponds to the transport of the initial distribution $Q_{\psi_0}(z)$ along the classical Hamiltonian flow. Here, $\Phi_{-t}(z)$ identifies which initial phase space point evolved to the current location z, allowing us to evaluate the initial Husimi distribution at that pre-image point.

This formulation recovers the leading-order semiclassical result derived by Milburn [66], who obtained the same flow law as the $\hbar \to 0$ limit of the differential equation for the evolution of $Q(z, t)$. In what follows, we illustrate this approximation using Milburn's original example, the Kerr anharmonic oscillator. Throughout the remainder of this chapter, we set $\hbar = 1$ and work in the rescaled variable z when addressing specific examples.

2.4 Kerr Hamiltonian

A standard example of an anharmonic oscillator is given by the Hamiltonian

$$\hat{\mathcal{H}} = \hat{a}^\dagger\hat{a} + \beta\,\hat{a}^\dagger\hat{a}^\dagger\hat{a}\hat{a}, \tag{2.55}$$

where $\beta \in \mathbb{R}^+$. This model describes a harmonic oscillator with a Kerr-type nonlinearity and is commonly referred to as the Kerr Hamiltonian. Physically, it models photons in a nonlinear medium and also appears as the single-mode limit of the Bose-Hubbard Hamiltonian, used to describe cold bosonic atoms with two-body onsite interactions [66].

This Hamiltonian has the advantage of being analytically solvable in both the quantum and classical

pictures, while still exhibiting nontrivial quantum-classical discrepancies. Its eigenvalues are

$$E_n = n + \beta n(n-1), \tag{2.56}$$

which lead to periodic quantum dynamics when $\beta \in \mathbb{Q}$. In particular, for $\beta = \frac{1}{4}$, the system undergoes a full revival of an initial coherent state after a finite time. This revival phenomenon was first demonstrated by Yurke and Stoler [84], who showed that coherent states evolving under the Kerr Hamiltonian can form superpositions of macroscopically distinguishable quantum states.

Semiclassical Husimi dynamics for the Kerr Hamiltonian were subsequently investigated by Milburn [66]. Here, we briefly review the quantum-classical correspondence in this model to set the stage for the generalisations to non-Hermitian dynamics discussed later in the thesis.

Under the coherent-state approximation, the classical Hamiltonian corresponding to $\hat{\mathcal{H}}$ takes the form

$$h = \frac{1}{2}(p^2 + q^2) + \frac{\beta}{4}(p^2 + q^2)^2. \tag{2.57}$$

The classical Hamiltonian h gives rise to the following equations of motion under the coherent-state approximation

$$\frac{\mathrm{d}q}{\mathrm{d}t} = p + \beta p(q^2 + p^2), \tag{2.58}$$

$$\frac{\mathrm{d}p}{\mathrm{d}t} = -q - \beta q(q^2 + p^2). \tag{2.59}$$

Introducing polar coordinates via $q = r\cos\theta, p = r\sin\theta$, these equations can be solved and the resulting trajectories can be written in terms of (r, θ) as

$$r(t) = r_0, \tag{2.60}$$

$$\theta(t) = \theta_0 - (1 + \beta r_0^2)t, \tag{2.61}$$

where r_0, θ_0 are the initial conditions.

For $\beta > 0$, the system has a single centre (elliptic fixed point in Hamiltonian dynamics) located at the origin, meaning that nearby trajectories remain bounded and orbit the fixed point. All trajectories lie on concentric circles around this fixed point, with the radius r conserved. However, the angular velocity depends on the radius: trajectories further from the origin evolve faster in phase space than those closer in. This radial dependence of frequency is a hallmark of the Kerr nonlinearity and results in dephasing over time for initially localised distributions [85].

Figure 2.2 illustrates this behaviour for $\beta = \frac{1}{4}$. Each trajectory begins at $p = 0, q > 0$ and is evolved up to time $t = \frac{\pi}{20}$, highlighting the angular shearing effect in phase space due to the nonlinear interaction.

To illustrate the quantum-classical correspondence in more detail, we consider the evolution of an initial coherent state centred at $(q, p) = (-3, 5)$. While the coherent-state approximation yields oscillatory dynamics around this initial point, the full quantum evolution of the expectation values

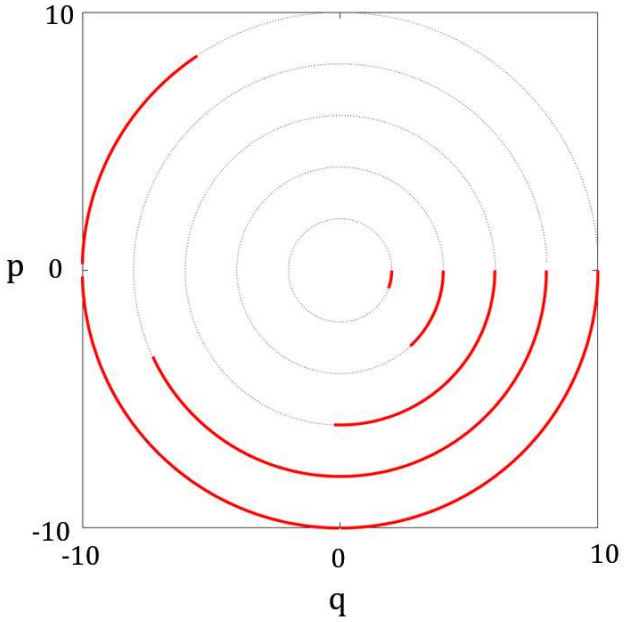


Figure 2.2: Trajectory of the evolution of coherent state approximation for the Kerr Hamiltonian with $\beta = \frac{1}{4}$ plotted at different radii. For each periodic orbit the trajectory at each radius is shown for the time interval $0 < t < \pi/20$ with solid red lines and for the remainder of the period of the orbit from $\pi/20 \leq t < T$ with dotted black lines.

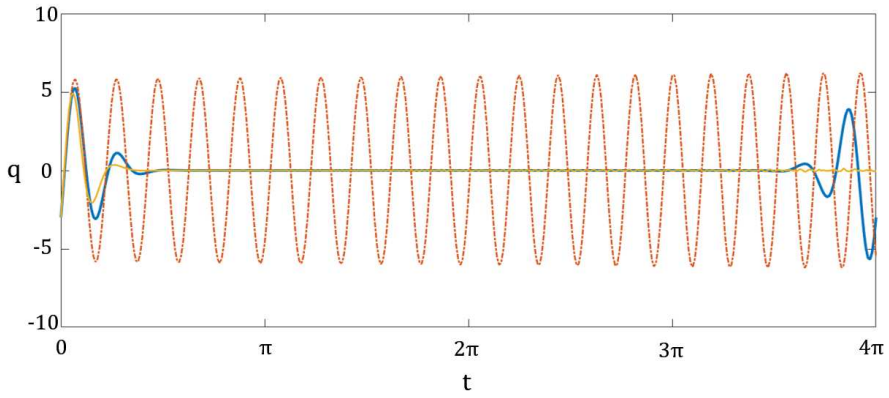


Figure 2.3: Comparison of values of q between quantum dynamics (solid blue line), semiclassical Husimi (solid yellow line) and the coherent-state approximation (dotted orange line) for the Kerr Hamiltonian for an initial coherent state centred at $(q, p) = (-3, 5)$.

$\langle \hat{q} \rangle$ and $\langle \hat{p} \rangle$ exhibits the characteristic breakdown and revival behaviour of anharmonic systems. This behaviour is shown in Figure 2.3, which compares the time evolution of $\langle \hat{q} \rangle$ (solid blue line), the coherent-state approximation for q (dotted orange line), and the semiclassical Husimi approximation (solid yellow line).

The initial deviation from the classical trajectory arises from the spreading and deformation of the Husimi distribution, caused by the variation in orbital frequencies with radius. This effect is well captured by the semiclassical Husimi dynamics, which go beyond the single-trajectory coherent-state approximation by evolving the full phase-space distribution.

To further visualise the dynamics, Figure 2.4 shows snapshots of the Husimi distribution at early times: the top row depicts the full quantum evolution, while the bottom row shows the corresponding semiclassical Husimi approximation. These plots correspond to an initial coherent state centred at $(q, p) = (-3, 5)$, matching the trajectories shown in Figure 2.2.

At short times, the semiclassical Husimi approximation captures the non-linear deformation of the initial coherent state with high fidelity. The phase-space flow induced by the Kerr nonlinearity causes the initial Gaussian to stretch and shear, an effect clearly visible in both the quantum and semiclassical distributions. A white line indicating the classical trajectory is overlaid to guide the eye; however, due to the nonlinear nature of the dynamics, the Husimi distribution does not remain sharply localised along this trajectory as time evolves. Instead, while the semiclassical Husimi distribution develops increasingly fine structure due to ongoing shearing, the full quantum Husimi remains comparatively broad. This discrepancy reflects a fundamental limitation: the quantum Husimi distribution cannot resolve phase-space features below the scale set by the uncertainty principle. In our examples, $\hbar = 1$, setting the effective resolution limit of the quantum phase-space representation. Consequently, while the classical trajectory provides initial insight, it becomes less relevant at later times when quantum spreading dominates.

For longer times, the semiclassical Husimi distribution will continue to evolve into a finer and finer spiral structure whilst the quantum Husimi distribution begins to exhibit coherent effects. In Figure 2.5 we depict the quantum Husimi distributions for the same initial coherent state as in Figure 2.4, but for longer times. For the quantum evolution one observes the appearance of “holes" due to quantum interference effects at time $t = \frac{3\pi}{10}$ (left) and quantum revival with states that are superpositions of four coherent states at time $t = \pi$ (middle) and two coherent states at time $t = 2\pi$ (right).

2.5 Non-Hermitian Quantum Dynamics

At its inception, quantum mechanics was developed to explain physical phenomena that could not be accounted for by classical physics, such as atomic spectra and the photoelectric effect. These phenomena involved measurable quantities, such as energy and position, that were inherently real-valued, motivating the representation of observables by Hermitian operators, whose eigenvalues are guaranteed to be real. The resulting formalism, centred on Hermitian operators and unitary time

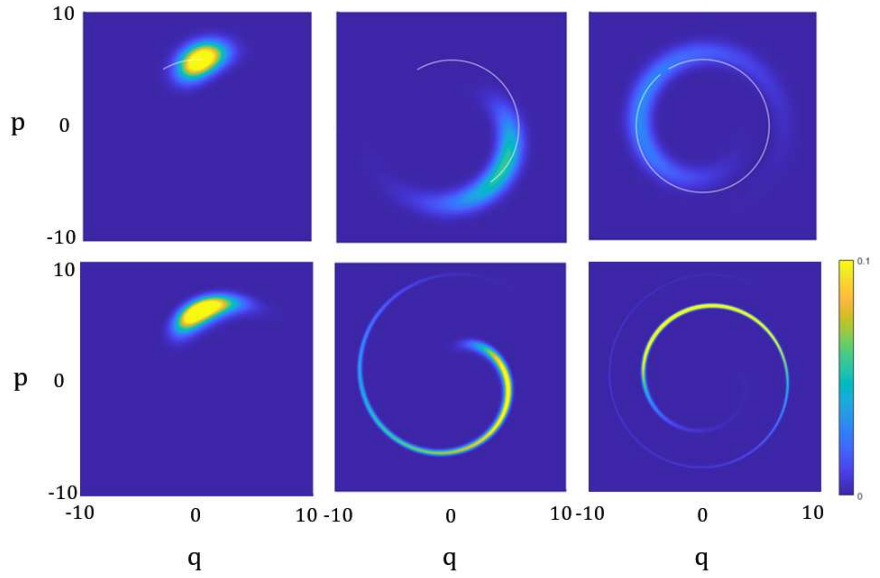


Figure 2.4: Evolution of the quantum Husimi distribution (top row) and the semiclassical Husimi distribution (bottom row) for the Kerr Hamiltonian with $\beta = \frac{1}{4}$ for an initial coherent state centred at $(q, p) = (-3, 5)$. The columns correspond to different snapshots of the evolution in time with $t = \frac{\pi}{50}$ (left), $t = \frac{\pi}{10}$ (middle) and $t = \frac{\pi}{5}$ (right).

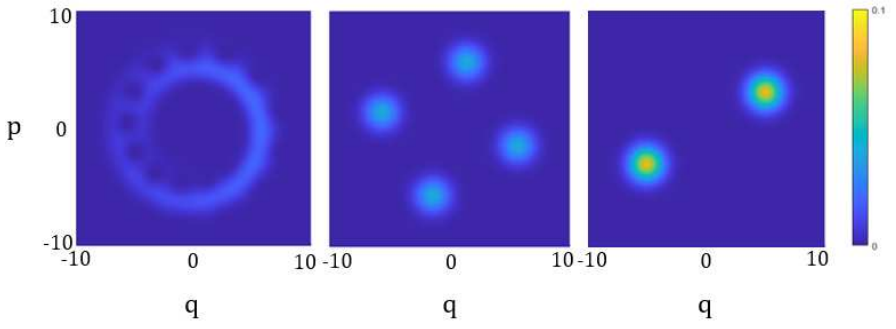


Figure 2.5: Evolution of the quantum Husimi distribution for the Kerr Hamiltonian with $\beta = \frac{1}{4}$ for an initial coherent state centred at $(q, p) = (-3, 5)$ at $t = \frac{3\pi}{10}$ (left), $t = \pi$ (middle) and $t = 2\pi$ (right).

evolution, naturally described isolated, or closed, systems, those not interacting with an external environment. Hermitian operators ensure real-valued measurement outcomes, while unitarity guarantees the conservation of probability. Although these assumptions were not imposed for idealistic reasons, they proved remarkably effective for describing a broad class of physically relevant systems [30].

Since its inception, quantum mechanics research has gradually evolved from foundational verification to practical implementation. Earlier experimental efforts were primarily aimed at testing the predictions of quantum theory and probing fundamental quantum phenomena. These included the observation of Bose-Einstein condensation [86], interference experiments with massive particles [87], quantum Hall effects, violations of Bell inequalities [88], and the realisation of quantum entanglement in optical and atomic systems. In these contexts, the emphasis was on isolating quantum systems as much as possible, treating environmental coupling as an unwanted source of noise to be minimised.

However, the field has increasingly pivoted towards harnessing quantum systems for many technological applications, with quantum computing being a particularly prominent example [89]. Unlike classical computers, whose capacity scales linearly with the number of bits, quantum computers scale exponentially with each added qubit. This exponential advantage opens the door to powerful applications in cryptography, drug discovery, optimisation and machine learning [89, 90].

This shift towards real-world implementation brings with it new challenges, chief among them the need to develop more accurate models of inherently non-linear quantum systems, and to understand open quantum systems that interact with their surrounding environment. Non-linearities introduce deviations from idealised linear quantum evolution, compromising applications such as state preparation and quantum control, while environmental interactions give rise to essential features such as decoherence, particle loss and dissipation. Both effects must be carefully modelled and controlled for quantum technologies to scale reliably [71, 91, 92].

As quantum technologies have advanced, there has been a shift from theoretical models based on idealised laboratory conditions toward the development of real-world applications that incorporate and model the effects of decoherence, noise, and other environmental perturbations. In this context, open quantum systems, those that interact with their surrounding environment, play a central role. These systems are most generally described by Lindblad-type master equations [17, 93]. Within this general framework, non-Hermitian Hamiltonians emerge as an effective description in regimes where environmental effects manifest as coherent gain, loss, or decay processes, providing the theoretical foundation for this thesis.

In single-particle quantum mechanics, complex energy values with negative imaginary parts naturally arise in models of decay, scattering and absorption. These are associated with a loss of norm in the wave function, which can be interpreted as the decay of probability. Positive imaginary parts, by contrast, imply amplification or gain, unphysical in closed quantum systems but meaningful in other wave-based settings, such as optics or acoustics, where the Schrödinger equation serves as a mathematical analogue.

In many-particle quantum systems, the use of non-Hermitian Hamiltonians is more subtle [30]. Since the norm of the wave function does not, in general, have a probabilistic interpretation for an ensemble of decaying particles, complex energies cannot directly represent loss. However, when post-selection is applied, restricting attention to only those experimental runs in which no particle decayed, non-Hermitian dynamics can effectively describe the conditional evolution of the system. In this context, the norm of the wave function encodes the probability that all particles remain unmeasured during the interval.

We denote a general non-Hermitian Hamiltonian as

$$\hat{\mathcal{K}} = \hat{\mathcal{H}} + \mathrm{i}\hat{\Gamma}, \tag{2.62}$$

where $\hat{\mathcal{H}}, \hat{\Gamma}$ are Hermitian operators. Unlike Hermitian Hamiltonians, $\hat{\mathcal{K}}$ can have complex eigenvalues, which reflect non-conservation of norm and are often interpreted in terms of gain or loss processes. In addition the eigenvectors of non-Hermitian operators are generally non-orthogonal, and may not form a complete orthonormal basis. This leads to subtleties in defining observables and requires the use of biorthogonal sets of left and right eigenvectors to preserve a consistent probability interpretation [94].

Away from the exceptional points, points where the eigenvalues and the eigenvectors of the Hamiltonian coalesce thereby making it non-diagonalisable, the eigenvectors of a non-Hermitian Hamiltnian $\hat{\mathcal{K}}$ form a complete basis. In this case,the time evolution of an initial state $|\psi(0)\rangle = \sum c_n |\phi_n\rangle$, where $|\phi_n\rangle$ are the right eigenvectors of $\hat{\mathcal{K}}$, is given by

$$\begin{aligned} |\psi(t)\rangle &= \sum_n e^{-\mathrm{i}\hat{\mathcal{K}}t/\hbar} c_n |\phi_n\rangle , \\ &= \sum_n c_n e^{-\mathrm{i}(\epsilon_n + \mathrm{i}\gamma_n)t/\hbar} |\phi_n\rangle , \\ &= \sum_n c_n e^{\gamma_n t/\hbar} e^{-\mathrm{i}\epsilon_n t/\hbar} |\phi_n\rangle \end{aligned} \tag{2.63}$$

where the eigenvalues are $E_n = (\epsilon_n + \mathrm{i}\gamma_n)$. Although the eigenvalues may be real, the non-orthogonality of eigenvectors means the norm of a generic state does not remain constant over time. Even when $\gamma_n = 0$, the time-dependent inner product

$$\langle\psi(t)|\psi(t)\rangle = \sum_{n,m} c_n^* c_m e^{-\mathrm{i}(\epsilon_m - \epsilon_n)t/\hbar} \langle\phi_n|\phi_m\rangle . \tag{2.64}$$

can show significant oscillatory behaviour due to this non-orthogonality.

A particularly well-studied subclass of non-Hermitian Hamiltonians are those with PT-symmetry, where the Hamiltonian commutes with the combined parity-time operator: $[\hat{P}\hat{T}, \hat{\mathcal{H}}] = 0$ [95, 96]. In this framework, $\hat{P}$ is the parity operator with $\hat{P}^2 = \hat{I}$, and $\hat{T}$ is the anti-linear time-reversal operator satisfying $\hat{T}i\hat{T}^{-1} = -i$ and acting on wavefunctions as $\hat{T}\psi(x) = \psi^*(x)$. When all eigenstates of $\hat{H}$ are also eigenstates of $\hat{P}\hat{T}$ (unbroken PT symmetry), the spectrum is real; when this condition is lost, eigenvalues appear in complex-conjugate pairs.

$\hat{P}$ is the parity operator with $\hat{P}^2 = \hat{I}$ and $[\hat{P}, \hat{T}] = 0$, while $\hat{T}$ is the anti-linear time-reversal

operator that sends $\mathrm{i} \to -\mathrm{i}$. When the PT symmetry is unbroken, all eigenvalues of $\hat{\mathcal{H}}$ are real; when it is broken, complex eigenvalues emerge.

Whether or not the spectrum is real has a significant impact on long-term dynamics:

In the case of complex eigenvalues, long-term behaviour is typically dominated by the subset of eigenstates associated with the largest imaginary part (growth rate). Defining this dominant set as D, the state evolves asymptotically as

$$|\psi(t)\rangle \to \sum_{n \in D} d_n e^{\gamma_n t/\hbar} e^{-\mathrm{i}\epsilon_n t/\hbar} |\phi_n\rangle \,. \tag{2.65}$$

Here, the coefficients d_n are given by projections onto the biorthogonal left eigenvectors $|\phi_n^L\rangle$, i.e., $d_n = \langle \phi_n^L | \psi(0) \rangle$. This formalism is necessary since $\langle \phi_n | \phi_m \rangle \neq \delta_{nm}$ in the non-Hermitian case.

On the other hand, when the system is PT-symmetric and unbroken, the eigenvalues are real, and the norm of the state remains bounded under time evolution. With an appropriate inner product (e.g., involving the CPT operator), the system can exhibit dynamics similar to Hermitian evolution, including periodic and quasi-periodic motion depending on the spectral structure.

In either regime, the structure of the eigenvalue spectrum and the overlaps of the initial state with the eigenbasis (or biorthogonal basis) determine the system's long-term behaviour. The analysis of this spectral data is therefore the essential first step in understanding non-Hermitian quantum dynamics.

We now derive the dynamics of expectation values under linear non-Hermitian Hamiltonians. Starting from the generalised Heisenberg equation[30] for an operator $\hat{A}$, we obtain

$$\mathrm{i}\hbar \frac{\mathrm{d}}{\mathrm{d}t} \langle \hat{A} \rangle = \langle [\hat{A}, \hat{\mathcal{H}}] \rangle + \mathrm{i}(\langle [\hat{A}, \hat{\Gamma}]_+ \rangle - 2 \langle \hat{A} \rangle \langle \hat{\Gamma} \rangle), \tag{2.66}$$

where $\hat{\mathcal{K}} = \hat{\mathcal{H}} + \mathrm{i}\hat{\Gamma}$ and the anticommutator is denoted by $[\hat{A}, \hat{\Gamma}]_+$.

To interpret the second term, we evaluate a covariance-like quantity $\Delta_{AB} = \langle [\hat{A}, \hat{B}]_+ \rangle - 2 \langle \hat{A} \rangle \langle \hat{B} \rangle$, for the canonical operators $\hat{q}, \hat{p}$ in a coherent state. One finds

$$\Delta_{qq} = \Delta_{pp} = 1, \qquad \Delta_{qp} = 0, \tag{2.67}$$

which we recognise as the components of the metric bracket on the canonical phase space spanned by (q, p). This yields the following relationship for the generators of $\mathfrak{h}_1$

$$\Delta_{qq} = \{\!\{q, q\}\!\}, \qquad \Delta_{pp} = \{\!\{p, p\}\!\}, \qquad \Delta_{qp} = \{\!\{q, p\}\!\}, \tag{2.68}$$

establishing the analogous relationship between the covariance term and the metric bracket as we did for commutation relationship with the Poisson bracket. A direct consequence of this result is that, for a linear non-Hermitian Hamiltonian defined on the Heisenberg-Weyl algebra, a Glauber coherent state remains coherent throughout the evolution. The dynamics consist of two components, symplectic motion on phase space governed by the classical Hamiltonian h,

and gradient flow arising from the classical non-Hermitian component $\gamma = \langle \Gamma \rangle$. The resulting equations of motion are

$$\frac{\mathrm{d}q}{\mathrm{d}t} = \{q, h\} + \{\!\{q, \gamma\}\!\}, \tag{2.69}$$

$$\frac{\mathrm{d}p}{\mathrm{d}t} = \{p, h\} + \{\!\{p, \gamma\}\!\}. \tag{2.70}$$

The dynamical equation for the the time evolution of the norm is given by

$$\begin{aligned}
\frac{\mathrm{d}n}{\mathrm{d}t} &= \frac{\mathrm{d}}{\mathrm{d}t} \langle \psi(t) | \psi(t) \rangle \,, \\
&= \frac{\mathrm{d} \langle \psi(t) |}{\mathrm{d}t} | \psi(t) \rangle + \langle \psi(t) | \frac{\mathrm{d} | \psi(t) \rangle}{\mathrm{d}t}, \\
&= \frac{\mathrm{i}}{\hbar} \langle \psi(t) | \hat{\mathcal{K}}^\dagger | \psi(t) \rangle - \frac{\mathrm{i}}{\hbar} \langle \psi(t) | \hat{\mathcal{K}} | \psi(t) \rangle \,,
\end{aligned} \tag{2.71}$$

which under the coherent-state approximation yields

$$\hbar \frac{\mathrm{d}n}{\mathrm{d}t} = 2\gamma n, \tag{2.72}$$

where $\gamma = \langle \Gamma \rangle$.

This result reflects the exponential growth or decay of the state norm depending on the sign of γ, and captures the influence of non-Hermiticity in the simplest case.

2.5.1 Non-Hermitian Harmonic Oscillator

As a representative example of non-Hermitian quantum dynamics, we now consider the non-Hermitian harmonic oscillator [45, 97]. This system provides a simple yet instructive example of Schrödinger-type evolution under a non-Hermitian Hamiltonian and is frequently employed as a phenomenological model for decay and dissipation in open quantum systems. Notably, the non-Hermitian harmonic oscillator exhibits exact classical–quantum correspondence, making it a valuable test case for validating phase-space approximation methods in the non-Hermitian regime.

The Hamiltonian is given by

$$\hat{\mathcal{K}} = (\omega + \mathrm{i}\kappa) \left(\hat{a}^\dagger \hat{a} + \frac{1}{2} \hat{I} \right), \tag{2.73}$$

where $\omega \in \mathbb{R}$ determines the harmonic frequency. The parameter $\kappa \in \mathbb{R}$ controls the strength of non-Hermiticity. In this chapter, we choose $\kappa < 0$, corresponding to a decaying system. This choice ensures that the non-Hermitian part models energy loss, as expected for open quantum systems with damping.

The eigenstates are the Fock states $|n\rangle$, with corresponding eigenvalues $E_n = (\omega + \mathrm{i}\kappa) \left(n + \frac{1}{2} \right)$, implying that the ground state $|0\rangle$ dominates the long-time behaviour due to its minimal imaginary component. The evolution under this Hamiltonian combines unitary rotation (from the real part of the spectrum) with exponential decay (from the imaginary part).

To demonstrate that the coherent state remains coherent under the action of a non-Hermitian Hamiltonian, we consider the evolution of an initial coherent state $|z_c\rangle$ under the non-Hermitian harmonic oscillator. Despite the non-unitarity of the evolution, the coherent-state structure is preserved [45]. This is somewhat surprising, as non-Hermitian dynamics typically lead to norm loss and deformation of quantum states. However, in this special case, the Hamiltonian remains linear in the Heisenberg-Weyl algebra generators, ensuring the time-evolution operator acts within the coherent-state manifold. The time evolution of the state is given by

$$|\psi(t)\rangle = e^{-\mathrm{i}(\omega+\mathrm{i}\kappa)\left(\hat{a}^\dagger\hat{a}+\frac{1}{2}\hat{I}\right)}\,|z_c\rangle\,. \tag{2.74}$$

As the eigenstates of the non-Hermitian harmonic oscillator are the Fock states, the action of $e^{\hat{a}^\dagger\hat{a}}$ on the state $|n\rangle$ is $e^n\,|n\rangle$, which enables the time evolved state to be expressed as

$$|\psi(t)\rangle = e^{-\mathrm{i}\frac{(\omega+\mathrm{i}\kappa)t}{2}}e^{-\frac{|z_c|^2}{2}}\sum_n \frac{(z_c e^{(-\mathrm{i}\omega t+\kappa t)})^n}{\sqrt{n!}}\,|n\rangle\,. \tag{2.75}$$

Defining

$$z_c(t) = z_c e^{-\mathrm{i}\omega t+\kappa t}, \tag{2.76}$$

we can express the associated normalised coherent state as

$$|z_c(t)\rangle = e^{-\frac{|z_c|^2}{2}}e^{2\kappa t}\sum_n \frac{(z_c e^{(-\mathrm{i}\omega t+\kappa t)})^n}{\sqrt{n!}}\,|n\rangle \tag{2.77}$$

which gives the final form of the time-evolved state as a coherent state with normalisation and phase prefactors

$$|\psi(t)\rangle = e^{-\mathrm{i}\frac{\omega+i\kappa}{2}t}e^{-\frac{|z_c|^2}{2}(1-e^{2\kappa t})}|z_c(t)\rangle. \tag{2.78}$$

This confirms that the coherent state remains coherent under time evolution. The dynamics consist of an exponentially damped spiral trajectory in the complex z-plane, governed by the $|z_c(t)\rangle$ term, and an exponentially reducing norm from the component of the prefactor $e^{\frac{\kappa t}{2}+\frac{|z_c|^2}{2}e^{2\kappa t}}$.

To analyse the corresponding classical dynamics, we work in terms of the phase-space variable z rather than the canonical variables q and p, as this simplifies the calculations due to the presence of the term $\hat{a}^\dagger\hat{a}$ in the Hamiltonian. The classical counterpart to the Hamiltonian is defined by taking the expectation value in a coherent state

$$k = \langle\hat{\mathcal{K}}\rangle = (\omega+\mathrm{i}\kappa)\left(zz^* + \frac{1}{2}\right). \tag{2.79}$$

Applying the semiclassical equations of motion derived earlier, the dynamics of the phase-space coordinate z obey

$$\begin{aligned}\frac{\mathrm{d}z}{\mathrm{d}t} &= \{z,h\} + \{\!\{z,\gamma\}\!\},\\ &= \{z,z^*\}\frac{\partial h}{\partial z^*} + \{\!\{z,z^*\}\!\}\frac{\partial\gamma}{\partial z^*},\\ &= -\mathrm{i}\omega z + \gamma z,\end{aligned} \tag{2.80}$$

using $\{z, z^*\} = -\mathrm{i}$, and $\{\{z, z^*\}\} = 1$ (see Appendix B for details).

This agrees with the quantum result in equation (2.76), confirming exact correspondence between the classical and quantum trajectories. The motion consists of a clockwise spiral in phase space, tending toward the origin, as depicted in Figures 2.6-2.7.

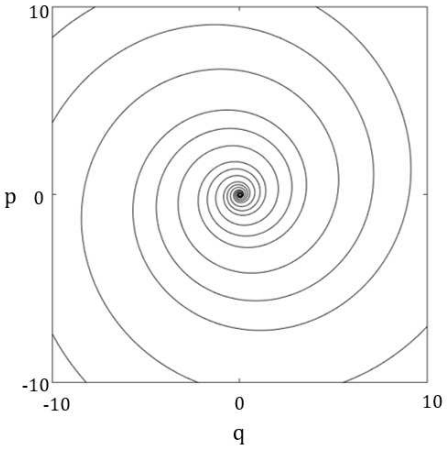


Figure 2.6: Phase-space trajectories for the non-Hermitian harmonic oscillator with $\omega = 1, \kappa = -0.15$.

To illustrate the exact quantum–classical correspondence in a non-Hermitian setting, Figure 2.7 presents the evolution of a coherent state under the non-Hermitian harmonic oscillator using a normalised Husimi distribution. The coherent state's trajectory exhibits both decay and rotation, reflecting the influence of the complex energy spectrum. The initial state is centred at $(q, p) = (4, 2)$, with parameters $\omega = 1$ and $\kappa = -0.15$.

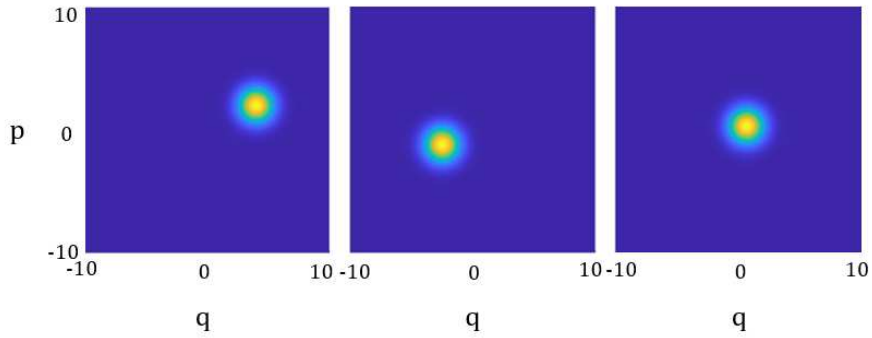


Figure 2.7: Evolution of the quantum Husimi distribution for the non-Hermitian harmonic oscillator Hamiltonian with $\omega = 1, \kappa = -0.15$. for an initial coherent state centred at $(q, p) = (4, 2)$ at $t = 0$ (left), $t = \pi$ (middle) and $t = 4\pi$ (right).

2.6 Coherent-State Approximations for Non-Hermitian Hamiltonians

Building on the coherent-state methods established for Hermitian systems, we now extend the coherent-state approximation framework to systems governed by non-Hermitian Hamiltonians.

We consider Hamiltonians that belong to the complexified universal enveloping algebra of a Lie algebra and admit a decomposition of the form

$$\hat{\mathcal{K}} = \hat{\mathcal{H}} + \mathrm{i}\hat{\Gamma}, \tag{2.81}$$

where $\hat{\mathcal{H}}$ and $\hat{\Gamma}$ are both Hermitian operators. This structure is general enough to describe non-conservative dynamics including dissipation, amplification, and effective decay processes commonly observed in open quantum systems.

In the calculations below, we will show that to leading order in $\hbar$, the dynamics of the phase-space coordinates $q = \langle \hat{q} \rangle$ and $p = \langle \hat{p} \rangle$ are governed by a combination of symplectic and gradient flows

$$\frac{\mathrm{d}q}{\mathrm{d}t} = \{q, h\} + \{\!\{q, \gamma\}\!\}, \tag{2.82}$$

$$\frac{\mathrm{d}p}{\mathrm{d}t} = \{p, h\} + \{\!\{p, \gamma\}\!\}, \tag{2.83}$$

where the effective classical Hamiltonians are given by

$$h = \lim_{\hbar \to 0} \langle z | \, \hat{\mathcal{H}} \, | z \rangle \,, \qquad \gamma = \lim_{\hbar \to 0} \langle z | \, \hat{\Gamma} \, | z \rangle \,, \tag{2.84}$$

and the Poisson bracket $\{\cdot, \cdot\}$ captures the symplectic contribution from the Hermitian part $\hat{\mathcal{H}}$, while the metric bracket $\{\!\{\cdot, \cdot\}\!\}$ accounts for the non-Hermitian gain/loss dynamics arising from $\hat{\Gamma}$. This decomposition reveals that non-Hermitian effects introduce a gradient flow on phase space, which is structurally distinct from the symplectic motion induced by Hermitian generators.

Previously, we derived the classical limit of Heisenberg's equations for Hermitian Hamiltonians using the $\mathcal{D}$-algebra formalism. For the anti-Hermitian part, a key difference emerges, the corresponding contribution to the classical dynamics involves a symmetric bracket rather than the antisymmetric Poisson bracket. In particular, while the Hermitian term gives rise to Hamiltonian flow, the anti-Hermitian term leads to a dissipative or amplifying flow aligned with the gradient of γ.

For linear observables (i.e., $n = 1$), this follows directly from the identity established in equation (2.69). The generalisation to polynomial observables proceeds analogously via induction, employing the same $\mathcal{D}$-algebra techniques used in the Hermitian case. We omit the full derivation here for brevity, but note that the symmetric structure of the metric bracket naturally arises when computing expectation values involving anti-Hermitian generators.

The key step involves the following identity

$$-\tfrac{1}{\hbar} \left(\langle [\hat{q}, \hat{p}^n]_+ \rangle - \langle \hat{q} \rangle \, \langle \hat{p}^n \rangle \right) = \{\!\{q, p^n\}\!\} + O(\hbar), \tag{2.85}$$

which holds in the limit $\hbar \to 0$. This result connects the expectation value of the symmetrised operator product with the metric bracket of the corresponding classical functions, and reflects the gradient component of the flow.

Combining this with the previously derived expression for the time derivative of $\langle \hat{q} \rangle$, we obtain

$$\begin{aligned} \mathrm{i}\hbar \frac{\mathrm{d}}{\mathrm{d}t} \langle \hat{q} \rangle &= \langle [\hat{q}, \hat{\mathcal{K}}] \rangle \\ &= \mathrm{i}\hbar \{q, h\} + \mathrm{i}\hbar \{\!\{q, \gamma\}\!\} + O(\hbar^2), \end{aligned} \tag{2.86}$$

which leads to the classical equation of motion

$$\frac{\mathrm{d}q}{\mathrm{d}t} = \{q, h\} + \{\!\{q, \gamma\}\!\} \quad \text{as } \hbar \to 0. \tag{2.87}$$

The equivalent expression for $\langle \hat{p} \rangle$ follows analogously, and together these yield the coherent-state approximation for non-Hermitian systems given in equations (2.82)–(2.83). These results were first established in [45].

2.7 Semiclassical Husimi Approximation for non-Hermitian Hamiltonians

In section 2.3 we derived a semiclassical Husimi approximation for nonlinear Hermitian systems. We now extend this to the non-Hermitian setting where new features arise due to the non-unitary nature of the dynamics. This generalisation provides original insights and forms the basis of recent published work [69].

As in the Hermitian case, we consider the state $|\epsilon(t)\rangle = \hat{U}^\dagger(t)\,|z\rangle$, which appears in the expression for the time-evolved Husimi distribution under the adjoint action of the time evolution operator. Since the evolution operator is now $\hat{U}(t) = e^{-\mathrm{i}\hat{\mathcal{K}}t/\hbar}$, its adjoint becomes

$$\hat{U}^\dagger(t) = e^{\mathrm{i}\hat{\mathcal{K}}^\dagger t/\hbar} = e^{-\mathrm{i}(-\hat{\mathcal{K}}^\dagger)t/\hbar}, \tag{2.88}$$

which corresponds to evolution under the Hamiltonian $-\hat{\mathcal{K}}^\dagger$. In general, $|\epsilon(t)\rangle$ is not a coherent state nor is it normalised. To construct the semiclassical Husimi approximation, we approximate both the coherent state structure and the norm evolution of $|\epsilon(t)\rangle$. We represent the state by a time-dependent normalised coherent state $|\tilde{z}(t)\rangle$, where $\tilde{z}(t)$ evolves under the time-reversed classical dynamics generated by $k^* = \lim_{\hbar\to 0} \langle z|\, \hat{\mathcal{K}}^\dagger\, |z\rangle$.

Since the norm of $|\epsilon(t)\rangle$ is not constant under non-Hermitian evolution, we additionally approximate this effect by introducing a time-dependent amplitude factor $w(z,t)$, which captures the norm evolution. The full approximation to $|\epsilon(t)\rangle$ is then given by

$$|\tilde{z}(t)\rangle = w^{1/2}(z,t)\,|\tilde{z}(t)\rangle\,, \tag{2.89}$$

which we refer to as the non-Hermitian coherent-state approximation. This state encodes both the transport of the phase-space coordinate $\tilde{z}(t)$, governed by classical flow, and the corresponding amplification or decay of its norm through the factor $w(z,t)$.

In contrast to the Hermitian case, where the dynamics of each phase-space point are confined to two dimensions, the non-Hermitian setting introduces an additional dimension associated with

norm evolution. Intuitively, one can view the phase space point as moving not just across the phase plane, but also in this third dimension due to the norm landscape shaped by the gain or loss properties of the system. This added structure will play a central role when we later construct the full Husimi distribution.

Thus, we arrive at the semiclassical Husimi approximation

$$Q_{\psi(t)}(z) = |\langle \bar{z}(t)|\psi_0\rangle\,|^2 = Q_{\psi_0}(\Phi_{-t}(z))\, w(z,t), \tag{2.90}$$

where $\Phi_{-t}(z)$ denotes the classical backward flow that identifies the initial phase space point (preimage) that evolved to the current location z under the complex-conjugated Hamiltonian k^*. The norm landscape function $w(z,t)$ accounts for the amplitude modulation arising from non-Hermitian dynamics, an effect absent in the Hermitian case where norms are preserved.

Unlike the Hermitian case, the dynamics here have a key additional feature: the presence of the norm landscape $w(z,t)$ [98], which modulates the amplitude of the Husimi distribution. This term often becomes the dominant feature, especially over long time scales, and captures the gain or loss induced by non-Hermiticity.

For an initial coherent state, the evolution of $w(z,t)$ follows from equation (2.72)

$$\frac{\mathrm{d}w(z,t)}{\mathrm{d}t} = \frac{2}{\hbar}\,\gamma(z(t))\, w(z,t). \tag{2.91}$$

Solving this yields

$$w(z,t) = \exp\left(\mathcal{N}(z,t)\right), \quad \text{where} \quad \mathcal{N}(z,t) = \int_0^t \frac{2}{\hbar}\gamma(z(t'))\, dt'. \tag{2.92}$$

Here, $z(t) = \Phi(z_0,t)$ denotes the phase-space trajectory evolved from an initial point z_0, governed by the flow of k^*. Crucially, the evaluation of $w(z,t)$ requires knowledge of the entire trajectory history, making this a path-dependent integral that cannot be expressed solely in terms of the final position z. To evaluate the integral over time, we substitute the inverse flow $z_0 = \Phi^{-1}(z,t)$, ensuring that the point z corresponds to the proper trajectory at time t.

Because k^* typically generates non-Hamiltonian dynamics, the resulting phase-space flow is not symplectic and can produce stretching, compression, and even topological changes in the Husimi distribution. These deformations, combined with the spatially varying norm landscape, give rise to rich and distinctive features in the semiclassical dynamics. We will explore these effects through explicit examples in the chapters that follow.

2.8 Examples

In the following examples, we apply the coherent-state approximation and the semiclassical Husimi approximation to a range of non-Hermitian systems to illustrate the features of quantum-classical correspondence in the presence of non-unitary dynamics. Each system highlights distinct physical features and types of non-Hermiticity.

We begin with the non-Hermitian Kerr oscillator, a nonlinear system in which the imaginary component introduces amplitude-dependent dissipation. This serves as a benchmark for comparing semiclassical and exact quantum dynamics in a well-understood setting. We then consider the damped tilted Mexican Hat potential, which exhibits a richer phase-space structure and a more intricate eigenvalue spectrum. Its multiple fixed points and nontrivial flow patterns illustrate how non-Hermitian terms induce strongly directional transport and damping effects. Finally, we examine a PT-symmetric Kerr oscillator, where gain and loss are spatially balanced. This system highlights the emergence of unbroken and broken PT-symmetric phases and demonstrates how the semiclassical Husimi method captures the transition between them.

Together, these examples demonstrate the effectiveness of the semiclassical approximation and reveal new insights into non-Hermitian quantum-classical correspondence across qualitatively different dynamical regimes.

2.8.1 Damped Kerr Hamiltonian

We begin with a damped version of the Kerr Hamiltonian from Section 2.4 as our first example of a nonlinear, non-Hermitian system. This case serves to explore phase-space approximations in a regime where quantum-classical correspondence is no longer exact. The damped Kerr Hamiltonian is given by

$$\hat{\mathcal{K}} = \hat{a}^\dagger\hat{a} + \beta\hat{a}^\dagger\hat{a}^\dagger\hat{a}\hat{a} + \mathrm{i}\kappa\hat{a}^\dagger\hat{a}, \tag{2.93}$$

with $\beta \in \mathbb{R}$ and $\kappa \in \mathbb{R}^-$. This extends the original Kerr Hamiltonian by incorporating a linear loss term, $\mathrm{i}\kappa\hat{a}^\dagger\hat{a}$.

To analyse the quantum dynamics of this non-Hermitian Hamiltonian, we begin with the eigenvalue spectrum. The Hamiltonian is diagonal in the Fock (oscillator) basis, with eigenvalues

$$E_n = \beta n^2 + (1 + \mathrm{i}\kappa)n. \tag{2.94}$$

The dominant eigenstate of a general initial state $|\psi\rangle = \sum c_n |n\rangle$ is determined by the smallest n such that $c_n \neq 0$. For an initial coherent state, the dominant contribution comes from the vacuum state $|0\rangle$.

Applying the coherent-state approximation, we obtain the classical counterpart to the Hamiltonian

$$k = \frac{1}{2}(p^2 + q^2) + \frac{\beta}{4}(p^2 + q^2)^2 + \frac{\mathrm{i}\kappa}{2}(p^2 + q^2), \tag{2.95}$$

from which we derive the equations of motion

$$\frac{\mathrm{d}q}{\mathrm{d}t} = p + \beta p(p^2 + q^2) + \kappa q, \tag{2.96}$$

$$\frac{\mathrm{d}p}{\mathrm{d}t} = -q - \beta q(p^2 + q^2) + \kappa p. \tag{2.97}$$

To solve these equations, we transform to polar coordinates with $r^2 = p^2 + q^2$ and $\tan\theta = p/q$,

yielding

$$r(t) = r_0 e^{\kappa t}, \tag{2.98}$$

$$\theta(t) = \theta_0 - t - \frac{\beta r_0^2}{2\kappa}\left(e^{2\kappa t} - 1\right), \tag{2.99}$$

where r_0 and θ_0 are determined by the initial conditions.

The trajectories generated by the coherent-state approximation form clockwise spirals that converge toward a single fixed point at the origin. Initially, the angular velocity of each spiral depends on its distance from the origin, trajectories that begin farther out rotate more rapidly than those that start closer in. Over time, however, as all trajectories approach the origin due to damping, their angular velocities converge toward a uniform value of 1.

In the left panel of Figure 2.8, we illustrate these coherent-state approximation trajectories for $\beta = 1$ and $\kappa = -\frac{1}{4}$ across a range of initial conditions in (q, p).

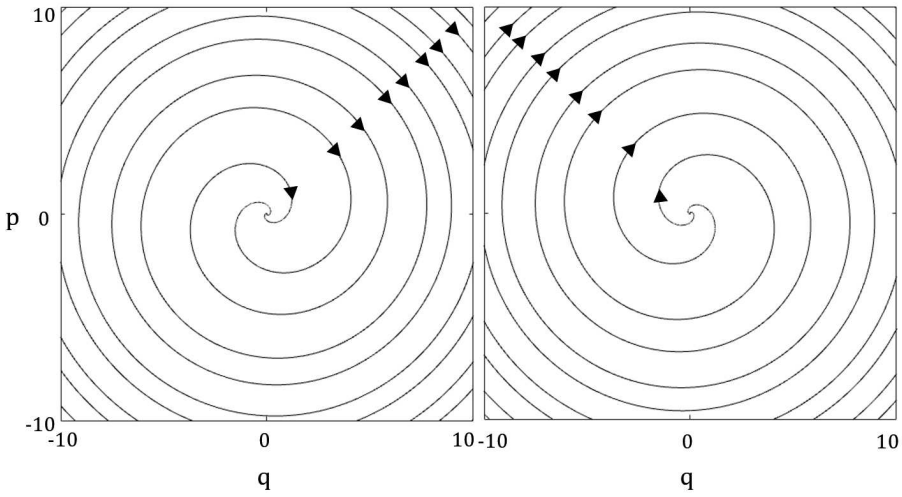


Figure 2.8: Phase-space trajectories for the damped Kerr Hamiltonian with $\beta = 1, \kappa = -\frac{1}{4}$. Left: the coherent-state approximation trajectories. Right: the trajectories derived from the classical Hamiltonian k^*.

For an initial coherent state, the full quantum evolution is dominated by the loss term in the Hamiltonian, leading to a more rapid decay of the expectation values of position and momentum compared to the coherent-state approximation. This stronger contraction toward the origin is evident in Figure 2.9, where $\langle \hat{q} \rangle$ (solid blue line) decays more quickly than its coherent-state approximation (dotted orange line).

We now turn to the semiclassical Husimi approximation for this system. The flow generated by k^* is obtained by reversing the sign of the κ terms in the coherent-state approximation equations, yielding the trajectories

$$r(t) = r_0 e^{-\kappa t}, \tag{2.100}$$

$$\theta(t) = \theta_0 - t + \frac{\beta r_0^2}{2\kappa}\left(e^{-2\kappa t} - 1\right). \tag{2.101}$$

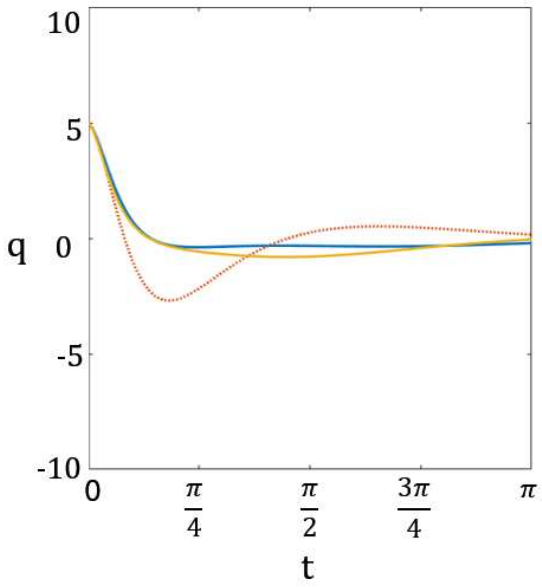


Figure 2.9: Comparison of values of q between quantum dynamics (solid blue line), semiclassical Husimi (solid yellow line) and the coherent-state approximation (dotted orange line) for the damped Kerr Hamiltonian $\beta = 1, \kappa = -\frac{1}{4}$ for an initial coherent state centred at $(q, p) = (0, 5)$

To incorporate the norm dynamics, we compute the norm landscape function $\mathcal{N}(r, t)$

$$\begin{aligned}\mathcal{N}(r,t) &= \int_0^t 2\gamma(q(t'), p(t'))\, dt' \\ &= \int_0^t \kappa r(t')^2\, dt' \\ &= \int_0^t \kappa r_0^2 e^{-2\kappa t'}\, dt' \\ &= \frac{r^2}{2}(e^{2\kappa t} - 1). \end{aligned} \tag{2.102}$$

This yields the norm landscape function

$$w(r,t) = e^{\frac{r^2}{2}(e^{2\kappa t}-1)}. \tag{2.103}$$

At $t = 0$, the norm landscape is unity, as expected. For $t > 0$, it takes the form of a Gaussian centred at the origin, with a width that decreases monotonically as time increases. In the limit $t \to \infty$, the landscape approaches $e^{-\frac{r^2}{2}}$.

The evolution of this norm landscape is illustrated in the bottom row of Figure 2.10, which shows snapshots of $w(r, t)$ at selected time points for the parameter values $\beta = 1$ and $\kappa = -\frac{1}{4}$.

These k^* trajectories are shown in the right panel of Figure 2.8, corresponding to coherent-state approximation trajectories with the transformation $p \to -p$. Counterintuitively, these trajectories form outward spirals that transport probability away from the origin, in stark contrast to the inward spirals of the original coherent-state dynamics. This outward flow would naturally be expected to disperse the initial Husimi distribution away from the origin and exhibit the characteristic Kerr

whorl structure. However, when combined with the norm decay landscape, these two competing effects of outward transport and norm landscape work together to produce the overall concentration of the distribution state at the origin, as expected.

Figure 2.10 displays snapshots of the normalised Husimi distributions for both the full quantum dynamics (top row) and the semiclassical Husimi approximation (bottom row), starting from a coherent state centred at $(q, p) = (0, 5)$. As observed in the Hermitian Kerr case, both distributions exhibit an initial rotational and whorling behaviour, with close agreement between them. Notably, the semiclassical Husimi distribution exhibits a finer structure than the quantum one.

Over time, both distributions converge to a Gaussian at the origin. The damping term substantially suppresses interference features in the quantum Husimi distribution, especially when κ is large relative to β. The semiclassical Husimi method provides a faithful approximation of the full quantum dynamics and surpasses the coherent-state approximation in accuracy. This is illustrated in Figure 2.9, where we compare the expectation value of q obtained from the semiclassical Husimi method (solid yellow line), the coherent-state approximation (dotted orange line), and the full quantum evolution (solid blue line).

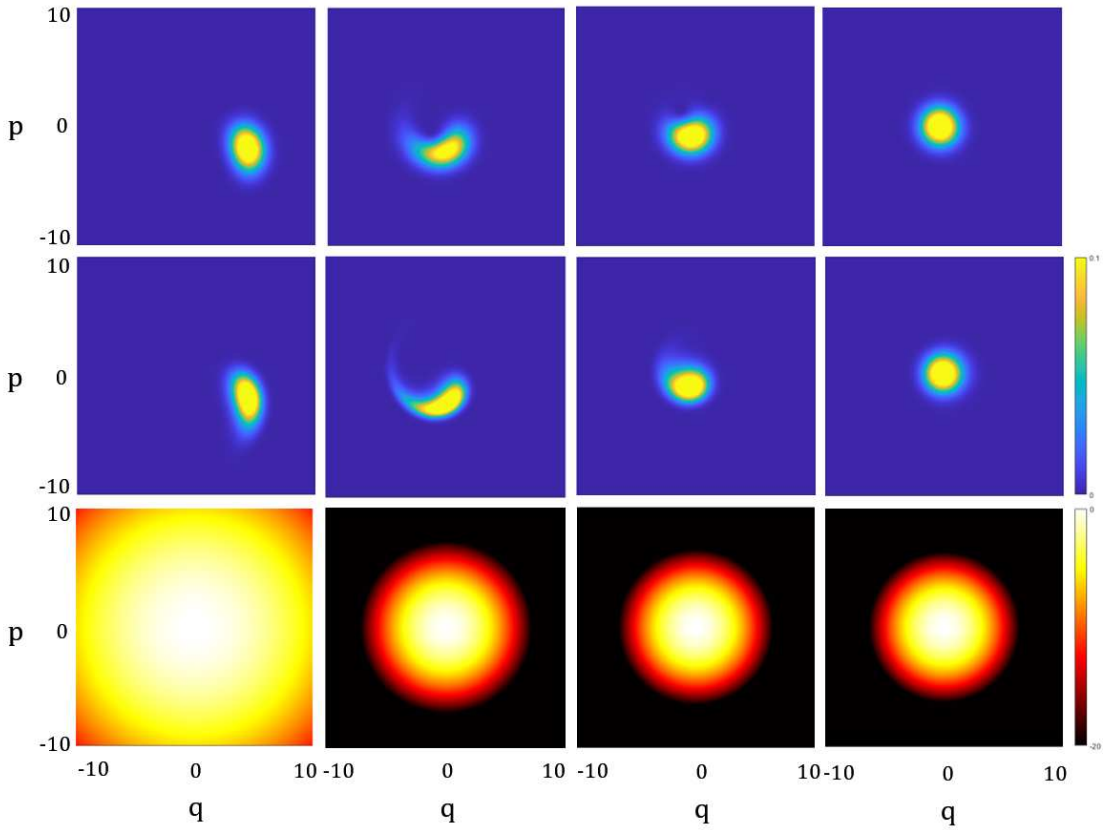


Figure 2.10: Evolution of the normalised quantum Husimi distribution (top row), the normalised semiclassical Husimi distribution (middle row) and the logarithm of the norm landscape (bottom row) for the damped Kerr Hamiltonian with $\beta = 1, \kappa = -\frac{1}{4}$ for an initial coherent state centred at $(q, p) = (0, 5)$. The columns correspond to different snapshots of the evolution in time with $t = \frac{\pi}{50}$ (left), $t = \frac{\pi}{4}$ (middle left), $t = \frac{\pi}{2}$ and (middle right) and $t = \pi$ (right).

This example demonstrates how the semiclassical Husimi method captures key features of the

behaviour of the full quantum evolution in a nonlinear non-Hermitian system. The k^* flow, which governs the classical transport in the Husimi approximation, corresponds to a reversal in the sign of the imaginary component of the Hamiltonian, effectively a flip in the p-axis for this system and the direction of the gradient component of the flow. In the case of the damped Kerr oscillator, we have explicitly shown how this flipped and reversed flow interacts with the norm landscape to accurately reproduce the convergence to the dominant eigenstate.

2.8.2 Damped Tilted Mexican Hat Hamiltonian

Having examined the damped Kerr oscillator, we now turn to a more structurally complex system, a non-Hermitian variant of the Kerr Hamiltonian in which the harmonic potential is inverted and a linear tilting term is introduced. This construction results in a damped, tilted Mexican Hat potential, a system with richer phase-space structure and more intricate quantum behaviour.

The Hamiltonian takes the form

$$\hat{\mathcal{K}} = -\hat{a}^\dagger\hat{a} + \beta\hat{a}^\dagger\hat{a}^\dagger\hat{a}\hat{a} + \frac{\delta}{\sqrt{2}}(\hat{a}^\dagger + \hat{a}) + \mathrm{i}\kappa\hat{a}^\dagger\hat{a}, \tag{2.104}$$

where $\beta \in \mathbb{R}^+$ controls the nonlinearity, $\delta \in \mathbb{R}$ introduces the tilt, and $\kappa \in \mathbb{R}^-$ encodes the damping. The negative sign in the first term inverts the Harmonic potential and when combined with the quartic term, it leads to the characteristic Mexican hat shape of the effective potential.

This Hamiltonian presents a more interesting eigenvalue structure than the damped Kerr case, with eigenvalues organised around three distinct branches in the complex plane: one set with $\mathrm{Re}(E_n) < -2$, another for $-0.5 < \mathrm{Im}(E_n) < 0$, and a third where $\mathrm{Re}(E_n) > -2$ and $\mathrm{Im}(E_n) < -0.5$. The first two branches contain a finite number of eigenvalues, while the last branch holds infinitely many eigenvalues. The dominant eigenstate, whose Husimi distribution is plotted in the right panel, is an approximately Gaussian state centred away from the origin at $(q, p) \approx (1.06, 0)$, highlighting the system's asymmetry and the impact of the tilt.

The corresponding classical counterpart of the Hamiltonian is

$$k = -\frac{1}{2}(p^2 + q^2) + \frac{\beta}{4}(p^2 + q^2)^2 + \delta q + \frac{\mathrm{i}\kappa}{2}(p^2 + q^2), \tag{2.105}$$

leading to the following equations of motion for the coherent-state approximation

$$\frac{\mathrm{d}q}{\mathrm{d}t} = -p + \beta p(p^2 + q^2) + \kappa q, \tag{2.106}$$

$$\frac{\mathrm{d}p}{\mathrm{d}t} = q - \beta q(p^2 + q^2) - \delta + \kappa p. \tag{2.107}$$

For the parameter choice $\beta = \frac{1}{20}$, $\delta = 1$, and $\kappa = -\frac{1}{20}$, we numerically verify that the coherent-state approximation exhibits three fixed points: two stable spirals (non-Hermitian continuations of elliptic centres) located at $(q_1, p_1) = (-4.75, 1.20)$ and $(q_2, p_2) = (1.06, -0.06)$, and an unstable saddle point at $(q_3, p_3) = (0.75, 3.80)$. The trajectories spiral toward one of the two stable fixed points, depending on the initial condition. This behaviour is illustrated in the left panel

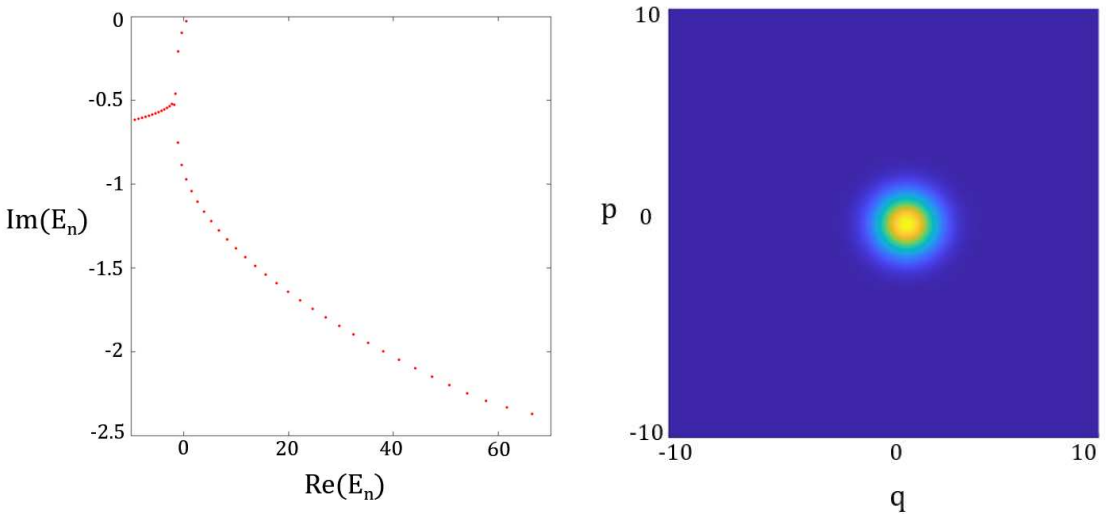


Figure 2.11: The damped, tilted Mexican Hat Hamiltonian with $\beta = \frac{1}{20}, \delta = 1, \kappa = -\frac{1}{20}$. Left: the eigenvalue spectrum for the 50 eigenvalues with largest imaginary components. Right: The dominant eigenstate centred at $(q, p) = (1.06, -0.06)$.

of Figure 2.12.

An especially illustrative example arises for an initial coherent state centred at $(q, p) = (3, 5)$, which lies in the basin of attraction of the fixed point at (q_1, p_1). While the coherent-state trajectory evolves toward this fixed point, the full quantum evolution tends instead to the dominant eigenstate, whose expectation values are $\langle \hat{q} \rangle = 1.06$ and $\langle \hat{p} \rangle = -0.06$. This discrepancy is clearly shown in the right panel of Figure 2.12, where we compare the coherent-state approximation for q (dotted orange line) with the quantum expectation value $\langle \hat{q} \rangle$ (solid blue line).

Interestingly, while in the damped Kerr example the dominant eigenstate coincided with the classical fixed point, in this case it is merely close to one. This suggests a more intricate relationship between classical fixed points, the norm landscape, and dominant quantum states. A more detailed investigation of this relationship, particularly in terms of k^*-generated flows and the structure of the norm landscape, is a promising direction for future research.

In Figure 2.13, we present snapshots of the normalised semiclassical and quantum Husimi distributions, alongside the norm landscape. As in the Hermitian Kerr case, both the semiclassical and quantum Husimi distributions exhibit similar qualitative features, most notably, the characteristic whorling and rotational deformation. The semiclassical Husimi distribution successfully captures these early-time dynamics with good fidelity.

Starting from approximately $t = \frac{\pi}{2}$, the norm landscape begins to concentrate the semiclassical Husimi distribution, progressively suppressing the fine spiral structures and guiding the dynamics toward a more localised state. As time advances, the norm landscape sharpens further and becomes concentrated around the same location as the dominant eigenstate of the quantum system.

Consequently, the semiclassical Husimi distribution evolves toward a final state centred near the fixed point (q_2, p_2), a point that lies very close to the expectation values of the position and momentum operators in the dominant eigenstate. This contrasts with the coherent-state

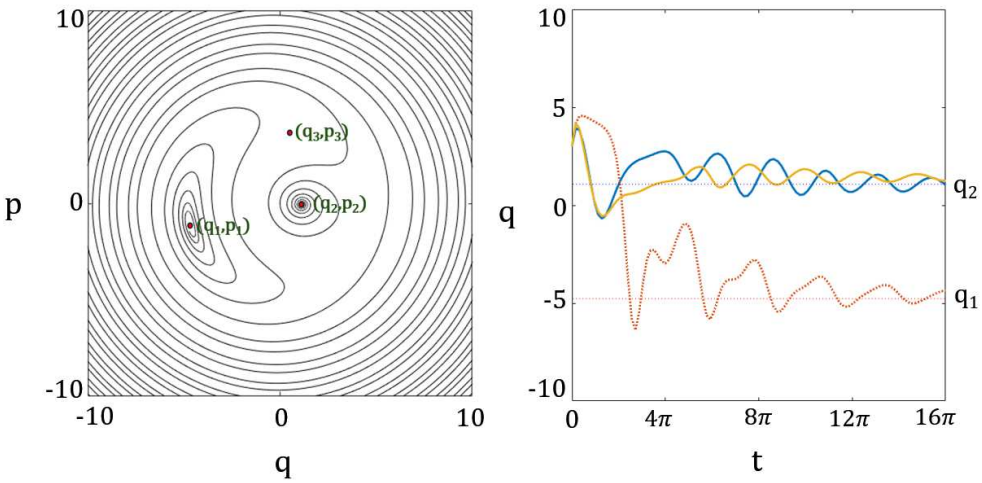


Figure 2.12: The damped tilted Mexican Hat Hamiltonian with $\beta = \frac{1}{20}, \delta = 1, \kappa = -\frac{1}{20}$. Left: phase-space trajectories from the coherent-state approximation. Right: Comparison of values of q between quantum dynamics (solid blue line), semiclassical Husimi (solid yellow line) and the coherent-state approximation (dotted orange line) for an initial coherent state centred at $(q, p) = (3, 5)$.

approximation, which instead converges to the fixed point (q_1, p_1). This divergence is highlighted in the right panel of Figure 2.12, where we compare the expectation value of q from the semiclassical Husimi dynamics (solid yellow line), the coherent-state approximation (dotted orange line), and the full quantum evolution (solid blue line).

As with the damped Kerr Hamiltonian, the evolution toward the dominant eigenstate in the damped tilted Mexican hat system leads to a suppression of quantum features such as holes, superpositions, and interference effects. These are gradually overridden as the state becomes increasingly localised and concentrated. This behaviour is illustrated in the left panel of Figure 2.14, which shows a snapshot of the normalised quantum Husimi distribution at $t = 16\pi$.

The semiclassical Husimi distribution also tends toward a localised stationary state, although this convergence occurs more gradually. The finer structures present in the semiclassical distribution persist longer, as they are dampened more slowly by the norm landscape. This is evident in the right panel of Figure 2.14, which displays the semiclassical Husimi distribution at the same time. The strong resemblance between the two final states underscores the effectiveness of the norm landscape in enhancing phase-space approximations for certain classes of non-Hermitian quantum systems.

2.8.3 PT Symmetric Kerr Hamiltonian

Having explored two non-Hermitian systems with complex eigenvalue spectra, we now turn to a PT-symmetric extension of the Kerr model. PT-symmetry, where the Hamiltonian commutes with the combined action of parity and time reversal, has emerged as a particularly important subclass of non-Hermitian quantum mechanics. Systems in this class can exhibit entirely real spectra and sustained norm dynamics despite being non-Hermitian, demonstrating that non-Hermitian systems need not necessarily exhibit dissipation and irreversibility.

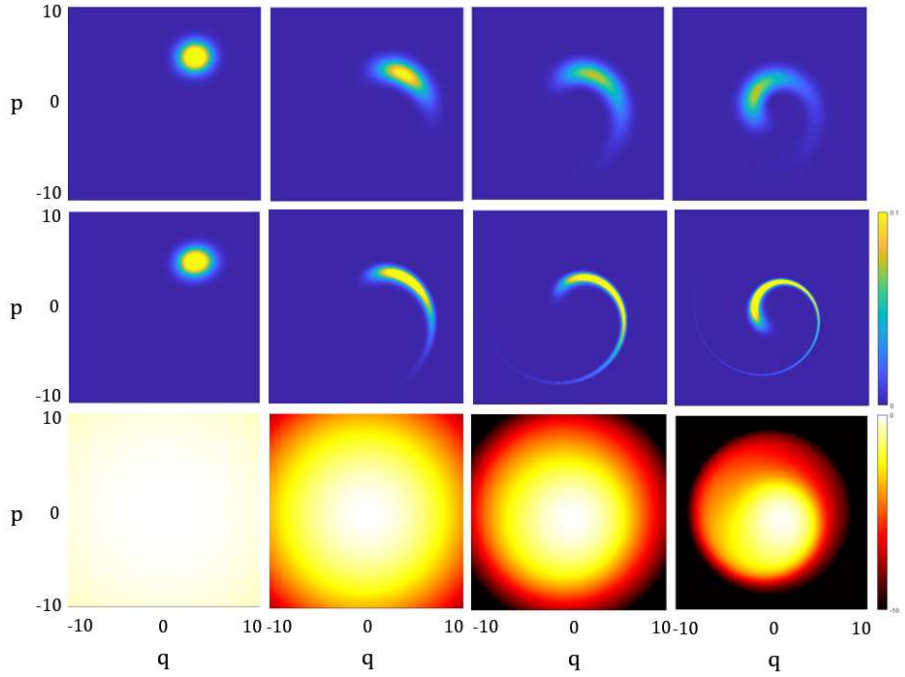


Figure 2.13: Evolution of the normalised quantum Husimi distribution (top row), the normalised semiclassical Husimi distribution (middle row) and the logarithm of the norm landscape (bottom row) for the damped, tilted Mexican hat Hamiltonian with $\beta = \frac{1}{20}, \delta = 1, \kappa = -\frac{1}{20}$ for an initial coherent state centred at $(q, p) = (3, 5)$. The columns correspond to different snapshots of the evolution in time with $t = \frac{\pi}{50}$ (left), $t = \frac{\pi}{4}$ (middle left), $t = \frac{\pi}{2}$ (middle right) and $t = \pi$ (right).

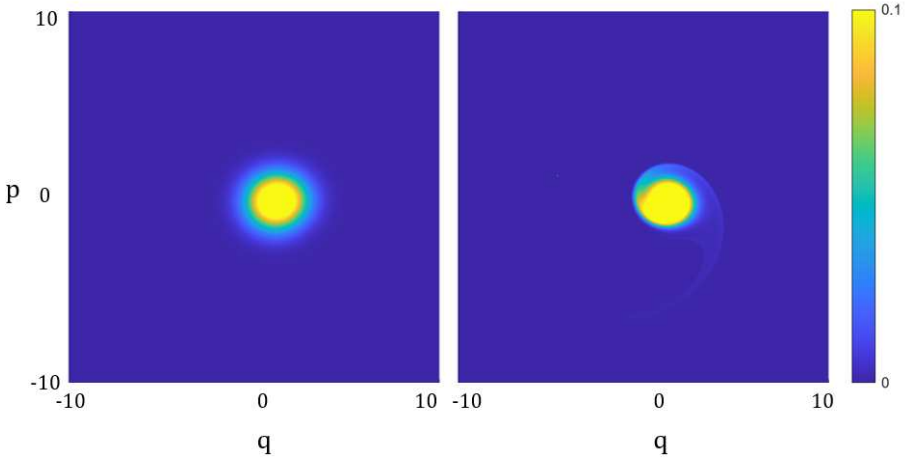


Figure 2.14: The normalised quantum Husimi distribution (left) and the normalised semiclassical Husimi distribution (right) for the damped, tilted Mexican hat Hamiltonian with $\beta = \frac{1}{20}, \delta = 1, \kappa = -\frac{1}{20}$ for an initial coherent state centred at $(q, p) = (3, 5)$ at time $t = 16\pi$.

To construct a PT-symmetric variant of the Kerr model, we introduce a balanced gain-loss profile along the q direction via the term $\hat{\Gamma} = \frac{\epsilon}{\sqrt{2}}(\hat{a}^\dagger + \hat{a})$, which is odd under parity and even under time reversal, ensuring that the total Hamiltonian is PT-symmetric.

This model exhibits behaviours that may appear counterintuitive: non-Hermitian systems do not necessarily evolve toward a fixed final state, and the presence of real eigenvalues does not imply unitary dynamics. As such, the PT-symmetric Kerr oscillator provides a compelling counterexample that reveals the nuanced structure of non-Hermitian evolution.

The Hamiltonian is given by

$$\hat{\mathcal{K}} = \hat{a}^\dagger \hat{a} + \beta \hat{a}^\dagger \hat{a}^\dagger \hat{a}\hat{a} + \frac{\mathrm{i}\epsilon}{\sqrt{2}}(\hat{a}^\dagger + \hat{a}), \tag{2.108}$$

where $\beta \in \mathbb{R}^+$ sets the strength of the Kerr nonlinearity and $\epsilon \in \mathbb{R}^-$ governs the gain–loss coupling. This system allows us to investigate how the semiclassical Husimi approximation captures dynamics within both the unbroken and broken PT-symmetric regimes.

This system is PT-symmetric. The parity operator $\hat{P}$ and time-reversal operator $\hat{T}$ act separately as

$$\hat{P}: \qquad \hat{q} \to -\hat{q}, \qquad \hat{p} \to \hat{p}, \tag{2.109}$$

$$\hat{T}: \qquad \hat{q} \to \hat{q}, \qquad \hat{p} \to \hat{p}, \qquad \mathrm{i} \to -\mathrm{i}, \tag{2.110}$$

so that the combined PT operation yields

$$\hat{P}\hat{T}: \qquad \hat{q} \to -\hat{q}, \qquad \hat{p} \to \hat{p}, \qquad \mathrm{i} \to -\mathrm{i}. \tag{2.111}$$

For the case $\beta = \frac{1}{4}$, $\epsilon = -1$ we have numerically verified that the eigenvalue spectrum is real, resulting in unbroken PT symmetry. The first 50 eigenvalues are shown in the left panel of Fig. 2.15.

The classical counterpart of the Hamiltonian is given by

$$k = \frac{p^2 + q^2}{2} + \frac{\beta}{4}(p^2 + q^2)^2 + \mathrm{i}\epsilon q. \tag{2.112}$$

The resulting coherent-state trajectory and norm landscape equations of motion are thus found as

$$\frac{\mathrm{d}q}{\mathrm{d}t} = p + \beta p(p^2 + q^2) + \epsilon, \tag{2.113}$$

$$\frac{\mathrm{d}p}{\mathrm{d}t} = -q - \beta q(p^2 + q^2), \tag{2.114}$$

$$\frac{\mathrm{d}w}{\mathrm{d}t} = 2qw. \tag{2.115}$$

This system does not yield analytical solutions for $q(t), p(t), w(t)$. There is a single elliptic fixed point located at $q = 0$ and $p_0 < 0$, where p_0 is the single real root of the polynomial $p_0^3 + \frac{1}{\beta}p_0 - \frac{\epsilon}{\beta} = 0$. The coherent-state approximation trajectories consist of clockwise orbits around the fixed point, with distorted non-circular paths that deviate from perfect circularity as

depicted in the right panel of Figure 2.15. The trajectories have the usual increase in frequency for orbits further associated with the Kerr nonlinearity. Although we cannot find a solution for $w(t)$, we observe that $\frac{1}{w}\frac{\mathrm{d}w}{\mathrm{d}t} = 2q$ and $q(t)$ are periodic in motion, thus $w(t)$ will have a periodic aspect. Again, the k^* trajectories are found from the coherent-state approximation trajectories via the transformation $p \to -p$ with a time reversal of the metric portion of the flow.

The full quantum evolution of the position and momentum expectation values experience the

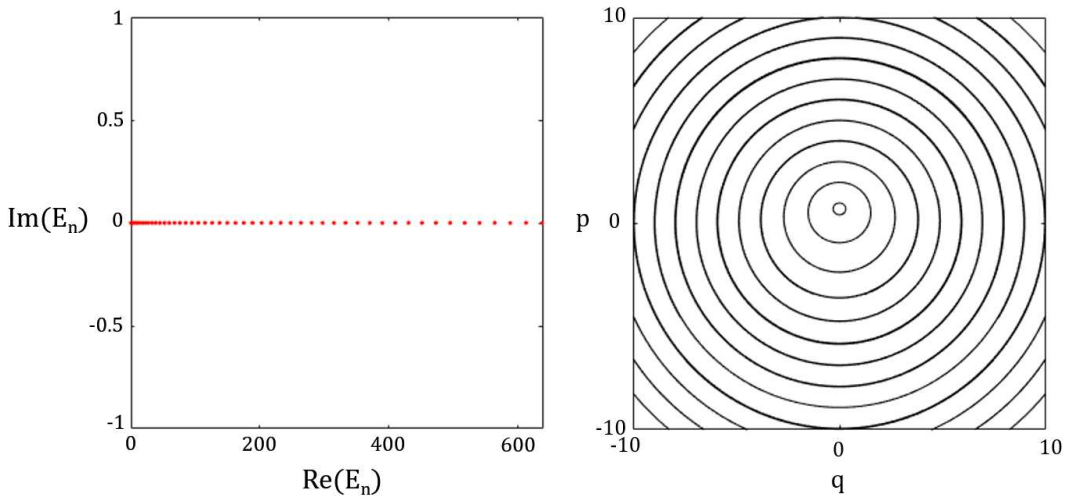


Figure 2.15: The PT-symmetric Kerr Hamiltonian with $\beta = \frac{1}{4}, \epsilon = 1$. Left: the eigenvalue spectrum for the first 50 eigenvalues. Right: The dominant eigenstate centred at $(q, p) = (1.06, 0)$. Left: the eigenvalue spectrum, right: Phase-space trajectories from the coherent-state approximation.

same characteristic breakdown and revival behaviour as the Hermitian case as demonstrated in Figure 2.16, which depicts the expectation values $\langle \hat{q} \rangle$ (solid blue line) and the coherent-state approximation for q (dotted orange line), as well as the expectation value obtained from the semiclassical Husimi dynamics (solid yellow line). As was the case for the Hermitian Kerr Hamiltonian, the initial breakdown and deformation of the Husimi distribution is well captured by the semiclassical Husimi dynamics.

We will now study the dynamics of the PT-symmetric Kerr oscillator using both the semiclassical Husimi approximation and exact quantum evolution. We fix the parameters $\beta = \frac{1}{4}$ and $\epsilon = -1$, and choose an initial coherent state centred at the phase-space point $(q, p) = (-3, 5)$. Figures 2.17 and 2.18 illustrate the behaviour of the quantum and semiclassical Husimi distributions over short and long times, alongside the corresponding norm landscape.

Figure 2.17 shows snapshots of the quantum Husimi distribution (top row), the semiclassical Husimi approximation (middle row), and the logarithm of the norm landscape (bottom row) at times $t = \frac{\pi}{50}$, $t = \frac{\pi}{10}$, and $t = \frac{\pi}{5}$.

At early times ($t = \frac{\pi}{50}$ and $t = \frac{\pi}{10}$), we observe strong agreement between the semiclassical and quantum Husimi distributions, indicating that the semiclassical transport accurately captures the quantum dynamics. As in the Hermitian Kerr model, the whorling of the distributions results from

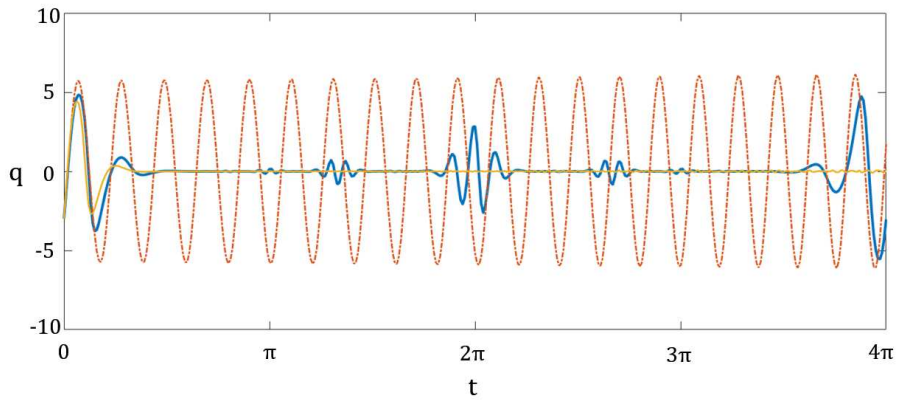


Figure 2.16: Comparison of values of q between quantum dynamics (solid blue line), semiclassical Husimi (solid yellow line) and the coherent-state approximation (dotted orange line) for the PT-symmetric Kerr Hamiltonian for an initial coherent state centred at $(q, p) = (-3, 5)$

the nonlinear frequency variation along the classical trajectories, which causes the coherent packet to shear over time.

By $t = \frac{\pi}{5}$, subtle discrepancies begin to appear as quantum interference effects emerge, marking the breakdown of classical correspondence. However, the overall structure remains largely consistent between the two approaches.

A key distinction from the Hermitian case is the asymmetric concentration of the distributions toward the upper half of the phase space. This bias arises from the non-Hermitian component of the Hamiltonian, encoded in the norm landscape, which favours certain trajectories over others. The norm landscape itself evolves in time due to the trajectory dependence of the gain/loss term, which breaks the rotational symmetry present in the Hermitian Kerr model.

In Figure 2.18, we focus on the quantum Husimi distribution at later times, $t = \frac{3\pi}{10}$, $t = \pi$, and $t = 2\pi$. As time progresses, the wavepacket becomes increasingly distorted, and quantum interference patterns become pronounced. The coherent whorling continues, but is now modulated by significant stretching and folding, which are hallmarks of quantum nonlinear evolution.

Throughout this evolution, the asymmetric gain/loss structure remains visible, with amplitude consistently drawn toward the upper regions of phase space, again reflecting the influence of the norm landscape shaped by the PT-symmetric term.

These simulations highlight how the semiclassical Husimi method remains effective at early times, even in the presence of non-Hermitian effects, and how quantum features such as interference and localisation gradually emerge. The evolution of the norm landscape, shaped by classical transport coupled with gain/loss terms, plays a central role in this deformation, biasing the flow of probability and breaking the symmetry of the classical phase space. It is an interesting topic for future research to explore the interplay between exact PT-symmetric quantum behaviour and its classical approximation, especially in regimes of broken symmetry or stronger nonlinearity.

In this chapter we have presented our original research into how the coherent-state approximation

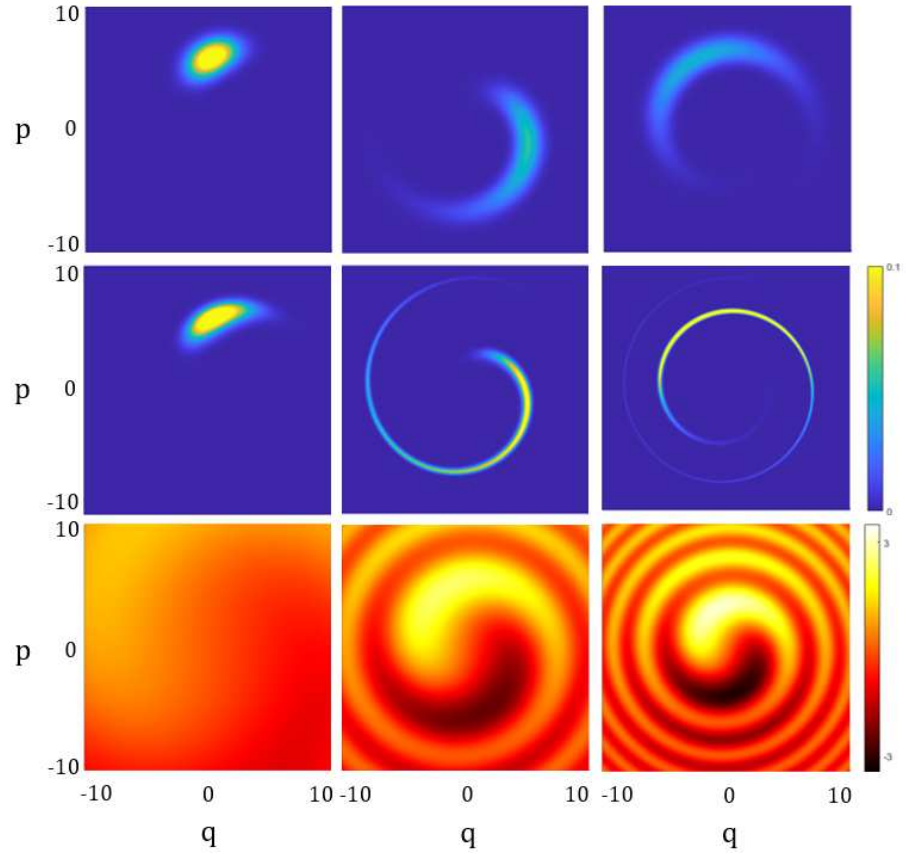


Figure 2.17: Evolution of the normalised quantum Husimi distribution (top row), the normalised semiclassical Husimi distribution (middle row), and the logarithm of the norm landscape (bottom row) for the PT-symmetric Kerr Hamiltonian with parameters $\beta = \frac{1}{4}$, $\epsilon = -1$. The initial state is a coherent state centred at $(q, p) = (-3, 5)$. Snapshots are shown at $t = \frac{\pi}{50}$ (left), $t = \frac{\pi}{10}$ (middle), and $t = \frac{\pi}{5}$ (right).

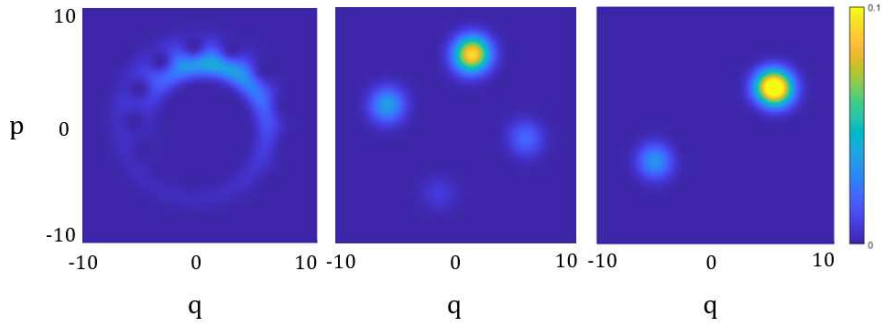


Figure 2.18: Evolution of the quantum Husimi distribution for the PT-symmetric Kerr Hamiltonian with $\beta = \frac{1}{4}$, $\epsilon = -1$, for an initial coherent state centred at $(q, p) = (-3, 5)$. Snapshots shown at $t = \frac{3\pi}{10}$ (left), $t = \pi$ (middle), and $t = 2\pi$ (right).

for the Heisenberg-Weyl algebra can be used to form the semiclassical Husimi approximation for non-Hermitian systems derived from the Harmonic oscillator operators. In our approach, the evolution of the Husimi distribution is governed by classical phase-space trajectories generated by the non-Hermitian Hamiltonian. The resulting dynamics comprise the classical transport of the initial Husimi distribution, modulated by a time and path-dependent norm landscape that reflects the non-Hermitian effects. The interplay between non-Hermitian dampening effects as shown in our first two examples or a balanced gain-loss profile as in our last example lead to fascinating dynamics effects. The semiclassical Husimi distribution provided an important improvement over the well-known coherent-state approximation, particularly for non-Hermitian systems with complex-valued eigenspectra where the long-term asymptotic dynamics appears to be well captured by the norm landscape evolution. We now extend this work to consider a wider range of non-Hermitian quantum systems.

Chapter 3

A Generalised Approach for Phase-Space Approximations of Quantum Systems

For quantum systems whose Hamiltonians can be expressed in terms of Lie algebra generators, quantum-classical correspondence follows well-established pathways. The Kirillov-Kostant-Souriau (KKS) construction [9–11] provides a canonical framework where classical phase spaces are identified with coadjoint orbits and Poisson bracket structures emerge directly from Lie algebra commutation relations. However, when moving beyond Lie algebraic structures to more general operator algebras, this correspondence becomes significantly more complex. The linear commutation relations that underpin the KKS construction may no longer hold, classical phase spaces need not be coadjoint orbits, and the geometric structures required for standard coherent state constructions may be absent or substantially modified. In such cases, establishing quantum-classical correspondence requires developing new frameworks that can accommodate non-linear algebraic relations, non-canonical symplectic structures, and emergent geometric properties that arise from the specific operator algebra under consideration.

This chapter presents original research that extends phase-space approximation methods, both coherent-state and semiclassical Husimi, to a wider class of quantum systems, including those governed by non-Hermitian dynamics. The main goal is to formulate a unifying framework that allows coherent-state approximations to be constructed for any system satisfying certain algebraic and dynamical conditions. This generalisation not only encompasses previously studied Hermitian cases but also provides a systematic path for treating non-Hermitian systems, which are of growing importance in open quantum systems and quantum technologies.

We begin by developing a general formalism for the coherent-state approximation, grounded in the geometric and algebraic structure of quantum phase space. Rather than working within the confines of particular Lie algebra representations or traditional canonical quantisation methods, we consider general operator algebras and establish a set of conditions for constructing what we term "generalised algebraic coherent states." These states extend beyond the traditional Gazeau-Klauder framework by relaxing the temporal stability requirement while maintaining the essential properties of continuity, normalisation, and overcompleteness [52]. This approach follows the

spirit of Klauder's original general framework [50, 51], allowing us to handle systems with complex algebraic structures, non-canonical symplectic forms, and emergent geometric properties that arise naturally from the underlying operator algebra. .

This is followed by the derivation of the semiclassical Husimi approximation, which leverages the coherent-state results to describe the evolution of general quantum states via the Husimi function.

In the existing literature, coherent-state approximations have often been approached from the bottom up, that is, researchers begin with a particular system or algebra and derive the relevant approximation scheme. For example, Graefe et al. [45] focused on systems described by the Heisenberg-Weyl algebra using Glauber coherent states. Gnutzmann [13, 46] applied these techniques to higher-rank algebras such as $\mathfrak{su}_3$ and $\mathfrak{su}_m$. Ohsawa [14] introduced a symplectic geometric approach to studying semiclassical dynamics of Gaussian wave packets. A more systematic and algebraically general treatment was offered by Kuś and Schäfer [12], who constructed classical limits for systems associated with compact semi-simple Lie algebras. Odzijewicz and Wawreniuk further extended these ideas to multi-boson systems [99] and those based on Kummer-type algebras [100], which lie outside the class of Lie algebras.

Building on this body of work, we propose a top-down strategy: rather than tailoring the approximation to each specific system, we first identify a set of sufficient (though not necessary) criteria that a quantum system must satisfy in order for the coherent-state approximation to apply. These criteria are algebraic in nature and relate to how the system's Hamiltonian acts on coherent states derived from an underlying Lie group structure. Once these conditions are verified for a given system, the coherent-state and semiclassical Husimi approximations can be directly applied without further derivation. This inversion of the conventional methodology streamlines the application of approximation techniques across a wide variety of models, clarifies the generality and limitations of existing approaches, and opens the door to systematic treatment of non-Hermitian quantum systems using tools originally developed for Hermitian dynamics.

Overall, this chapter sets the stage for a systematic and unified treatment of coherent-state and Husimi approximations in both Hermitian and non-Hermitian quantum mechanics. The examples explored in subsequent sections will highlight the broad applicability of this approach and its potential to uncover subtle features of quantum-classical correspondence in systems beyond the Heisenberg-Weyl paradigm.

3.1 Coherent-State Approximations for General Quantum Systems

To construct coherent-state approximations in a more general algebraic framework, we begin by considering a quantum system characterised by an underlying general algebra, $\mathfrak{A}$, with m Hermitian generators, denoted as $\{\hat{X}_i\}_{i=1}^m$. These generators satisfy a fixed set of commutation relations, defining the structure of the algebra. The goal of this chapter is to develop coherent-state approximations for non-Hermitian quantum systems using coherent states associated with $\mathfrak{A}$, focusing on the approximations that emerge in the classical limit.

When moving beyond Lie algebras, several fundamental challenges emerge that require careful

consideration. The commutation relations may be nonlinear in the generators themselves, such as $[\hat{a}, \hat{a}^\dagger] = f(\hat{n})$, where f is a nonlinear function of the number operator $\hat{n} = \hat{a}^\dagger\hat{a}$ [100]. This breaks the linear algebraic structure underpinning the Kirillov-Kostant-Souriau construction and standard group-theoretic quantisation methods. Moreover, the resulting classical phase space may no longer be a coadjoint orbit, and its symplectic geometry can deviate significantly from the Lie–Poisson form. The phase space itself may lose its smooth manifold structure or develop singularities that render standard symplectic methods inapplicable. Furthermore, the geometric properties of the coherent state manifold, including its curvature, topology, and measure, must then be derived directly from the operator algebra, rather than inherited from a Lie group manifold.

The Gazeau–Klauder framework [52] provides a systematic method for constructing coherent states when an action-angle structure exists. Their approach requires the identification of a self-adjoint action operator $\hat{J}$ with discrete, non-negative eigenvalues $\{J_n\}_{n=0}^{\infty}$, interpreted as the action variable. The coherent states form a two-parameter family $|J, \gamma\rangle$ where $J \geq 0$ represents the action and $\gamma \in [0, 2\pi)$ represents the angle variable, satisfying the action identity $\hat{J}|J, \gamma\rangle = J|J, \gamma\rangle$. Under time evolution generated by a Hamiltonian $\hat{H}$, these states exhibit temporal stability, evolving as $|J, \gamma, t\rangle = |J, \gamma + \omega(J)t\rangle$, where $\omega(J) = \partial\langle H\rangle/\partial J$. The classical phase space emerges naturally with canonical coordinates (J, γ) and symplectic form $\omega = dJ \wedge d\gamma$. However, this approach is restrictive as it requires both the existence of well-defined action-angle variables and the preservation of the coherent state structure under time evolution and fails for systems with complex reduction procedures or non-canonical classical structures.

Klauder's original approach [50, 51] offers greater flexibility and requires only three essential conditions. The coherent states $|\chi\rangle$ must depend continuously on the parameter χ belonging to some manifold $\mathbf{M}$, satisfy normalisation $\langle\chi|\chi\rangle = 1$ for all $\chi \in \mathbf{M}$, and admit a resolution of the identity $\int_{\mathbf{M}} |\chi\rangle\langle\chi|\, d\mu(\chi) = \hat{I}$ for some measure μ. While expectation values $\langle\chi|\hat{A}|\chi\rangle$ are often required to admit well-defined classical limits in applications, this is not a formal part of the core definition. Notably, temporal stability, central to the Gazeau-Klauder construction is not required in Klauder's original framework.

In this work, we follow Klauder's framework to construct generalised algebraic coherent states tailored to the specific algebraic structure of $\mathfrak{A}$. This approach accommodates systems beyond traditional Lie algebras, including those with nonlinear commutation relations and non-canonical symplectic structures. The framework also enables systematic treatment of non-Hermitian systems, where the classical phase space and its geometric properties emerge naturally from the quantum algebraic structure. The classical limit is achieved through appropriate scaling of representation parameters, where $\hbar$ emerges implicitly through dimensional analysis and the scaling of quantum numbers relative to classical actions.

An essential aspect of our approach involves understanding the representation of the algebra and how to form a classical limit. Specifically, we assume that the algebra admits a family of finite-dimensional irreducible representations labelled by a single parameter $\lambda \in \mathbb{N}^+$, which serves as a scaling parameter controlling the classical limit. In many physically relevant examples, λ corresponds to a conserved quantity such as total particle number or spin length, and increasing λ

allows us to access the semiclassical regime.

A concrete example is provided by the $\mathfrak{su}_2$ algebra, where irreducible representations are labelled by the total angular momentum j (or equivalently, by $N = 2j$ for systems of indistinguishable bosons). In this case, the large-λ limit corresponds to $N \to \infty$. The framework naturally extends to higher-rank algebras such as $\mathfrak{su}_m$, whose irreducible representations are characterised by $m-1$ non-negative integers $(n_1, n_2, \ldots, n_{m-1})$. By fixing the ratios between these integers, we define a direction in the weight space, often called a ray or a path in the Weyl chamber, that parametrises inequivalent irreducible representations. We then generate a sequence of representations along this ray, $(\lambda n_1, \lambda n_2, \ldots, \lambda n_{m-1})$, by varying λ while preserving the relative weights.

This construction ensures a controlled and systematic approach to the classical limit by scaling the size of the representation while maintaining the system's qualitative structure. It enables us to apply coherent-state approximations in a wide range of settings where the dynamics become increasingly classical as λ grows. Importantly, while our presentation here focuses on algebras with finite-dimensional representations, the coherent-state approximation is not restricted to this case. For example, the Glauber coherent states discussed in the previous chapter are associated with the Heisenberg–Weyl algebra, which has infinite-dimensional representations. Nonetheless, these states provide accurate semiclassical approximations in many physical contexts, illustrating that our framework can be extended to infinite-dimensional cases with appropriate care.

This formulation connects the algebraic construction of coherent states with the emergence of classical dynamics, capturing both the underlying structure of the system and the geometry of coherent states, and sets the stage for deriving the leading-order semiclassical dynamics of expectation values.

Let us now introduce the criteria required for a general coherent-state approximation.

3.1.1 General Coherent-State Approximation Criteria for Hermitian Systems

To systematically approximate quantum dynamics with classical equations of motion, we need to ensure that the coherent states under consideration exhibit certain structural and scaling properties. These properties guarantee that the phase-space description retains consistency with both the algebraic structure and the semiclassical limit. In what follows, we outline the key assumptions and conditions that must be satisfied for the coherent-state approximation to apply to Hermitian systems.

First, we assume the existence of a well-defined family of coherent states, $|\chi\rangle$, which are elements of the projective Hilbert space $\mathbb{P}\mathbf{H}$, that is, quantum states defined up to a global phase. Each coherent state is parametrised by a real vector $\chi \in \mathbb{R}^n$, or equivalently by a complex vector $\chi \in \mathbb{C}^{n/2}$ when such parametrisation is convenient, where $n \leq m$. These coherent states depend continuously on the parameters χ and satisfy a resolution of the identity $\int |\chi\rangle \langle\chi| \, d\mu(\chi) = \hat{I}$ for some appropriate measure μ. These coherent states depend implicitly on the representation label λ, and we denote the family of all such states for fixed λ as $\mathcal{CS}_\lambda$.

Second, we require that the expectation values of the generators scale linearly with λ: the quantity

$\langle\chi|\,\hat{X}_i\,|\chi\rangle$ should be proportional to λ. To obtain finite classical variables in the limit $\lambda \to \infty$, we define rescaled expectation values

$$x_i(\chi) = \frac{1}{\lambda}\,\langle\chi|\,\hat{X}_i\,|\chi\rangle\,, \tag{3.1}$$

which become the classical observables.

Third, the set of all such rescaled expectation values at fixed λ defines an n-dimensional quantum phase space

$$\mathcal{P}_\lambda = \{\vec{x}(\chi) \in \mathbb{R}^m : |\chi\rangle \in \mathcal{CS}_\lambda\}\,. \tag{3.2}$$

The classical phase space $\mathcal{P}$ is then defined by the large-λ limit

$$\mathcal{P} = \lim_{\lambda\to\infty} \mathcal{P}_\lambda. \tag{3.3}$$

Fourth, the classical phase space is equipped with a Poisson bracket $\{\cdot,\cdot\}$, which encodes the structure of the classical dynamics. This bracket arises naturally from the commutator structure of the quantum observables in the limit $\lambda \to \infty$. Specifically, we require

$$\lim_{\lambda\to\infty} -\frac{\mathrm{i}}{\lambda}\,\langle\chi|\,[\hat{X}_i, \hat{X}_j]\,|\chi\rangle = \{x_i, x_j\}. \tag{3.4}$$

Finally, we require a factorisation property for the generators in coherent states. In the large-λ limit, the symmetrised product of any two generators must approximately factorise as the product of their individual expectation values

$$\langle\chi|\left(\hat{X}_i\hat{X}_j + \hat{X}_j\hat{X}_i\right)|\chi\rangle = 2\,\langle\chi|\,\hat{X}_i\,|\chi\rangle\,\langle\chi|\,\hat{X}_j\,|\chi\rangle + O(\lambda), \tag{3.5}$$

or equivalently, after normalisation,

$$\lim_{\lambda\to\infty} \frac{1}{\lambda^2}\,\langle\chi|\left(\hat{X}_i\hat{X}_j + \hat{X}_j\hat{X}_i\right)|\chi\rangle = 2x_ix_j. \tag{3.6}$$

These conditions are satisfied for a broad class of physically relevant algebras and their associated coherent states, including all finite-dimensional Lie algebras—particularly compact semisimple, reductive, solvable, and nilpotent cases.

3.1.2 Factorisation Property using $\mathcal{D}$-Algebra

Before turning to explicit calculations in the subsequent sections, we identify a structural condition on the $\mathcal{D}$-algebra operators that will be essential for establishing a factorisation property at the core of our coherent-state approximation framework [12]. This property allows certain expectation values to decompose into products, significantly simplifying the analysis.

We express a general $\mathcal{D}$-algebra operator $\mathcal{D}_A$ as

$$\mathcal{D}_A = u_A + v_A \mathbf{d}_A, \tag{3.7}$$

where u_A is a scalar multiplicative term and $v_A \mathbf{d}_A$ is a linear differential operator [81]. For the factorisation property to hold, we will now show that we require that u_A is at least of one order higher in the parameter λ than v_A.

The generalised expression for the expectation value of a product of operators, derived via $\mathcal{D}$-algebra methods, is given by [80, 81]

$$\langle\chi|\,\hat{F}\hat{A}\,|\chi\rangle = \frac{1}{\mathcal{M}}\mathcal{D}_A(f\mathcal{M}), \tag{3.8}$$

where $\hat{A}$ is an element of the generating algebra $\mathfrak{A}$, $\hat{F}$ is an element of the enveloping algebra $\mathcal{U}(\mathfrak{A})$, and $\mathcal{M} = \langle\chi||\chi\rangle$ is the normalisation function defined as the inner product of non-normalised coherent states. We define $f = \langle\hat{F}\rangle$, which we assume scales on the order of λ^{m_F}. Expanding equation (3.8) using the decomposed $\mathcal{D}$-algebra from from equation (3.7) we obtain

$$\begin{aligned}
\langle\chi|\,\hat{F}\hat{A}\,|\chi\rangle &= \frac{1}{M}(u_A + v_A\mathbf{d}_A)(fM), \\
&= u_A f + \frac{f}{M}v_A\mathbf{d}_A(M) + v_A\mathbf{d}_A(f), \\
&= f\frac{1}{M}\mathcal{D}_A(M) + v_A\mathbf{d}_A(f), \\
&= fa + v_A\mathbf{d}_A(f),
\end{aligned} \tag{3.9}$$

where we have defined $a = \langle\hat{A}\rangle = \frac{1}{M}\mathcal{D}_A(M)$ which is also of order λ.

Here, the first term in equation (3.9) scales as λ^{m_F+k}, where k is the order of u_A, while the second term scales as $\lambda^{m_F+k'}$, with k' the order of v_A. In order for the factorisation $\langle\hat{F}\hat{A}\rangle \approx \langle\hat{F}\rangle\langle\hat{A}\rangle$ to hold at leading order in λ, we require $k > k'$, that is, the multiplicative component u_A must dominate the differential component v_A in the large-λ limit. Under this assumption, the second term in equation (3.9) becomes subleading and the expectation value approximately factorises as $\langle\hat{F}\hat{A}\rangle \approx \langle\hat{F}\rangle\langle\hat{A}\rangle$ at leading order.

Since $\hat{A}$ is an element of the generating algebra, and $\hat{F}$ can be an arbitrary element of the enveloping algebra, the argument can be recursively applied to any product of generators. Consequently, for two operators $\hat{F}$ and $\hat{G}$ of orders m_F and m_G respectively in $\mathcal{U}(\mathfrak{A})$, we obtain the general factorisation property

$$\langle\hat{F}\hat{G}\rangle = \langle\hat{F}\rangle\langle\hat{G}\rangle + O(\lambda^{m_F+m_G-1}), \tag{3.10}$$

where all expectation values are evaluated in the coherent states.

In summary, the factorisation property holds provided that the multiplicative terms in the $\mathcal{D}$-algebra dominate over the derivative terms in the large-λ limit. Verifying this dominance for a given algebraic structure confirms the validity of the coherent-state approximation framework.

3.1.3 General Coherent-State Approximation Criteria for Hermitian Systems

Having established the general criteria under which coherent-state approximations are valid, including the factorisation property conditions that ensure operator products can be approximated as products of expectation values, we now apply this framework to Hamiltonians constructed from the universal enveloping algebra of $\mathfrak{A}$. To ensure a finite classical limit, we impose a systematic scaling rule: the expectation value of a product of k generators scales as λ^k, and we therefore include a compensating factor of λ^{-k+1} for each such term. This leads to Hamiltonians of the form

$$\hat{\mathcal{H}} = \sum_{l_1=1}^{m} a_{l_1}^{(1)} \hat{X}_{l_1} + \sum_{l_1,l_2=1}^{m} \frac{a_{l_1 l_2}^{(2)}}{\lambda} \left(\hat{X}_{l_1} \hat{X}_{l_2} + \hat{X}_{l_2} \hat{X}_{l_1} \right) + \cdots , \tag{3.11}$$

where the coefficients $a_{l_1,l_2,\ldots}^{(k)} \in \mathbb{R}$ are λ-independent and the symmetrisation ensures Hermiticity. This structure guarantees that the expectation value $\langle \hat{\mathcal{H}} \rangle$ scales linearly with λ, making the classical Hamiltonian

$$h = \lim_{\lambda \to \infty} \frac{1}{\lambda} \langle \chi | \, \hat{\mathcal{H}} \, | \chi \rangle \tag{3.12}$$

well-defined.

We now show that, under the coherent-state approximation, the dynamics of the expectation values $x_i = \frac{1}{\lambda} \langle \chi | \, \hat{X}_i \, | \chi \rangle$ follow classical Hamiltonian equations of motion

$$\frac{\mathrm{d}x_i}{\mathrm{d}t} = \{x_i, h\}. \tag{3.13}$$

That is, the evolution of the classical observables x_i obtained from the expectation values of the generators $\hat{X}_i$ is governed by the Hamiltonian flow generated by h on the classical phase space.

To establish this result, we proceed inductively by considering each term in the Hamiltonian expansion (3.11), beginning with the linear term. Following the same approach as the Heisenberg–Weyl case, we evaluate the classical limit of each term by computing expectation values in coherent states.

To begin, we consider the linear part of the Hamiltonian in equation (3.11), where $\hat{\mathcal{H}}_1 = \hat{X}_j$. Its classical counterpart is simply

$$h_1 = \lim_{\lambda \to \infty} \frac{1}{\lambda} \langle \chi | \, \hat{X}_j \, | \chi \rangle = x_j. \tag{3.14}$$

From the Heisenberg equation of motion, we have

$$\frac{\mathrm{d}\hat{X}_i}{\mathrm{d}t} = -\mathrm{i}[\hat{X}_i, \hat{X}_j]. \tag{3.15}$$

Using the commutator–Poisson bracket correspondence introduced in equation (3.4), we take the expectation value in a coherent state and apply the large-λ limit

$$\lim_{\lambda \to \infty} \left(\frac{1}{\lambda} \frac{\mathrm{d}}{\mathrm{d}t} \langle \hat{X}_i \rangle \right) = - \lim_{\lambda \to \infty} \left(\frac{\mathrm{i}}{\lambda} \langle [\hat{X}_i, \hat{X}_j] \rangle \right),$$

$$\frac{\mathrm{d}x_i}{\mathrm{d}t} = \{x_i, x_j\} = \{x_i, h_1\}. \tag{3.16}$$

We now turn to the quadratic term in equation (3.11),

$$\hat{\mathcal{H}}_2 = \frac{1}{\lambda}\left(\hat{X}_j\hat{X}_k + \hat{X}_k\hat{X}_j\right), \tag{3.17}$$

with classical counterpart

$$h_2 = 2x_jx_k. \tag{3.18}$$

Taking the Heisenberg equation and evaluating the time derivative of the expectation value, we find

$$\frac{1}{\lambda}\frac{\mathrm{d}}{\mathrm{d}t}\langle\hat{X}_i\rangle = -\frac{\mathrm{i}}{\lambda^2}\left(\langle[\hat{X}_i, \hat{X}_j\hat{X}_k]\rangle + \langle[\hat{X}_i, \hat{X}_k\hat{X}_j]\rangle\right). \tag{3.19}$$

Expanding the first commutator

$$[\hat{X}_i, \hat{X}_j\hat{X}_k] = [\hat{X}_i, \hat{X}_j]\hat{X}_k + \hat{X}_j[\hat{X}_i, \hat{X}_k], \tag{3.20}$$

and using the factorisation property (3.5) we obtain

$$-\frac{\mathrm{i}}{\lambda^2}\langle[\hat{X}_i, \hat{X}_j\hat{X}_k]\rangle = -\frac{\mathrm{i}}{\lambda^2}\left(\langle[\hat{X}_i, \hat{X}_j]\rangle\langle\hat{X}_k\rangle + \langle\hat{X}_j\rangle\langle[\hat{X}_i, \hat{X}_k]\rangle\right) + O\left(\frac{1}{\lambda}\right). \tag{3.21}$$

Applying the same reasoning to the second commutator and taking the large-λ limit, we find

$$\begin{aligned}
\lim_{\lambda\to\infty}\frac{1}{\lambda}\frac{\mathrm{d}}{\mathrm{d}t}\langle\hat{X}_i\rangle &= \lim_{\lambda\to\infty}\left(-\frac{\mathrm{i}}{\lambda^2}\left(\langle[\hat{X}_i, \hat{X}_j\hat{X}_k]\rangle + \langle[\hat{X}_i, \hat{X}_k\hat{X}_j]\rangle\right)\right), \\
&= \{x_i, x_j\}x_k + \{x_i, x_k\}x_j + \{x_i, x_k\}x_j + \{x_i, x_j\}x_k, \\
&= 2\{x_i, x_j\}x_k + 2\{x_i, x_k\}x_j, \\
&= \{x_i, 2x_jx_k\} = \{x_i, h_2\}.
\end{aligned} \tag{3.22}$$

This confirms that the coherent-state approximation reproduces the classical dynamics for both linear and quadratic Hamiltonians. Having verified that the classical equations of motion are correctly reproduced by the coherent-state approximation for both linear and quadratic Hamiltonians, we now proceed to complete the argument by induction. This will establish that the result holds for general polynomial Hamiltonians constructed from symmetrised products of the algebra generators.

We begin by considering a Hamiltonian of the form

$$\hat{\mathcal{H}}_s = \frac{1}{\lambda^{s-1}}\left(\hat{f} + \hat{f}^\dagger\right), \tag{3.23}$$

where $\hat{f} = \prod_j \hat{X}_j^{d_j}$ is a monomial of order s in the generators $\hat{X}_i$, with $d_j \geq 0$ and $\sum_j d_j = s$.

We assume as the induction hypothesis that the coherent-state approximation reproduces classical dynamics up to leading order, i.e.,

$$\frac{1}{\lambda}\frac{\mathrm{d}}{\mathrm{d}t}\langle\hat{X}_i\rangle = \frac{1}{\lambda^s}\left(\langle[\hat{X}_i,\hat{f}]\rangle + \langle[\hat{X}_i,\hat{f}^\dagger]\rangle\right) = \{x_i,h_s\} + O\left(\frac{1}{\lambda}\right), \tag{3.24}$$

or equivalently,

$$\frac{\mathrm{d}x_i}{\mathrm{d}t} = \{x_i,h_s\} \quad \text{in the limit } \lambda\to\infty, \tag{3.25}$$

where the corresponding classical Hamiltonian is

$$h_s = \lim_{\lambda\to\infty}\tfrac{1}{\lambda}\langle\chi|\,\hat{\mathcal{H}}_s\,|\chi\rangle = 2\prod_j x_j^{d_j}. \tag{3.26}$$

To complete the induction step, we now consider the Hamiltonian

$$\hat{\mathcal{H}}_{s+1} = \tfrac{1}{\lambda}\left(\hat{\mathcal{H}}_s\hat{X}_k + \hat{X}_k\hat{\mathcal{H}}_s\right) = \tfrac{1}{\lambda^s}\left(\left(\hat{f}+\hat{f}^\dagger\right)\hat{X}_k + \hat{X}_k\left(\hat{f}+\hat{f}^\dagger\right)\right). \tag{3.27}$$

Using the Heisenberg equation of motion and taking expectation values in a coherent state, we obtain

$$\frac{1}{\lambda}\frac{\mathrm{d}}{\mathrm{d}t}\langle\hat{X}_i\rangle = -\frac{\mathrm{i}}{\lambda^{s+1}}\langle[\hat{X}_i,\hat{f}\hat{X}_k]\rangle - \frac{\mathrm{i}}{\lambda^{s+1}}\langle[\hat{X}_i,\hat{f}^\dagger\hat{X}_k]\rangle + \text{H.c.}. \tag{3.28}$$

Let us focus on the first commutator. Using linearity and the Leibniz rule

$$[\hat{X}_i,\hat{f}\hat{X}_k] = [\hat{X}_i,\hat{f}]\hat{X}_k + \hat{f}[\hat{X}_i,\hat{X}_k]. \tag{3.29}$$

Applying the factorisation property (3.5) in the large-λ limit yields

$$-\frac{\mathrm{i}}{\lambda^{s+1}}\langle[\hat{X}_i,\hat{f}\hat{X}_k]\rangle - \mathrm{i}\frac{\langle\hat{f}\rangle}{\lambda^s}\frac{\langle[\hat{X}_i,\hat{X}_k]\rangle}{\lambda} + O(\tfrac{1}{\lambda}). \tag{3.30}$$

Including the contributions from $\hat{f}^\dagger$ and the Hermitian conjugates, and collecting terms, we find that

$$\begin{aligned}\frac{1}{\lambda}\frac{\mathrm{d}}{\mathrm{d}t}\langle\hat{X}_i\rangle &= 2\{x_i,h_s\}x_k + 2\{x_i,x_k\}h_s + O\left(\tfrac{1}{\lambda}\right),\\ &= 2\{x_i,h_sx_k\} + O\left(\tfrac{1}{\lambda}\right),\end{aligned} \tag{3.31}$$

which implies

$$\frac{\mathrm{d}x_i}{\mathrm{d}t} = \{x_i,h_{s+1}\}, \quad \text{where } h_{s+1} = 2h_sx_k, \tag{3.32}$$

thereby completing the inductive step.

Since any symmetrised polynomial in the generators can be built recursively from lower-order monomials, it follows that the result holds for arbitrary Hamiltonians of the form (3.11).

By a recursive argument, we have shown that for Hamiltonians constructed from symmetrised products of algebra generators with appropriate λ-dependent scaling, the coherent-state approximation reproduces classical symplectic motion on the phase space to leading order in the large-λ limit.

Having established the coherent-state approximation for Hermitian systems, we now turn to its extension to non-Hermitian dynamics. In this setting, the evolution no longer preserves the norm of quantum states, and as discussed previously, the metric bracket plays a central role in capturing this norm evolution within the phase-space formalism.

To ensure the validity of the coherent-state approximation for non-Hermitian systems, an additional requirement must be satisfied: the metric bracket must admit a well-defined large-λ limit, analogous to the Poisson bracket condition in the Hermitian case. In the next section, we formalise this extension and establish the criteria necessary for coherent-state dynamics to remain consistent under non-Hermitian evolution.

3.1.4 General Coherent-State Approximation Criteria for non-Hermitian Systems

We now extend the coherent-state approximation to quantum systems governed by non-Hermitian dynamics. In this case, the approximation requires one additional structural condition: the phase space must be equipped with a metric bracket that captures the effects of norm non-conservation. Specifically, we require that the following limit exists

$$\lim_{\lambda\to\infty}\frac{1}{\lambda}\left(\langle\chi|\left[\hat{X}_i,\hat{X}_j\right]_+|\chi\rangle-2\langle\chi|\hat{X}_i|\chi\rangle\langle\chi|\hat{X}_j|\chi\rangle\right)=\{\!\{x_i,x_j\}\!\}. \tag{3.33}$$

The non-Hermitian analogue of the Hamiltonian from equation (3.11) takes the form

$$\hat{\mathcal{K}}=\sum_{l_1}^{3}a_{l_1}^{(1)}\hat{X}_{l_1}+\sum_{l_1,l_2=1}^{3}\frac{a_{l_1l_2}^{(2)}}{\lambda}\hat{X}_{l_1}\hat{X}_{l_2}+\dots \tag{3.34}$$

where $a^{(k)}_{l_1,l_2,\dots}\in\mathbb{C}$. Each monomial term can be decomposed into Hermitian and anti-Hermitian parts, yielding

$$\hat{\mathcal{K}}=\hat{\mathcal{H}}+\mathrm{i}\hat{\Gamma}, \tag{3.35}$$

with

$$\hat{\mathcal{H}}=\sum_{l_1}^{3}b_{l_1}^{(1)}\hat{X}_{l_1}+\sum_{l_1,l_2=1}^{3}\frac{b_{l_1l_2}^{(2)}}{\lambda}\left[\hat{X}_{l_1},\hat{X}_{l_2}\right]_++\dots \tag{3.36}$$

$$\hat{\Gamma}=\sum_{l_1}^{3}c_{l_1}^{(1)}\hat{X}_{l_1}+\sum_{l_1,l_2=1}^{3}\frac{c_{l_1l_2}^{(2)}}{\lambda}\left[\hat{X}_{l_1},\hat{X}_{l_2}\right]_++\dots \tag{3.37}$$

where all the coefficients $b^{(k)}_{l_1,l_2,\ldots}, c^{(k)}_{l_1,l_2,\ldots} \in \mathbb{R}$.

To establish the classical dynamics generated by a general non-Hermitian Hamiltonian within the coherent-state approximation, we now proceed case by case, mirroring the approach used in the Hermitian setting. Specifically, we demonstrate how the evolution of expectation values decomposes into a symplectic (Poisson) and gradient (metric) component. This is achieved by analysing the Heisenberg equations for increasingly complex anti-Hermitian Hamiltonians, beginning with linear and quadratic terms before generalising the result through induction.

We begin by considering the simplest non-Hermitian scenario in which the Hamiltonian is purely anti-Hermitian and linear in the generators

$$\hat{\mathcal{K}} = \mathrm{i}\hat{\Gamma}_1 = \mathrm{i}\hat{X}_k, \tag{3.38}$$

where $\hat{X}_k$ is a Hermitian generator of the underlying algebra. The classical counterpart is given by the expectation value,

$$\gamma_1 = \lim_{\lambda\to\infty} \frac{1}{\lambda} \langle\chi|\, \hat{\Gamma}_1 \,|\chi\rangle = x_k. \tag{3.39}$$

The Heisenberg equation of motion for an observable $\hat{X}_i$ under this Hamiltonian reads

$$\begin{aligned} \frac{\mathrm{d}\langle\hat{X}_i\rangle}{\mathrm{d}t} &= \langle\Big[\hat{X}_i, \hat{\Gamma}_1\Big]_+\rangle - 2\,\langle\hat{X}_i\rangle\,\langle\hat{\Gamma}_1\rangle\,, \\ &= \langle\Big[\hat{X}_i, \hat{X}_k\Big]_+\rangle - 2\,\langle\hat{X}_i\rangle\,\langle\hat{X}_k\rangle\,. \end{aligned} \tag{3.40}$$

Taking the expectation value in a coherent state and applying the large λ limit, we find

$$\begin{aligned} \lim_{\lambda\to\infty}\left(\frac{1}{\lambda}\frac{\mathrm{d}\,\langle\hat{X}_i\rangle}{\mathrm{d}t}\right) = \lim_{\lambda\to\infty}\left(\frac{1}{\lambda}\,\langle\Big[\hat{X}_i, \hat{X}_k\Big]_+\rangle - \frac{2}{\lambda}\,\langle\hat{X}_i\rangle\,\langle\hat{X}_k\rangle\right), \\ \frac{\mathrm{d}x_i}{\mathrm{d}t} = \{\!\{x_i, x_k\}\!\}, \end{aligned} \tag{3.41}$$

where $\{\!\{\cdot,\cdot\}\!\}$ denotes the metric bracket, which is equivalent to

$$\frac{\mathrm{d}x_i}{\mathrm{d}t} = \{\!\{x_i, \gamma_1\}\!\}. \tag{3.42}$$

This confirms that the coherent-state approximation recovers the correct leading-order dynamics for the linear anti-Hermitian Hamiltonian.

Having established the result for a linear anti-Hermitian Hamiltonian, we now extend the coherent-state approximation to a quadratic setting. Specifically, we consider a Hamiltonian constructed from symmetric (Hermitian) products of two generators

$$\hat{\Gamma}_2 = \frac{1}{\lambda}\left(\hat{X}_j\hat{X}_k + \hat{X}_k\hat{X}_j\right). \tag{3.43}$$

whose classical counterpart is given by

$$\gamma_2 = 2x_j x_k. \tag{3.44}$$

This case serves as the next step in a recursive argument and illustrates how the metric bracket governs the non-Hermitian contributions to the classical dynamics at higher orders.

Taking the expectation values of the Heisenberg equation of motion, we obtain

$$\frac{1}{\lambda}\frac{\mathrm{d}\langle\hat{X}_i\rangle}{\mathrm{d}t} = \frac{1}{\lambda^2}\left\langle\left[\hat{X}_i, \hat{X}_j\hat{X}_k\right]_+\right\rangle - \frac{2}{\lambda^2}\left\langle\hat{X}_i\right\rangle\left\langle\hat{X}_j\hat{X}_k\right\rangle \tag{3.45}$$

$$+ \frac{1}{\lambda^2}\left\langle\left[\hat{X}_i, \hat{X}_k\hat{X}_j\right]_+\right\rangle - \frac{2}{\lambda^2}\left\langle\hat{X}_i\right\rangle\left\langle\hat{X}_k\hat{X}_j\right\rangle. \tag{3.46}$$

Using the identity

$$\left[\hat{X}_i, \hat{X}_j\hat{X}_k\right]_+ = \left[\hat{X}_i, \hat{X}_j\right]_+\hat{X}_k + \hat{X}_j\left[\hat{X}_i, \hat{X}_k\right]_+ - 2\hat{X}_j\hat{X}_i\hat{X}_k, \tag{3.47}$$

we expand the first two terms in the equation (3.46) as

$$\frac{1}{\lambda^2}\left(\left\langle\left[\hat{X}_i, \hat{X}_j\hat{X}_k\right]_+\right\rangle - 2\left\langle\hat{X}_i\right\rangle\left\langle\hat{X}_j\hat{X}_k\right\rangle\right) = \frac{1}{\lambda^2}\left(\left\langle\left[\hat{X}_i, \hat{X}_j\right]_+\right\rangle\left\langle\hat{X}_k\right\rangle + \left\langle\hat{X}_j\right\rangle\left\langle\left[\hat{X}_i, \hat{X}_k\right]_+\right\rangle\right.$$
$$\left. -2\left\langle\hat{X}_j\right\rangle\left\langle\hat{X}_i\right\rangle\left\langle\hat{X}_k\right\rangle - 2\left\langle\hat{X}_i\right\rangle\left\langle\hat{X}_j\right\rangle\left\langle\hat{X}_k\right\rangle\right) + O\left(\lambda^{-1}\right). \tag{3.48}$$

Taking the large-λ limit and using the definition of the metric bracket, we obtain

$$\lim_{\lambda\to\infty}\left(\frac{1}{\lambda^2}\left(\left\langle\left[\hat{X}_i, \hat{X}_j\hat{X}_k\right]_+\right\rangle - 2\left\langle\hat{X}_i\right\rangle\left\langle\hat{X}_j\hat{X}_k\right\rangle\right)\right) = \{\!\{x_i, x_j\}\!\}x_k + \{\!\{x_i, x_k\}\!\}x_j,$$
$$= \{\!\{x_i, x_j x_k\}\!\}. \tag{3.49}$$

Applying the same analysis to the remaining terms in equation (3.45) and collecting all contributions, we find

$$\lim_{\lambda\to\infty}\frac{1}{\lambda}\frac{\mathrm{d}\langle\hat{X}_i\rangle}{\mathrm{d}t} = 2\{\!\{x_i, x_j x_k\}\!\}, \tag{3.50}$$

$$= \{\!\{x_i, \gamma_2\}\!\}. \tag{3.51}$$

Now that we have shown that equation (3.13) holds for both linear and quadratic anti-Hermitian Hamiltonians, we proceed with an inductive argument to extend this result to arbitrary polynomial Hamiltonians of the form (3.34).

We begin by assuming the result holds for a Hamiltonian of the form

$$\hat{\mathcal{K}}_s = \mathrm{i}\hat{\Gamma}_s = \frac{1}{\lambda^{s-1}}\left(\hat{f} + \hat{f}^\dagger\right), \tag{3.52}$$

where $\hat{f} = \prod_j \hat{X}_j^{d_j}$ is a monomial of order s in the generators $\hat{X}_i$, with $\sum_j d_j = s$ and $d_j \geq 0$.

We assume the inductive hypothesis

$$\frac{1}{\lambda}\frac{\mathrm{d}\langle\hat{X}_i\rangle}{\mathrm{d}t} = \frac{1}{\lambda^s}\left(\langle[\hat{X}_i,\hat{f}]_+\rangle - 2\langle\hat{X}_i\rangle\langle\hat{f}\rangle + \langle[\hat{X}_i,\hat{f}^\dagger]_+\rangle - 2\langle\hat{X}_i\rangle\langle\hat{f}^\dagger\rangle\right), \tag{3.53}$$

$$= \{\!\{x_i,\gamma_s\}\!\} + O\left(\tfrac{1}{\lambda}\right), \tag{3.54}$$

i.e.,

$$\frac{\mathrm{d}x_i}{\mathrm{d}t} = \{\!\{x_i,\gamma_s\}\!\} \quad \text{in the limit } \lambda\to\infty, \tag{3.55}$$

with

$$\gamma_s = \lim_{\lambda\to\infty}\tfrac{1}{\lambda}\left(\langle\chi|\,\hat{\Gamma}_s\,|\chi\rangle\right) = 2\prod_j {x_j}^{d_j} \tag{3.56}$$

We now construct the next order Hamiltonian

$$\hat{\mathcal{K}}_{s+1} = \mathrm{i}\hat{\Gamma}_{s+1}, \quad \text{where} \quad \hat{\Gamma}_{s+1} = \frac{1}{\lambda}\left(\hat{\mathcal{K}}_s\hat{X}_k + \hat{X}_k\hat{\mathcal{K}}s\right). \tag{3.57}$$

This expands to

$$\hat{\Gamma}_{s+1} = \frac{1}{\lambda^s}\left(\left(\hat{f}+\hat{f}^\dagger\right)\hat{X}_k + \hat{X}_k\left(\hat{f}+\hat{f}^\dagger\right)\right). \tag{3.58}$$

Taking the Heisenberg equation of motion and evaluating expectation values in coherent states, we obtain

$$\frac{1}{\lambda}\frac{\mathrm{d}\langle\hat{X}_i\rangle}{\mathrm{d}t} = \frac{1}{\lambda^{s+1}}\left(\langle\left[\hat{X}_i,\hat{f}\hat{X}_k\right]_+\rangle - 2\langle\hat{X}_i\rangle\langle\hat{f}\hat{X}_k\rangle\right) \tag{3.59}$$

$$+\frac{1}{\lambda^{s+1}}\left(\langle\left[\hat{X}_i,\hat{f}^\dagger\hat{X}_k\right]_+\rangle - 2\langle\hat{X}_i\rangle\langle\hat{f}^\dagger\hat{X}_k\rangle\right) + \text{H.c.} \tag{3.60}$$

Applying the factorisation property and the inductive hypothesis to the resulting terms, we find

$$\frac{1}{\lambda}\frac{\mathrm{d}\langle\hat{X}_i\rangle}{\mathrm{d}t} = 2\{\!\{x_i,\gamma_s\}\!\}x_k + 2\{\!\{x_i,x_k\}\!\}\gamma_s + O\left(\tfrac{1}{\lambda}\right)$$

$$= 2\{\!\{x_i,\gamma_s x_k\}\!\} + O\left(\tfrac{1}{\lambda}\right). \tag{3.61}$$

Therefore, in the large-λ limit,

$$\frac{\mathrm{d}x_i}{\mathrm{d}t} = \{\!\{x_i,\gamma_{s+1}\}\!\}, \tag{3.62}$$

with $\gamma_{s+1} = 2\gamma_s x_k$, as expected.

This completes the inductive step. Since any polynomial Hamiltonian can be written as a sum of such monomials, the general result follows directly by linearity. Thus, we have shown that, for appropriately scaled non-Hermitian Hamiltonians, the coherent-state approximation yields classical dynamics generated by symplectic and gradient flow, respectively corresponding to the

Hermitian and anti-Hermitian parts of the Hamiltonian.

3.2 Generalised Semiclassical Husimi Dynamics

Having established the coherent-state approximation for both Hermitian and non-Hermitian quantum systems, including the conditions under which classical dynamics emerge from the quantum Heisenberg equations, we now turn to an important application of this framework in the form of the semiclassical Husimi approximation.

In Chapter 2, we introduced a semiclassical Husimi approximation specifically for systems built on the Heisenberg-Weyl algebra. Here, we generalise this construction beyond the Heisenberg-Weyl case using the coherent-state approximation developed in the previous sections.

This generalised approach rests on the key insight that if a quantum system satisfies the necessary criteria, namely, the existence of coherent states, the large-λ Poisson and metric bracket limits, and factorisation of operator products, then the classical dynamics of expectation values can be used to propogate the Husimi distribution semiclassically.

One important distinction must be highlighted, the Husimi distribution is defined on the quantum phase space, which is typically associated with the parameters of the coherent states. In contrast, the classical dynamics evolve on the classical phase space derived from the expectation values of the generators. This distinction becomes particularly significant for generalised algebras, especially beyond Lie algebras where these two phase spaces might not coincide at finite λ.

For non-Hermitian systems that meet the required conditions, the semiclassical Husimi approximation takes the form

$$Q_{\psi(t)}(\chi) = |\langle\bar{\chi}(t)|\psi_0\rangle|^2 = Q_{\psi_0}\left(\Phi_{-t}(\chi)\right) w(\chi, t), \tag{3.63}$$

in which $\bar{\chi}(t)$ is the non-Hermitian coherent-state approximation and $\Phi(t)(\chi)$ is the classical flow generated by the Hamiltonian $k^* = h - \mathrm{i}\gamma$ and $w(\chi, t)$ accounts for the norm evolution induced by the anti-Hermitian part. This expression shows that the initial Husimi distribution is transported along classical trajectories and modulated by a non-unitary weight.

In summary, the generalised coherent-state approximation provides a principled route to generalising the semiclassical Husimi method across a broad class of algebras and quantum systems.

In the following chapters, we demonstrate the general framework through two concrete examples. Chapter 4 focuses on the $\mathfrak{su}_2$ algebra, a standard compact Lie algebra, to illustrate the coherent-state approximation in a well-understood setting. Chapter 5 addresses a deformed $\mathfrak{su}_2$ algebra, whose commutation relations deviate from the standard Lie form, thereby demonstrating the flexibility of the framework beyond conventional algebraic structures. The non-Hermitian coherent-state approximation and the semiclassical Husimi formulation presented in Chapter 4 are new contributions for the $\mathfrak{su}_2$ case. In Chapter 5, the coherent-state approximation for a non-Hermitian deformed $\mathfrak{su}_2$ system is also original, as is the semiclassical Husimi formulation for both the Hermitian and non-Hermitian regimes.

In addition to these two main case studies, we also examine the Jacobi algebra, which underlies Gaussian wave packet dynamics. By treating Gaussian states as coherent states of the Jacobi group, we interpret the method of Ohsawa and Leok [14] as a coherent-state approximation. Although we do not explore detailed dynamical examples, this algebra provides a novel and unifying perspective within our general framework. This equivalence enables extensions to non-Hermitian systems and the application of semiclassical Husimi approximations, while revealing four distinct approximation methods for Heisenberg-Weyl algebra systems: the Glauber coherent-state and semiclassical Husimi approximations, alongside their Jacobi algebra counterparts. These connections are explored further in in Appendix C.

Chapter 4

Applications of Phase-Space Approximations to $\mathfrak{su}_2$ Spin Systems

In this chapter, we apply the coherent-state and semiclassical Husimi approximation frameworks developed in previous chapters to quantum systems governed by the $\mathfrak{su}_2$ algebra. These systems are of central importance in quantum mechanics, arising naturally in contexts involving angular momentum, spin dynamics, and two-level systems [101].

It is important to note that quantum-classical correspondence for systems with Hermitian Hamiltonians expressible in terms of Lie algebra generators, including $\mathfrak{su}_2$, is well established in the literature. In particular, Kus and Schäfer introduced a coherent-state approximation for all compact semi-simple Lie algebras, which encompasses the $\mathfrak{su}_2$ case as a special instance [12]. While we could have employed existing techniques such as the Kirillov orbit method [102], our treatment here serves as a valuable illustrative example of the more general framework we have constructed. The original contributions of this work lie in extending both the coherent-state approximation and the semiclassical Husimi approximation to systems with non-Hermitian Hamiltonians that incorporate $\mathfrak{su}_2$ structure, thereby going beyond the traditional Hermitian case to encompass gain-loss dynamics that have not been previously considered.

The $\mathfrak{su}_2$ algebra describes the symmetry of spin systems, with its generators corresponding to the components of angular momentum. In all these examples, the finite-dimensional Hilbert space and the compact geometry of the associated phase space, the Bloch sphere, impose constraints and structure that distinguish them sharply from systems built on the Heisenberg-Weyl algebra.

A key physical feature of $\mathfrak{su}_2$ systems is the interplay between discrete quantum levels and smooth classical-like behaviour in the large-spin (large-j or large-λ) limit. This makes them ideal candidates for exploring quantum-classical correspondence: how classical mechanics emerges from quantum theory in appropriate limits, and how semiclassical approximations can capture the essential dynamics even in the presence of non-Hermitian effects.

We begin with a detailed overview of the $\mathfrak{su}_2$ algebra, its finite-dimensional irreducible representations, and the associated spin coherent states. The coherent-state formalism naturally produces

a classical phase space with spherical geometry, corresponding to the Kirillov orbit of the group action. When recast in terms of canonical coordinates, specifically (ϕ, s_z), where ϕ is the azimuthal angle and s_z denotes the population imbalance, the phase space adopts the form of a flat strip with periodic boundary conditions in ϕ. This representation is particularly convenient for visualisation and for implementing our phase-space methods.

We then demonstrate that $\mathfrak{su}_2$ systems satisfy the necessary algebraic and asymptotic conditions for the application of both the coherent-state approximation and the semiclassical Husimi dynamics.

Following this foundational setup, we present a series of Hermitian and non-Hermitian $\mathfrak{su}_2$ Hamiltonians that serve to illustrate the effectiveness and limitations of our methods. Through these case studies, we show how the semiclassical Husimi approach captures both the classical flow and the evolving norm, often improving upon the coherent-state approximation, particularly over longer timescales or in regimes where the quantum state becomes significantly deformed.

By the end of the chapter, we will have demonstrated how the semiclassical framework adapts to curved phase spaces arising from finite-dimensional Hilbert spaces, and how the classical-quantum correspondence manifests in one of the most fundamental quantum algebras. This exploration reveals both the power and limitations of semiclassical approximation methods, especially in capturing dynamics on compact, non-Euclidean geometries such as the Bloch sphere.

The $\mathfrak{su}_2$ algebra is generated by three operators $\hat{J}_x$, $\hat{J}_y$, and $\hat{J}_z$ satisfying the commutation relations [103]

$$[\hat{J}_i, \hat{J}_j] = \mathrm{i}\varepsilon_{ijk}\hat{J}_k, \tag{4.1}$$

where ε_{ijk} is the Levi-Civita symbol and the indices i, j, k range over x, y, and z.

These commutation relations define the structure of the $\mathfrak{su}_2$ Lie algebra, and physically they encode the fundamental non-commutativity of angular momentum components. This framework underlies both intrinsic spin (such as spin-1/2 particles) and orbital angular momentum in quantum systems. It also serves as the mathematical backbone for a wide range of finite-dimensional quantum systems, particularly those with two-level or collective spin-like structure.

A particularly instructive physical realisation of the $\mathfrak{su}_2$ algebra arises in the context of a two-mode Bose-Hubbard model. In such a system, two bosonic modes are described by annihilation and creation operators $\hat{a}_1$, $\hat{a}_2$ and $\hat{a}_1^\dagger$, $\hat{a}_2^\dagger$, which satisfy the standard bosonic commutation relations:

$$[\hat{a}_i, \hat{a}_j^\dagger] = \delta_{ij}, \quad [\hat{a}_i, \hat{a}_j] = [\hat{a}_i^\dagger, \hat{a}_j^\dagger] = 0. \tag{4.2}$$

From these, one can construct operators that obey the $\mathfrak{su}_2$ algebra

$$\hat{J}_x = \frac{1}{2}\left(\hat{a}_1^\dagger\hat{a}_2 + \hat{a}_2^\dagger\hat{a}_1\right), \tag{4.3}$$

$$\hat{J}_y = \frac{1}{2\mathrm{i}}\left(\hat{a}_1^\dagger\hat{a}_2 - \hat{a}_2^\dagger\hat{a}_1\right), \tag{4.4}$$

$$\hat{J}_z = \frac{1}{2}\left(\hat{a}_1^\dagger\hat{a}_1 - \hat{a}_2^\dagger\hat{a}_2\right). \tag{4.5}$$

This realisation provides a bridge between second-quantised bosonic systems and finite-dimensional angular momentum representations, and will serve as a concrete setting for applying the coherent-state and semiclassical techniques developed earlier.

The total number operator $\hat{N} = \hat{a}_1^\dagger \hat{a}_1 + \hat{a}_2^\dagger \hat{a}_2$ commutes with all three generators. This implies that the total number of bosons is conserved under $\mathfrak{su}_2$ dynamics, and the eigenvalue of $\hat{N}$ determines the dimension of the corresponding irreducible representation.

This algebra has a single Casimir operator,

$$\hat{C} = \hat{J}_x^2 + \hat{J}_y^2 + \hat{J}_z^2. \tag{4.6}$$

In terms of the bosonic operators, it takes the form

$$\hat{C} = \frac{1}{4}\hat{N}\left(\hat{N} + 2\right), \tag{4.7}$$

indicating that the Casimir eigenvalue, which labels the irreducible representation, is determined entirely by the total boson number. This reinforces the correspondence between fixed-particle-number subspaces and finite-dimensional spin representations of $\mathfrak{su}_2$.

It is also convenient to introduce the ladder operators (also known as raising and lowering operators), defined as

$$\hat{J}_+ = \hat{J}_x + \mathrm{i}\hat{J}_y, \quad \hat{J}_- = \hat{J}_x - \mathrm{i}\hat{J}_y. \tag{4.8}$$

In terms of the bosonic operators, these take the particularly simple form

$$\hat{J}_+ = \hat{a}_1^\dagger \hat{a}_2, \quad \hat{J}_- = \hat{a}_2^\dagger \hat{a}_1. \tag{4.9}$$

These operators satisfy the standard $\mathfrak{su}_2$ commutation relations

$$[\hat{J}_+, \hat{J}_-] = 2\hat{J}_z, \quad [\hat{J}_z, \hat{J}_\pm] = \pm\hat{J}_\pm. \tag{4.10}$$

To define the $\mathfrak{su}_2$ coherent states, we begin by identifying the group structure and an appropriate reference state. The Hilbert space is constructed in the standard angular momentum basis, where each basis state $|j\rangle$ is an eigenstate of $\hat{J}_z$,

$$\hat{J}_z |j\rangle = \left(\frac{N}{2} - j\right)|j\rangle, \quad j = 0, 1, \ldots, N, \tag{4.11}$$

with total particle number N, so that the dimension of the representation is $N + 1$.

In the two-mode Bose-Hubbard realisation, each $|j\rangle$ corresponds to a Fock state with $N - j$ bosons in mode 1 and j bosons in mode 2

$$|j\rangle = |N - j, j\rangle = \frac{\left(\hat{a}_1^\dagger\right)^{N-j}\left(\hat{a}_2^\dagger\right)^j}{\sqrt{(N-j)!j!}}|0, 0\rangle. \tag{4.12}$$

We construct the coherent states as group displacements of a fixed reference state. Here, we choose the highest weight state $|0\rangle = |N, 0\rangle$, which is invariant under the U(1) subgroup generated by $\hat{J}_z$. The coherent states then correspond to points on the coset space $\mathrm{SU}(2)/U(1)$, which is topologically equivalent to the Bloch sphere S^2.

The coherent state manifold is generated by acting on a reference state with elements of the coset, implemented via the generalised displacement operator

$$D(\xi) = e^{\left(\xi \hat{J}_+ - \xi^* \hat{J}_-\right)}. \tag{4.13}$$

To obtain a more convenient parametrisation, we apply the Baker–Campbell–Hausdorff (BCH) decomposition and introduce a stereographic coordinate $\zeta \in \mathbb{C}$, related to ξ by a non-linear transformation that ensures alignment with the complex projective structure of the Bloch sphere.[1] This leads to the disentangled form

$$D(\zeta) = \left(1 + |\zeta|^2\right)^{-\frac{N}{2}} e^{\zeta \hat{J}_-} e^{-\ln(1+|\zeta|^2)\hat{J}z} e^{-\zeta^* \hat{J}_+}. \tag{4.14}$$

However, when acting on the highest weight state $|0\rangle$, as defined above, this simplifies to

$$|\zeta\rangle = D(\zeta)\,|0\rangle = \left(1 + |\zeta|^2\right)^{-\frac{N}{2}} e^{\zeta \hat{J}_-}\,|0\rangle\,, \tag{4.15}$$

where $|0\rangle \equiv |N, 0\rangle$ is the state with all bosons in the first mode.

Applying the disentangled operator to the extremal (highest-weight) state $|0\rangle$ yields the expression for a normalised $\mathfrak{su}_2$ coherent state, labelled by $\zeta \in \mathbb{C}$

$$|\zeta\rangle = \frac{1}{(1 + |\zeta|^2)^{\frac{N}{2}}} \sum_{j=0}^{N} \sqrt{\binom{N}{j}}\, \zeta^j\,|j\rangle\,. \tag{4.16}$$

This state is a superposition of the angular momentum basis states $|j\rangle$, weighted by binomial coefficients and the complex coordinate ζ. It represents a quantum state peaked around a corresponding classical point on the Bloch sphere.

The associated non-normalised coherent state takes the simpler form

$$||\zeta\rangle = e^{\zeta \hat{J}_-}\,|0\rangle\,, \tag{4.17}$$

with a normalisation function given by

$$\mathcal{M} = \langle\zeta||\zeta\rangle = \left(1 + |\zeta|^2\right)^N. \tag{4.18}$$

A crucial property of these states is that they form an overcomplete set and satisfy a resolution of

[1] Explicitly, $\zeta = \tan\left(\frac{\theta}{2}\right) e^{-i\phi}$ in terms of spherical angles, while ξ parametrises the exponential map.

the identity. Specifically, the normalised coherent states $|\zeta\rangle$ obey

$$\int_{\mathbb{C}} |\zeta\rangle \langle\zeta| \; d\mu(\zeta) = \hat{I}, \tag{4.19}$$

where the integration measure is

$$d\mu(\zeta) = \frac{N+1}{\pi} \left(1 + |\zeta|^2\right)^{-(N+2)} \; d^2\zeta, \tag{4.20}$$

and $d^2\zeta = d\mathrm{Re}(\zeta)\, d\mathrm{Im}(\zeta)$ denotes the Lebesgue measure on the complex plane.

This resolution of identity confirms that any state in the finite-dimensional Hilbert space can be decomposed in terms of the coherent states. This property, combined with the fact that $\mathfrak{su}_2$ coherent states are parametrised by points on the classical phase space (a sphere), makes them ideally suited for semiclassical approximation schemes such as the one developed in this thesis.

To describe classical dynamics on this phase space, we introduce real Cartesian coordinates $s_i \in \mathbb{R}$ that correspond to the scaled expectation values of the $\mathfrak{su}_2$ generators. We define the scaling factor as $\eta = \frac{2}{N}$, so that the classical variables are given by

$$s_i = \eta \langle \hat{J}_i \rangle = \frac{2}{N} \langle \hat{J}_i \rangle. \tag{4.21}$$

This normalisation ensures that the classical variables s_i remain finite in the large-N (i.e., classical) limit. It also constrains the total spin vector to lie on the unit sphere, $\sum_i s_i^2 = 1$, consistent with the geometry of the classical phase space. This scaling approach is standard in semiclassical treatments (see, e.g., [76]), and has been generalised in constructions involving higher-rank algebras [46].

The quantities (s_x, s_y, s_z) represent the components of a point on the unit Bloch sphere, and are related to the complex coordinate $\zeta \in \mathbb{C}$, introduced earlier as a parametrisation of the coherent state, via the stereographic projection from the south pole. The explicit relations are

$$s_x = \frac{\zeta + \zeta^*}{1 + |\zeta|^2}, \tag{4.22}$$

$$s_y = \mathrm{i}\frac{\zeta^* - \zeta}{1 + |\zeta|^2}, \tag{4.23}$$

$$s_z = \frac{1 - |\zeta|^2}{1 + |\zeta|^2}. \tag{4.24}$$

The classical dynamics are governed by two complementary geometric structures on the sphere. The symplectic structure is encoded in the Poisson bracket

$$\{s_i, s_j\} = \epsilon_{ijk} s_k, \tag{4.25}$$

which generates Hamiltonian flow. The Riemannian structure is encoded in the metric bracket

$$\{\!\{s_i, s_j\}\!\} = \delta_{ij} - s_i s_j, \tag{4.26}$$

which generates gradient flow and arises naturally in non-Hermitian settings.

Alternatively, the sphere can be parametrised using canonical cylindrical coordinates (ϕ, s_z), where

$$\phi = \arctan\left(\frac{s_y}{s_x}\right). \tag{4.27}$$

This coordinate system proves particularly advantageous for formulating the system dynamics while simultaneously providing a compact phase space representation that facilitates visualisation of dynamics.

A full list of Poisson brackets, and metric brackets for multiple coordinate systems is provided in Appendix B. For a detailed derivation of these structures, including their relation to the coherent-state manifold, we refer the reader to [76].

To apply the general coherent-state semiclassical framework developed in earlier chapters, we must determine the associated $\mathcal{D}$-algebra operators for the $\mathfrak{su}_2$ coherent states. These operators encode the action of the quantum algebra on the coherent-state manifold and are essential for computing expectation values and the emergence of classical dynamics in the large-N limit. A key step in this approach is verifying the factorisation property via the $\mathcal{D}$-algebra structure.

The computation of the $\mathcal{D}$-algebra operators corresponding to the generators $\hat{J}_-, \hat{J}_z, \hat{J}_+$ provides the foundation for verifying the semiclassical criteria in the $\mathfrak{su}_2$ case, such as the metric bracket limits introduced earlier.

Starting with $\mathcal{D}_{J_-}$, the non-normalised coherent state is given by $||\zeta\rangle = e^{\zeta \hat{J}_-} |0\rangle$. Acting with $\hat{J}_-$ yields

$$\begin{aligned} \hat{J}_- ||\zeta\rangle &= \hat{J}_- e^{\zeta \hat{J}_-} |0\rangle\,, \\ &= \frac{\partial}{\partial \zeta} ||\zeta\rangle\,, \end{aligned} \tag{4.28}$$

which implies that the differential operator is simply

$$\mathcal{D}_{J_-} = \frac{\partial}{\partial \zeta}. \tag{4.29}$$

To compute $\mathcal{D}_{J_z}$, we define the operator-valued function $f_1(\zeta) \equiv e^{-\zeta \hat{J}_-} \hat{J}_z e^{\zeta \hat{J}_-}$, following the approach in [82]. Differentiating f_1 with respect to ζ, we obtain

$$\begin{aligned} \frac{df_1(\zeta)}{d\zeta} &= e^{-\zeta \hat{J}_-} [\hat{J}_z, \hat{J}_-] e^{\zeta \hat{J}_-}, \\ &= -\hat{J}_-. \end{aligned} \tag{4.30}$$

Integrating this equation and using the initial condition $f_1(0) = \hat{J}_z$, we find

$$f_1(\zeta) = \hat{J}_z - \zeta \hat{J}_-. \tag{4.31}$$

Rewriting this result yields the identity

$$\hat{J}_z e^{\zeta \hat{J}_-} = e^{\zeta \hat{J}_-} \hat{J}_z - \zeta e^{\zeta \hat{J}_-} \hat{J}_-. \tag{4.32}$$

Acting on the vacuum $|0\rangle$, we obtain

$$\begin{aligned} \hat{J}_z ||\zeta\rangle &= \hat{J}_z e^{\zeta \hat{J}_-} |0\rangle , \\ &= \left(e^{\zeta \hat{J}_-} \hat{J}_z - \zeta e^{\zeta \hat{J}_-} \hat{J}_- \right) |0\rangle , \\ &= \left(\frac{N}{2} - \zeta \frac{\partial}{\partial \zeta} \right) ||\zeta\rangle , \end{aligned} \tag{4.33}$$

where we used $\hat{J}_z |0\rangle = \frac{N}{2} |0\rangle$. Therefore, the corresponding differential operator is

$$\mathcal{D}_{J_z} = \frac{N}{2} - \zeta \frac{\partial}{\partial \zeta}. \tag{4.34}$$

We now derive the differential operator $\mathcal{D}_{J_+}$ following the same procedure. Define the operator-valued function

$$f_2(\zeta) = e^{-\zeta \hat{J}_-} \hat{J}_+ e^{\zeta \hat{J}_-}. \tag{4.35}$$

Differentiating f_2 with respect to ζ, we obtain

$$\begin{aligned} \frac{df_2(\zeta)}{d\zeta} &= \frac{d}{d\zeta} \left(e^{-\zeta \hat{J}_-} \hat{J}_+ e^{\zeta \hat{J}_-} \right) \\ &= -\hat{J}_- e^{-\zeta \hat{J}_-} \hat{J}_+ e^{\zeta \hat{J}_-} + e^{-\zeta \hat{J}_-} \hat{J}_+ \hat{J}_- e^{\zeta \hat{J}_-} \\ &= e^{-\zeta \hat{J}_-} [\hat{J}_+, \hat{J}_-] e^{\zeta \hat{J}_-} \\ &= 2 f_1(\zeta), \end{aligned} \tag{4.36}$$

where we have used the previously defined function $f_1(\zeta) = e^{-\zeta \hat{J}_-} \hat{J}_z e^{\zeta \hat{J}_-}$. Integrating and applying the initial condition $f_2(0) = \hat{J}_+$, we obtain

$$f_2(\zeta) = \hat{J}_+ + 2\zeta \hat{J}_z - \zeta^2 \hat{J}_-. \tag{4.37}$$

To find $\mathcal{D}_{J_+}$, we act with $\hat{J}_+$ on the non-normalised coherent state

$$\begin{aligned} \hat{J}_+ ||\zeta\rangle &= \hat{J}_+ e^{\zeta \hat{J}_-} |0\rangle \\ &= e^{\zeta \hat{J}_-} \left(\hat{J}_+ + 2\zeta \hat{J}_z - \zeta^2 \hat{J}_- \right) |0\rangle \\ &= \left(\zeta N - \zeta^2 \hat{J}_- \right) |\zeta\rangle , \end{aligned} \tag{4.38}$$

where we used $\hat{J}_z |0\rangle = \frac{N}{2} |0\rangle$ and the earlier result for $\mathcal{D}_{J_-}$.

Substituting $\hat{J}_- = \frac{\partial}{\partial \zeta}$, we conclude that the differential operator is

$$\mathcal{D}_{J_+} = \zeta N - \zeta^2 \frac{\partial}{\partial \zeta}. \tag{4.39}$$

With the normalisation function $\mathcal{M}(\zeta) = \left(1 + |\zeta|^2\right)^N$ for the $\mathfrak{su}_2$ coherent states, the $\mathcal{D}$-algebra formalism provides a convenient way to compute expectation values involving operator products. In particular, for any operator $\hat{F}$ whose expectation value in the coherent state $|\zeta\rangle$ is denoted by $f(\zeta) = \langle\zeta|\,\hat{F}\,|\zeta\rangle$, the following identities hold [82]

$$\langle\zeta|\,\hat{F}\hat{J}_-\,|\zeta\rangle = \left(1+|\zeta|^2\right)^{-N} \frac{\partial}{\partial\zeta}\left[\left(1+|\zeta|^2\right)^N f(\zeta)\right], \tag{4.40}$$

$$\langle\zeta|\,\hat{F}\hat{J}_+\,|\zeta\rangle = \left(1+|\zeta|^2\right)^{-N} \left(N\zeta - \zeta^2\frac{\partial}{\partial\zeta}\right)\left[\left(1+|\zeta|^2\right)^N f(\zeta)\right], \tag{4.41}$$

$$\langle\zeta|\,\hat{F}\hat{J}_z\,|\zeta\rangle = \left(1+|\zeta|^2\right)^{-N} \left(\frac{N}{2} - \zeta\frac{\partial}{\partial\zeta}\right)\left[\left(1+|\zeta|^2\right)^N f(\zeta)\right]. \tag{4.42}$$

By choosing $\hat{F} = \hat{I}$, we obtain the expectation values of the generators in terms of the coherent state parameter ζ

$$\langle\hat{J}_x\rangle = \frac{N}{2}\frac{\zeta+\zeta^*}{1+|\zeta|^2}, \tag{4.43}$$

$$\langle\hat{J}_y\rangle = \frac{iN}{2}\frac{\zeta^*-\zeta}{1+|\zeta|^2}, \tag{4.44}$$

$$\langle\hat{J}_z\rangle = \frac{N}{2}\frac{1-|\zeta|^2}{1+|\zeta|^2}. \tag{4.45}$$

These results are consistent with the earlier expressions for the rescaled classical variables $s_i = \frac{2}{N}\langle\hat{J}_i\rangle$, which were related to the stereographic projection from the complex plane to the Bloch sphere. This agreement confirms that the $\mathcal{D}$-algebra formalism naturally reproduces the classical phase-space coordinates of the coherent state.

We now focus on systems governed by the $\mathfrak{su}_2$ algebra. These possess finite-dimensional representations, with one irreducible representation for each $N \in \mathbb{N}^+$. The classicality parameter λ is identified with N, and the algebra has $m = 3$ generators. The necessary criteria are satisfied as follows

i. **Coherent States:** The $\mathfrak{su}_2$ coherent states constructed above, parametrised by $\zeta \in \mathbb{C}$, depend smoothly on this parameter and form an overcomplete set. They satisfy the resolution of the identity,

$$\int |\zeta\rangle\,\langle\zeta|\; d\mu(\zeta) = \hat{I}, \tag{4.46}$$

as required [8]. The associated phase space is two-dimensional ($n = 2$), consistent with the number of real degrees of freedom.

ii. **Scaling of Generator Expectation Values:** The expectation values of the generators scale linearly with N, as demonstrated in equations (4.43–4.45), satisfying the scaling condition for the coherent-state approximation.

iii. **Phase Space:** The classical phase space corresponding to the $\mathfrak{su}_2$ algebra is the unit sphere $S^2 \subset \mathbb{R}^3$, consistent with the coset structure $SU(2)/U(1)$.

iv. **Poisson Bracket:** The Poisson bracket structure on S^2 follows directly from the $\mathfrak{su}_2$ Lie algebra. For each finite N, the bracket retains the same functional form as in the classical limit, differing only by an overall scaling factor. To establish this correspondence, we consider the expectation value of the commutator of two generators

$$\langle [\hat{J}_i, \hat{J}_j] \rangle = \mathrm{i} \sum_k \epsilon_{ijk} \langle \hat{J}_k \rangle . \tag{4.47}$$

Multiplying both sides by the scaling factor $\eta = \frac{2}{N}$, we obtain

$$\eta \langle [\hat{J}_i, \hat{J}_j] \rangle = \mathrm{i} \epsilon_{ijk} s_k, \tag{4.48}$$

where $s_k = \eta \langle \hat{J}_k \rangle$. This yields the Poisson bracket relation on the classical phase space S^2

$$\{s_i, s_j\} = \lim_{\hbar \to 0} \frac{1}{\mathrm{i}} \eta \langle [\hat{J}_i, \hat{J}_j] \rangle = \epsilon_{ijk} s_k. \tag{4.49}$$

Thus, the classical bracket structure on S^2 emerges naturally from the scaled quantum commutator, retaining the same algebraic form in the semiclassical limit.

v. **Factorisation Property:** As seen in the $\mathcal{D}$-algebra expressions (4.28), (4.34), and (4.39), multiplicative terms scale with N while derivative terms remain of order unity. This confirms the required factorisation between “classical" and “quantum" contributions.

vi. **Metric Bracket:** For the metric bracket criteria, this structure retains its functional form across quantum and classical phase spaces, like the Poisson bracket.

To establish this connection, we use the following identity for $\mathfrak{su}_2$ operators, which is established using the $\mathcal{D}$-algebra formalism [104]

$$\langle [\hat{J}_i, \hat{J}_j]_+ \rangle = 2 \left(1 - \frac{1}{N}\right) \langle \hat{J}_i \rangle \langle \hat{J}_j \rangle + \delta_{ij} \frac{N}{2}. \tag{4.50}$$

To find the corresponding metric bracket on phase space, we multiply equation (4.50) by η and rearrange to obtain

$$\eta \left(\langle [\hat{J}_i, \hat{J}_j]_+ \rangle - 2 \langle \hat{J}_i \rangle \langle \hat{J}_j \rangle \right) = \delta_{ij} - \eta^2 \langle \hat{J}_i \rangle \langle \hat{J}_j \rangle \tag{4.51}$$

$$= \delta_{ij} - s_i s_j. \tag{4.52}$$

This result is precisely the form of the metric bracket on S^2 from equation (4.26). Thus, for $\mathfrak{su}_2$, the correspondence between the expectation of operator covariance and the metric bracket on phase space is exact for all N-representations.

Having verified that the $\mathfrak{su}_2$ algebra satisfies the criteria for the coherent-state approximation, we now proceed to study phase-space approximations for a class of two-mode Bose-Hubbard systems. These models are naturally expressed in terms of the $\mathfrak{su}_2$ generators and provide a physically rich setting in which to apply and benchmark our approximation methods.

The Hermitian two-mode Bose-Hubbard Hamiltonian is given by

$$\hat{\mathcal{H}} = \nu \hat{J}_x + \frac{2g}{N} \hat{J}_z^2 + \epsilon \hat{J}_z, \tag{4.53}$$

where $\hat{J}_x$ describes tunnelling between the two modes, $\hat{J}_z$ measures the population imbalance, g is the interaction strength, and N is the total number of particles. This model was studied in detail by Milburn et al. [105], who investigated quantum-classical correspondence in this context. Importantly, this Hamiltonian includes the nonlinear term $\hat{J}_z^2$, which plays a role analogous to the Kerr interaction $\hat{a}^\dagger \hat{a}^\dagger \hat{a} \hat{a}$ in the Heisenberg–Weyl setting discussed in Chapter 2. While the models differ in symmetry and physical interpretation, both exhibit nonlinear interactions that generate complex many-body dynamics..

To model non-Hermitian effects, we introduce the term $\mathrm{i}\kappa \hat{J}_z$ that represents symmetric gain and loss between the two modes. The resulting non-Hermitian two-mode Bose-Hubbard Hamiltonian reads

$$\hat{\mathcal{K}} = \nu \hat{J}_x + \frac{2g}{N} \hat{J}_z^2 + \epsilon \hat{J}_z + \mathrm{i}\kappa \hat{J}_z. \tag{4.54}$$

This extension has been previously explored by Graefe et al. [45] using a mean-field coherent-state approach. We build upon their work by applying the semiclassical Husimi approximation to this system. This constitutes original research, and we are currently preparing these results for publication.

For the classical analysis, we first derive the classical counterparts of these Hamiltonians in the $N \to \infty$ limit. The corresponding equations of motion for the variables s_x, s_y, and s_z are then obtained via the coherent-state approximation. The resulting dynamics are governed by a system of nonlinear differential equations, whose fixed-point structure underlies much of the observed behaviour.

4.1 Examples

In Chapter 2, we analysed several non-Hermitian systems based on the Heisenberg–Weyl algebra, using the coherent-state approximation and the semiclassical Husimi approach to explore their phase-space behaviour. We now extend this methodology to systems governed by the $\mathfrak{su}_2$ algebra, where the underlying geometry is that of the Bloch sphere and the Hilbert space is finite-dimensional. Although the topology and curvature of the phase space differ, the essential ingredients for our approximation scheme remain intact: a well-defined set of coherent states, a clear classical limit structure, and an emergent norm landscape under non-Hermitian dynamics.

To illustrate the framework, we consider a sequence of increasingly rich examples. We begin with a linear Hermitian Hamiltonian of the form $\hat{\mathcal{H}} = \nu \hat{J}_x + \epsilon \hat{J}_z$, which serves as a baseline for comparison between classical, quantum, and semiclassical trajectories. We then turn to a linear non-Hermitian model, $\hat{\mathcal{K}} = \mathrm{i}\hat{J}_z$, in which the interplay between the norm landscape and the classical trajectories become nontrivial even in the absence of interactions. Next, we examine

the Hermitian two-mode Bose–Hubbard model, $\hat{\mathcal{H}} = \nu\hat{J}_x + \frac{2g}{N}\hat{J}_z^2$, a nonlinear system that shares structural features with the Kerr model studied in Chapter 2. Finally, we consider a non-Hermitian extension of this model, $\hat{\mathcal{K}} = \nu\hat{J}_x + \frac{2g}{N}\hat{J}_z^2 + \mathrm{i}\kappa\hat{J}_z$, where the interplay between interaction and dissipation yields rich dynamical behaviour.

These examples not only serve to demonstrate the utility of the coherent-state and semiclassical Husimi approximations in finite-dimensional settings, but also provide a bridge between the algebraic structures introduced earlier and the dynamical phenomena of interest in non-Hermitian quantum systems.

4.1.1 Linear Hermitian Hamiltonian

We begin our exploration of $\mathfrak{su}_2$ phase-space dynamics with the simplest nontrivial case: a linear Hermitian Hamiltonian that lies entirely within the algebra itself. Setting $g = 0$ and $\kappa = 0$, we obtain the Hamiltonian

$$\hat{\mathcal{H}} = \nu\hat{J}_x + \epsilon\hat{J}_z, \tag{4.55}$$

which describes a combination of tunnelling between two modes (via $\hat{J}_x$) and an energy offset or bias (via $\hat{J}_z$). Physically, this corresponds to coherent oscillations in a two-mode Bose–Hubbard system with no interaction or loss terms, analogous to Rabi oscillations in a two-level atom or a double-well potential with no nonlinearity.

This Hamiltonian is an element of the $\mathfrak{su}_2$ Lie algebra, and as such, the quantum dynamics exactly match the classical dynamics derived from the coherent-state approximation. That is, the expectation values $\langle\hat{J}_i\rangle$ evolve according to the same equations as the classical variables s_i. This exact correspondence arises from the linearity of the Hamiltonian in the algebra generators and is a hallmark of systems governed by compact Lie algebras like $\mathfrak{su}_2$ [106].

The Heisenberg equations of motion for the $\hat{J}_i$ operators are

$$\frac{\mathrm{d}\hat{J}_x}{\mathrm{d}t} = -\epsilon\hat{J}_y, \tag{4.56}$$

$$\frac{\mathrm{d}\hat{J}_y}{\mathrm{d}t} = -\nu\hat{J}_z + \epsilon\hat{J}_x, \tag{4.57}$$

$$\frac{\mathrm{d}\hat{J}_z}{\mathrm{d}t} = \nu\hat{J}_y. \tag{4.58}$$

These describe precession on the Bloch sphere, where the vector $(\hat{J}_x, \hat{J}_y, \hat{J}_z)$ undergoes uniform rotation around a fixed axis in the x–z plane determined by the coefficients ν and ϵ.

The direction of this rotation axis corresponds to the two fixed points of the classical dynamics

$$(s_x, s_y, s_z) = \left(\pm\frac{\nu}{\sqrt{\nu^2+\epsilon^2}},\ 0,\ \pm\frac{\epsilon}{\sqrt{\nu^2+\epsilon^2}}\right), \tag{4.59}$$

which lie symmetrically on the unit Bloch sphere. The angular frequency of rotation is $\Omega = \sqrt{\nu^2+\epsilon^2}$, and the orbits are great circles perpendicular to the rotation axis. Because the system is

linear, the evolution preserves the shape and spread of any coherent state; there is no deformation of the Husimi distribution beyond rigid motion on the sphere.

This example serves as a baseline test case for our approximation methods, since there is no nonlinearity or non-Hermiticity, the semiclassical Husimi dynamics reduce to the exact classical flow, and both coherent-state and Husimi approximations coincide with the quantum evolution. More complex behaviour, such as dephasing, norm loss, or nonlinear twisting of phase-space trajectories, only emerges in subsequent examples with interaction and dissipation. Nevertheless, this linear case illustrates the geometric intuition of coherent-state dynamics and the classical-quantum correspondence that holds when the Hamiltonian is simply a generator of symmetry transformations on the sphere.

In Figure 4.1, we present snapshots of the quantum Husimi distribution at selected times for an initial coherent state centred at $(\phi, s_z) = \left(\frac{3\pi}{2}, 0\right)$, with parameters $\nu = -1$, $\epsilon = \frac{1}{2}$, and total boson number $N = 40$. The top row shows the distribution in the classical phase space parametrised by (s_x, s_y, s_z), which we refer to as the "spherical" phase space. In contrast, the bottom row depicts the evolution of the same state in the (ϕ, s_z) coordinates, which represent the "canonical" phase space.

We include both visualisations to aid the development of geometric and dynamical intuition. The canonical phase space allows the entire sphere to be displayed in a compact two-dimensional format, making it useful for comparing trajectories and tracking spreading effects. Meanwhile, the spherical representation more directly conveys the three-dimensional rotational motion intrinsic to the $\mathfrak{su}_2$ structure. Throughout the thesis, we will draw on both visual formats, selecting the one that best illustrates the key dynamics in each example.

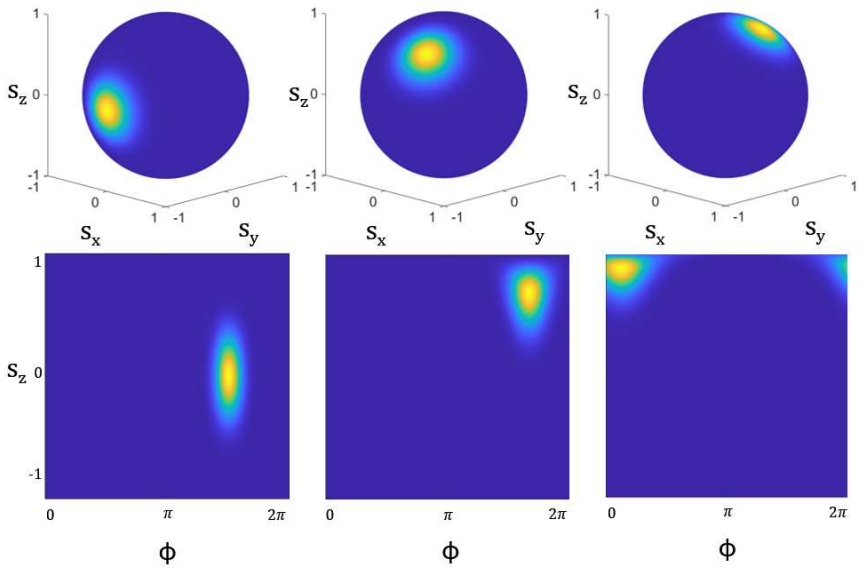


Figure 4.1: Evolution of the quantum Husimi distribution for the Hamiltonian $\hat{\mathcal{H}} = \nu\hat{J}_x + \epsilon\hat{J}_z$ with $\nu = -1, \epsilon = \frac{1}{2}$ and $N = 40$, for an initial coherent state centred at $(\phi, s_z) = \left(\frac{3\pi}{2}, 0\right)$. Husimi distributions are shown on spherical (top) and canonical (bottom) phase spaces at $t = 0$ (left), $t = \frac{\pi}{4}$ (middle) and $t = \frac{\pi}{2}$ (right).

To conclude this example, we note that the classical counterpart of the linear Hermitian Hamiltonian (4.55) is given by

$$h = \nu s_x + \epsilon s_z, \tag{4.60}$$

which generates uniform rotational dynamics on the Bloch sphere. In Figure 4.2, we display the corresponding coherent-state trajectories for a selection of initial conditions. These trajectories illustrate the classical flow induced by the Hamiltonian and, in this linear case, coincide exactly with the evolution of the quantum expectation values due to the perfect quantum-classical correspondence characteristic of $\mathfrak{su}_2$ systems with linear Hamiltonians.

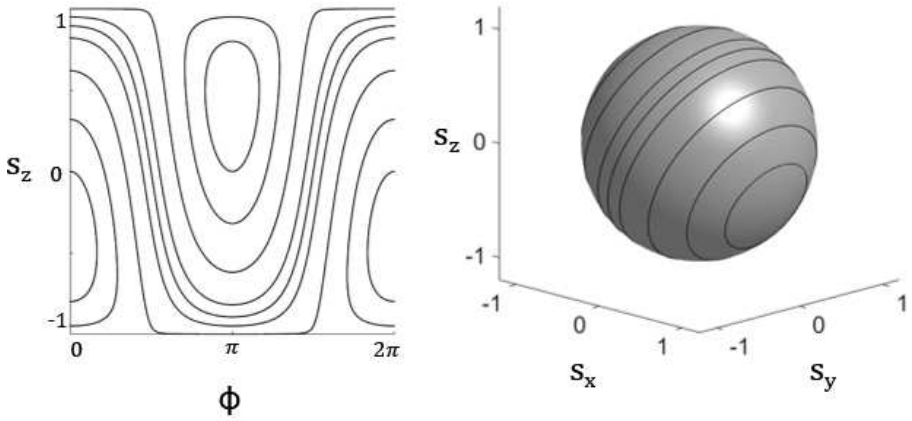


Figure 4.2: Phase-space trajectories from the coherent-state approximation for the Hamiltonian $\hat{\mathcal{H}} = \nu \hat{J}_x + \epsilon \hat{J}_z$ with $\nu = -1, \epsilon = \frac{1}{2}$ and $N = 40$. The trajectories are shown on the canonical (left) and spherical (right) phase spaces.

4.1.2 Linear Non-Hermitian Hamiltonian

We now examine the dynamics generated by the linear non-Hermitian Hamiltonian

$$\hat{\mathcal{K}} = \mathrm{i}\hat{J}_z. \tag{4.61}$$

This model provides a minimal yet instructive example of non-Hermitian dynamics within the $\mathfrak{su}_2$ setting. Physically, it corresponds to a system with purely imaginary energy levels, resulting in exponential amplification of components aligned with the $+J_z$ direction and decay of those aligned with $-J_z$ on the Bloch sphere.

The eigenstates of $\hat{\mathcal{K}}$ are the $\mathfrak{su}_2$ angular momentum basis states $|n\rangle = |N-n, n\rangle$, with corresponding eigenvalues

$$E_n = \mathrm{i}\left(\frac{N}{2} - n\right). \tag{4.62}$$

Thus, the eigenstate with the largest imaginary part, and hence, the dominant eigenstate under time evolution is $|0\rangle = |N, 0\rangle$, located at the north pole of the Bloch sphere. (We retain the $|n\rangle$ notation for continuity, but refer to $|N, 0\rangle$ when spatial intuition is required.)

Despite the non-Hermiticity of the Hamiltonian, the dynamics preserve the coherent-state form. That is, an initial coherent state remains coherent throughout its evolution. This mirrors the behaviour observed in the complex harmonic oscillator and simplifies the analysis significantly.

Let $|\psi(0)\rangle = |\zeta_c\rangle$ denote an initial $\mathfrak{su}_2$ coherent state. Then the time-evolved state remains a coherent state up to a time-dependent scalar prefactor

$$|\psi(t)\rangle = e^{\frac{Nt}{2}} \left(\frac{1 + |\zeta_c(t)|^2}{1 + |\zeta_c|^2} \right)^{\frac{N}{2}} |\zeta_c(t)\rangle \,, \tag{4.63}$$

where the phase-space coordinate evolves according to

$$\zeta_c(t) = \zeta_c e^{-t}. \tag{4.64}$$

This result can be derived by solving the Schrödinger equation in the ζ representation or by using the known transformation properties of $\mathfrak{su}_2$ coherent states under $\hat{J}_z$ evolution. Since the dynamics only scale ζ exponentially in time, we find the motion contracts all trajectories toward the origin $\zeta = 0$, corresponding to the north pole of the Bloch sphere. The underlying steps are analogous to those shown for the non-Hermitian harmonic oscillator in chapter 2, so we omit them here for brevity.

We choose to express this evolution in the ζ coordinate representation for its notational and computational simplicity. This parametrisation simplifies the flow induced by $\hat{\mathcal{K}}$ to a simple exponential scaling, making it particularly effective for describing systems with purely longitudinal non-Hermitian effects.

The classical counterpart to the Hamiltonian (4.61) is obtained by evaluating the expectation of $\hat{\mathcal{K}}$ in a coherent state, yielding the classical Hamiltonian function

$$k = \mathrm{i} \left(\frac{1 - |\zeta|^2}{1 + |\zeta|^2} \right). \tag{4.65}$$

To derive the classical dynamics, we employ the metric bracket structure defined on the coherent-state manifold (see Appendix B). The equation of motion for ζ is given by

$$\begin{aligned} \frac{\mathrm{d}\zeta}{\mathrm{d}t} &= \{\!\{\zeta^*, k\}\!\}, \\ &= \{\!\{\zeta, \zeta^*\}\!\} \frac{\partial k}{\partial \zeta^*}, \\ &= -\zeta. \end{aligned} \tag{4.66}$$

Solving this equation yields the simple exponential decay

$$\zeta(t) = \zeta_0 e^{-t}, \tag{4.67}$$

which agrees precisely with the evolution of the coherent state parameter $\zeta_c(t)$ in the quantum solution (4.63).

The classical and quantum trajectories coincide exactly in this system, with all motion contracting radially toward the origin $\zeta = 0$, which corresponds to the north pole of the Bloch sphere and aligns with the dominant eigenstate $|N, 0\rangle$.

Within the framework of the semiclassical Husimi method, it is instructive to examine the interplay between the classical trajectory flow and the norm landscape evolution. While the classical trajectories associated with the k^* flow move in the opposite direction toward the south pole, the norm landscape simultaneously concentrates and grows at the north pole. These seemingly contradictory effects combine constructively: the coherent state remains coherent throughout its evolution and is transported to the north pole in exact correspondence with its classical counterpart. Non-Hermitian quantum-classical correspondence emerges from the balance between trajectory dynamics and the norm landscape.

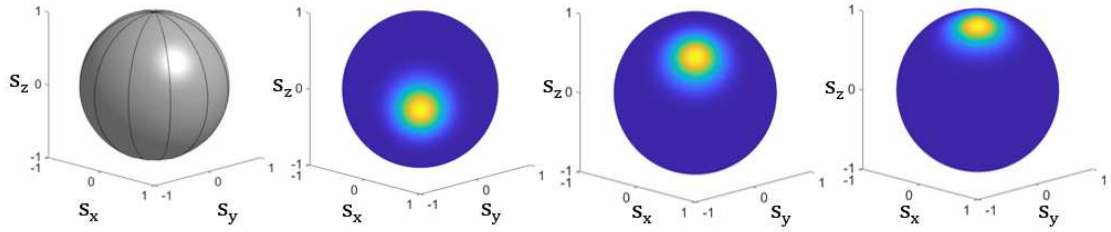


Figure 4.3: For the Hamiltonian $\hat{\mathcal{K}} = \mathrm{i}\hat{J}_z$, left: phase-space trajectories plotted on the spherical phase space. Middle left, middle right, right: evolution of the quantum Husimi distribution plotted on the spherical phase space at $t = 0, \frac{\pi}{4}$ and $\frac{\pi}{2}$ for an initial coherent state centred at $(\phi, s_z) = \left(\frac{7\pi}{4}, 0\right)$.

A useful point of comparison is the complex harmonic oscillator introduced in Chapter 2, which provides a parallel case of non-Hermitian dynamics in the Heisenberg–Weyl setting. There, the Hamiltonian takes the form

$$\hat{\mathcal{K}} = (\omega + \mathrm{i}\kappa)\left(\hat{a}^\dagger\hat{a} + \frac{1}{2}\hat{I}\right), \tag{4.68}$$

and the dynamics of an initial coherent state are governed by a combination of harmonic rotation and exponential amplification or decay, depending on the sign of κ. In the associated classical phase space, this results in spiralling trajectories: the radius evolves due to the non-Hermitian component, while angular motion is preserved from the Hermitian term. The coherent states remain coherent throughout, and their evolution is captured exactly by the classical dynamics.

By contrast, in the spin case considered here, with the non-Hermitian Hamiltonian

$$\hat{\mathcal{K}} = \mathrm{i}\hat{J}_z, \tag{4.69}$$

The evolution of coherent states also preserves coherence, and the classical trajectories are again exactly reproduced in phase space. However, the geometric nature of the motion differs. The stereographic coordinate ζ evolves as $\zeta(t) = \zeta_0 e^{-t}$, implying that its modulus decays exponentially while its phase remains constant. This corresponds to radial motion in the complex plane toward the north pole of the Bloch sphere. All trajectories follow straight lines directed inward from their

initial position ζ_0, with no angular rotation. Thus, even in the absence of a Hermitian term, the dynamics generate longitudinal flow without inducing any azimuthal motion.

To fully recover the spiralling behaviour seen in the complex harmonic oscillator more generically, one can consider a Hamiltonian with both Hermitian and anti-Hermitian components, for instance,

$$\hat{\mathcal{K}} = \hat{J}_z + \mathrm{i}\hat{J}_z. \tag{4.70}$$

In this case, the dynamics of coherent states combine angular rotation about the z-axis with exponential contraction or expansion along the polar direction, yielding spiralling trajectories directly analogous to those in the complex harmonic oscillator. This highlights a deep structural parallel between the Heisenberg–Weyl and $\mathfrak{su}_2$ settings under non-Hermitian evolution, and provides geometric intuition for how Hermitian and anti-Hermitian terms shape classical flows on their respective phase spaces.

These observations suggest potential broader connections for non-Hermitian quantum-classical correspondence across Lie algebraic structures. Previous work by Brody [107] demonstrated that linear non-Hermitian Hamiltonians on state space result in symplectic and gradient motion, while Burns [108] et al outlined a treatment of complex-valued classical Hamiltonians that showed symplectic and gradient motion on classical spaces. However, establishing when such quantum-classical correspondence holds more generally for the classes of Lie algebras where the Kirillov method applies in Hermitian cases requires further investigation. Specifically, determining for which classes of algebras there is an analogous relationship between anticommutators and metric brackets as there is between commutators and Poisson brackets in the Hermitian case presents an important area for further analysis. The coherent-state framework developed here provides a promising avenue for exploring these connections within the coadjoint orbit geometry of phase spaces, though the extent of this correspondence across different algebraic structures requires further study.

4.1.3 Hermitian Two-Mode Bose–Hubbard Hamiltonian

We now turn to a nonlinear Hermitian Hamiltonian that represents the two-mode Bose–Hubbard model without detuning or gain/loss. This is achieved by setting $\epsilon = 0$ and $\kappa = 0$ in (4.54), yielding the Hamiltonian

$$\hat{\mathcal{H}} = \nu\hat{J}_x + \frac{2g}{N}\hat{J}_z^2. \tag{4.71}$$

The prefactor $2g/N$ ensures that the interaction strength remains finite in the semiclassical limit $N \to \infty$, allowing for a well-defined classical Hamiltonian per particle. This scaling choice is standard in the literature and facilitates meaningful comparison between quantum and classical dynamics.

This model describes coherent tunnelling between two bosonic modes (governed by $\hat{J}_x$) combined with on-site interactions proportional to the square of the population imbalance (encoded in $\hat{J}_z^2$). It is a well-known and widely studied system in the context of bosonic Josephson junctions [109]

and has been previously analysed in the literature, notably by Milburn et al. [105].

The quantum evolution under this Hamiltonian is characterised by two competing effects. First, the $\hat{J}_x$ term induces a uniform rotation about the s_x-axis, leading to coherent oscillations between the two modes. Second, the nonlinear $\hat{J}_z^2$ term introduces a shearing effect, which distorts the state in phase space, producing a differential twisting around the s_z-axis. The strength of this shearing increases with $|s_z|$, leading to the generation of non-classical features such as squeezing and phase-space interference fringes over time.

This Hamiltonian serves as an important testbed for semiclassical approximations, as it combines integrable dynamics with nontrivial nonlinear effects, allowing us to observe how well the coherent-state and semiclassical Husimi approximations capture quantum evolution in regimes beyond linear or purely quadratic systems. Using the coherent-state approximation, we obtain the corresponding classical Hamiltonian

$$h = \nu s_x + g s_z^2. \tag{4.72}$$

This leads to the classical equations of motion

$$\frac{\mathrm{d}s_x}{\mathrm{d}t} = -2g s_y s_z, \tag{4.73}$$

$$\frac{\mathrm{d}s_y}{\mathrm{d}t} = -\nu s_z + 2g s_x s_z, \tag{4.74}$$

$$\frac{\mathrm{d}s_z}{\mathrm{d}t} = \nu s_y. \tag{4.75}$$

These equations describe nonlinear dynamics on the Bloch sphere. The ν term drives a rotation about the s_x-axis, as in the linear case, while the $g s_z^2$ term introduces a rotation about the s_z-axis with angular frequency proportional to s_z. The structure of the dynamics is determined by the system's fixed points. These are found by setting the time derivatives in equations (4.73)–(4.75) to zero. In particular, from $\frac{\mathrm{d}s_z}{\mathrm{d}t} = \nu s_y = 0$, we obtain $s_y = 0$. Substituting this into the remaining equations, we find two cases:

- If $s_z = 0$, then $\frac{\mathrm{d}s_x}{\mathrm{d}t} = 0$ automatically, and $\frac{\mathrm{d}s_y}{\mathrm{d}t} = -\nu s_z = 0$ is satisfied. Thus, the fixed points lie at $s_z = 0$, $s_y = 0$, and $s_x = \pm 1$, corresponding to the poles of the s_x-axis.
- Alternatively, if $s_z \neq 0$, we require $\frac{\mathrm{d}s_y}{\mathrm{d}t} = -\nu s_z + 2g s_x s_z = 0$, which gives $s_x = \frac{\nu}{2g}$. Substituting into the unit-sphere constraint $s_x^2 + s_y^2 + s_z^2 = 1$, we find $s_z = \pm\sqrt{1 - \left(\frac{\nu}{2g}\right)^2}$.

These solutions are real only when $|g| > |\nu|/2$, in which case the dynamical equations admit four fixed points. If this condition is not met, only the two equatorial fixed points at $s_z = 0, s_x = \pm 1$ remain.

We first focus on the case $|g| > \frac{|\nu|}{2}$, where four distinct fixed points arise. These consist of three centres and one saddle point, classified as follows

- A centre located on the equator

$$(s_x, s_y, s_z) = (-1, 0, 0), \tag{4.76}$$

- Two additional centres located symmetrically in the northern and southern hemispheres

$$(s_x, s_y, s_z) = \left(\frac{\nu}{2g}, 0, \pm\sqrt{1 - \frac{\nu^2}{4g^2}} \right), \tag{4.77}$$

- And a saddle point on the equator

$$(s_x, s_y, s_z) = (1, 0, 0). \tag{4.78}$$

In Figure 4.4, we present trajectories of the classical dynamical system generated by the coherent-state approximation for the Hermitian two-mode Bose-Hubbard Hamiltonian, with parameters $\nu = 1$ and $g = 1$, corresponding to the regime $|g| > \frac{|\nu|}{2}$ where four fixed points exist. The left panel depicts trajectories projected onto the canonical phase space (ϕ, s_z), while the right panel shows the corresponding paths in the spherical phase space (s_x, s_y, s_z). Together, these two visualisations offer complementary insights into the global geometry of the flow and the detailed structure around fixed points.

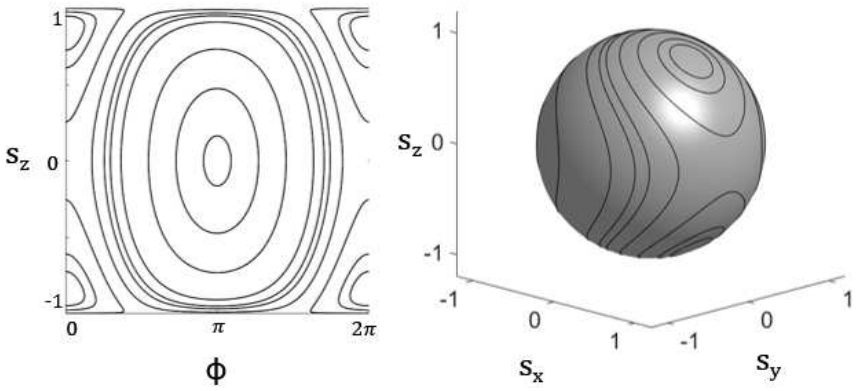


Figure 4.4: Phase-space trajectories from the coherent-state approximation for the Hermitian two-mode Bose-Hubbard Hamiltonian with parameters $\nu = 1, g = 1$. The trajectories are shown in the canonical phase space (left) and spherical phase space (right).

For comparison, when $|g| < \frac{|\nu|}{2}$, the dynamics simplify significantly. In this regime, the system exhibits only two fixed points, both of which are centres, located on the equator

$$(s_x, s_y, s_z) = (1, 0, 0),$$
$$(s_x, s_y, s_z) = (-1, 0, 0).$$

These correspond to symmetric configurations in which the population imbalance vanishes ($s_z = 0$), and the entire evolution is a smooth rotation about the s_x-axis, reminiscent of the linear case but slightly modified by the presence of weak nonlinearity.

In Figure 4.5, we show the phase-space trajectories generated by the coherent-state approximation for the Hermitian two-mode Bose-Hubbard Hamiltonian in the regime $|g| < \frac{|\nu|}{2}$, taking $\nu = 1$ and $g = \frac{1}{4}$. As before, the left panel displays the dynamics on the canonical phase space (ϕ, s_z), while the right panel shows the corresponding evolution in the spherical phase space (s_x, s_y, s_z).

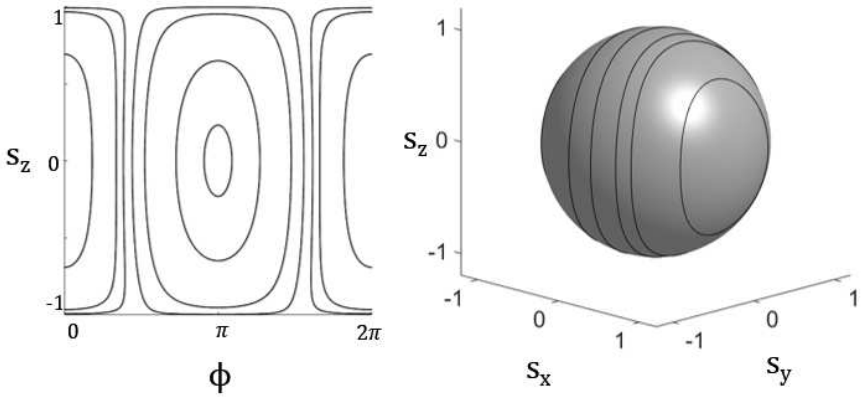


Figure 4.5: Phase-space trajectories from the coherent-state approximation for the Hermitian two-mode Bose-Hubbard Hamiltonian with $\nu = 1, g = \frac{1}{4}$. Trajectories are shown in the canonical phase space (left) and the spherical phase space (right).

In this parameter regime, the dynamics are governed by two centre fixed points at $(s_x, s_y, s_z) = (\pm 1, 0, 0)$, consistent with the earlier analysis. Figure 4.5 illustrates how the resulting motion consists of regular closed orbits around these centres. Compared to the richer dynamics of the strong interaction regime, this case lacks bifurcations or separatrix structures, highlighting how weak nonlinearity preserves near-linear behaviour while subtly modifying the classical flow.

In the following examples, we focus on the parameter regime $\nu = 1, g = 1$, corresponding to the four fixed-point case. This regime exhibits richer dynamical behaviour, making it an ideal setting for illustrating the differences between classical, coherent-state, and full quantum dynamics.

Case 1: Initial coherent state located near the equatorial centre. We consider an initial coherent state centred at $(\phi, s_z) = \left(\frac{3\pi}{2}, 0\right)$, which lies close to the equatorial fixed point at $(\phi, s_z) = (\pi, 0)$. In Figure 4.6, we compare the time evolution of the scaled quantum expectation value $s_z = \eta \langle \hat{J}_z \rangle$ (solid blue line), the coherent-state approximation (dotted orange line), and the semiclassical Husimi approximation (solid yellow line), for two different system sizes: $N = 10$ (left panel) and $N = 40$ (right panel).

In both cases, the coherent-state approximation produces oscillatory dynamics around the fixed point. The quantum evolution, however, exhibits the characteristic collapse and revival behaviour seen in finite-dimensional systems. For N = 10, the quantum expectation value collapses and fully revives around $t \approx 20\pi$. For $N = 40$, the revival is incomplete at this time, with a full cycle taking proportionally longer. This behaviour is consistent with the revival time scaling as approximately $\sim \frac{2}{N}$, highlighting how the quantum-classical correspondence improves in the large-N limit. In Figure 4.7, we present snapshots of the Husimi distribution for both the full quantum dynamics

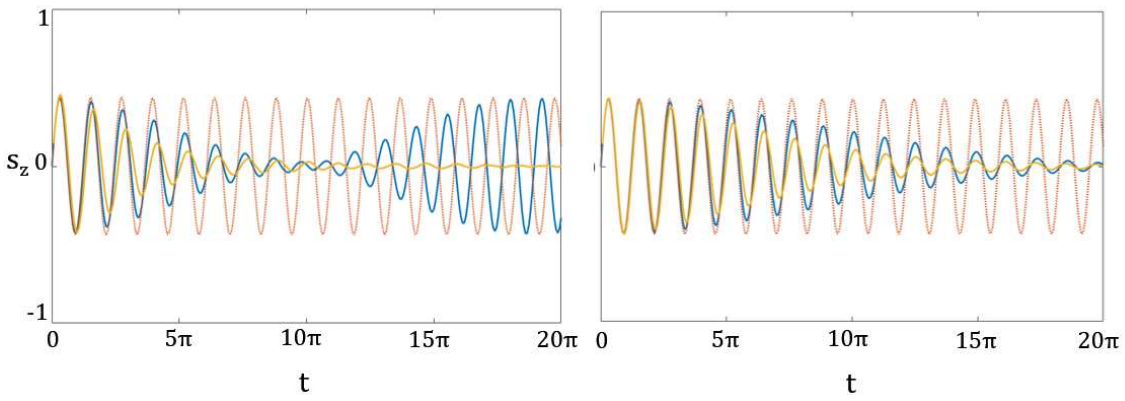


Figure 4.6: Comparison of s_z between quantum dynamics (solid blue line), semiclassical Husimi approximation (solid yellow line) and the coherent-state approximation (dotted orange line) for the Hermitian two-mode Bose-Hubbard Hamiltonian with $\nu = 1, g = 1$ and an initial coherent state centred at $(\phi, s_z) = \left(\frac{3\pi}{2}, 0\right)$. Results are shown for $N = 10$ (left panel) and $N = 40$ (right panel).

(top row) and the semiclassical Husimi approximation (bottom row), for an initial coherent state centred at $(\phi, s_z) = \left(\frac{3\pi}{2}, 0\right)$. The system parameters are $\nu = 1, g = 1$, and N = 40. At early times, the semiclassical Husimi approximation successfully captures the key features of the deformation induced by the nonlinear interaction term $\hat{J}_z^2$. Specifically, the evolution is governed by the underlying classical phase-space trajectories shown in Figure 4.4, along which the Husimi distribution is transported. Similar to the Kerr Hamiltonian case studied in Chapter 2, we observe that the semiclassical Husimi distribution develops increasingly fine structures due to the shearing dynamics, while the quantum Husimi distribution exhibits broader, smoother features.

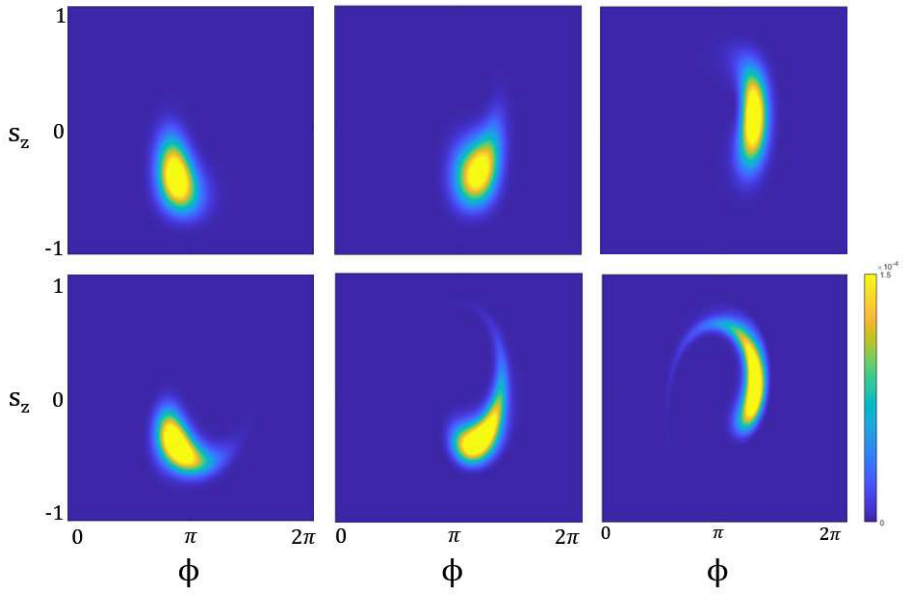


Figure 4.7: Evolution of the quantum Husimi distribution (top row) and the semiclassical Husimi distribution (bottom row) for the Hermitian two-mode Bose-Hubbard Hamiltonian, $\hat{\mathcal{H}} = \nu \hat{J}_x + \frac{2g}{N}\hat{J}_z^2$, with $\nu = 1, g = 1$, and $N = 40$. The initial coherent state is centred at $(\phi, s_z) = \left(\frac{3\pi}{2}, 0\right)$. Snapshots are shown at times $t = \pi$ (left), $t = 2\pi$ (middle) and $t = 3\pi$ (right).

As time progresses, the semiclassical Husimi distribution continues to evolve into increasingly intricate spiral structures due to the persistent nonlinear shearing. In contrast, the quantum Husimi distribution begins to display more prominent interference effects. In Figure 4.8, we show the full quantum Husimi distribution at longer times for the same initial state. As in the Kerr case, we observe the emergence of characteristic interference features such as local minima ("holes", left), the onset of revival (middle), and partial reformation of the initial coherent state structure (right).

These revival phenomena arise from the discrete and structured energy spectrum of the system, which leads to periodic or quasi-periodic rephasing of the quantum state. While the finite-dimensional Hilbert space of the spin system contributes to the regularity of the revivals, such effects are not limited to finite-dimensional settings, as evidenced by revivals in the infinite-dimensional Kerr model.

At these later times, the semiclassical Husimi approximation significantly deviates from the full quantum dynamics, as already evident in the mismatch shown in Figure 4.6.

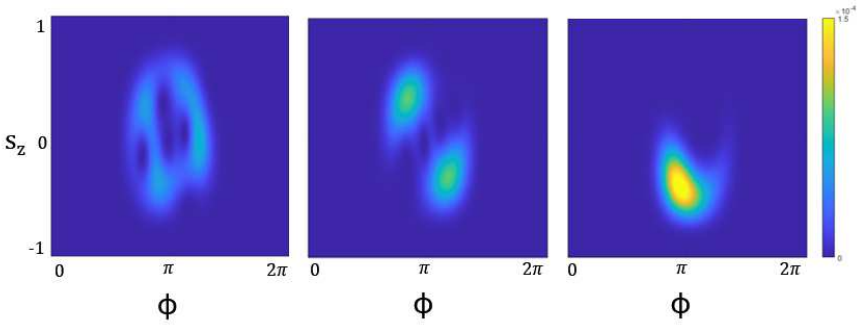


Figure 4.8: Evolution of the quantum Husimi distribution for the Hermitian two-mode Bose-Hubbard Hamiltonian $\hat{\mathcal{H}} = \nu \hat{J}_x + \frac{2g}{N}\hat{J}_z^2$ with $\nu = 1, g = 1$ and $N = 40$, for an initial coherent state centred at $(\phi, s_z) = \left(\frac{3\pi}{2}, 0\right)$ at $t = 20\pi$ (left), $t = 40\pi$ (middle) and $t = 80\pi$ (right).

Case 2: Initial coherent state located near the northern hemisphere centre. In this case, we consider an initial coherent state centred at $(\phi, s_z) = \left(0, \frac{3}{4}\right)$, situated near the fixed point in the northern hemisphere at $(\phi, s_z) = \left(0, \frac{\sqrt{3}}{2}\right)$. This fixed point corresponds to a dynamically stable centre in the classical phase space. In Figure 4.9, we compare the time evolution of the scaled observable $s_z = \eta \langle \hat{J}_z \rangle$ (solid blue line), the coherent-state approximation (dotted orange line), and the semiclassical Husimi approximation (solid yellow line), for both $N = 10$ and $N = 40$.

In the classical and semiclassical descriptions, the state remains trapped in the northern hemisphere, undergoing regular oscillations around the fixed point. However, in the full quantum evolution, the system exhibits tunnelling to the classically inaccessible southern fixed point at $(\phi, s_z) = \left(0, -\frac{\sqrt{3}}{2}\right)$. This transition is a hallmark of quantum tunnelling in finite systems and marks the breakdown of the classical approximation over sufficiently long timescales. As expected, the tunnelling time increases with N: in the left panel ($N = 10$), the tunnelling occurs relatively early, whereas in the right panel ($N = 40$), the state remains self-trapped in the northern hemisphere over a longer time.

This behaviour is closely related to the phenomenon of macroscopic self-trapping, where nonlinear

interactions prevent the population from oscillating freely between the two modes [105]. In the semiclassical picture, this manifests as confinement near a local centre; in the quantum picture, it corresponds to slow tunnelling across the dynamical barrier. The self-trapping is more pronounced and more persistent for larger N, again illustrating how increasing the number of particles enhances the quantum-classical correspondence and delays quantum tunnelling. In Figure 4.10, we display

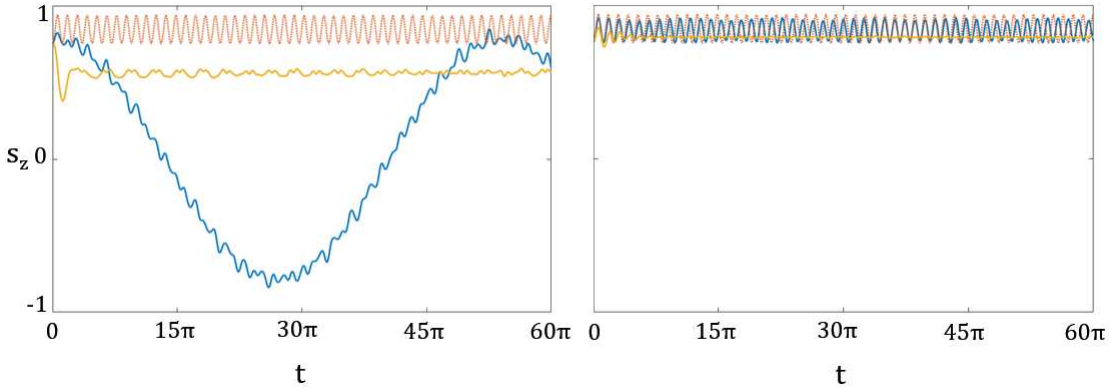


Figure 4.9: Comparison of q values between quantum dynamics (solid blue line), semiclassical Husimi approximation (solid yellow line) and coherent-state approximation (dotted orange line) for the Hermitian two-mode Bose-Hubbard Hamiltonian $\hat{\mathcal{H}} = \nu\hat{J}_x + \frac{2g}{N}\hat{J}_z^2$ with $\nu = 1, g = 1$ and an initial coherent state centred at $(\phi, s_z) = \left(0, \frac{3}{4}\right)$. Results are shown for $N = 10$ (left panel) and $N = 40$ (right panel).

snapshots of the Husimi distribution from the full quantum dynamics (top row) and the semiclassical Husimi approximation (bottom row) for an initial coherent state centred at $(\phi, s_z) = \left(0, \frac{3}{4}\right)$, focusing on the short-time behaviour. In this regime, the semiclassical Husimi approximation successfully captures the nonlinear deformation of the initial coherent state induced by the interaction term $\hat{J}_z^2$. The semiclassical Husimi distribution is transported along the classical phase-space trajectories shown in Figure 4.4.

Notably, the portion of the state initially lying outside the basin of attraction of the northern fixed point is carried along trajectories that circulate around the equatorial saddle point. As a result, the state develops a characteristic structure: a concentrated lobe near the northern fixed point, combined with an extended tail wrapping around the saddle. Over time, this tail exhibits the familiar filamentation seen in earlier examples, with the distribution stretching into finer and finer structures. This behaviour highlights both the predictive power and limitations of the semiclassical Husimi method over longer time scales.

For longer evolution times, the semiclassical Husimi distribution continues to develop along the same qualitative pattern: a dominant lobe remains concentrated near the north fixed point, executing oscillatory motion, while a secondary tail becomes increasingly filamented as it wraps around the nearby saddle points. This extended tail reflects the nonlinear shearing dynamics and the progressive divergence of nearby classical trajectories.

In Figure 4.11, we present the quantum Husimi distributions for the same initial coherent state as in Figure 4.10, but now observed at longer timescales. At $t = 14\pi$ (left panel), the distribution

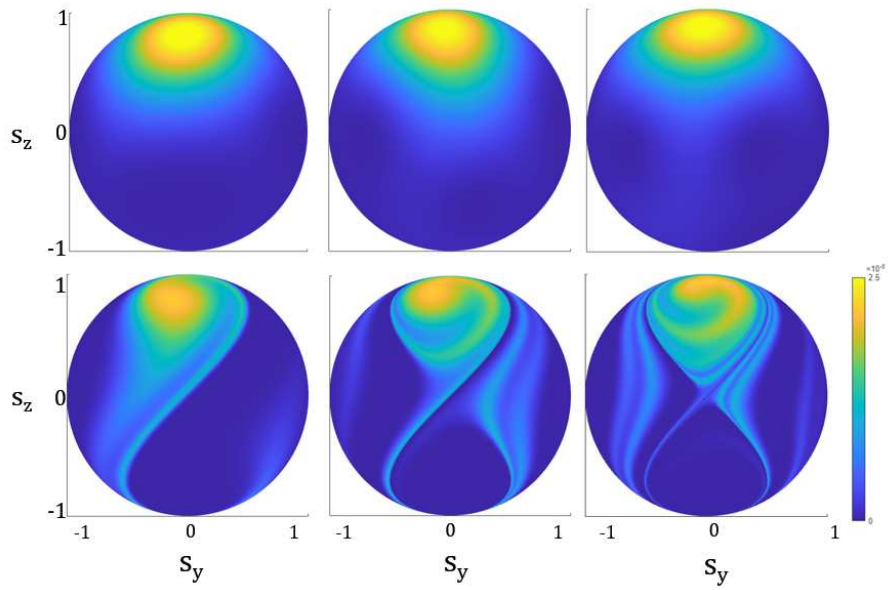


Figure 4.10: Evolution of the quantum Husimi distribution (top row) and the semiclassical Husimi distribution (bottom row) for the Hermitian two-mode Bose-Hubbard Hamiltonian, $\hat{\mathcal{H}} = \nu \hat{J}_x + \frac{2g}{N}\hat{J}_z^2$, with $\nu = 1, g = 1$ and $N = 40$, for an initial coherent state centred at $(\phi, s_z) = \left(0, \frac{3}{4}\right)$. The columns correspond to different snapshots of the evolution in time with $t = \pi$ (left), $t = 2\pi$ (middle) and $t = 3\pi$ (right).

has partially tunnelled through the classically forbidden region toward the south pole. By $t = 28\pi$ (middle panel), the state has completely transferred its population to the southern fixed point. Eventually, at $t = 50\pi$ (right panel), the state returns to the northern hemisphere, completing a full tunnelling cycle. This periodic tunnelling behaviour is purely quantum mechanical and is not captured by the semiclassical Husimi approximation, which lacks the mechanism to describe classically forbidden transitions. Nonetheless, the coherent-state and semiclassical methods remain effective for characterising the intrawell motion and local phase-space deformation over moderate times.

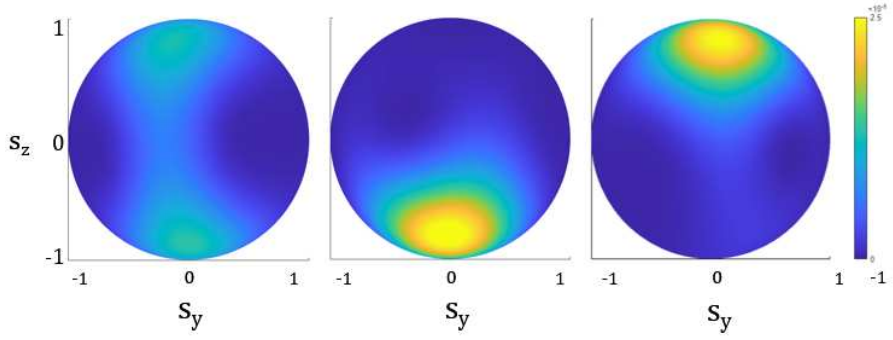


Figure 4.11: Evolution of the quantum Husimi distribution for the Hermitian two-mode Bose-Hubbard Hamiltonian $\hat{\mathcal{H}} = \nu \hat{J}_x + \frac{2g}{N}\hat{J}_z^2$ with $\nu = 1, g = 1$ and $N = 10$ for an initial coherent state centred at $(\phi, s_z) = \left(0, \frac{3}{4}\right)$ at at $t = 14\pi$ (left), $t = 28\pi$ (middle) and $t = 50\pi$ (right).

Having explored both linear and nonlinear Hermitian dynamics in $\mathfrak{su}_2$ systems, we have seen

how the interplay of coherent-state approximations and semiclassical Husimi evolution captures key features such as shearing, tunnelling, and revival. In particular, the Hermitian two-mode Bose-Hubbard model illustrates the richness of classical phase-space structure and the limitations of semiclassical methods over long times due to inherently quantum effects like interference and tunnelling. We now turn our attention to the non-Hermitian extension of this model, where gain and loss mechanisms are introduced via an imaginary component in the Hamiltonian. This setting opens a new window onto the role of non-Hermiticity in spin systems, and allows us to examine how classical phase-space methods behave in the presence of complex dynamics and non-unitary evolution.

4.1.4 Non-Hermitian Two-Mode Bose-Hubbard Hamiltonian

We now turn to the non-Hermitian extension of the two-mode Bose-Hubbard model, obtained by setting $\epsilon = 0$ in the previously studied Hermitian Hamiltonian in equation (4.54)

$$\hat{\mathcal{K}} = \nu \hat{J}_x + \frac{2g}{N}\hat{J}_z^2 + \mathrm{i}\kappa \hat{J}_z, \tag{4.79}$$

where $\nu, g, \kappa \in \mathbb{R}$. This Hamiltonian incorporates both nonlinearity and gain/loss dynamics through the imaginary term $\mathrm{i}\kappa\hat{J}_z$.

Consistent with the framework of PT-symmetric quantum mechanics, this Hamiltonian is PT-symmetric under the action of a suitably defined parity and time-reversal operation. We define the parity operator as $\hat{P} = e^{\mathrm{i}\pi\hat{J}_x}$, which implements the transformation $\hat{J}_z \mapsto -\hat{J}_z$ and leaves $\hat{J}_x$ invariant. The time-reversal operator $\hat{T}$ corresponds to complex conjugation. Under the combined action of $\hat{P}\hat{T}$, the imaginary term transforms as

$$\hat{P}\hat{T}(\mathrm{i}\kappa\hat{J}_z)(\hat{P}\hat{T})^{-1} = -\mathrm{i}\kappa(-\hat{J}_z) = \mathrm{i}\kappa\hat{J}_z, \tag{4.80}$$

thus leaving the Hamiltonian invariant. This confirms that $\hat{\mathcal{K}}$ is PT-symmetric in the standard sense.

We will consider two parameter regimes to illustrate the dynamical richness of this model. In the first case, we take $\nu = 1$, $g = 1$, and $\kappa = \frac{1}{4}$, which leads to a complex-valued spectrum associated with the PT-broken phase. In the second case, we use $\nu = 1$, $g = \frac{1}{4}$, and $\kappa = \frac{1}{4}$, which results in a real spectrum corresponding to the PT-unbroken phase. Figure 4.12 shows the eigenenergies for both parameter sets across a range of N values. The transition between these two phases occurs at a critical value of κ and is characterised by the emergence of an exceptional point, a hallmark of PT-symmetric systems where eigenstates coalesce and the spectrum ceases to be real.

As shown in Figure 4.12, the spectrum corresponding to the parameter regime $\nu = 1$, $g = 1$, and $\kappa = \frac{1}{4}$ displays complex eigenvalues for all three values of N considered. This indicates that the system resides in the PT-broken phase, characterised by a non-degenerate eigenvalue structure and a single dominant eigenstate that governs the long-time quantum dynamics. While this dominant-state behaviour is a generic feature of non-Hermitian systems and already familiar from earlier examples, it remains useful to highlight how it manifests here within the $\mathfrak{su}_2$ framework.

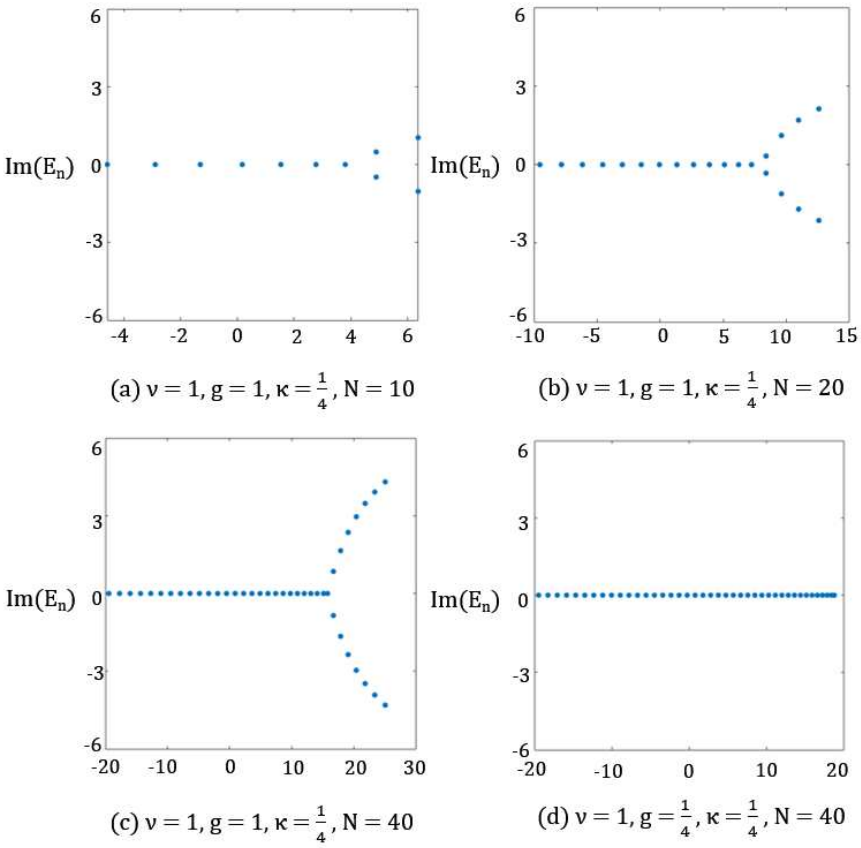


Figure 4.12: Eigenvalue spectrum for the non-Hermitian two-mode Bose-Hubbard Hamiltonian, $\hat{\mathcal{H}} = \nu \hat{J}_x + \frac{2g}{N}\hat{J}_z^2 + \mathrm{i}\kappa \hat{J}_z$, for selected values of the parameters ν, g, κ, and N.

In contrast, the case $\nu = 1$, $g = \frac{1}{4}$, and $\kappa = \frac{1}{4}$ with $N = 40$ yields an entirely real eigenvalue spectrum, placing the system in the PT-unbroken regime. In the following section, we examine the phase-space structure of this spectrum by presenting the Husimi representations. In Figure 4.13, we give three examples of the Husimi distributions for three eigenstates: two representative eigenstates with real eigenvalues, alongside the dominant eigenstate identified in the broken phase.

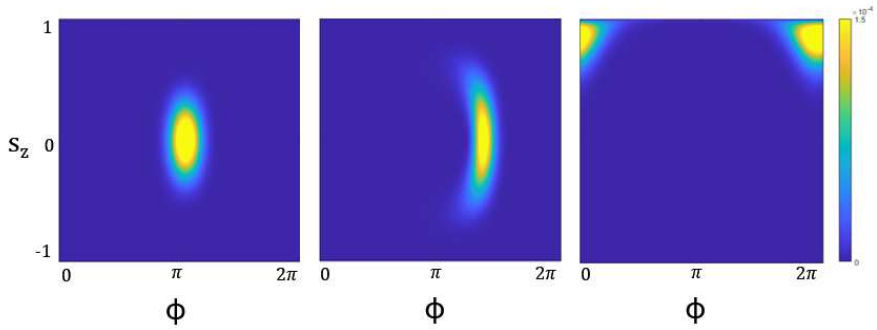


Figure 4.13: Quantum Husimi distribution plots for the eigenstates corresponding to left: $E_1 = -19.43$, middle: $E_8 = -7.91$ and right: the dominant state $E = 25.03 + \mathrm{i}4.31$.

The classical counterpart to this Hamiltonian is given by

$$k = \nu s_x + g s_z^2 + \mathrm{i}\kappa s_z, \tag{4.81}$$

with the corresponding equations of motion

$$\frac{\mathrm{d}s_x}{\mathrm{d}t} = -2g s_y s_z - \kappa s_x s_z, \tag{4.82}$$

$$\frac{\mathrm{d}s_y}{\mathrm{d}t} = -\nu s_z + 2g s_x s_z - \kappa s_y s_z, \tag{4.83}$$

$$\frac{\mathrm{d}s_z}{\mathrm{d}t} = \nu s_y + \kappa\left(1 - s_z^2\right). \tag{4.84}$$

To identify the fixed points of the dynamics, we first consider equation (4.82), from which either $s_z = 0$ or $s_x = -\frac{2g s_y}{\kappa}$ must hold.

Case 1: $s_z = 0$

In this case, equations (4.83) and (4.84) yield the solutions

$$s_y = -\frac{\kappa}{\nu}, \quad s_x = \pm\sqrt{1 - \frac{\kappa^2}{\nu^2}}. \tag{4.85}$$

These give rise to two fixed points provided that $|\kappa| < |\nu|$. Linear stability analysis shows that:

- The point $(s_x, s_y, s_z) = \left(-\sqrt{1 - \frac{\kappa^2}{\nu^2}}, -\frac{\kappa}{\nu}, 0\right)$ is a centre.
- The point $(s_x, s_y, s_z) = \left(\sqrt{1 - \frac{\kappa^2}{\nu^2}}, -\frac{\kappa}{\nu}, 0\right)$ is a saddle.

Case 2: $s_x = -\frac{2gs_y}{\kappa}$
Using equation (4.83), we obtain

$$s_y = -\frac{\nu\kappa}{4g^2+\kappa^2}. \tag{4.86}$$

Substituting into (4.84) gives

$$s_z = \pm\sqrt{1-\frac{\nu^2}{4g^2+\kappa^2}}, \quad s_x = \frac{2\nu g}{4g^2+\kappa^2}. \tag{4.87}$$

These solutions exist only if $4g^2+\kappa^2 > \nu^2$. This yields two additional fixed points:

- An *unstable spiral* at

$$(s_x, s_y, s_z) = \left(\frac{2\nu g}{4g^2+\kappa^2}, -\frac{\nu\kappa}{4g^2+\kappa^2}, -\sqrt{1-\frac{\nu^2}{4g^2+\kappa^2}}\right). \tag{4.88}$$

- A *stable spiral* at

$$(s_x, s_y, s_z) = \left(\frac{2\nu g}{4g^2+\kappa^2}, -\frac{\nu\kappa}{4g^2+\kappa^2}, \sqrt{1-\frac{\nu^2}{4g^2+\kappa^2}}\right). \tag{4.89}$$

The system exhibits distinct dynamical regimes based on parameter values

- **Region 1:** Two fixed points, a centre and a saddle, when $4g^2+\kappa^2 < \nu^2$.
- **Region 2:** Four fixed points, a centre, a saddle, a stable spiral, and an unstable spiral, when $4g^2+\kappa^2 > \nu^2$ and $|\kappa| < |\nu|$.
- **Region 3:** Two fixed points, a stable spiral and an unstable spiral, when $|\kappa| > |\nu|$.

In Figures 4.15, 4.16, and 4.17, we display the phase-space trajectories obtained from the coherent-state approximation for Region 1, Region 2, and Region 3, respectively, using parameter choices of ν, g, and κ appropriate to each regime.

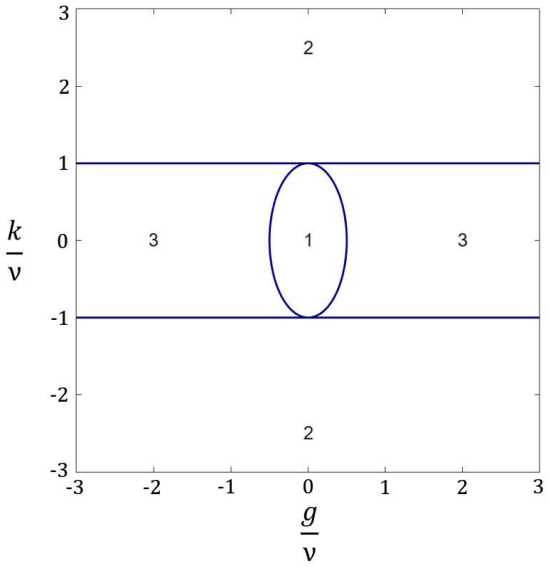


Figure 4.14: Regions of the fixed points in the parameter plane $\left(\frac{g}{\nu}, \frac{\kappa}{\nu}\right)$ for the dynamics generated from the classical Hamiltonian $k = \nu s_x + g s_z^2 + \mathrm{i}\kappa s_z$. Region 1: two fixed points (centre and saddle). Region 2: four fixed points (centre, saddle, stable spiral, unstable spiral). Region 3: two fixed points (stable spiral and unstable spiral).

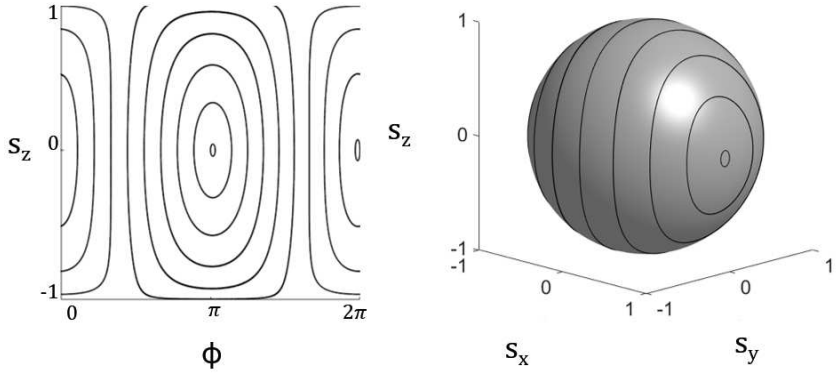


Figure 4.15: Phase-space trajectories from the coherent-state approximation for the non-Hermitian two-mode Bose-Hubbard Hamiltonian, $\hat{\mathcal{H}} = \nu \hat{J}_x + \frac{2g}{N}\hat{J}_z^2 + \mathrm{i}\kappa \hat{J}_z$, with $\nu = 1, g = \frac{1}{4}, \kappa = \frac{1}{20}$ (Region 1). The trajectories are shown on the canonical (left) and spherical (right) phase spaces.

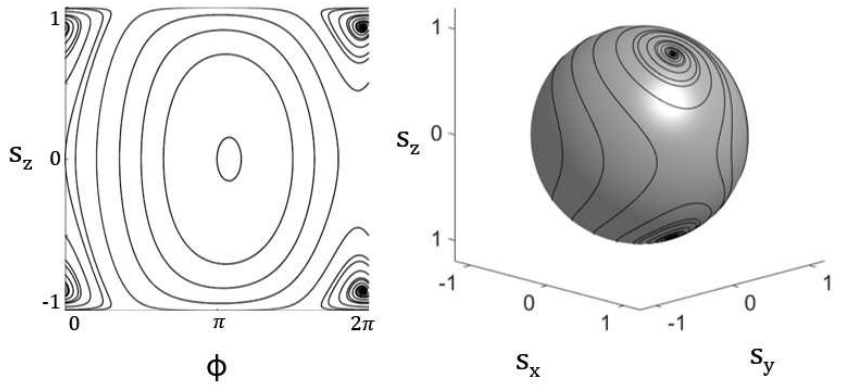


Figure 4.16: Phase-space trajectories from the coherent-state approximation for the non-Hermitian two-mode Bose-Hubbard Hamiltonian, $\hat{\mathcal{H}} = \nu\hat{J}_x + \frac{2g}{N}\hat{J}_z^2 + \mathrm{i}\kappa\hat{J}_z$ with $\nu = 1, g = 1, \kappa = \frac{1}{4}$ (Region 2). The trajectories are shown on the canonical (left) and spherical (right) phase spaces.

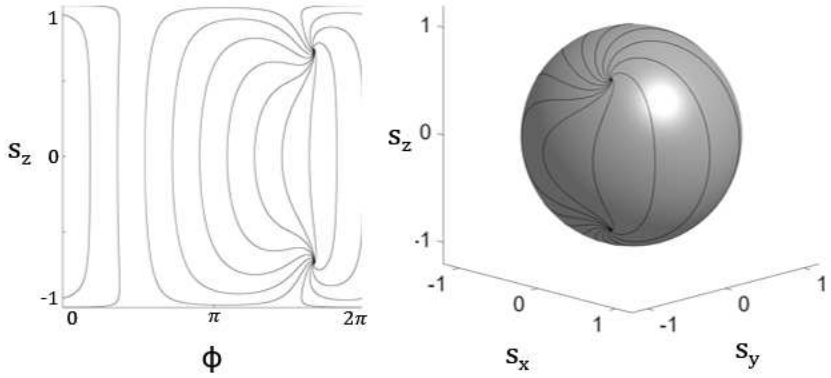


Figure 4.17: Phase-space trajectories from the coherent-state approximation for the non-Hermitian two-mode Bose-Hubbard Hamiltonian, $\hat{\mathcal{H}} = \nu\hat{J}_x + \frac{2g}{N}\hat{J}_z^2 + \mathrm{i}\kappa\hat{J}_z$ with $\nu = 1, g = 1.8, \kappa = 3.2$. The trajectories are shown on the canonical (left) and spherical (right) phase spaces.

In the following analysis, we examine a range of initial coherent states with parameters lying in Region 1 and Region 2, as these regimes exhibit the most dynamically rich behaviour.

Case 1: Four fixed point regime - initial coherent state near the equatorial centre, with $\nu = 1$, $g = 1$, $\kappa = \frac{1}{4}$. This example represents the non-Hermitian analogue of the Hermitian case 1, in which we observed quantum breakdown and revival phenomena. Here, we consider an initial coherent state centred at $(\phi, s_z) = \left(\frac{3\pi}{4}, 0\right)$, which lies close to the equatorial centre located approximately at $(\phi, s_z) = (0.92\pi, 0)$. This fixed point was determined numerically based on the classical equations of motion.

In Figure 4.18, we present a comparison between the expectation value of the scaled observable $s_z = \eta\,\langle\hat{J}_z\rangle$ (solid blue line), the coherent-state approximation of s_z (dotted orange line), and the semiclassical Husimi approximation (solid yellow line) for the case $N = 40$. We observe that the coherent-state approximation exhibits bounded oscillations around the equatorial centre, whereas the full quantum evolution decays toward the dominant eigenstate, shown in the right panel of Figure 4.13. In Figure 4.19, we depict the evolution of a coherent state under the non-Hermitian

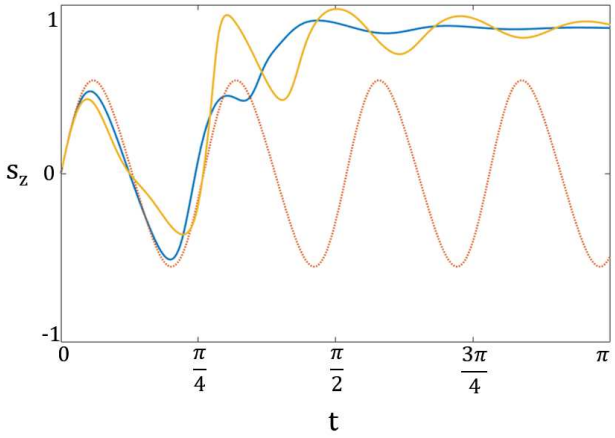


Figure 4.18: Comparison of values of s_z between quantum dynamics (solid blue line), semiclassical Husimi (solid yellow line) and the coherent-state approximation (dotted orange line) for the non-Hermitian two-mode Bose-Hubbard Hamiltonian, $\hat{\mathcal{K}} = \nu\hat{J}_x + \frac{2g}{N}\hat{J}_z^2 + \mathrm{i}\kappa\hat{J}_z$ with $\nu = 1, g = 1, \kappa = \frac{1}{4}$ and $N = 40$, for an initial coherent state centred at $(\phi, s_z) = (\frac{3\pi}{4}, 0)$.

Hamiltonian $\hat{\mathcal{K}} = \nu\hat{J}_x + \frac{2g}{N}\hat{J}_z^2 + \mathrm{i}\kappa\hat{J}_z$ in the $N = 40$ representation. The top row shows the normalised quantum Husimi distributions at times $t = \frac{\pi}{4}$ (left), $t = \frac{\pi}{2}$ (middle), and $t = \pi$ (right), the middle row displays the corresponding semiclassical Husimi approximations, and the bottom row presents the norm landscapes at the same times.

The semiclassical Husimi approximation closely follows the quantum dynamics at short times and later relaxes toward the same final state set by the norm landscape. Initially, both the quantum and semiclassical distributions display similar behaviour, developing the characteristic spiral structures on the Bloch sphere.

From $t = \pi$ onward, the effect of the norm landscape becomes significant. It begins to concentrate the semiclassical distribution, smoothing out the finer spiral structure. This concentration continues with time, guiding the distribution toward a more localised region aligned with the dominant eigenstate. The semiclassical Husimi distribution thus converges to a steady state located near the centre of the dominant eigenstate. In contrast, the coherent-state approximation continues along a trajectory that fails to capture these non-Hermitian effects. This observation mirrors the behaviour found in the damped Kerr Hamiltonian (Chapter 2, Section 2.8.2), where the semiclassical Husimi approximation was shown to outperform the coherent-state approximation in reproducing the long-term quantum dynamics.

Case 2: Four fixed point regime, initial coherent state near unstable spiral with $\nu = 1, g = 1, \kappa = \frac{1}{4}$. In the Hermitian counterpart of this system, the quantum dynamics exhibited tunnelling between the north and south fixed points. Here, we investigate the non-Hermitian extension by considering an initial coherent state centred at $(\phi, s_z) = (0, -\frac{3}{4})$, positioned slightly above the southern fixed point, which now manifests as an unstable spiral located at $(\phi, s_z) \approx (0.04\pi, -0.87)$.

Figure 4.20 shows a comparison between the expectation value of the scaled operator $s_z = \eta\langle\hat{J}_z\rangle$ (solid blue line), the coherent-state approximation (dotted orange line), and the semiclassical Husimi approximation (solid yellow line), for $N = 40$. The coherent-state approximation ini-

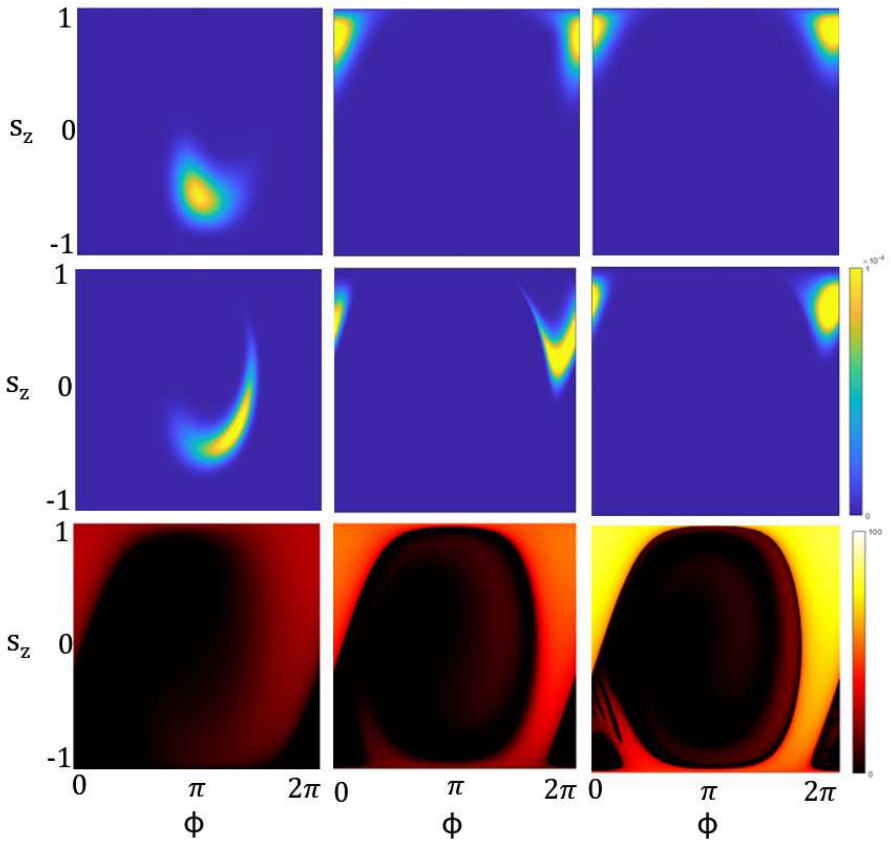


Figure 4.19: Evolution of the normalised quantum Husimi distribution (top row), the normalised semiclassical Husimi distribution (middle row) and the logarithm of the norm landscape (bottom row) for the non-Hermitian two-mode Bose-Hubbard Hamiltonian $\hat{\mathcal{H}} = \nu\hat{J}_x + \frac{2g}{N}\hat{J}_z^2 + \mathrm{i}\kappa\hat{J}_z$ with $\nu = 1, g = 1, \kappa = \frac{1}{4}$ and $N = 40$, for an initial coherent state centred at $(\phi, s_z) = (\frac{3\pi}{4}, 0)$. The columns correspond to different snapshots of the evolution in time with $t = \frac{\pi}{4}$ (left), $t = \frac{\pi}{2}$ (middle) and $t = \pi$ (right).

tially spirals outward, completing approximately two orbits before being drawn inward toward the unstable spiral, continuing to oscillate around it. In contrast, the quantum evolution converges more rapidly to the dominant eigenstate, which determines the system's long-time behaviour. This dominant eigenstate is shown in the right panel of Figure 4.21.

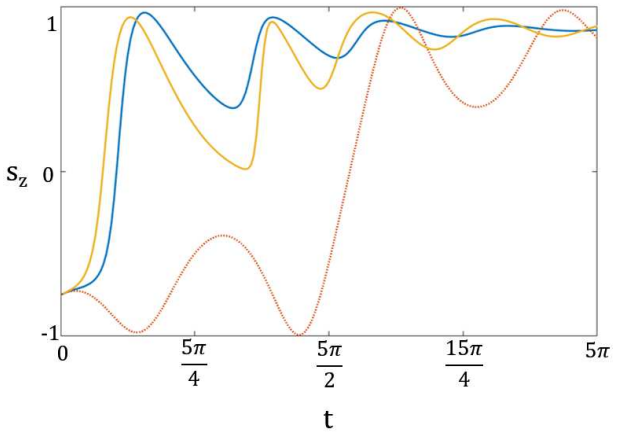


Figure 4.20: Comparison of values of s_z between quantum dynamics (solid blue line), semiclassical Husimi (solid yellow line) and the coherent-state approximation (dotted orange line) for the non-Hermitian two-mode Bose-Hubbard Hamiltonian, $\hat{\mathcal{H}} = \nu\hat{J}_x + \frac{2g}{N}\hat{J}_z^2 + \mathrm{i}\kappa\hat{J}_z$ with $\nu = 1, g = 1, \kappa = \frac{1}{4}$ and $N = 40$, for an initial coherent state at $(\phi, s_z) = (0, -\frac{3}{4})$

Figure 4.21 presents snapshots of the normalised quantum and semiclassical Husimi distributions at selected times. As in Case 1, the semiclassical Husimi approximation accurately captures the quantum evolution, reflecting both the initial deformation of the coherent state and its trajectory as it evolves toward the dominant eigenstate.

A key distinction from the Hermitian counterpart is the absence of quantum tunnelling: in the non-Hermitian regime, the system no longer exhibits tunnelling between the fixed points. Additionally, the long trailing structures typically seen in semiclassical Husimi distributions, especially in Hermitian or weakly non-Hermitian systems, are noticeably absent. This suppression is a direct consequence of the evolving norm landscape, which increasingly concentrates probability density near the dominant eigenstate.

These findings further reinforce the conclusions drawn in Case 1: while the coherent-state approximation diverges from the true quantum dynamics at long times, the semiclassical Husimi approach continues to provide a reliable and qualitatively accurate representation of the system's evolution under non-Hermitian dynamics.

While we have not included an explicit plot of the norm map, its influence is nonetheless evident in the behaviour of the semiclassical Husimi distributions. In both examples, the norm landscape implicitly shapes the long-time dynamics by concentrating probability density toward regions of maximal growth, as expected in non-Hermitian systems. Specifically, in the PT-broken regime considered here, the norm map acts as a gradient flow guiding the semiclassical Husimi distribution toward the vicinity of the dominant eigenstate. This effect is especially pronounced in the suppression of the long tails seen in Hermitian or weakly non-Hermitian cases, illustrating

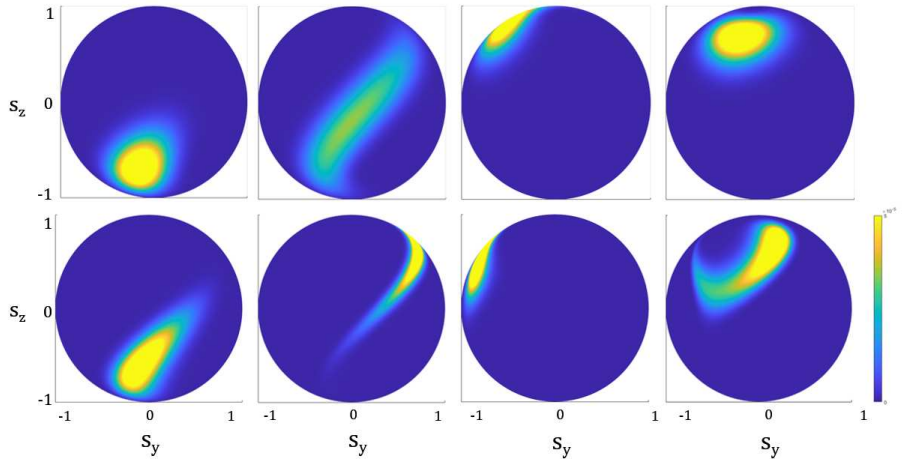


Figure 4.21: Evolution of the normalised quantum Husimi distribution (top row) and the normalised semiclassical Husimi distribution (bottom row) for the non-Hermitian two-mode Bose-Hubbard Hamiltonian $\hat{\mathcal{H}} = \nu\hat{J}_x + \frac{2g}{N}\hat{J}_z^2 + \mathrm{i}\kappa\hat{J}_z$ with $\nu = 1, g = 1, \kappa = \frac{1}{4}$ and $N = 40$, for an initial coherent state at $(\phi, s_z) = (0, -\frac{3}{4})$. The columns correspond to different snapshots of the evolution in time with $t = \frac{\pi}{4}$ (left), $t = \frac{\pi}{2}$ (middle left), $t = \pi$ (middle right) and $t = \frac{5\pi}{2}$ (right).

how non-Hermitian effects enforce localisation. Even without direct visualisation, the agreement between the final distribution and the dominant eigenstate confirms the role of the norm landscape in governing asymptotic behaviour.

Case 3: Centre and saddle fixed point regime, initial coherent state near the centre, with $\nu = 1$, $g = \frac{1}{4}$, $\kappa = \frac{1}{20}$. We now consider the PT-unbroken regime of the non-Hermitian two-mode Bose-Hubbard Hamiltonian, in which the eigenvalue spectrum remains entirely real. This corresponds to parameters $\nu = 1$, $g = \frac{1}{4}$, and $\kappa = \frac{1}{20}$, where the classical dynamics comprise a centre and a saddle point, as discussed in the fixed-point analysis. The real-valued spectrum for this parameter choice is shown in the bottom right panel of Figure 4.12, confirming the system lies within the PT-symmetric (unbroken) phase.

We begin by examining the dynamics of a coherent state initially centred at $(\phi, s_z) = (\frac{3\pi}{4}, 0)$, near the classical centre. In Figure 4.22, we present a comparison between the expectation value $s_z = \eta \langle \hat{J}_z \rangle$ from quantum evolution (solid blue), the coherent-state approximation (dotted orange), and the semiclassical Husimi approximation (solid yellow), for $N = 10$ (left) and $N = 40$ (right). As with previous cases, we observe that the semiclassical Husimi method closely tracks the quantum evolution over moderate timescales, capturing the amplitude and frequency of oscillations with high fidelity. The coherent-state approximation performs similarly in the short term but deviates more significantly at later times.

To further illustrate the phase-space dynamics, we show in Figures 4.23 and 4.24 the evolution of the Husimi distributions. The top row of each figure displays the quantum Husimi distribution, the middle row the semiclassical Husimi distribution, and the bottom row the logarithm of the norm landscape. At early times ($t = \pi$ to $t = 3\pi$), both the quantum and semiclassical Husimi distributions remain well-localised near the classical centre, following periodic orbits that reflect the underlying Hamiltonian flow. Over longer timescales ($t = 10\pi$ to $t = 30\pi$), this periodicity persists

and the norm landscape shows only mild variation, consistent with the absence of exponential amplification or decay typical of PT-broken systems.

Notably, in contrast to the earlier examples from the PT-broken regime, the distributions in this case do not tend toward a single dominant eigenstate. Instead, they preserve their localisation and structure over time, reflecting the unitary-like dynamics characteristic of PT-symmetric systems. The semiclassical Husimi approximation continues to accurately reproduce the key features of the quantum evolution, confirming its effectiveness even in weakly non-Hermitian but spectrally real regimes. This example highlights the qualitative difference in behaviour across the PT-transition and illustrates the stability of phase-space structures in the PT-unbroken domain.

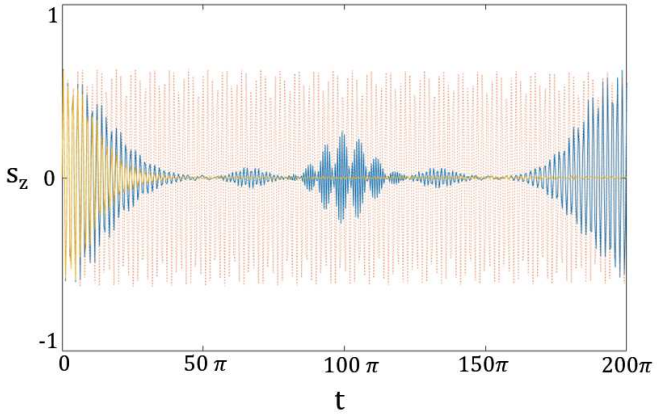


Figure 4.22: Comparison of s_z between quantum dynamics (solid blue line), semiclassical Husimi approximation (solid yellow line) and the coherent-state approximation (dotted orange line) for the non-Hermitian two-mode Bose-Hubbard Hamiltonian with $\nu = 1, g = \frac{1}{4}, \kappa = \frac{1}{10}$ and an initial coherent state centred at $(\phi, s_z) = \left(\frac{3\pi}{4}, 0\right)$. Results are shown for $N = 10$ (left panel) and $N = 40$ (right panel).

In this chapter, we applied the coherent-state and semiclassical Husimi approximation frameworks to quantum systems governed by the $\mathfrak{su}_2$ algebra. After reviewing Hermitian cases, including the two-mode Bose-Hubbard model, we extended the framework to non-Hermitian spin systems and demonstrated how classical and semiclassical dynamics can be captured through symplectic and metric flows on the Bloch sphere. This not only confirmed the validity of our generalised approximation scheme in a well-understood algebraic setting but also illustrated its applicability to non-Hermitian dynamics, which are not covered by standard Lie-algebraic approaches. In the next chapter, we extend this programme to quantum systems that fall outside the conventional Lie algebra framework, focusing on bosonic conversion models governed by polynomially deformed algebras.

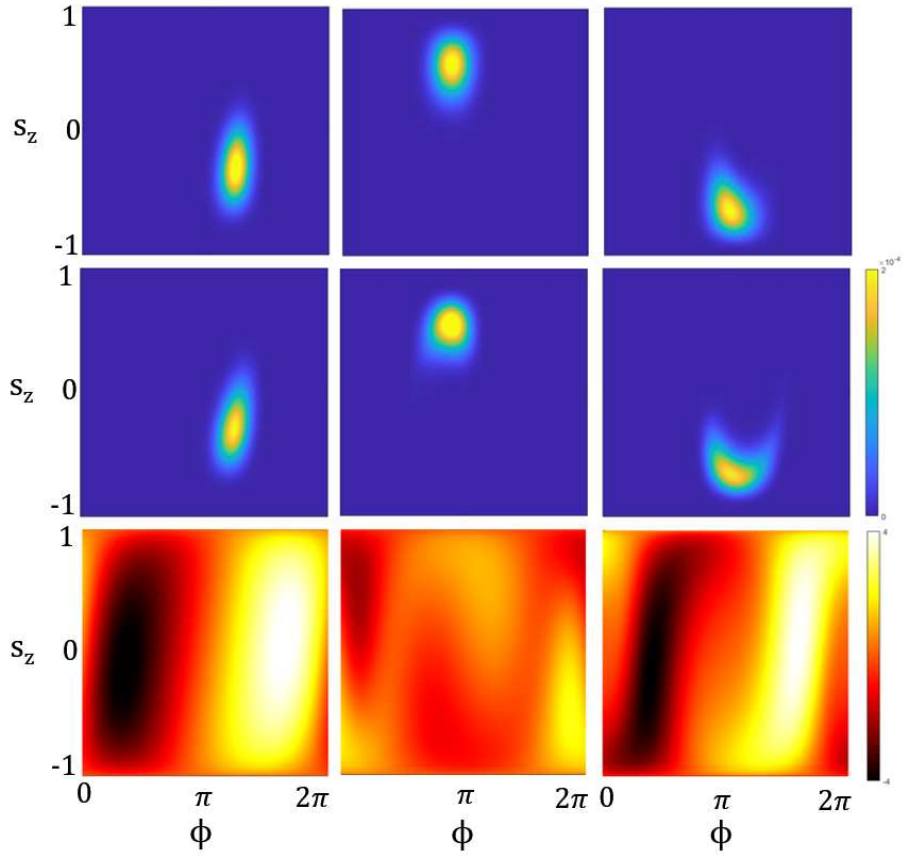


Figure 4.23: Evolution of the normalised quantum Husimi distribution (top row), the normalised semiclassical Husimi distribution (middle row) and the logarithm of the norm landscape (bottom row) for the non-Hermitian two-mode Bose-Hubbard Hamiltonian $\hat{\mathcal{H}} = \nu\hat{J}_x + \frac{2g}{N}\hat{J}_z^2 + \mathrm{i}\kappa\hat{J}_z$ with $\nu = 1, g = \frac{1}{4}, \kappa = \frac{1}{20}$ and $N = 40$, for an initial coherent state centred at $(\phi, s_z) = (\frac{3\pi}{4}, 0)$. The columns correspond to different snapshots of the evolution in time with $t = \pi$ (left), $t = 2\pi$ (middle) and $t = 3\pi$ (right).

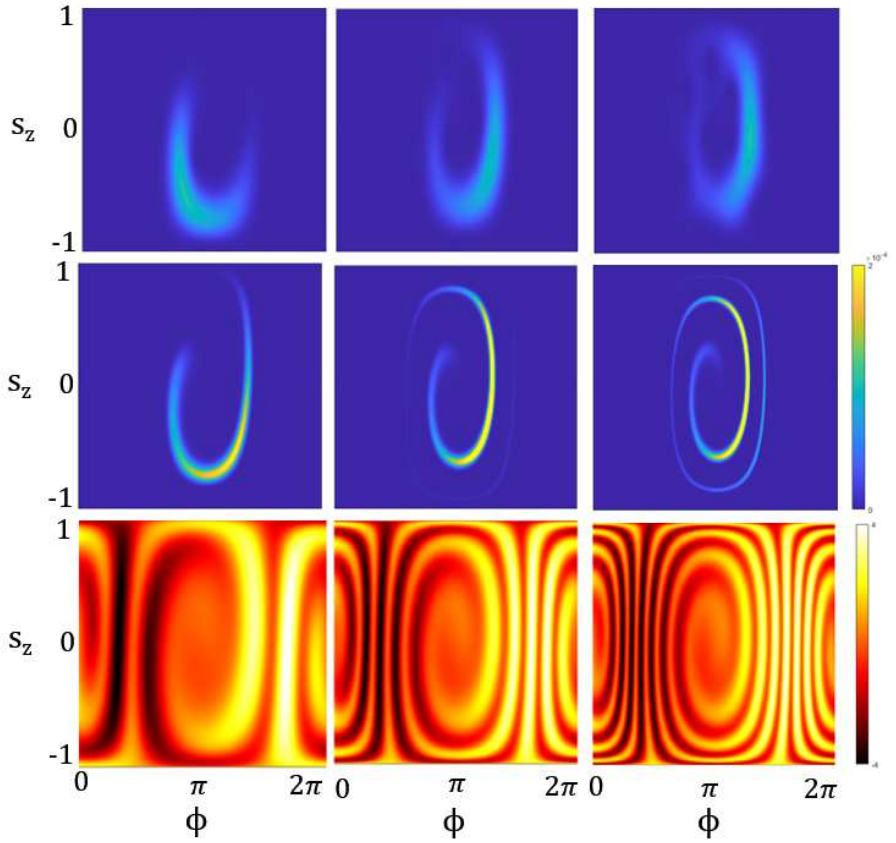


Figure 4.24: Evolution of the normalised quantum Husimi distribution (top row), the normalised semiclassical Husimi distribution (middle row) and the logarithm of the norm landscape (bottom row) for the non-Hermitian two-mode Bose-Hubbard Hamiltonian $\hat{\mathcal{H}} = \nu\hat{J}_x + \frac{2g}{N}\hat{J}_z^2 + \mathrm{i}\kappa\hat{J}_z$ with $\nu = 1, g = \frac{1}{4}, \kappa = \frac{1}{20}$ and $N = 40$, for an initial coherent state centred at $(\phi, s_z) = (\frac{3\pi}{4}, 0)$. The columns correspond to different snapshots of the evolution in time with $t = 10\pi$ (left), $t = 20\pi$ (middle) and $t = 30\pi$ (right).

Chapter 5

Bosonic Conversion Algebra: A Deformed $\mathfrak{su}_2$ and Applications of Phase-Space Approximations

In this chapter, we examine bosonic conversion processes as a representative example to demonstrate that our generalised phase-space approximation framework extends beyond conventional Lie algebra structures. These systems exhibit rich many-particle dynamics governed by deformed $\mathfrak{su}_2$-type algebras, making them an ideal testing ground for the methods developed in Chapter 3.

The class of bosonic systems considered consists of N bosons distributed across two modes, M_1 and M_2, with interconversion processes occurring between them. These models are physically motivated by contexts in quantum optics and cold atom physics, where particles may undergo state transitions or molecular association [110–112]. In mode M_j, bosons are created and annihilated in multiples of k_j, with $k_j \in \mathbb{N}^+$, giving rise to algebraic structures that go beyond the standard harmonic oscillator framework.

Each mode is associated with bosonic creation and annihilation operators $\hat{a}_1$, $\hat{a}_2$ satisfying the canonical commutation relations

$$[\hat{a}_j, \hat{a}_k^\dagger] = \delta_{jk}, \quad [\hat{a}_j, \hat{a}_k] = 0 = [\hat{a}_j^\dagger, \hat{a}_k^\dagger]. \tag{5.1}$$

A defining feature of these systems is that transitions between modes involve the conversion of k_1 particles in mode M_1 into k_2 particles in mode M_2, described by the operator $\hat{a}_1^{k_1}\hat{a}_2^{\dagger k_2}$. A physically relevant example is provided by cold atom systems in which two atoms form a diatomic molecule, with atoms and molecules occupying distinct modes, corresponding to $k_1 = 2$ and $k_2 = 1$.

Bosonic conversion systems of this type were studied in [100], where the associated algebraic structure was termed a "quantum Kummer algebra," reflecting the fact that the classical limit of these systems corresponds to Kummer surfaces [113, 114] in algebraic geometry. In this chapter, we demonstrate, via our phase-space construction, that the classical counterparts of these quantum systems indeed correspond to Kummer shapes. This provides a geometric validation

of the algebraic classification and establishes a concrete bridge between quantum dynamics and classical geometry. We conclude by outlining a potential generalisation of our approach to d-mode systems.

Our phase-space approximations rely on coherent states. For systems not based on conventional Lie algebra structures, this requires the generalised algebraic framework developed in Chapter 3. While inspired by the Gazaeau-Klauder generalised coherent-state formalism, our approach relaxes the requirement of temporal stability of coherent states while maintaining continuity, normalisation, and resolution of identity. Within this setting, we construct coherent states tailored to general two-mode bosonic systems, which form the basis of our semiclassical approximation techniques.

The chapter is organised in two main parts. In the first, we systematically address the key criteria laid out in Chapter 3 for constructing coherent-state approximations. This includes verifying the existence of appropriate coherent states, constructing the associated quantum phase space, and deriving its Poisson and metric bracket structures. We also compute the $\mathcal{D}$-algebra operators and demonstrate that the factorisation property holds, enabling us to recover the classical phase space and its dynamics.

In the second part, we apply the framework to a specific system with $k_1 = 2$ and $k_2 = 1$, illustrating the practical implementation of the method. This includes analysing the performance of the coherent-state approximation for non-Hermitian Hamiltonians, thereby extending the reach of our techniques to models with both interaction and dissipation.

5.1 Bosonic Conversion Algebra

Having established the physical motivation for bosonic conversion systems in the chapter introduction, we now turn to the algebraic structures that govern their dynamics. These models bo beyond the standard $\mathfrak{su}_2$ framework by incorporating nonlinear conversion processes in which multiple particles in one mode are transformed into a different number in another. Such transformations naturally lead to a deformation of the familiar angular momentum algebra.

To describe these systems algebraically, we extend the conventional Jordan–Schwinger construction [101] to accommodate nonlinear processes, following the approach of [115]. In the standard two-mode bosonic case, the angular momentum operators $\hat{J}_x$, $\hat{J}_y$, and $\hat{J}_z$ are expressed as bilinear combinations of bosonic creation and annihilation operators. Here, we generalise this to higher-order combinations corresponding to the conversion of k_1 bosons in mode M_1 into k_2 bosons in mode M_2.

The generalised Jordan–Schwinger operators are defined as

$$\hat{K}_+ = \frac{\hat{a}_1^{\dagger k_1}\hat{a}_2^{k_2}}{N^{\frac{k_1+k_2}{2}-1}}, \quad \hat{K}_- = \frac{\hat{a}_1^{k_1}\hat{a}_2^{\dagger k_2}}{N^{\frac{k_1+k_2}{2}-1}}, \quad \hat{K}_z = \frac{1}{2}\left(\frac{\hat{a}_1^\dagger\hat{a}_1}{k_1} - \frac{\hat{a}_2^\dagger\hat{a}_2}{k_2}\right). \tag{5.2}$$

We define $\hat{N} = k_2\hat{a}_1^\dagger\hat{a}_1 + k_1\hat{a}_2^\dagger\hat{a}_2$ as the total particle number operator, which commutes with all the $\hat{K}_i$ operators since the total particle number is conserved in these conversion processes. These

operators encode the fundamental mode-conversion processes in the system. The prefactor involving N ensures the correct scaling in the semiclassical limit and makes the algebra dimensionally consistent across different values of k_1 and k_2.

As in the standard $\mathfrak{su}_2$ case, we define the Hermitian observables

$$\hat{K}_x = \frac{\hat{K}_+ + \hat{K}_-}{2}, \quad \hat{K}_y = \frac{\hat{K}_+ - \hat{K}_-}{2\mathrm{i}}, \tag{5.3}$$

which form the basis for constructing classical phase-space observables.

As discussed above, when $k_1 + k_2 > 2$, the operators $\hat{K}_x$, $\hat{K}_y$, and $\hat{K}_z$ do not satisfy the linear commutation relations of a Lie algebra. Instead, they generate a polynomially deformed algebra, in which the commutators involve higher-order functions of the generators. These take the form [70]

$$[\hat{K}_x, \hat{K}_y] = \frac{\mathrm{i}}{2} F(\hat{K}_z, \hat{N}), \tag{5.4}$$

$$[\hat{K}_y, \hat{K}_z] = \mathrm{i}\hat{K}_x, \tag{5.5}$$

$$[\hat{K}_z, \hat{K}_x] = \mathrm{i}\hat{K}_y, \tag{5.6}$$

$$[\hat{K}_i, \hat{N}] = 0 \quad \text{for } i = x, y, z. \tag{5.7}$$

The non-closure of the algebra is captured by the function $F(\hat{K}_z, \hat{N})$, which introduces a deformation of the commutation structure

$$F(\hat{K}_z, \hat{N}) = -\frac{k_1^{k_1} k_2^{k_2}}{N^{k_1+k_2-2}} \left[P(\hat{K}_z) - P(\hat{K}_z - 1) \right], \tag{5.8}$$

where $P(\hat{K}_z)$ is a polynomial in $\hat{K}_z$ defined by

$$P(\hat{K}_z) = \prod_{m=1}^{k_1} \left(\frac{\hat{N}}{2k_1 k_2} + \hat{K}_z + \frac{m}{k_1} \right) \prod_{n=1}^{k_2} \left(\frac{\hat{N}}{2k_1 k_2} - \hat{K}_z - 1 + \frac{n}{k_2} \right). \tag{5.9}$$

This structure reduces to the familiar $\mathfrak{su}_2$ algebra when $k_1 = k_2 = 1$, for which the deformation function simplifies to

$$F(\hat{K}_z, \hat{N}) = 2\hat{K}_z, \tag{5.10}$$

thus recovering the standard linear commutation relations. For all other (k_1, k_2) pairs, the algebra is inherently nonlinear, with commutators involving higher-order operator-valued polynomials, a central feature of the systems explored in this chapter.

To explicitly confirm the deformation, we now compute the commutator $[\hat{K}_x, \hat{K}_y]$ directly using the bosonic creation and annihilation operators. This calculation reveals the emergence of the polynomial structure when $k_1 + k_2 > 2$, illustrating the non-closure characteristic of polynomially deformed algebras

$$[\hat{K}_x, \hat{K}_y] = \frac{1}{2\mathrm{i}N^{k_1+k_2-2}} \left(\hat{a}_1^{k_1} \hat{a}_1^{\dagger k_1} \hat{a}_2^{\dagger k_2} \hat{a}_2^{k_2} - \hat{a}_1^{\dagger k_1} \hat{a}_1^{k_1} \hat{a}_2^{k_2} \hat{a}_2^{\dagger k_2} \right). \tag{5.11}$$

Using the identity for nested powers of creation and annihilation operators,

$$\hat{a}_j^k \hat{a}_j^{\dagger k} = \prod_{m=1}^{k} \left(\hat{a}_j^\dagger \hat{a}_j + m \right), \tag{5.12}$$

$$\hat{a}_j^{\dagger k} \hat{a}_j^k = \prod_{m=1}^{k} \left(\hat{a}_j^\dagger \hat{a}_j + 1 - m \right), \tag{5.13}$$

we can rewrite the commutator (5.11) entirely in terms of number operators

$$[\hat{K}_x, \hat{K}_y] = \frac{1}{2\mathrm{i}N^{k_1+k_2-2}} \left[\prod_{m=1}^{k_1} \left(\hat{a}_1^\dagger \hat{a}_1 + m \right) \prod_{n=1}^{k_2} \left(\hat{a}_2^\dagger \hat{a}_2 + 1 - n \right) - \prod_{m=1}^{k_1} \left(\hat{a}_1^\dagger \hat{a}_1 + 1 - m \right) \prod_{n=1}^{k_2} \left(\hat{a}_2^\dagger \hat{a}_2 + n \right) \right]. \tag{5.14}$$

This expression highlights the polynomial nature of the commutator and confirms that the algebra generated by $\hat{K}_x, \hat{K}_y, \hat{K}_z$ is not a Lie algebra. The structure depends explicitly on the occupation numbers of the modes, resulting in a deformation that reflects the underlying many-particle conversion dynamics.

Once this product has been evaluated, we can express the number operators $\hat{a}_1^\dagger \hat{a}_1$ and $\hat{a}_2^\dagger \hat{a}_2$ as linear combinations of $\hat{K}_z$ and $\hat{N}$. Specifically,

$$\hat{a}_1^\dagger \hat{a}_1 = \frac{\hat{N} + 2k_1 k_2 \hat{K}_z}{2k_2}, \tag{5.15}$$

$$\hat{a}_2^\dagger \hat{a}_2 = \frac{\hat{N} - 2k_1 k_2 \hat{K}_z}{2k_1}. \tag{5.16}$$

Using the formalism described in [47, 116], we can derive a Casimir operator for this deformed algebra, given by

$$\hat{C} = \hat{K}_x^2 + \hat{K}_y^2 + G(\hat{K}_z, \hat{N}), \tag{5.17}$$

where the function $G(z, \hat{N})$ satisfies the recurrence relation

$$G(z, \hat{N}) - G(z-1, \hat{N}) = \frac{1}{2} \left(F(z, \hat{N}) + F(z-1, \hat{N}) \right), \tag{5.18}$$

and $F(z, \hat{N})$ is the polynomial defined previously in equation (5.8), arising from the commutator $[\hat{K}_x, \hat{K}_y]$.

Equation (5.18) is readily solved by

$$G\left(\hat{K}_z, \hat{N}\right) = -\frac{k_2^{k_1} k_1^{k_2}}{2N^{k_1+k_2-2}} \left(P\left(\hat{K}_z\right) + P\left(\hat{K}_z - 1\right) \right). \tag{5.19}$$

This represents one solution within a broader class, up to an arbitrary function of $\hat{N}$. We thereby

obtain the conservation relation

$$\hat{K}_z^2 + \hat{K}_y^2 = \hat{C} - G\left(\hat{K}_z, \hat{N}\right). \tag{5.20}$$

Taking expectation values in coherent states, we obtain the equation

$$\left\langle \hat{K}_z^2 \right\rangle + \left\langle \hat{K}_y^2 \right\rangle = \left\langle \hat{C} \right\rangle - \left\langle G\left(\hat{K}_z, \hat{N}\right) \right\rangle, \tag{5.21}$$

which defines a generalised Bloch sphere, a surface known as a quantum Kummer shape [100]. The term reflects its connection to classical Kummer surfaces [114], a relationship we explore in more detail when analysing the classical phase-space structure in the $N \to \infty$ limit.

5.2 Phase-Space Approximations

In this section, we apply the generalised phase-space approximation framework developed in Chapter 3 to construct the coherent-state approximation for two-mode bosonic conversion systems. We systematically address the key criteria required to implement the method, thereby validating its applicability beyond standard Lie-algebraic settings.

5.2.1 Coherent States

These systems do not possess a conventional Lie algebra structure that would enable a standard group-theoretic construction of coherent states. To apply the generalised phase-space framework introduced in Chapter 3, we require the existence of a family of coherent states that satisfy key structural properties, continuity, normalisation, and resolution of identity. One natural class of such states, relevant to our analysis, is constructed via the action of a ladder operator on an extremal state, as proposed in [99, 100, 117]. This construction requires a set of operators satisfying an algebra of the form

$$[\hat{A}_0, \hat{A}] = -\hat{A}, \tag{5.22}$$

$$[\hat{A}_0, \hat{A}^*] = \hat{A}^*, \tag{5.23}$$

$$[\hat{A}, \hat{A}^*] = f(\hat{A}_0), \tag{5.24}$$

where $\hat{A}$ and $\hat{A}^*$ act as ladder operators and the function $f(\hat{A}_0)$ determines the structure of the underlying algebra.

For the two-mode bosonic conversion systems, we make the following identifications

$$\hat{A}_0 \leftrightarrow \hat{K}_z, \quad \hat{A} \leftrightarrow \hat{K}_-, \quad \hat{A}^* \leftrightarrow \hat{K}_+, \tag{5.25}$$

with the associated structure function given by

$$f(\hat{A}_0) \leftrightarrow F(\hat{K}_z, \hat{N}), \tag{5.26}$$

as introduced in the previous section. This correspondence embeds the bosonic conversion model

within the broader class of polynomially deformed algebras, for which coherent-state constructions of this type are known to be valid.

Since the Hilbert space of the two-mode bosonic conversion system is finite-dimensional, coherent states can be constructed by applying a ladder operator to an extremal state

$$||\chi\rangle = e^{\chi \hat{A}} |E\rangle , \tag{5.27}$$

where $\chi \in \mathbb{C}$, $||\chi\rangle$ denotes a non-normalised coherent state, and $|E\rangle$ is an extremal state such that $\hat{A}^* |E\rangle = 0$.

To provide context, consider the familiar $\mathfrak{su}_2$ case, where coherent states are generated by the operators $\hat{J}_z$, $\hat{J}_-$, and $\hat{J}_+$. These take the form

$$|\xi\rangle = \hat{D}(\xi) |N\rangle = e^{\xi \hat{J}_+ - \xi^* \hat{J}_-} |N\rangle . \tag{5.28}$$

Using the Baker–Campbell–Hausdorff (BCH) formula, the displacement operator simplifies, after an appropriate coordinate transformation, to a single exponentiated lowering operator

$$||\zeta\rangle = e^{\zeta \hat{J}_-} |N\rangle , \tag{5.29}$$

where ζ is related to ξ via a stereographic mapping. This simplification is enabled by the closed commutation relations of the $\mathfrak{su}_2$ algebra.

In contrast, for generalised or polynomially deformed algebras, the commutator $[\hat{A}, \hat{A}^*]$ typically lies outside the original algebra, preventing the application of the BCH formula. The extremal-state ladder operator construction introduced above circumvents this issue, defining coherent states via repeated action of $\hat{A}$ on the extremal state $|E\rangle$, without relying on group-theoretic exponentiation.

Using the operator identifications introduced above, we define the extremal state as $|E\rangle = |\frac{N}{k_2}, 0\rangle$. The corresponding (non-normalised) coherent state vector for the bosonic conversion system is then given by

$$\begin{aligned} ||\chi\rangle &= e^{\left(N^{\frac{k_1+k_2}{2}-1} \chi \hat{K}_-\right)} |\tfrac{N}{k_2}, 0\rangle , && (5.30) \\ &= \sum_{n=0}^{\frac{N}{k_1 k_2}} \frac{\left(\hat{a}_1^{k_1} \hat{a}_2^{\dagger k_2} \chi\right)^n}{n!} |\tfrac{N}{k_2}, 0\rangle , \\ &= \sum_{n=0}^{\frac{N}{k_1 k_2}} \frac{\chi^n \sqrt{(\frac{N}{k_2})!} \sqrt{(k_2 n)!}}{n! \sqrt{\left(\frac{N}{k_2} - k_1 n\right)!}} |\tfrac{N}{k_2} - k_1 n,\, k_2 n\rangle . && (5.31) \end{aligned}$$

Normalising this expression gives the coherent states in the form

$$|\chi\rangle = \frac{1}{\sqrt{\mathcal{M}}} \sum_{n=0}^{\frac{N}{k_1 k_2}} \frac{\chi^n \sqrt{(k_2 n)!}}{n! \sqrt{\left(\frac{N}{k_2} - k_1 n\right)!}} \, |\tfrac{N}{k_2} - k_1 n,\, k_2 n\rangle \,, \tag{5.32}$$

where the constant prefactor $\sqrt{\left(\frac{N}{k_2}\right)!}$ has been absorbed into the normalisation. The normalisation factor is then

$$\mathcal{M}(|\chi|^2) = \sum_{n=0}^{\frac{N}{k_1 k_2}} \frac{|\chi|^{2n} (k_2 n)!}{\left(\frac{N}{k_2} - k_1 n\right)! (n!)^2}. \tag{5.33}$$

To simplify notation in later calculations, we absorb the factor $N^{\frac{k_1+k_2}{2}-1}$ into a rescaled variable χ. This leads to the modified expressions

$$|\chi\rangle = \frac{1}{\sqrt{\mathcal{M}}} \sum_{n=0}^{\frac{N}{k_1 k_2}} \frac{\chi^n \sqrt{(k_2 n)!}}{n! \sqrt{N^{k_1+k_2-2} \left(\frac{N}{k_2} - k_1 n\right)!}} \, |\tfrac{N}{k_2} - k_1 n,\, k_2 n\rangle \,, \tag{5.34}$$

$$\mathcal{M}(|\chi|^2) = \sum_{n=0}^{\frac{N}{k_1 k_2}} \frac{|\chi|^{2n} (k_2 n)!}{N^{k_1+k_2-2} \left(\frac{N}{k_2} - k_1 n\right)! (n!)^2}. \tag{5.35}$$

It is worth noting that for the special case $k_1 = k_2 = 1$, equation (5.30) yields the standard $\mathfrak{su}_2$ coherent states as follows

$$||\chi\rangle = \sum_{n=0}^{N} \frac{\chi^n}{\sqrt{(N-n)!\, n!}} \, |N-n, n\rangle \,, \tag{5.36}$$

$$= \frac{1}{\sqrt{N}} \sum_{n=0}^{N} \sqrt{\binom{N}{n}} \chi^n \, |N-n, n\rangle \,, \tag{5.37}$$

with the corresponding normalisation function

$$\mathcal{M}(|\chi|^2) = (1 + |\chi|^2)^N. \tag{5.38}$$

To establish that our coherent states form an overcomplete set, we must demonstrate the existence of a measure $d\mu(\chi^*, \chi)$ such that the resolution of identity holds

$$\hat{I} = \int \frac{|\chi\rangle\langle\chi|}{\langle\chi|\chi\rangle} \, d\mu(\chi^*, \chi). \tag{5.39}$$

As we have established a well-defined normalisation function $\mathcal{M}(|\chi|^2) = \langle\chi||\chi\rangle$ for our coherent

states, the resolution of identity follows from Klauder's general framework for overcomplete sets [51]. The measure is constructed directly from the normalisation function through

$$d\mu(\chi^*, \chi) = \frac{\partial^2}{\partial\chi^* \partial\chi} \ln \mathcal{M}(|\chi|^2)\, d\chi^* d\chi. \tag{5.40}$$

For our finite-dimensional Hilbert space (dimension $\frac{N}{k_1 k_2} + 1$), this yields a measure of the form

$$d\mu(\chi^*, \chi) = \rho(|\chi|^2) d|\chi|^2 d\arg(\chi), \tag{5.41}$$

where the density function $\rho(|\chi|^2)$ is determined by evaluating the derivative formula above with our specific normalisation function.

Although these states were initially constructed using the parameter χ, it is advantageous to describe them in terms of the scaled expectation values where the classical phase space variables s_x, s_y, and s_z are defined as

$$s_x = 2^{\frac{k_1+k_2}{2}-1} k_1^{\frac{k_2}{2}-1} k_2^{\frac{k_1}{2}-1} \eta \langle \hat{K}_x \rangle , \tag{5.42}$$

$$s_y = 2^{\frac{k_1+k_2}{2}-1} k_1^{\frac{k_2}{2}-1} k_2^{\frac{k_1}{2}-1} \eta \langle \hat{K}_y \rangle , \tag{5.43}$$

$$s_z = \eta \langle \hat{K}_z \rangle . \tag{5.44}$$

where the scaling factor $\eta = \frac{2k_1 k_2}{N}$ is chosen to ensure that $s_z \in [-1, 1]$, facilitating comparison with the classical phase space. The additional scaling factors in the definitions of s_x and s_y are introduced to align our formulation with the conventions established in the existing literature.

To aid geometric interpretation and visualisation, we also define a polar angle variable

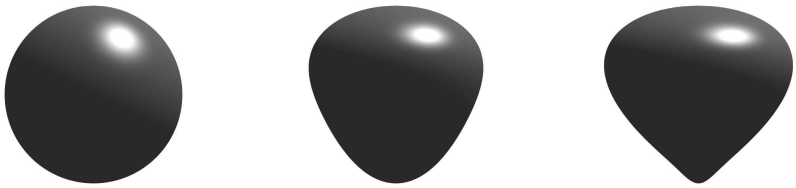
$$\phi = \arctan\left(\frac{s_y}{s_x}\right), \tag{5.45}$$

allowing the state to be parametrised in terms of (s_z, ϕ). This representation provides a geometrically intuitive description of the quantum Kummer shapes and offers a natural way to compare the quantum and classical trajectories, particularly when projected onto shape space.

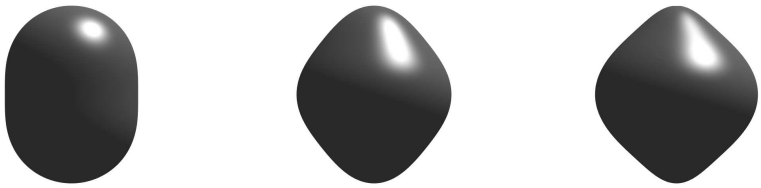
5.2.2 Quantum Phase Space

In this section, we outline the quantum phase space and the associated Poisson and metric brackets, where we will denote the phase space as the quantum Kummer shapes following the convention set by Odzijewicz and Wawreniuk [100]. Using the coherent states in equation (5.32), we are now able to determine the quantum Kummer shapes defined by equation (5.21). When $k_1 = k_2 = 1$, the surface reduces to the standard spherical form of $\mathfrak{su}_2$. Figure 5.1 illustrates several examples of these surfaces for parameter values that deviate from unity. As the parameters deviate from unity, the shapes develop characteristic deformations that vary with N. For $k_1 > 1$, the north pole develops a pronounced peaked dome structure, while for $k_2 > 1$, a similar dome appears at the south pole. As N increases, these domes sharpen and tend toward cusp-like singularities, signalling the approach to the classical limit. Despite these local changes, the global topological

features of the surfaces remain invariant, and the shapes converge to well-defined classical Kummer forms.



(a) $k_1 = 2, k_2 = 1, N = 2$ (b) $k_1 = 2, k_2 = 1, N = 4$ (c) $k_1 = 2, k_2 = 1, N = 16$



(d) $k_1 = 2, k_2 = 2, N = 8$ (e) $k_1 = 2, k_2 = 2, N = 16$ (f) $k_1 = 2, k_2 = 2, N = 24$

Figure 5.1: Selected quantum Kummer shapes for different values of k_1, k_2, and N. As N increases, the surfaces approach their classical counterparts, exhibiting sharper geometrical features.

The quantum Kummer shapes can also serve as a canvas for visualising the Husimi distributions of quantum states. Figure 5.2 presents several examples of Husimi distributions for coherent states centred at $(\phi, s_z) = (\frac{\pi}{2}, 0)$. These distributions highlight the localised, classical-like character of coherent states within the deformed phase-space geometry.

Having established the quantum Kummer shapes as our quantum phase spaces, we now turn to the associated geometric structures. The normalisation function can be used to determine the Poisson bracket on the quantum Kummer shape [118], given by

$$\{\chi, \chi^*\} = \mathrm{i} \left(\frac{\partial^2}{\partial\chi\partial\chi^*} \ln \mathcal{M} \right)^{-1}. \tag{5.46}$$

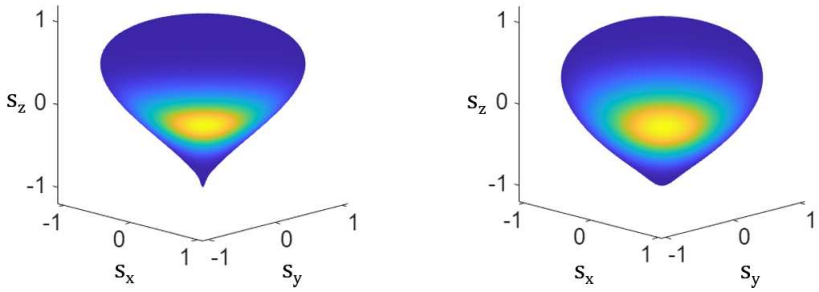
To evaluate the bracket explicitly, we first compute the second-order derivative appearing in equation (5.46)

$$\begin{aligned} \frac{\partial^2}{\partial\chi\partial\chi^*} \ln \mathcal{M} &= \frac{\partial}{\partial\chi} \left(\frac{\chi \mathcal{M}'}{\mathcal{M} N^{k_1+k_2-1}} \right) \\ &= \frac{\mathcal{M}'}{\mathcal{M} N^{k_1+k_2-1}} + \frac{\chi\chi^*}{N^{2k_1+2k_2-2}} \left(\frac{\mathcal{M}'^2}{\mathcal{M}^2} - \frac{\mathcal{M}''}{\mathcal{M}} \right), \end{aligned} \tag{5.47}$$

where $\mathcal{M}' = \frac{d\mathcal{M}}{dx}$ and $\mathcal{M}'' = \frac{d^2\mathcal{M}}{dx^2}$ with $x = |\chi|^2$.

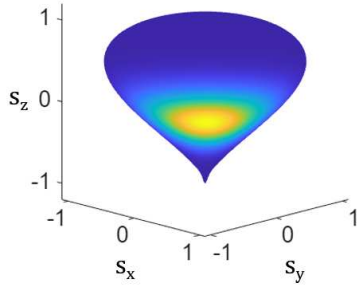
Substituting back, the Poisson bracket becomes

$$\{\chi, \chi^*\} = \frac{\mathrm{i}}{\frac{\mathcal{M}'}{\mathcal{M} N^{k_1+k_2-1}} + \frac{\chi\chi^*}{N^{2k_1+2k_2-2}} \left(\frac{\mathcal{M}'^2}{\mathcal{M}^2} - \frac{\mathcal{M}''}{\mathcal{M}} \right)}. \tag{5.48}$$

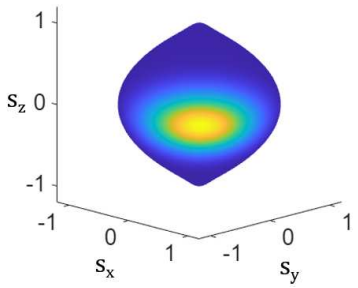


(a) $k_1 = 2, k_2 = 1, N = 20$

(b) $k_1 = 2, k_2 = 1, N = 40$



(c) $k_1 = 3, k_2 = 1, N = 36$



(d) $k_1 = 2, k_2 = 2, N = 64$

Figure 5.2: Husmi distributions plotted on the quantum Kummer shapes for coherent states centred at $(\phi, s_z) = (\frac{\pi}{2}, 0)$ with various values of k_1, k_2 and N.

Using a standard result from Kähler geometry[119], we use the fact that the metric bracket is defined by $\{\{\chi, \chi^*\}\} = \mathrm{i}\{\chi, \chi^*\}$, and we find

$$\{\{\chi, \chi^*\}\} = -\frac{1}{\frac{\mathcal{M}'}{\mathcal{M}N^{k_1+k_2-1}} + \frac{\chi\chi^*}{N^{2k_1+2k_2-2}}\left(\frac{\mathcal{M}'^2}{\mathcal{M}^2} - \frac{\mathcal{M}''}{\mathcal{M}}\right)}. \tag{5.49}$$

While the Poisson bracket formulation could, in principle, be used to compute coherent-state dynamics on quantum Kummer shapes, it becomes impractical in application. This is primarily due to the normalisation function $\mathcal{M}$, which is a high-degree polynomial of order $N/2$. For finite N, this structure renders explicit calculations cumbersome, and in the $N \to \infty$ limit, the expressions involving ratios such as $\mathcal{M}'/\mathcal{M}$ lack simple closed-form approximations. As a result, the algebraic complexity obscures physical interpretation and limits the tractability of this approach for practical computation.

To obtain classical analogues of the quantum dynamics, it is therefore more effective to adopt the phase-space variables (s_x, s_y, s_z). In this representation, the classical limit arises naturally and avoids the complications inherent in the χ-dependent formulation. Accordingly, we will carry out our classical analysis on the standard classical phase spaces and subsequently map the resulting trajectories onto the corresponding quantum Kummer shapes.

5.2.3 $\mathcal{D}$-Algebra

In this section, we establish the $\mathcal{D}$-algebra operators for the bosonic conversion algebra and demonstrate that the conditions required for the factorisation property, as outlined in Section 3.1.2,

are satisfied. Specifically, we aim to verify that the multiplicative (leading-order) terms in the differential operator representation are of one order higher in N than the derivative components, a necessary condition for the factorisation property to hold.

To achieve this, we derive explicit expressions for the $\mathcal{D}$-algebra operators corresponding to the algebra generators and confirm that the associated u_A and v_A properties hold. While our general framework is applicable to arbitrary (k_1, k_2), we focus here on the illustrative case $(k_1, k_2) = (2, 1)$, which will serve as a running example in later sections. The techniques used are readily generalisable to other combinations of k_1 and k_2.

Although the two-mode bosonic conversion algebra is not a Lie algebra, the presence of a ladder-type structure in the operators allows us to define a $\mathcal{D}$-algebra in terms of the coherent states constructed previously. This approach follows general strategies developed for non-Lie algebras with ladder operators [99].

We begin by computing the differential representation for $\hat{K}_-$. By definition of the coherent states, we have

$$\begin{aligned} \hat{K}_- ||\chi\rangle &= \hat{K}_- e^{\chi \hat{K}_-} |\tfrac{N}{2}, 0\rangle \\ &= \frac{\partial}{\partial \chi} ||\chi\rangle \,. \end{aligned} \tag{5.50}$$

Thus, we obtain

$$\mathcal{D}_{K_-} = \frac{\partial}{\partial \chi}, \tag{5.51}$$

$$\mathcal{D}^0_{K_-} = 0, \tag{5.52}$$

$$\mathcal{D}^D_{K_-} = \frac{\partial}{\partial \chi}, \tag{5.53}$$

where $\mathcal{D}^0_{K_-}$ denotes the multiplicative (algebraic) component, and $\mathcal{D}^D_{K_-}$ denotes the differential part.

To calculate $\mathcal{D}_{K_z}$, we follow the approach outlined in the appendix of [82]. We begin by defining the auxiliary function

$$f_1(\chi) = e^{-\chi \hat{K}_-} \hat{K}_z e^{\chi \hat{K}_-}. \tag{5.54}$$

Differentiating $f_1(\chi)$ with respect to χ yields

$$\begin{aligned} \frac{\mathrm{d}f_1(\chi)}{\mathrm{d}\chi} &= e^{-\chi \hat{K}_-} [\hat{K}_z, \hat{K}_-] e^{\chi \hat{K}_-}, \\ &= -\hat{K}_-, \end{aligned} \tag{5.55}$$

where we have used the algebraic commutation relation $[\hat{K}_z, \hat{K}_-] = -\hat{K}_-$. Integrating this equation and applying the initial condition $f_1(0) = \hat{K}_z$, we find

$$f_1(\chi) = \hat{K}_z - \chi \hat{K}_-. \tag{5.56}$$

Rearranging, we obtain the identity

$$\hat{K}_z e^{\chi \hat{K}_-} = e^{\chi \hat{K}_-} \left(\hat{K}_z - \chi \hat{K}_- \right). \tag{5.57}$$

We now apply this to compute the action of $\hat{K}_z$ on the coherent state

$$\begin{aligned} \hat{K}_z ||\chi\rangle &= \hat{K}_z e^{\chi \hat{K}_-} |\tfrac{N}{k_1}, 0\rangle, \\ &= e^{\chi \hat{K}_-} \left(\hat{K}_z - \chi \hat{K}_- \right) |\tfrac{N}{k_1}, 0\rangle, \\ &= \left(\frac{N}{2k_1} - \chi \frac{\partial}{\partial \chi} \right) ||\chi\rangle, \end{aligned} \tag{5.58}$$

where we used that $\hat{K}_z |\frac{N}{k_1}, 0\rangle = \frac{N}{2k_1} |\frac{N}{k_1}, 0\rangle$ and $\hat{K}_- |\frac{N}{k_1}, 0\rangle = 0$.

We therefore identify the differential operator representation as

$$\mathcal{D}_{K_z} = \frac{N}{2k_1} - \chi \frac{\partial}{\partial \chi}, \tag{5.59}$$

$$\mathcal{D}^0_{K_z} = \frac{N}{2k_1}, \tag{5.60}$$

$$\mathcal{D}^D_{K_z} = -\chi \frac{\partial}{\partial \chi}. \tag{5.61}$$

Repeating the process for $\mathcal{D}_{K_+}$ we begin by defining $f_2(\chi) = e^{-\chi \hat{K}_-} \hat{K}_+ e^{\chi \hat{K}_-}$ Differentiating f_2 we obtain

$$\begin{aligned} \frac{\mathrm{d}f_2(\chi)}{d\chi} &= -\chi \hat{K}_- e^{-\chi \hat{K}_-} \hat{K}_+ e^{\chi \hat{K}_-} + e^{-\chi \hat{K}_-} \hat{K}_+ \chi \hat{K}_- e^{\chi \hat{K}_-}, \\ &= e^{-\chi \hat{K}_-} [\hat{K}_+, \hat{K}_-] e^{\chi \hat{K}_-}, \\ &= e^{-\chi \hat{K}_-} F(\hat{K}_z) e^{\chi \hat{K}_-}. \end{aligned} \tag{5.62}$$

As the expression for $F(\hat{K}_z)$ depends upon the parameters k_1, k_2, we now specify $(k_1, k_2) = (2, 1)$ to determine the explicit form for $\mathcal{D}_{K+}$. This particular choice of parameters yields a more instructive and tangible representation, revealing the underlying mathematical structure and relationship to N more effectively than the general case. With $(k_1, k_2) = (2, 1)$ equation (5.62) becomes

$$\begin{aligned} \frac{\mathrm{d}f_2(\chi)}{d\chi} = e^{-\chi \hat{K}_-} \left(-\frac{\hat{N}}{N} \right) e^{\chi \hat{K}_-} + e^{-\chi \hat{K}_-} \left(-\frac{\hat{N}^2}{4N} \right) e^{\chi \hat{K}_-} + e^{-\chi \hat{K}_-} \left(-\frac{2\hat{K}_z \hat{N}}{N} \right) e^{\chi \hat{K}_-} \\ + e^{-\chi \hat{K}_-} \left(-\frac{12 \hat{K}_z^2}{N} \right) e^{\chi \hat{K}_-}, \end{aligned}$$

using the expression for f_1 we obtain

$$\begin{aligned} &= -\frac{\hat{N}}{N} - \frac{\hat{N}^2}{4N} + \frac{2\hat{N}}{N} (\hat{K}_z - \chi \hat{K}_-) + \frac{12}{N} (\hat{K}_z - \chi \hat{K}_-)^2, \\ &= -\frac{\hat{N}}{N} - \frac{\hat{N}^2}{4N} + \frac{2\hat{N}\hat{K}_z}{N} - \frac{2\chi \hat{N} \hat{K}_-}{N} \end{aligned}$$

$$+\frac{12\hat{K}_z^2}{N}-\frac{12\chi\hat{K}_-\hat{K}_z}{N}-\frac{12\chi\hat{K}_z\hat{K}_-}{N}+\frac{12\chi^2\hat{K}_-^2}{N}, \tag{5.63}$$

Integrating this, we obtain f_2 as, where in the second line we have used the $[\hat{K}_z,\hat{K}_-]$ relation to keep the $\hat{K}_z$ terms to the right as they act in a trivial manner on the extremal state.

$$\begin{aligned}
f_2(\chi) &= -\frac{\hat{N}\chi}{N}-\frac{\hat{N}^2\chi}{4N}+\frac{2\hat{N}\hat{K}_z\chi}{N}-\frac{\chi^2\hat{N}\hat{K}_-}{N} \\
&\quad +\frac{12\hat{K}_z^2\chi}{N}-\frac{6\chi^2\hat{K}_-\hat{K}_z}{N}-\frac{6\chi^2\hat{K}_z\hat{K}_-}{N}+\frac{4\chi^3\hat{K}_-^2}{N}, \\
&= -\frac{\hat{N}\chi}{N}-\frac{\hat{N}^2\chi}{4N}+\frac{2\hat{N}\hat{K}_z\chi}{N}-\frac{\chi^2\hat{N}\hat{K}_-}{N} \\
&\quad +\frac{12\hat{K}_z^2\chi}{N}-\frac{12\chi^2\hat{K}_-\hat{K}_z}{N}+\frac{6\chi^2\hat{K}_-}{N}+\frac{4\chi^3\hat{K}_-^2}{N}.
\end{aligned} \tag{5.64}$$

To find $\mathcal{D}_{K_+}+$ we use the relation from f_2 as follows

$$\begin{aligned}
\hat{K}_+||\chi\rangle &= \hat{K}_z e^{\chi\hat{K}_-}|\tfrac{N}{k_1},0\rangle\,, \\
&= e^{\sqrt{N}\chi\hat{K}_-}\left(-\frac{\hat{N}\chi}{N}-\frac{\hat{N}^2\chi}{4N}+\frac{2\hat{N}\hat{K}_z\chi}{N}-\frac{\chi^2\hat{N}\hat{K}_-}{N}\right. \\
&\quad \left.+\frac{12\hat{K}_z^2\chi}{N}-\frac{12\chi^2\hat{K}_-\hat{K}_z}{N}+\frac{6\chi^2\hat{K}_-}{N}+\frac{4\chi^3\hat{K}_-^2}{N}\right)|\tfrac{N}{k_1},0\rangle\,, \\
&= \left(\chi+N\chi-4\chi^2\hat{K}_-+\frac{6\chi^2\hat{K}_-}{N}+4\chi^3\hat{K}_-^2\right)e^{\sqrt{N}\chi\hat{K}_-}|\tfrac{N}{k_1},0\rangle\,, \\
&= \left(\chi+N\chi-4\chi^2\hat{K}_-+\frac{6\chi^2\hat{K}_-}{N}+4\chi^3\hat{K}_-^2\right)||\chi\rangle\,.
\end{aligned} \tag{5.65}$$

Using the relation $\hat{K}_- = \frac{\partial}{\partial\chi}$ we obtain $\mathcal{D}_{K_+}$ as

$$\mathcal{D}_{K_+} = \chi+N\chi-4\chi^2\frac{\partial}{\partial\chi}+\frac{6\chi^2}{N}\frac{\partial}{\partial\chi}+\frac{4\chi^3}{N}\frac{\partial^2}{\partial\chi^2}, \tag{5.66}$$

$$\mathcal{D}^0_{K_+} = \chi+N\chi, \tag{5.67}$$

$$\mathcal{D}^D_{K_+} = -4\chi^2\frac{\partial}{\partial\chi}+\frac{6\chi^2}{N}\frac{\partial}{\partial\chi}+\frac{4\chi^3}{N}\frac{\partial^2}{\partial\chi^2}. \tag{5.68}$$

Collating the results for all of the operators we have

$$\mathcal{D}_{K_-} = \frac{\partial}{\partial\chi}, \tag{5.69}$$

$$\mathcal{D}_{K_+} = \chi+N\chi-4\chi^2\frac{\partial}{\partial\chi}+\frac{6\chi^2}{N}\frac{\partial}{\partial\chi}+\frac{4\chi^3}{N}\frac{\partial^2}{\partial\chi^2}, \tag{5.70}$$

$$\mathcal{D}_{K_z} = \frac{N}{4}-\chi\frac{\partial}{\partial\chi}, \tag{5.71}$$

from which we note the conditions for the factorisation property are satisfied.

Having established the $\mathcal{D}$-algebra framework and demonstrated its application for the specific case

of $k_1 = 2, k_2 = 1$, we now return to the general (k_1, k_2) case to derive universal expressions for the expectation values. Using the $\mathcal{D}$-algebra identity $\langle \hat{K}_i \rangle = \frac{1}{\mathcal{M}} \mathcal{D}_{K_i} \mathcal{M}$, which holds for any (k_1, k_2) bosonic conversion system, we arrive at the analytic expressions for the expectation values of the generating operators in terms of χ as

$$\langle \hat{K}_x \rangle = \frac{(\chi + \chi^*)\mathcal{M}'}{2\mathcal{M}N^{k_1+k_2-1}}, \tag{5.72}$$

$$\langle \hat{K}_y \rangle = \frac{(\chi - \chi^*)\mathcal{M}'}{2\mathrm{i}\mathcal{M}N^{k_1+k_2-1}}, \tag{5.73}$$

$$\langle \hat{K}_z \rangle = \frac{N}{2k_1k_2} - \frac{\chi\chi^*\mathcal{M}'}{\mathcal{M}N^{k_1+k_2-1}}. \tag{5.74}$$

These identities, derived previously in the general framework, continue to hold across all (k_1, k_2) conversion systems. While the explicit form of the normalisation function $\mathcal{M}(|\chi|^2)$ varies with the specific model, the structural relationship between operator expectation values and its derivatives remains universal. In practical applications, it is often natural to specify a coherent state by its location on the classical phase space using the coordinates (ϕ, s_z), which have clear geometric and physical interpretation. For instance, when initialising a coherent state at a particular point for dynamical evolution, or when analysing the quantum-classical correspondence, we typically think in terms of these classical coordinates rather than the abstract coherent state parameter χ. However, given the polynomial form of $\mathcal{M}$, the relationships between χ and the classical coordinates are not analytically invertible. To address this challenge, we employ the following technique: we first calculate ϕ and s_z values for a comprehensive range of χ values using the expressions above. Then, when a coherent state centred at a specific point in the (ϕ, s_z) coordinate system is required, we numerically interpolate to determine the corresponding χ value. This approach effectively establishes the mapping between classical phase-space coordinates and the quantum coherent state parameter, enabling us to work naturally with physically meaningful coordinates while maintaining access to the full quantum formalism.

5.2.4 Classical Phase Space

We now proceed to find the classical phase space and the associated Poisson and metric brackets corresponding to our bosonic conversion system. The classical phase space is obtained by taking the classical limit of the generalised Bloch sphere in equation (5.21). Following this, we will introduce two additional convenient coordinate systems for the phase space. The first comprises the canonical coordinates, which provide a useful coordinate system for plotting Husimi distributions, as was the case for $\mathfrak{su}_2$. The second utilises a modified stereographic projection, which we derive a regularisation approach employed in [120]. This technique relates the (k_1, k_2) resonance to the standard 1:1 resonant case by establishing a coordinate transformation that regularises the singularities that arise in Kummer shapes, effectively providing a smooth mapping between the deformed phase space and the standard spherical geometry.

Recalling our definition of the classical phase space, $\mathcal{P}$, as an n-dimensional subspace of $\mathbb{R}^m$

defined by the image of the mapping

$$|\chi\rangle \mapsto \vec{x}(\chi) = (x_1(\chi), x_2(\chi), \ldots, x_m(\chi)) \,, \tag{5.75}$$

where each component is given by

$$x_i(\chi) = \lim_{\lambda\to\infty} \frac{1}{\lambda} \langle\chi| \hat{X}_i |\chi\rangle \,. \tag{5.76}$$

Thus, $\mathcal{P} = \{\vec{x}(\chi) \in \mathbb{R}^m : |\chi\rangle \in \mathcal{CS}\}$, where $\mathcal{CS}$ denotes the set of all coherent states of the system.

For the (k_1, k_2) bosonic conversion algebra, we have three generating operators $(\hat{K}_x, \hat{K}_y, \hat{K}_z)$ and one Casimir invariant, giving $m = 3$ and $n = 2$ respectively.

In the classical limit, the geometry of the phase space is governed by a constraint relation derived from the Casimir and algebraic structure of the quantum system. This was established in [70], which showed that the classical phase space is constrained to lie on a deformed two-dimensional surface in $\mathbb{R}^3$, known as a Kummer shape. Adapting this result to our coherent-state framework, we apply the factorisation property to determine the large-N limit of equation (5.21), yielding

$$\begin{aligned} &\lim_{N\to\infty} \eta^2 \left(\langle \hat{K}_z^2 \rangle + \langle \hat{K}_y^2 \rangle - \langle \hat{C} \rangle + \langle G\left(\hat{K}_z, \hat{N}\right) \rangle \right) \\ &\qquad = s_x^2 + s_y^2 - (1+s_z)^{k_1}(1-s_z)^{k_2}. \end{aligned} \tag{5.77}$$

This defines the classical constraint surface for the dynamics, generalising the unit sphere of the $\mathfrak{su}_2$ case to a broader class of algebraic geometries. Thus we arrive at the classical phase spaces as the Kummer shapes defined as

$$s_x^2 + s_y^2 = (1+s_z)^{k_1}(1-s_z)^{k_2}. \tag{5.78}$$

This surface is the classical phase space, which is a two-dimensional surface embedded in $\mathbb{R}^3$. The Kummer shapes are used to describe coupled oscillators of different frequencies and are orbifolds, that is they are manifolds everywhere except for isolated points, in our case these are at the north and south pole. In Figure 5.3 we plot some examples for a range of k_1, k_2, N. The classical phase space inherits a natural coordinate system from the quantum case, where the classical ϕ and s_z correspond to the limiting values of their quantum counterparts. These form a canonical coordinate system (ϕ, s_z) defined by

$$s_x = r(s_z)\cos(\phi), \qquad s_y = r(s_z)\sin(\phi), \tag{5.79}$$

where $r(s_z) = \sqrt{(1+s_z)^{k_1}(1-s_z)^{k_2}}$. In this coordinate system ϕ represents the azimuthal angle and the entire surface is parametrised by $\phi \in [0, 2\pi)$ and $s_z \in [-1, 1]$. As an example of the convergence of the quantum Kummer shapes, in Figure 5.4 we plot a cross-section of generalised Bloch spheres for a set of values of N alongside the classical counterpart's cross-section with $k_1 = 2, k_2 = 1$.

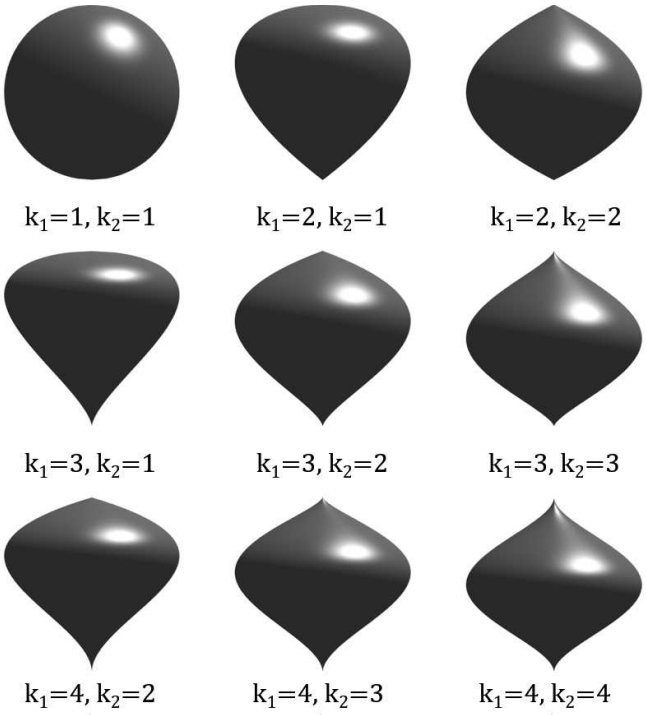


Figure 5.3: Selected classical phase- spaces, the classical Kummer shapes, with various values of k_1 and k_2

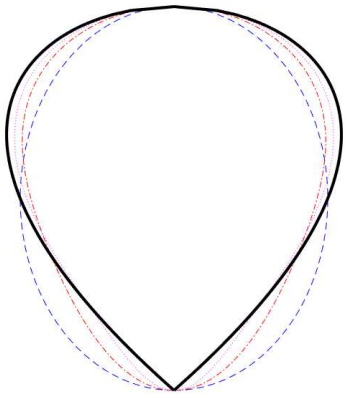


Figure 5.4: Scaled expectation values, $\eta \langle \hat{K}_x \rangle$ and $\eta \langle \hat{K}_z \rangle$ (horizontal and vertical axes, respectively), with $\langle \hat{K}_y \rangle = 0$. The cross-sections of the quantum phase spaces are shown for $N = 2$ (dashed blue line), $N = 4$ (dot-dashed red line), and $N = 8$ (dotted magenta line), alongside the classical phase-space limit (black line).

This convergence underscores the geometric consistency between quantum and classical phase spaces. However, to facilitate analytic calculations and visualisations, especially in cases where the phase space becomes sharply curved near the poles, we adopt a more regular coordinate description.

To this end, we now apply Ohsawa's regularisation technique [120], which provides a coordinate transformation from Kummer shapes to the unit sphere. Specifically, we define a coordinate transformation from the orbifold variables (s_x, s_y, s_z) to regularised spherical coordinates (x, y, z) as follows

$$x = \frac{s_x}{\left(\sqrt{1+s_z}\right)^{k_1-1}\left(\sqrt{1-s_z}\right)^{k_2-1}}, \tag{5.80}$$

$$y = \frac{s_y}{\left(\sqrt{1+s_z}\right)^{k_1-1}\left(\sqrt{1-s_z}\right)^{k_2-1}}, \tag{5.81}$$

$$z = s_z. \tag{5.82}$$

This transformation relates the $k_1 : k_2$ resonance with any $(k_1, k_2) \in \mathbb{N}^2$ to the $1 : 1$ resonant case, which corresponds to the standard spherical phase space associated with $\mathfrak{su}_2$ dynamics. Calculations verify that x, y, z satisfy $x^2+y^2+z^2 = 1$ and the Poisson bracket relations $\{x_i, x_j\} = \epsilon_{ijk}x_k$. The metric on the sphere is

$$\{\!\{x_i, x_j\}\!\} = \delta_{ij} - x_i x_j. \tag{5.83}$$

With this coordinate transformation established, we can now express the classical phase space in terms of a complex stereographic projection parameter $\zeta \in \mathbb{C}$

$$\zeta = \frac{x+iy}{1+z} \tag{5.84}$$

$$= \frac{s_x + is_y}{(1+s_z)^{\frac{k_1-1}{2}}(1-s_z)^{\frac{k_2-1}{2}}(1+s_z)} \tag{5.85}$$

It's important to note that, unlike in the $\mathfrak{su}_2$ case, the quantum and classical phase spaces here are distinct. Consequently, we conjecture that the stereographic projection parameter ζ and the coherent-state parameter χ are related as follows

$$\chi = \zeta \frac{(1+\zeta\zeta^*)^{\frac{k_1+k_2}{2}-1}}{2^{\frac{k_1+k_2}{2}-1}(\zeta\zeta^*)^{\frac{k_2-1}{2}}}. \tag{5.86}$$

Our initial calculations and numerical verification provide strong evidence supporting this relationship. However, a rigorous mathematical proof requires calculating the limit of $\frac{\mathcal{M}'}{\mathcal{M}}$ as $N \to \infty$, which presents significant technical challenges that we defer to future research. As can be seen, for the case $k_1 = k_2 = 1$, we recover $\chi = \zeta$.

Having established the classical phase space geometry, we now turn to deriving the associated bracket structures. For the Poisson bracket on the classical phase space, we recall that the required

condition is: the phase space is equipped with a Poisson bracket, and the following limit holds

$$\lim_{\lambda\to\infty} -\frac{\mathrm{i}}{\lambda}\langle\chi|\,[\hat{X}_i,\hat{X}_j]\,|\chi\rangle = \{x_i,x_j\}. \tag{5.87}$$

For the (k_1,k_2) system we recall the commutation relations from the background material,

$$[\hat{K}_x,\hat{K}_y] = \frac{i}{2}F\left(\hat{K}_z,\hat{N}\right), \tag{5.88}$$

$$[\hat{K}_y,\hat{K}_z] = i\hat{K}_x, \tag{5.89}$$

$$[\hat{K}_z,\hat{K}_x] = i\hat{K}_y. \tag{5.90}$$

Utilising the factorisation property and building upon the results from [70], we find the Poisson brackets on the classical phase-space. The detailed steps for taking the limit are omitted for brevity, but we establish

$$\lim_{N\to\infty}\eta[\hat{K}_x,\hat{K}_y] = \lim_{N\to\infty}\frac{\mathrm{i}\eta}{2}F\left(\hat{K}_z,\hat{N}\right) \tag{5.91}$$

$$= \frac{1}{2}(1+s_z)^{k_1-1}(1-s_z)^{k_2-1}(k_1(1-s_z)-k_2(1+s_z)), \tag{5.92}$$

thus yielding

$$\{s_x,s_y\} = \frac{1}{2}(1+s_z)^{k_1-1}(1-s_z)^{k_2-1}(k_1(1-s_z)-k_2(1+s_z)), \tag{5.93}$$

$$\{s_y,s_z\} = s_x, \tag{5.94}$$

$$\{s_z,s_x\} = s_y. \tag{5.95}$$

These expressions are consistent with those obtained from the coordinate transformation of the spherical Poisson brackets $\{x_i,x_j\} = \epsilon_{ijk}x_k$ using the Ohsawa regularisation technique, providing validation of our approach.

Similarly, the metric bracket is defined as

$$\lim_{\lambda\to\infty}\frac{1}{\lambda}\left(\langle\chi|\,[\hat{X}_i,\hat{X}_j]_+\,|\chi\rangle - 2\,\langle\chi|\,\hat{X}_i\,|\chi\rangle\,\langle\chi|\,\hat{X}_j\,|\chi\rangle\right) = \{\!\{x_i,x_j\}\!\}. \tag{5.96}$$

The conventional approach would require utilising $\mathcal{D}$-algebra to find an expression for the product terms in the left hand side of equation (5.96), which is a function of χ, change coordinates to the s_x,s_y,s_z and take the limit. In practice, unlike for $\mathfrak{su}_2$, the anti-commutator terms for the two-mode bosonic conversion systems do not have a convenient factorisation into operators. Thus this approach is algebraically cumbersome. Whilst the link between a quantum commutator and the symplectic form is deeply rooted in the algebra, the relationship between the anti-commutator and the metric structure on the quantum phase-space is more intricate and system specific.

To address this issue, we take an alternative approach and derive the metric bracket directly on the classical phase-space using the regularisation technique outlined above. Using the coordinate transform to the spherical coordinates x,y,z and then transforming back, we can derive the metric on the classical phase-space for the case $k_1,k_2>1$. Using this approach, we arrive at the complete

list of metric bracket components

$$\{\!\{s_x, s_x\}\!\} = \frac{1}{4\left(1-s_z^2\right)}\Big[4\left(1-s_z\right)^{k_2}\left(1+s_z\right)^{k_1} + s_x^2\left(-4+k_1^2\left(1-s_z\right)^2+k_2^2\left(1+s_z\right)^2+2k_1k_2\left(1-s_z^2\right)\right)\Big], \tag{5.97}$$

$$\{\!\{s_x, s_y\}\!\} = \frac{s_x s_y}{4\left(1-s_z^2\right)}\left[-4+k_1^2\left(1-s_z\right)^2+k_2^2\left(1+s_z\right)^2+2k_1k_2\left(1-s_z^2\right)\right], \tag{5.98}$$

$$\{\!\{s_x, s_z\}\!\} = \frac{s_x}{2}\left[k_1\left(1-s_z\right)-k_2\left(1+s_z\right)\right], \tag{5.99}$$

$$\{\!\{s_y, s_y\}\!\} = \frac{1}{4\left(1-s_z^2\right)}\Big[4\left(1-s_z\right)^{k_2}\left(1+s_z\right)^{k_1} + s_y^2\left(-4+k_1^2\left(1-s_z\right)^2+k_2^2\left(1+s_z\right)^2+2k_1k_2\left(1-s_z^2\right)\right)\Big], \tag{5.100}$$

$$\{\!\{s_y, s_z\}\!\} = \frac{s_y}{2}\left[k_1\left(1-s_z\right)-k_2\left(1+s_z\right)\right], \tag{5.101}$$

$$\{\!\{s_z, s_z\}\!\} = 1-s_z^2. \tag{5.102}$$

5.3 Phase-space approximation for the $(2,1)$ Bosonic Conversion System

In the preceding section, we established that the necessary properties for non-Hermitian coherent-state approximations are satisfied by the two-mode bosonic conversion system. Now, we will examine both the coherent-state approximation and the semiclassical Husimi approximation for the specific case where $(k_1, k_2) = (2, 1)$ across a range of illustrative Hamiltonians. Precursors of coherent-state approximations for Hermitian systems have been explored in Graefe et al. [70, 121].

Although the quantum and classical phase spaces are distinct surfaces, we can establish a one-to-one correspondence between them through the coordinate system (ϕ, s_z). This parameterisation uniquely identifies points on both spaces, creating a bijective mapping between them. It is important to note that for each (ϕ, s_z) coordinate pair, the values of s_x and s_y on the quantum phase space depend on N. To avoid ambiguity, we will use the (ϕ, s_z) coordinate system to label initial coherent states.

The natural surfaces for the quantum and semiclassical Husimi distributions are the quantum Kummer shapes, while classical dynamics naturally unfold on the classical Kummer shapes. This distinction presents us with two alternative approaches for performing semiclassical approximations. We could calculate classical trajectories on the quantum Kummer shape using the associated Poisson and metric brackets, and then project these trajectories onto the classical Kummer shape. Alternatively, we can compute classical trajectories on the classical Kummer shape and subsequently project these onto the quantum Kummer shape to perform the semiclassical Husimi approximation. We adopt the latter approach, as the formidable complexity of $\mathcal{M}$ as an $N/2$ order polynomial renders calculations in the χ variable analytically challenging, while the classical variables s_x, s_y, and s_z provide a more geometrically intuitive framework. Throughout our analysis, we will plot the quantum and semiclassical Husimi distributions on the quantum phase space while depicting coherent-state approximations on the classical phase space.

We shall analyse the resulting quantum-classical correspondence for several examples from the family of non-Hermitian Hamiltonians of the form

$$\hat{\mathcal{K}} = \nu \hat{K}_x + \frac{4g}{N}\hat{K}_z^2 + (\epsilon + \mathrm{i}\kappa)\hat{K}_z, \tag{5.103}$$

where $\nu, g, \epsilon, \kappa \in \mathbb{R}$. We will refer to this Hamiltonian as the $(2,1)$ Bose-Hubbard Hamiltonian, as it represents the bosonic conversion analog of the Bose-Hubbard model examined in Chapter 4. The non-closure of the commutation relations $[\hat{K}_x, \hat{K}_y]$ in this system leads to intriguing dynamical features not present in the $\mathfrak{su}_2$ case. A particularly significant consequence is that coherent states will not remain coherent even under a linear Hamiltonian (with the exception of Hamiltonians being proportional to $\hat{K}_z$).

For the case $(k_1, k_2) = (2, 1)$, substituting these values into the general expressions yields coherent states of the form

$$|\chi\rangle = \frac{1}{\sqrt{\mathcal{M}}} \sum_{n=0}^{\frac{N}{2}} \frac{\chi^n}{\sqrt{N^n (N-2n)! n!}} |N-2n, n\rangle\,, \tag{5.104}$$

with

$$\mathcal{M}(|\chi|^2) = \sum_{n=0}^{\frac{N}{2}} \frac{|\chi|^{2n}}{N^n (N-2n)! n!}. \tag{5.105}$$

The corresponding classical phase space is the (2,1) Kummer shape referred to as the teardrop, obtained from Eq. (5.78), and is given by the constraint

$$s_x^2 + s_y^2 = (1+s_z)^2(1-s_z), \tag{5.106}$$

which is depicted in the middle panel of the top row of Figure 5.3.

The Poisson brackets are explicitly given by

$$\{s_x, s_y\} = -\frac{1}{2}(1-3s_z)(1+s_z), \tag{5.107}$$
$$\{s_y, s_z\} = s_x, \tag{5.108}$$
$$\{s_z, s_x\} = s_y, \tag{5.109}$$

and the metric brackets are

$$\{\!\{s_x, s_x\}\!\} = (1+s_z) - \frac{3s_x^2(1+3s_z)}{4(1+s_z)}, \tag{5.110}$$
$$\{\!\{s_x, s_y\}\!\} = \frac{3s_x s_y(1+3s_z)}{4(1+s_z)}, \tag{5.111}$$
$$\{\!\{s_x, s_z\}\!\} = \frac{1}{2}s_x(1-3s_z), \tag{5.112}$$
$$\{\!\{s_y, s_y\}\!\} = (1+s_z) - \frac{3s_y^2(1+3s_z)}{4(1+s_z)}, \tag{5.113}$$
$$\{\!\{s_y, s_z\}\!\} = \frac{1}{2}s_y(1-3s_z), \tag{5.114}$$

$$\{\{s_z, s_z\}\} = 1 - s_z^2. \tag{5.115}$$

The classical counterpart of the Hamiltonian (5.103) is given by

$$\begin{aligned} k &= \lim_{N\to\infty} \eta \langle\chi| \hat{\mathcal{K}} |\chi\rangle, \\ &= \nu s_x + g s_z^2 + \epsilon s_z + \mathrm{i}\kappa s_z, \end{aligned} \tag{5.116}$$

where $\eta = \frac{4}{N}$ for the $(2,1)$ case.

5.3.1 Linear Hermitian Hamiltonian

As first examples we briefly discuss two linear Hermitian Hamiltonians, $\hat{\mathcal{H}} = \hat{K}_z$ and $\hat{\mathcal{H}} = \hat{K}_x$, respectively. The quantum-classical correspondence is exact for $\hat{\mathcal{H}} = \hat{K}_z$ but not for $\hat{\mathcal{H}} = \hat{K}_x$, highlighting the different dynamical behaviours in these seemingly simple systems.

Although the algebra is not a Lie algebra, the special case of a Hermitian Hamiltonian that is proportional to $\hat{K}_z$ result in equations of motion linear in the generators just as in $\mathfrak{su}_2$. As a result, the quantum and classical equations coincide. In this case the Heisenberg equations of motion simplify to

$$\frac{\mathrm{d}\hat{K}_x}{\mathrm{d}t} = -\hat{K}_y, \tag{5.117}$$

$$\frac{\mathrm{d}\hat{K}_y}{\mathrm{d}t} = \hat{K}_x, \tag{5.118}$$

$$\frac{\mathrm{d}\hat{K}_z}{\mathrm{d}t} = 0. \tag{5.119}$$

The resulting evolution corresponds to a rotation around the s_z-axis, with the coherent state preserving its coherence over the periodic time evolution. To illustrate the dynamics, in the left panel of Figure 5.5 the coherent-state trajectories and snapshots of the quantum Husimi are displayed for an initial coherent state centred at $(\phi, s_z) = (\frac{3\pi}{2}, 0)$ with $N = 40$.

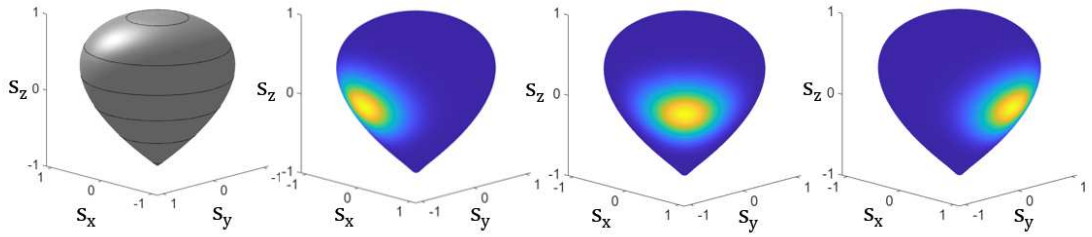


Figure 5.5: The linear Hamiltonian $\hat{\mathcal{H}} = \hat{K}_z$ with $N = 40$. left: phase-space trajectories plotted on the teardrop phase space. Middle left, middle right, right: evolution of the quantum Husimi distribution plotted on the teardrop at $t = 0, \frac{\pi}{4}$ and $\frac{\pi}{2}$ for an initial coherent state centred at $(\phi, s_z) = \left(\frac{3\pi}{2}, 0\right)$.

For the Hamiltonian $\hat{\mathcal{H}} = \hat{K}_x$, on the other hand, in stark contrast to the Lie algebraic case, the coherent state approximation is indeed only an approximation. The Heisenberg equations of

motion for the generating operators are given by

$$\frac{\mathrm{d}\hat{K}_x}{\mathrm{d}t} = 0, \tag{5.120}$$

$$\frac{\mathrm{d}\hat{K}_y}{\mathrm{d}t} = \frac{1}{2} + \frac{1}{8N}\left(\hat{N}^2 - 8\hat{K}_z\hat{N} - 48\hat{K}_z^2\right), \tag{5.121}$$

$$\frac{\mathrm{d}\hat{K}_z}{\mathrm{d}t} = \hat{K}_y. \tag{5.122}$$

From the classical Hamiltonian one finds the equations of motion for the coherent-state approximation as

$$\frac{\mathrm{d}s_x}{\mathrm{d}t} = 0, \tag{5.123}$$

$$\frac{\mathrm{d}s_y}{\mathrm{d}t} = \frac{1}{2}(1 - 3s_z)(1 + s_z), \tag{5.124}$$

$$\frac{\mathrm{d}s_z}{\mathrm{d}t} = s_y, \tag{5.125}$$

which coincide with the $N \to \infty$ limit of equations (5.120)-(5.122).

The dynamical equations (5.123)-(5.125) have three fixed points, two centres located at the eastern and western extremes,

$$(s_x, s_y, s_z) = \left(\frac{4\sqrt{2}}{3\sqrt{3}}, 0, \frac{1}{3}\right),$$

$$(s_x, s_y, s_z) = \left(-\frac{4\sqrt{2}}{3\sqrt{3}}, 0, \frac{1}{3}\right),$$

and a saddle point at the southern tip,

$$(s_x, s_y, s_z) = (0, 0, -1).$$

The velocity along the trajectory is given by

$$\left[(\dot{s_x})^2 + (\dot{s_y})^2 + (\dot{s_z})^2\right]^{\frac{1}{2}} = (1 + s_z)^2\left(\frac{5}{4} - \frac{5}{2}s_z + \frac{9}{4}s_z^2\right), \tag{5.126}$$

The system exhibits distinctive orbital behaviour in the (s_y, s_z) plane while maintaining constant s_x values. When the initial condition includes $s_x \neq 0$, we observe closed orbits whose frequencies depend on the magnitude of $|s_x|$. Specifically, orbits with larger $|s_x|$ values complete their cycles more rapidly and the angular velocity is not constant over time. This characteristic distinguishes our system from the standard $\mathfrak{su}_2$ case, where all trajectories maintain uniform frequency regardless of initial conditions. To illustrate the dynamics, in Figure 5.6 we present coherent-state trajectories (left panel), the eigenvalue of the spectrum of the Hamiltonian $\hat{\mathcal{H}} = \hat{K}_x$ (middle panel) and a comparison of $s_z(t)$ values between quantum dynamics, semi-classical dynamics and the coherent-state approximation (right panel). The spectrum offers insights into the structure of energy levels underlying the observed dynamics, while the s_z time series highlights the fidelity and limitations

of each approximation across different time scales.

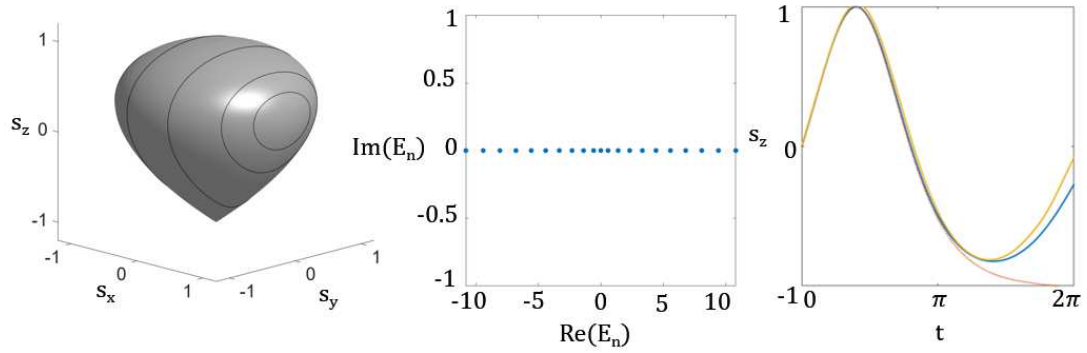


Figure 5.6: The linear Hamiltonian $\hat{\mathcal{H}} = \hat{K}_x$ with $N = 40$. Left: phase-space trajectories from the coherent-state approximation plotted on the teardrop phase space. Middle: the eigenvalue spectrum for the Hamiltonian. Right: comparison of values of s_z between quantum dynamics (solid blue line), semiclassical Husimi (solid yellow line) and the coherent-state approximation (dotted orange line) for an initial state centred at $(\phi, s_z) = (0, \frac{\pi}{2})$.

The $s_x = 0$ case reveals particularly interesting dynamics near the critical point at the southern tip where $s_z = -1$, which functions as a saddle point in the system. The trajectory behaviour bifurcates based on the sign of s_y

- When $s_y > 0$, trajectories experience a repulsive force from the saddle point, causing them to accelerate toward the north pole.
- When $s_y < 0$, trajectories are drawn toward the saddle point, with their velocity progressively decreasing as they approach this fixed point.

This creates a flow for the $s_x = 0$ case characterised by asymptotic convergence toward the saddle point, demonstrating the system's sensitivity to initial conditions and revealing the fundamental structure of its phase space.

Figure 5.7 shows snapshots of both quantum and semiclassical Husimi distributions for an initial coherent state is centred at $(\phi, s_z) = (\frac{\pi}{2}, 0)$ with $N = 40$. The quantum Husimi distribution follows an orbit with constant s_x, initially moving toward the north pole with minimal deformation. From $t = 0$ to $t = \pi$, the distribution traverses over the north pole, completing half of its periodic orbit. Between $t = \pi$ and $t = \frac{3\pi}{2}$, it moves across the south pole, which induces significant distortion in the state. The semiclassical Husimi distribution effectively approximates its quantum counterpart until the quantum state encounters the south pole, after which substantial deviation between the two approaches becomes evident at $t = 2\pi$.

The deviation between the semiclassical Husimi approximation and the quantum evolution stems from the classical dynamics around the saddle point. As the semiclassical Husimi is transported along coherent-state approximation trajectories, points with $s_x = 0$ approach the saddle point asymptotically, while the remaining points maintain periodic motion. Figure 5.8 depicts snapshots of the semiclassical Husimi distribution at times $t = \pi$ (left) and $t = \frac{3\pi}{2}$ (right), plotted on the teardrop phase-space with a viewing angle from the south. These images demonstrate how the

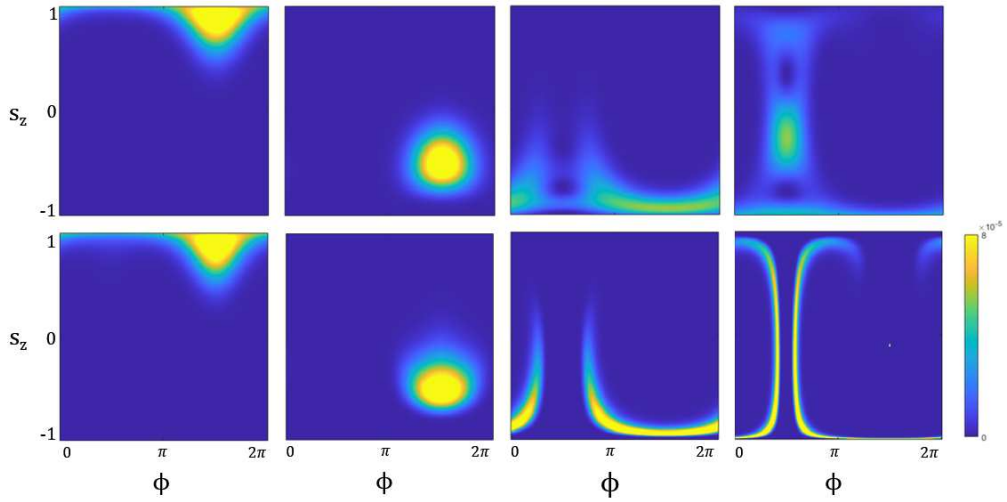


Figure 5.7: Evolution of the quantum Husimi distribution (top row) and the semiclassical Husimi distribution (bottom row) for the linear Hamiltonian $\hat{\mathcal{H}} = \hat{K}_x$ with $N = 40$ for an initial coherent state centred at $(\phi, s_z) = (\frac{\pi}{2}, 0)$. The columns correspond to different snapshots of the evolution in time with $t = \frac{\pi}{2}$ (left), $t = \pi$ (middle left), $t = \frac{3\pi}{2}$ (middle right) and $t = t = 2\pi$ (right).

semiclassical Husimi distribution becomes distorted around the saddle point. In contrast, the quantum Husimi distribution is plotted on quantum phase-spaces, which are smooth manifolds lacking the sharp tip at the south pole that generates this interesting semiclassical effect.

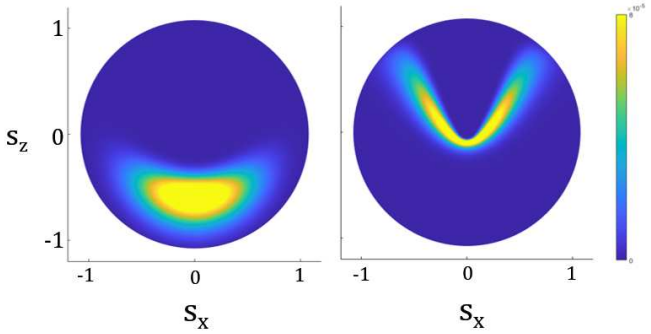


Figure 5.8: Evolution of the quantum Husimi distribution for the linear Hamiltonian. $\hat{\mathcal{H}} = \hat{K}_x$ with $N = 40$, for an initial coherent state centred at $(\phi, s_z) = (\frac{\pi}{2}, 0)$ at $t = \pi$ (left) and at $t = \frac{3\pi}{2}$ (right).

To illustrate further the effect of the deformation from the south pole, in Figure 5.9 we display snapshots of the initial quantum Husimi distribution (left), the quantum Husimi distribution at $t = 2\pi$ (middle) and the semiclassical Husimi distribution at $t = 2\pi$ (right).

In summary, we observe that the $(2, 1)$ bosonic conversion system exhibits more nuanced dynamics than standard $\mathfrak{su}_2$ systems when terms s_x and s_y are included in linear Hamiltonians. Furthermore, the semiclassical Husimi distribution approximation deviates significantly from the quantum evolution when the dynamics encounter the southern pole, highlighting the limitations of semiclassical approaches in regions with singular classical behaviour.

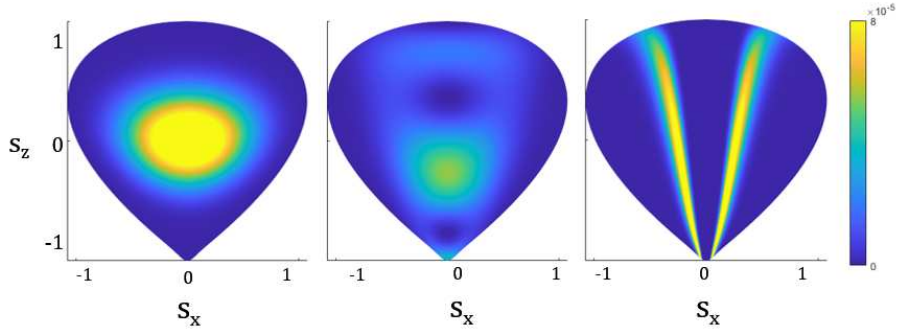


Figure 5.9: The linear Hamiltonian, $\hat{\mathcal{H}} = \hat{K}_x$, with $N = 40$, for an initial coherent state centred at $(\phi, s_z) = (\frac{\pi}{2}, 0)$. Left: the normalised quantum Husimi distributions at $t = 0$. Middle: the normalised quantum Husimi distribution at $t = 2\pi$. Right: the normalised semiclassical Husimi distribution at $t = 2\pi$

5.3.2 Linear non-Hermitian Hamiltonian

We now consider the linear non-Hermitian Hamiltonian

$$\hat{\mathcal{K}} = \mathrm{i}\hat{K}_z. \tag{5.127}$$

The eigenstates for this system are the basis vectors $|N - 2n, n\rangle$, with corresponding complex eigenenergies $E_n = \mathrm{i}(\frac{N}{4} - n)$. Thus the dominant eigenstate is $|\frac{N}{2}, 0\rangle$. The quantum dynamics result in a coherent state remaining coherent. For an initial coherent state, $|\psi(0)\rangle = |\chi_c\rangle$ the solution to the time-dependent Schrödinger equation is given by

$$|\psi(t)\rangle = \frac{e^{\frac{Nt}{4}}\mathcal{M}(|\chi_c(t)|^2)}{\mathcal{M}(|\chi_c|^2)}\,|\chi_c(t)\rangle\,, \tag{5.128}$$

with

$$\chi_c(t) = \chi_c e^{-t}. \tag{5.129}$$

Thus in the case $\kappa > 0$ the quantum evolution consists of an initial coherent state moving along a line of longitude from the initial point to the north pole of the quantum phase space with the norm growing at an exponential rate. In the case $\kappa < 0$ an initial coherent state moves in the reverse direction along the line of longitude towards the south pole.

This Hamilton presents a rare case in which we can calculate the coherent state dynamics using the Poisson bracket on the quantum phase space. Whilst this is a short departure from our framework of calculating classical motion on the classical phase space, we include this for illustrative purposes.

The classical counterpart to Hamiltonian is

$$k = 1 - \frac{\eta\chi\chi^*\mathcal{M}'}{N\mathcal{M}}. \tag{5.130}$$

Thus we have the classical equation of motion

$$\begin{aligned}\frac{\mathrm{d}\chi}{\mathrm{d}t} &= \{\!\{\chi, k\}\!\}, \\ &= -\frac{\eta\chi}{N}\left(\{\!\{\chi,\chi^*\}\!\}\frac{\mathcal{M}'}{\mathcal{M}} + \{\!\{\chi,\mathcal{M}'\}\!\}\frac{\chi^*}{\mathcal{M}} + \{\!\{\chi,\frac{1}{\mathcal{M}}\}\!\}\chi\mathcal{M}'\right), \\ &= -\chi\eta\{\!\{\chi,\chi^*\}\!\}\left(\frac{\mathcal{M}'}{N\mathcal{M}} + \frac{\chi\chi^*}{N^2}\left(\frac{\mathcal{M}'^2}{\mathcal{M}^2} - \frac{\mathcal{M}''}{\mathcal{M}}\right)\right) \\ &= -\chi, \end{aligned} \tag{5.131}$$

the solution to which aligns with equation (5.129) demonstrating the the quantum-classical correspondence is exact for this case if we consider classical trajectories on the quantum Kummer shape. As this calculation is performed on the quantum Kummer shape, we refer to the solution to this equation as the 'finite-N' coherent-state trajectory.

We now turn our attention to the corresponding coherent-state approximation which is governed by the equation

$$\begin{aligned}\frac{\mathrm{d}s_x}{\mathrm{d}t} &= \{\!\{s_x, s_z\}\!\}, \\ &= \frac{s_x}{2}(1-3s_z), \end{aligned} \tag{5.132}$$

$$\begin{aligned}\frac{\mathrm{d}s_y}{\mathrm{d}t} &= \{\!\{s_y, s_z\}\!\}, \\ &= \frac{s_y}{2}(1-3s_z), \end{aligned} \tag{5.133}$$

$$\begin{aligned}\frac{\mathrm{d}s_z}{\mathrm{d}t} &= \{\!\{s_z, s_z\}\!\}, \\ &= (1-s_z^2). \end{aligned} \tag{5.134}$$

The resulting coherent-state approximation trajectories also consist of longitudinal motion to the north pole on the classical phase space as depicted in the left panel of Figure 5.10. The coherent-state approximation trajectories are driven by the metric which is derived via the coordinate transform from the sphere to the teardrop. Thus the metric arises from the $N \to \infty$ limit and so in the finite N case whilst a coherent state remains coherent, the quantum and classical phase-space trajectories do not correspond due to the differences in respective phase spaces and assumptions on N when computing the metric.

In the right panel of Figure 5.10 we plot a comparison between the expectation values of the scaled operator $s_z = \eta\langle\hat{K}_z\rangle$ (solid blue line), the coherent-state approximation for s_z (dotted orange line) and the semiclassical Husimi approximation (solid yellow line) for an initial coherent state located at $(\phi, s_z) = (0, -0.5)$, with $N = 40$. The k^* trajectories consist of the longitudinal trajectories to the south pole of the classical phase space.

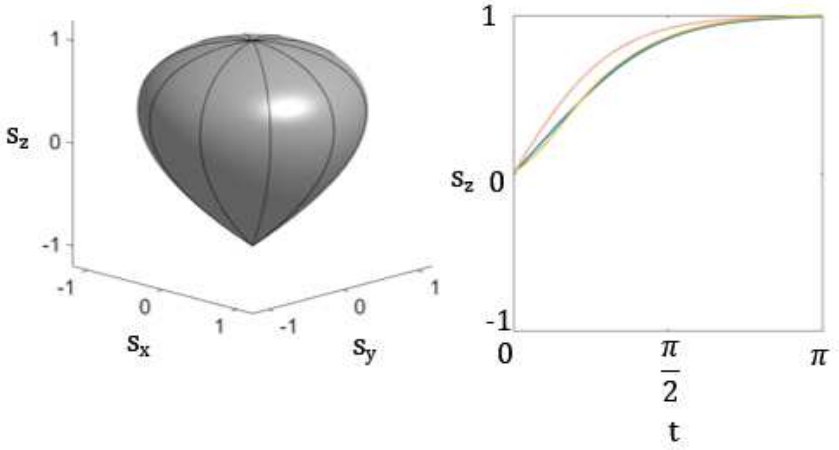


Figure 5.10: The linear non-Hermitian Hamiltonian, $\hat{\mathcal{K}} = i\hat{K}_z$, with $N = 40$. Left: Phase-space trajectories from the coherent-state approximation plotted on the teardrop phase space. Right: Comparison of values of s_z between quantum dynamics (solid blue line), semiclassical Husimi (solid yellow line) and the coherent-state approximation (dotted orange line) for an initial state centred at $(\phi, s_z) = (\frac{\pi}{2}, 0)$.

5.3.3 $(2, 1)$ 2-mode Bose-Hubbard Model Hamiltonian

As a nonlinear Hermitian example we will consider a modified version of the two mode Bose-Hubbard Hamiltonian,

$$\hat{\mathcal{H}} = \nu\hat{K}_x + \frac{4g}{N}\hat{K}_z^2, \tag{5.135}$$

As with the analogous $\mathfrak{su}_2$ Hamiltonian, the quantum evolution of a state is a combination of a rotation around the s_x-axis and a nonlinear shearing motion around the s_z-axis.

Using the coherent-state approximation, one finds the classical counterpart of the Hamiltonian as

$$h = \nu s_x + g s_z^2. \tag{5.136}$$

The resulting equations of motion for the coherent-state approximation are

$$\frac{\mathrm{d}s_x}{\mathrm{d}t} = -2g s_y s_z, \tag{5.137}$$

$$\frac{\mathrm{d}s_y}{\mathrm{d}t} = \frac{\nu}{2}(1 - 3s_z)(1 + s_z) + 2g s_x s_z, \tag{5.138}$$

$$\frac{\mathrm{d}s_z}{\mathrm{d}t} = \nu s_y. \tag{5.139}$$

To find the fixed points we first note that equation (5.139) requires $s_y = 0$, which also results equation (5.137) being equal to zero. To solve equation (5.138) we recall the constraint equation (5.3), which with $s_y = 0$ reduces to

$$s_x^2 = (1 + s_z)^2(1 - s_z). \tag{5.140}$$

Substituting the square root of (5.140) into equation (5.138) we obtain

$$\frac{\nu}{2}(1-3s_z)(1+s_z)+2gs_z(1+s_z)\sqrt{(1-s_z)}=0, \tag{5.141}$$

which is satisfied by $s_z=-1$. Dividing equation (5.141) by $(1+s_z)$ and then squaring the obtain a cubic equation in s_z,

$$\frac{\nu^2}{4}(1-3s_z)^2-4g^2(1-s_z)=0, \tag{5.142}$$

that is,

$$16g^2s_z^3+(9\nu^2-16g^2)s_z^2-6\nu^2s_z+\nu^2=0. \tag{5.143}$$

Thus there will always be a fixed point located at $s_z=-1$ with an additional one, two or three fixed points determined by the solution of the cubic equation (5.143).

As a first case, let us isolate the effect of $\hat{K}_z^2$ by setting $\nu=0, g=10$ with $N=40$ resulting in the Hamiltonian $\hat{\mathcal{H}}=\hat{K}_z^2$ which has the same periodicity as the Kerr Hamiltonian and the 2-mode Bose-Hubbard $\mathfrak{su}_2$ Hamiltonian. As explored in the research by Milburn, the Kerr Hamiltonian for longer times results in the evolution of an initial coherent state to the superposition of four coherent states, then two coherent states and finally the periodic evolution to the initial coherent state [66] with analogous results for $\mathfrak{su}_2$ [105]. Interestingly, for this case the four coherent-state super position which appears in the Kerr Hamiltonian and the 2-mode Bose-Hubbard model does not appear, as shown in the left panel of Figure 5.11 which depicts a snapshot of the quantum Husimi distribution at time $t=\frac{\pi}{2}$. However the two coherent state superposition and the reformation of the initial state are maintained as shown in the middle and right panel of the same figure which depicts the respective snapshots at $t=\pi$ and $t=2\pi$.

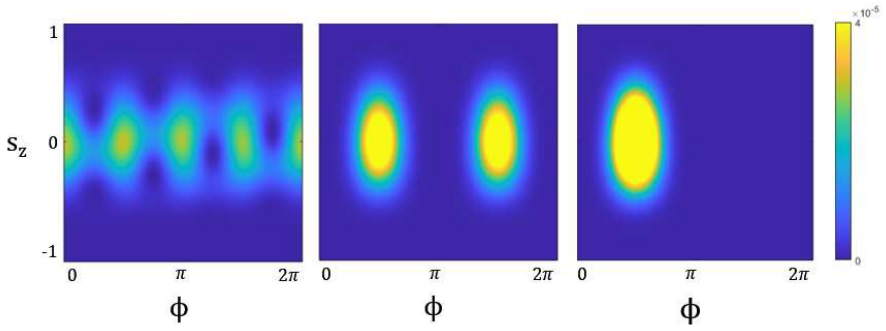


Figure 5.11: Evolution of the quantum Husimi distribution for the non-linear Hamiltonian, $\hat{\mathcal{H}}=\hat{K}_z^2$, with $N=40$ for an initial coherent state centred at $(\phi,s_z)=(\frac{\pi}{2},0)$ at $t=\frac{\pi}{2}$ (left), $t=\pi$ (middle) and $t=2\pi$ (right)

We now examine the case where $\nu=\frac{1}{2}$, $g=2$, and $N=40$. By numerically solving the cubic equation in s_z from equation (5.143), we determine that the coherent-state approximation

trajectories exhibit four distinct fixed points on the teardrop located at:

$$\text{1. saddle point: } (0.9599, 0, -0.0736)\,, \tag{5.144}$$

$$\text{2. centre: } (-1.0251, 0, 0.0539)\,, \tag{5.145}$$

$$\text{3. centre: } (0.2461, 0, 0.9846)\,, \tag{5.146}$$

$$\text{4. centre: } (0, 0, -1)\,, \tag{5.147}$$

where we have expressed the fixed points in terms of s_x, s_y, s_z.

An interesting feature of the dynamics of this system, in comparison to the equivalent $\mathfrak{su}_2$ system, is the breakdown in symmetry. For the $\mathfrak{su}_2$ system, symmetry exists in the plane $s_z = 0$, resulting in a paired set of centres. In contrast, for the $(2, 1)$ bosonic conversion system, this symmetry no longer holds. While the north center still exists, the south center has relocated to the southern tip of the teardrop.

The resulting coherent-state approximation trajectories are depicted in Figure 5.12 for both the canonical (left) and the teardrop (right) phase spaces.

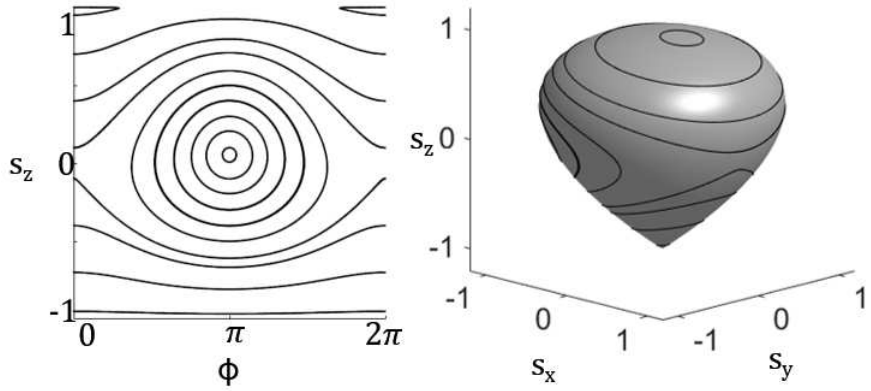


Figure 5.12: Phase-space trajectories from the coherent-state approximation for the $(2, 1)$ 2 mode Bose-Hubbard Hamiltonian, $\hat{\mathcal{H}} = \nu\hat{K}_x + \frac{4g}{N}\hat{K}_z^2$, with $\nu = \frac{1}{2}, g = 2$ and $N = 40$. The trajectories are shown on the canonical (left) and teardrop (right) phase spaces.

To analyse the semiclassical dynamics within the bosonic conversion systems, we now examine the time evolution of selected initial coherent states. This approach follows the methodology established in previous chapters. In Chapter 2, we studied initial coherent states centred near classical fixed points in the Kerr system and observed a characteristic sequence of quantum deformation followed by revival. A similar pattern emerged in Chapter 4 for the two-mode Bose–Hubbard model, where coherent states near stable centres exhibited comparable behaviour.

Additionally, in Section 4.1.4, we explored an initial coherent state located near the north pole (a classical centre) of the Bose–Hubbard system and observed a tunnelling-like transition between the north and south poles. Motivated by these earlier findings, we now investigate analogous dynamics in the $(k_1, k_2) = (2, 1)$ bosonic conversion system. Specifically, we initialise coherent states near classical centres and examine whether similar features, such as deformation, tunnelling,

and revival, persist in this more general algebraic setting.

Case 1: Initial Coherent State located near fixed point 2. In this example, we consider the dynamics for an initial coherent state located at $(\phi, s_z) = (\frac{\pi}{2}, 0)$ which is near to fixed point 2. The coherent-state approximation oscillates around fixed point, as expected, whilst the full quantum evolution experiences the same breakdown and revival as witness for the Hermitian Kerr system and 2-mode Bose-Hubbard model as can be seen in Figure 5.13 which depicts the scaled expectation values of s_z for quantum evolution (solid blue line), the coherent-state approximation (dotted orange line) and the semiclassical Husimi dynamics (solid yellow line). In Figure 5.14

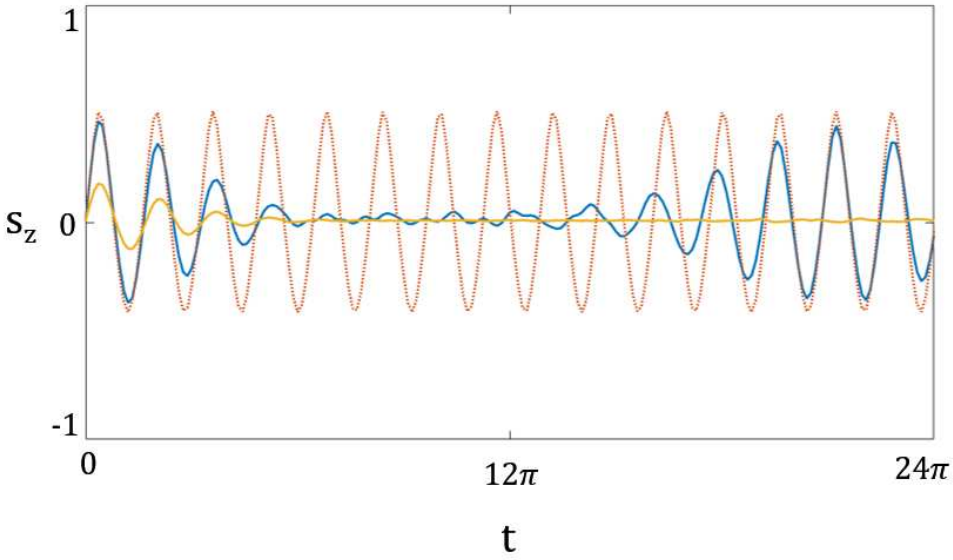


Figure 5.13: Comparison of values of s_z between quantum dynamics (solid blue line), semiclassical Husimi (solid yellow line) and the coherent-state approximation (dotted orange line) for the $(2, 1)$ Bose-Hubbard Hamiltonian, $\hat{\mathcal{H}} = \nu\hat{K}_x + \frac{4g}{N}\hat{K}_z^2$, with $\nu = 1, g = 1, \kappa = \frac{1}{4}$ and $N = 40$, for an initial coherent state at $(\phi, s_z) = \left(\frac{3\pi}{4}, 0\right)$.

we display snapshots of the Husimi distribution of the full quantum dynamics (top row) and the semiclassical Husimi distribution (bottom row) for short times. As with the Kerr Hamiltonian and the 2-mode Bose-Hubbard systems, the semiclassical Husimi approximation approach provides a good approximations in the short term. We observe the same phenomena of the semiclassical Husimi creating increasingly fine structures over time which are not apparent in the quantum evolution. In Figure 5.15 we depict the quantum Husimi distribution for longer times, we observe that the quantum state exhibits "holes" at times $t = \frac{5\pi}{2}$ (left) and $t = 5\pi$ (middle) and quantum revival at $t = 10\pi$. We would expect the semiclassical Husimi to continue to be transported along the coherent-state approximation trajectories with increasing fine structures, which is orbifold equivalent of the 'whorling' observed by Milburn for the anharmonic Kerr oscillator.

To conclude, our analysis of this initial coherent state reveals phenomena similar to those observed in the Kerr anharmonic oscillator and the 2-mode Bose-Hubbard model. Specifically, we observe quantum deformation followed by revival, with the coherent-state approximation providing accurate predictions for short-time dynamics while diverging over longer timescales. The

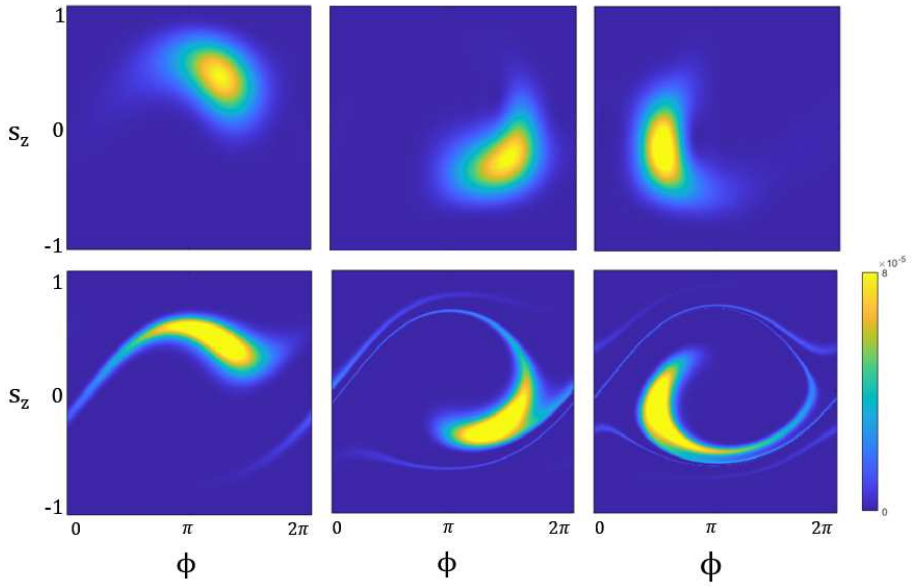


Figure 5.14: Evolution of the quantum Husimi distribution (top row) and the semiclassical Husimi distribution (bottom row) for the $(2,1)$ Bose-Hubbard Hamiltonian, $\hat{\mathcal{H}} = \nu\hat{K}_x + \frac{4g}{N}\hat{K}_z^2$, with $\nu = \frac{1}{2}, g = 2$ and $N = 40$, for an initial coherent state centred at $(\phi, s_z) = (\frac{\pi}{2}, 0)$. The columns correspond to different snapshots of the evolution in time with $t = \frac{\pi}{2}$ (left), $t = \pi$ (middle) and $t = \frac{3\pi}{2}$ (right).

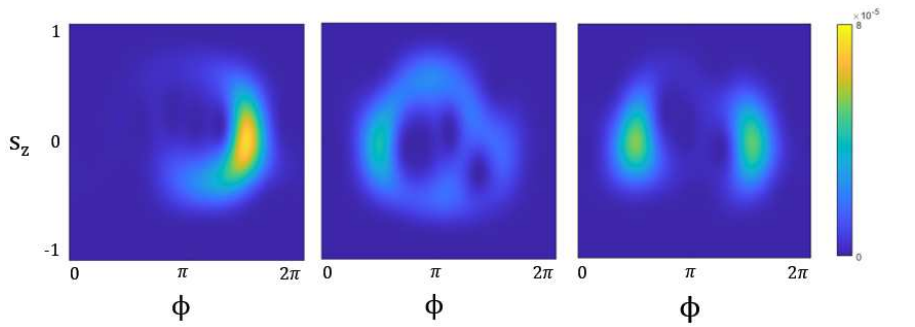


Figure 5.15: Evolution of the quantum Husimi distribution for the $(2,1)$ Bose-Hubbard Hamiltonian, $\hat{\mathcal{H}} = \nu\hat{K}_x + \frac{4g}{N}\hat{K}_z^2$, with $\nu = \frac{1}{2}, g = 2$ and $N = 40$, for an initial coherent state centred at $(\phi, s_z) = (\frac{\pi}{2}, 0)$ at times $t = \frac{5\pi}{2}$ (left), $t = 5\pi$ (middle) and $t = 10\pi$ (right).

semiclassical Husimi approximation approach successfully captures the initial quantum evolution before developing increasingly fine structures which are inconsistent with the quantum evolution.

Case 2: Initial Coherent State near fixed point 3. In this example, we examine the dynamics for an initial coherent state located at $(\phi, s_z) = (0, 0.85)$, which is in proximity to fixed point 3. Unlike the $\mathfrak{su}_2$ case, where we observed tunnelling between the north and south fixed points, the $(2, 1)$ bosonic conversion system exhibits no such quantum tunnelling. Instead, the quantum evolution demonstrates oscillatory motion around the fixed point, characterised by initial deformation followed by revival, as illustrated in Figure 5.16. This figure presents the scaled expectation values of s_z for quantum evolution (solid blue line), the coherent-state approximation (dotted orange line), and the semiclassical Husimi dynamics (solid yellow line).

The dynamics for this case exhibit features remarkably similar to those observed in case 1, as demonstrated in figures 5.17 and 5.18, which display snapshots of the quantum and semiclassical Husimi distributions for short and extended time periods, respectively. The quantum Husimi distribution clearly undergoes revival, while the semiclassical Husimi distribution progressively develops increasingly fine structures. This difference highlights the fundamental distinction between quantum evolution, which preserves coherence and enables revival, and semiclassical approximations, which are unable to capture these quintessentially quantum mechanical phenomena.

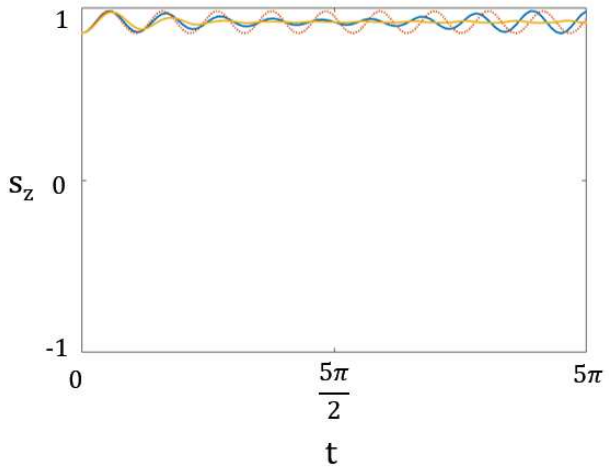


Figure 5.16: Comparison of values of s_z between quantum dynamics (solid blue line), semiclassical Husimi (solid yellow line) and the coherent-state approximation (dotted orange line) for the $(2, 1)$ Bose-Hubbard Hamiltonian, $\hat{\mathcal{H}} = \nu\hat{K}_x + \frac{4g}{N}\hat{K}_z^2$, with $\nu = \frac{1}{2}, g = 2$ and $N = 40$, for an initial state centred at $(\phi, s_z) = (0, 0.85)$.

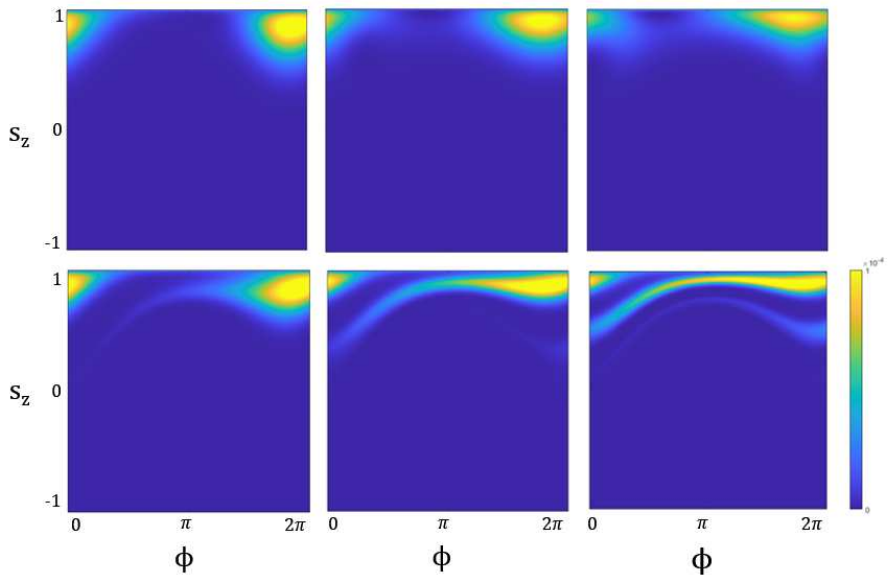


Figure 5.17: Evolution of the quantum Husimi distribution (top row) and the semiclassical Husimi distribution (bottom row) for the $(2,1)$ Bose-Hubbard Hamiltonian, $\hat{\mathcal{H}} = \nu\hat{K}_x + \frac{4g}{N}\hat{K}_z^2$, with $\nu = \frac{1}{2}, g = 2$ and $N = 40$, for an initial coherent state centred at $(\phi, s_z) = (0, 0.85)$. The columns correspond to different snapshots of the evolution in time with $t = \frac{\pi}{2}$ (left), $t = \pi$ (middle) and $t = \frac{3\pi}{2}$ (right).

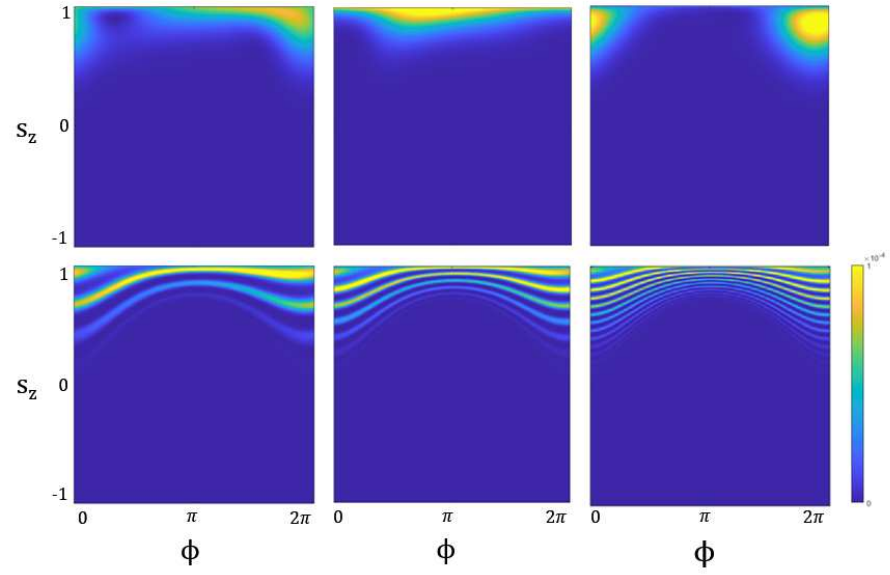


Figure 5.18: Evolution of the quantum Husimi distribution (top row) and the semiclassical Husimi distribution (bottom row) for the $(2,1)$ Bose-Hubbard Hamiltonian, $\hat{\mathcal{H}} = \nu\hat{K}_x + \frac{4g}{N}\hat{K}_z^2$, with $\nu = \frac{1}{2}, g = 2$ and $N = 40$, for an initial coherent state centred at $(\phi, s_z) = (0, 0.85)$. The columns correspond to different snapshots of the evolution in time with $t = \frac{5\pi}{2}$ (left), $t = 5\pi$ (middle) and $t = 10\pi$ (right).

5.3.4 $(2,1)$ 2-mode non-Hermitian Bose-Hubbard Hamiltonian

We now consider a non-Hermitian version of $(2,1)$ Bose-Hubbard model by introducing the term $i\kappa\hat{K}_z$, from a physical perspective this term models balanced gain of bosons in mode 1 with loss of bosons in mode 2. The resulting Hamiltonian is given by

$$\hat{\mathcal{K}} = \nu\hat{K}_x + \frac{4g}{N}\hat{K}_z^2 + \mathrm{i}\kappa\hat{K}_z. \tag{5.148}$$

In contrast to the corresponding $\mathfrak{su}_2$ Hamiltonian, this does not exhibit PT-symmetry with respect to the parity transformation $\hat{K}_x \to -\hat{K}_x, \hat{K}_y \to \hat{K}_y, \hat{K}_z \to \hat{K}_z$. In the left panel of Figure 5.19 the eigenvalue spectrum have been plotted for the case $\nu = \frac{1}{2}, g = 2, \kappa = \frac{1}{5}$ with $N = 40$, for which all of the eigenvalues are complex-valued. In the right panel of Figure 5.19 we depict the Husimi distribution for the dominant eigenstate. The corresponding classical Hamiltonian is given

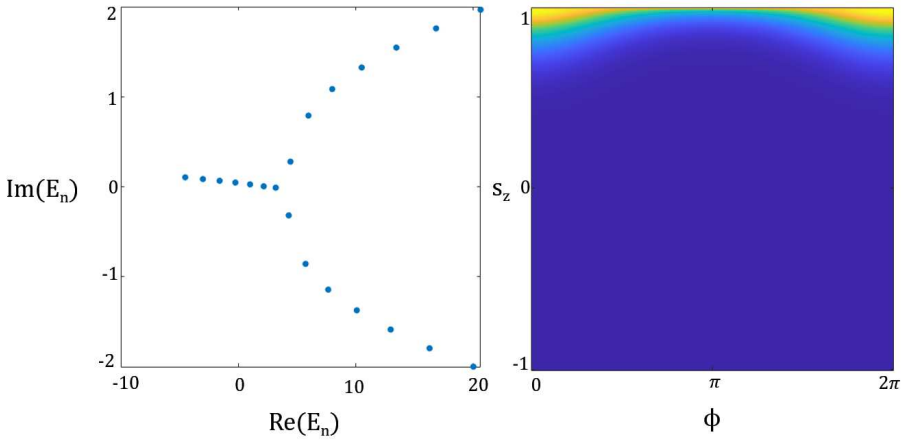


Figure 5.19: The non-Hermitian $(2,1)$ Bose-Hubbard Hamiltonian with $\nu = \frac{1}{2}, g = 2, \kappa = \frac{1}{5}$ and $N = 40$. Left: The eigenvalue spectrum for the Hamiltonian. Right: the Husimi distribution of the dominant eigenstate.

$$k = \nu s_x + g s_z^2 + \mathrm{i}\kappa s_z, \tag{5.149}$$

with the equations of motion for the coherent-state approximation as

$$\frac{\mathrm{d}s_x}{\mathrm{d}t} = -2g s_y s_z + \frac{\kappa}{2}s_x(1-3s_z), \tag{5.150}$$

$$\frac{\mathrm{d}s_y}{\mathrm{d}t} = \frac{\nu}{2}(1-3s_z)(1+s_z) + 2g s_x s_z + \frac{\kappa}{2}s_y(1-3s_z), \tag{5.151}$$

$$\frac{\mathrm{d}s_z}{\mathrm{d}t} = \nu s_y + \kappa(1-s_z^2). \tag{5.152}$$

Through numerical analysis, we have identified and characterised the fixed points of the system. Our investigation reveals three distinct regimes:

1. When $\kappa > \nu$: Two fixed points emerge, a stable spiral and a source located at the southern tip.

2. When $\kappa < \nu$ with large g: Four fixed points manifest, two stable spirals, a saddle point, and

an unstable spiral at the southern tip. Notably, the three-dimensional fixed point analysis reveals that these points, which appear stable in the two-dimensional analysis, exhibit saddle-like behaviour in the full three-dimensional phase space when subjected to small deviations from the surface.

3. When $\kappa < \nu$ with small g: Three fixed points emerge, a stable spiral, a saddle with inward spiral dynamics, and a bifurcated source/saddle at the tip.

The coherent-state approximation trajectories for the $\mathfrak{su}_2$ non-Hermitian Bose-Hubbard system also contains a three fixed-point regimes as discussed in Chapter 4 Section 4.1.4. However, unlike the $\mathfrak{su}_2$ case, the coherent-state approximation dynamics here exhibit no completely stable fixed points in any regime.

To investigate the dynamics further, we study the case $\nu = \frac{1}{2}, g = 2, \kappa = \frac{1}{5}$ for which we have numerically found the fixed points as

$$\text{1. stable spiral: } (-0.9915, -0.3298, 0.1036)\,, \tag{5.153}$$

$$\text{2. saddle: } (0.8118, -0.3193, -0.2055)\,, \tag{5.154}$$

$$\text{3. stable spiral: } (0.5451, -0.0521, 0.9185)\,, \tag{5.155}$$

$$\text{4. unstable spiral: } (0, 0, -1)\,, \tag{5.156}$$

where we have expressed the fixed points in terms of s_x, s_y, s_z. In Figure 5.20 we display the coherent-state approximation trajectories for a range of initial values on the canonical phase space.

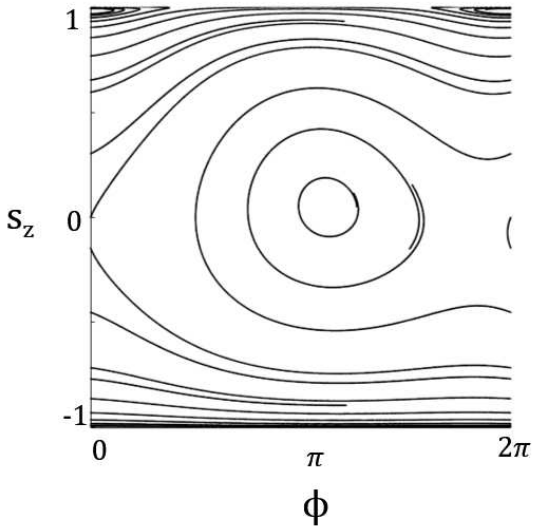
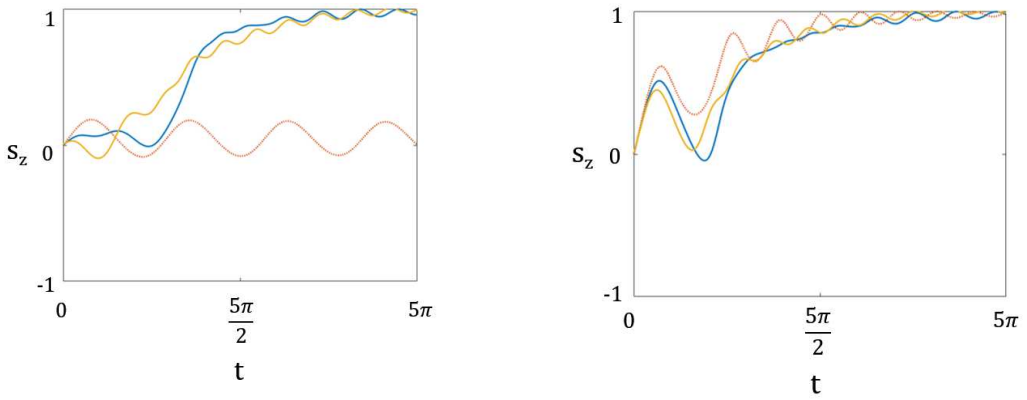


Figure 5.20: Phase-space trajectories from the coherent-state approximation for the non-Hermitian $(2, 1)$ Bose-Hubbard Hamiltonian with $\nu = \frac{1}{2}, g = 2, \kappa = \frac{1}{5}$.

Notably, fixed point 1 exhibits characteristics of a stable spiral but with an extremely slow rate of spiralling. As a result, a coherent state within the basin of attraction of this point performs persistent oscillations around the fixed point with very gradual decay in amplitude. This contrasts

sharply with the quantum dynamics, which are driven by evolution toward the dominant eigenstate, as demonstrated in the left panel of Figure 5.21, which depicts the scaled expectation values of s_z for quantum evolution (blue solid line), the coherent-state approximation (orange dashed-dot line) and the semiclassical Husimi dynamics (solid yellow line) for an initial coherent state centred at $(\phi, s_z) = (\pi, 0)$. Whilst in the right panel of Figure 5.21 we consider an initial coherent state centred at $(\phi, s_z) = (\frac{\pi}{2}, 0)$ which is outside the basin of attraction of fixed point 1 and thus converges to fixed point 3, the stable spiral located near the north pole.



(a) Initial state centred at $(\phi, s_z) = (\pi, 0)$

(b) Initial state centred at $(\phi, s_z) = (\frac{\pi}{2}, 0)$

Figure 5.21: Comparison of values of s_z between quantum dynamics (solid blue line), semiclassical Husimi (solid yellow line) and the coherent-state approximation (dotted orange line) for the non-Hermitian $(2, 1)$ Bose-Hubbard Hamiltonian with $\nu = \frac{1}{2}, g = 2, \kappa = \frac{1}{5}$ and $N = 40$ for two initial coherent states.

In Figure 5.22 we depict snapshots of the semiclassical and quantum normalised Husimi distributions, and the norm landscape at selected times for an initial coherent state centred at $(\phi, s_z) = (\frac{\pi}{2}, 0)$. Similar to the Hermitian $(2, 1)$ Bose-Hubbard system, both the semiclassical and quantum Husimi distributions initially evolve in comparable ways, exhibiting clockwise rotation and deformation up to $t = \frac{\pi}{2}$. By $t = \pi$, quantum effects become apparent with the emergence of holes in the quantum Husimi distribution. Concurrently, the semiclassical Husimi distribution splits along k^* trajectories due to the influence of two stable spiral fixed points. During this phase, the norm landscape begins to intensify in the northern region, though not yet strongly enough to dominate the dynamics. At $t = \frac{3\pi}{2}$, the norm landscape exerts a more significant influence, causing the portion of the semiclassical Husimi distribution near fixed point 3 to exceed that near fixed point 1. The quantum state at this time displays further quantum-specific phenomena, including reinforcement patterns and delocalisation across the phase space. The norm landscape (bottom row) exhibits an interesting feature, in regions near fixed point 1 where the basin of attraction results in stable orbits, the norm landscape remains relatively constant, whereas outside this basin—particularly near fixed point 3, the norm landscape grows exponentially over time, eventually dominating the long-term dynamics.

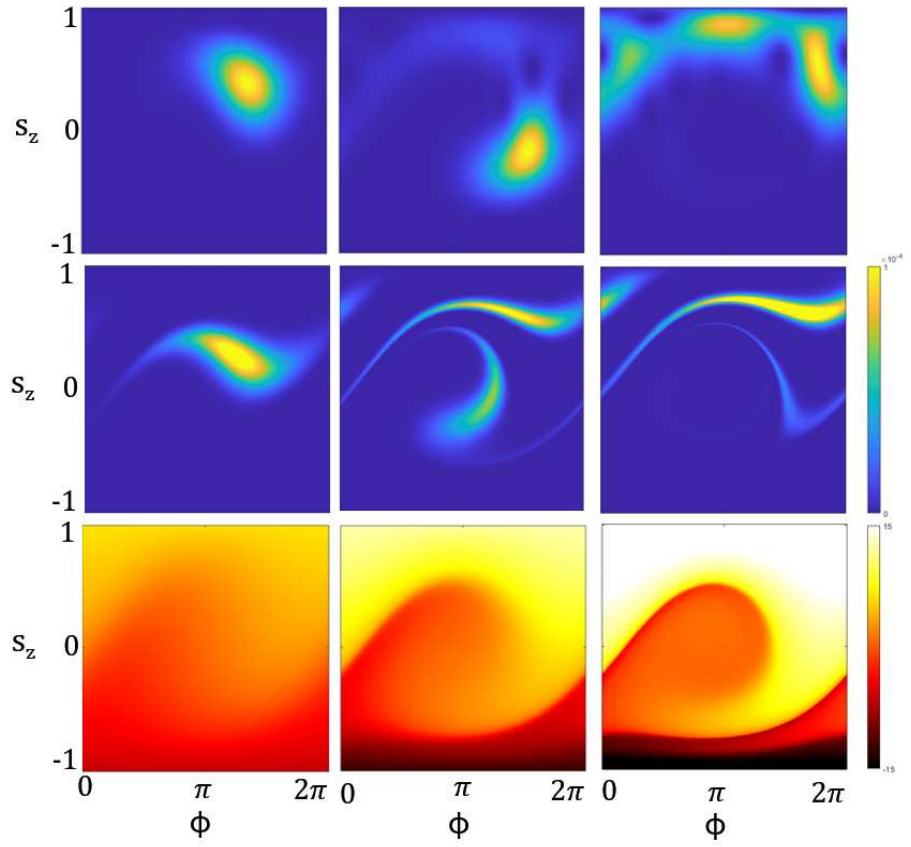


Figure 5.22: Evolution of the normalised quantum Husimi distribution (top row), the normalised semiclassical Husimi distribution (middle row) and the logarithm of the norm landscape (bottom row) for the non-Hermitian $(2,1)$ Bose-Hubbard Hamiltonian with $\nu = \frac{1}{2}, g = 2, \kappa = \frac{1}{5}$ and $N = 40$, for an initial coherent state centred at $(\phi, s_z) = (\frac{\pi}{2}, 0)$. The columns correspond to different snapshots of the evolution in time with $t = \frac{\pi}{2}$ (left), $t = \pi$ (middle) and $t = \frac{3\pi}{2}$ (right).

Over longer time, the quantum Husimi distribution converges to that of the dominant eigenstate, while the semiclassical distribution is increasingly influenced by the exponential growth of the norm landscape around fixed point 3, eventually localising at this fixed point. This behaviour aligns with our observations in other non-Hermitian systems, such as the Heisenberg-Weyl and $\mathfrak{su}_2$ systems with complex-valued eigenvalue spectra, where the semiclassical Husimi approximation correlates well with the quantum Husimi distribution as illustrated in figures 5.23 and the right panel of 5.21.

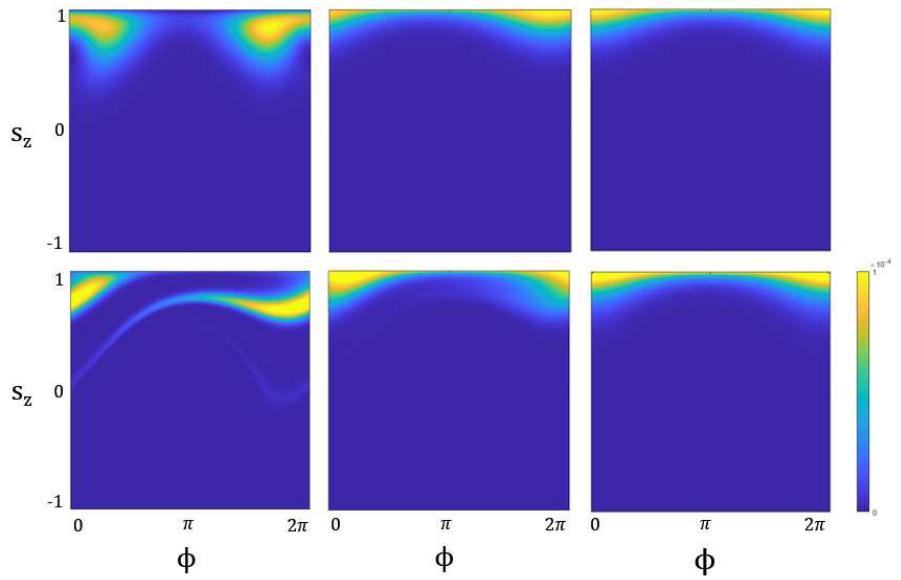


Figure 5.23: Evolution of the normalised quantum Husimi distribution (top row) and the normalised semiclassical Husimi distribution (bottom row) for the non-Hermitian $(2,1)$ Bose-Hubbard Hamiltonian with $\nu = \frac{1}{2}, g = 2, \kappa = \frac{1}{5}$ and $N = 40$, for an initial coherent state centred at $(\phi, s_z) = (\frac{\pi}{2}, 0)$. The columns correspond to different snapshots of the evolution in time with $t = \frac{5\pi}{2}$ (left), $t = 5\pi$ (middle) and $t = 10\pi$ (right).

This concludes our analysis of $(2,1)$ bosonic conversion examples. We complete this chapter with a discussion on how to generalise the approach to multi-mode systems.

5.4 Generalised Multi-Mode Bosonic Conversion Systems

Having established the theoretical framework for two-mode bosonic conversion systems, we now generalise our analysis to the broader class of d-mode systems. We examine bosonic systems comprising B bosons distributed across d distinct modes, denoted $M_1, M_2, \ldots, M_d$, where bosons can transfer between different modes according to specific rules. Each mode M_j is characterised by bosonic excitations occurring in discrete multiples of k_j, where $k_j \in \mathbb{N}^+$ represents the fundamental excitation quantum for that mode. The generalisation to multiple modes requires extending our notation to accommodate the increased complexity. We define a binary parameter $l_j \in \{-1, 1\}$, which indicates whether the corresponding operator destroys ($l_j = -$) or creates ($l_j = -1$) a boson in mode j. Following the same bosonic commutation relations as established previously

$$[\hat{a}_j, \hat{a}_k^\dagger] = \delta_{jk}, \quad [\hat{a}_j, \hat{a}_k] = 0, \quad [\hat{a}_j^\dagger, \hat{a}_k^\dagger] = 0. \tag{5.157}$$

We will use the following notational convention

$$a_i^{k_i l_i} = \begin{cases} a_i^{k_i}, & \text{for } l_i = 0, \\ \left(a_i^\dagger\right)^{k_i}, & \text{for } l_i = -1. \end{cases} \tag{5.158}$$

We allow for transitions between these modes by creation and annihilation of the clusters of the bosonic modes described by the operator $\hat{a}_1^{k_1 * l_1} ... \hat{a}_d^{k_d * l_d}$. In the case where $\frac{l_i}{l_j} < 0$ for some i, j then the state space is finite-dimensional, otherwise it is infinite-dimensional [100]. If we define the set $\{k_i\}$ as $\{k_i \in \{0,1\}^d : \|k_i\|_1 = 2\}$ and for each vector k_i assign $l_1 = 1$, $l_2 = -1$ at the positions where the ones appear, we obtain the transition operators that generate the $\mathfrak{su}_d$ algebra,

$$\hat{a}_i^\dagger \hat{a}_j. \tag{5.159}$$

If in addition we define diagonal generators

$$\hat{a}_i^\dagger \hat{a}_i - \frac{1}{d} \sum \hat{a}_j^\dagger \hat{a}_j \tag{5.160}$$

we form the complete set of generators for the $\mathfrak{su}_d$ algebra. In the above case, if either or both values of the k_i are greater than 1, then we have a deformed $\mathfrak{su}(d)$ algebra. More generally, if more than 2 of the k_i are non-zero, then we have a generalised bosonic algebra. For example, consider a 3-mode system consisting of atoms, diatomic molecules, and triatomic molecules. Assuming a total number of bosons that is a multiple of six, the k_i sets would be $(1,0,3)$, $(1,2,0)$, $(0,2,3)$ and the corresponding l_i values are $(\pm 1, 0, \mp 1)$, $(\pm 1, \mp 1, 0)$, $(0, \pm 1, \mp 1)$. A physical process with three non-zero k_i values could be a reaction where two atoms and two diatomic molecule combine to form two triatomic molecules, described by $k_i = (2,1,2)$ with $l_i = (-1,-1,+1)$. The key point to note in all of the above examples is that the framework we have developed can be applied for phase-space approximations, demonstrating its power and applicability to a large class of physical non-Hermitian systems. We will now end this thesis with a discussion on potential avenues for further research, focusing on deeper investigations into the relationship between the norm landscape and dynamics, as well as applications to more general non-Hermitian systems.

Chapter 6

Conclusions

This thesis has developed a theoretical framework for phase-space approximations in non-Hermitian quantum systems, extending classical and semiclassical methods beyond their traditional Hermitian domains. The aim has been to create a unified approach applicable to diverse open physical systems that satisfy a set of general criteria.

We have proposed two complementary phase-space approximations: a classical approach via the coherent-state approximation, and a semiclassical approach via the semiclassical Husimi approximation method. The latter applies the coherent-state approximation across the entire phase space. The resulting dynamics for Husimi distributions combine transport over classical trajectories, comprising symplectic and gradient motion, with the effect of a norm landscape that applies an overriding factor to the transported distribution [69].

As observed for Hermitian systems, the semiclassical Husimi distributions for non-Hermitian systems improved upon coherent-state approximations for short times in all examples studied. For non-Hermitian systems with complex-valued eigenvalue spectra, we found that the long-term behaviour of quantum systems comprises asymptotic evolution to a final state that is approximated well by the semiclassical Husimi approximation method. Observations from the systems studied here indicate that this is related to the correspondence between the dominant eigenstate set for the quantum evolution and the norm landscape for the semiclassical Husimi approximation method, with the latter becoming the dominant factor in the semiclassical approach. This connection between spectral properties and phase-space dynamics provides an illuminating insight into the role of the norm landscape in non-Hermitian systems and merits further analytical investigation in future research.

The work presented in this thesis represents an important step toward both understanding and approximating quantum-classical correspondence in open quantum systems where coherent quantum dynamics are coupled to non-conservative environmental effects.

6.1 Summary

In Chapter 2, following the established tradition in quantum mechanics literature, we began with the canonical example of the Heisenberg-Weyl algebra, which generates the quantum harmonic oscillator and whose associated coherent states are the well-known Glauber coherent states.

The chapter commenced by presenting the essential background material for this algebra, including the associated coherent states, the classical counterpart to the quantum system, the $\mathcal{D}$-algebra formalism, and the Husimi function, a quasi-probability distribution used to represent quantum states in phase space. This foundational algebra served to introduce the key ingredients that would form the basis for later applications and generalisations.

The discussion proceeded to introduce the background material for non-Hermitian quantum dynamics, including consideration of PT-symmetric systems. A noteworthy observation was that for complex-valued Hamiltonians, there exists a dominant eigenstate determined by the eigenvalue spectrum, which governs the long-term quantum evolution.

Following this foundation, two complementary phase-space approximations were formulated for non-Hermitian Heisenberg-Weyl systems: a classical approach via the coherent-state approximation, and a semiclassical approach via the semiclassical Husimi method. The latter combines transport along classical trajectories generated by the complex-conjugated Hamiltonian k^* with modulation by a time-dependent norm landscape $w(z,t)$ that captures the non-unitary aspects of the evolution.

With these two methods established, their application was demonstrated through a series of examples, each incorporating additional complexity. The analysis commenced with the nonlinear Hermitian Kerr Hamiltonian to demonstrate the methods on a well-studied system. For this case, the semiclassical Husimi method was shown to outperform the coherent-state approximation at short times; however, both methods failed to capture the revival phenomena characteristic of the underlying periodic unitary evolution at longer times. A characteristic feature observed across multiple examples was that the semiclassical Husimi distributions developed increasingly fine spiral and filamentary structures over time due to classical phase-space shearing, while the quantum Husimi distributions remained smoother due to the uncertainty principle's resolution limit.

The chapter concluded with an analysis of four non-Hermitian systems. The first examination focused on the non-Hermitian harmonic oscillator, for which exact quantum-classical correspondence was demonstrated. The second study involved a damped version of the Kerr Hamiltonian, where both approximation methods successfully modelled the long-term quantum dynamics, which comprised state deformation and spiralling motion toward the origin. The semiclassical Husimi approximation provided superior accuracy in this case.

A more complex example followed: the damped tilted Mexican Hat potential. Here, limitations in the coherent-state approximation were observed, which in certain cases produced trajectories leading to classical fixed points distinct from the quantum evolution's final state. The additional feature of the norm landscape enabled the semiclassical Husimi method to perform better, converging to

a final state located near, though not identical to, the final quantum state.

The final investigation examined a PT-symmetric example, demonstrating a complex, non-asymptotic norm landscape with rich dynamical features that can arise for PT systems. Similar to the Hermitian case, whilst short-time dynamics could be accurately modelled, the longer evolution times and quantum effects remained beyond the scope of these phase-space approximations.

In Chapter 3, using the Heisenberg-Weyl algebra as a guiding example, a set of key ingredients for the approximation methods was established, thereby developing a generalised coherent-state approximation framework that leads to a generalised semiclassical Husimi method. This approach mirrors the historical evolution of coherent state theory, which began with Glauber's coherent states for the Heisenberg-Weyl algebra, progressed through Gilmore-Perelomov coherent states for classes of Lie algebras, and culminated in Gazeau and Klauder's work on generalised coherent states. By adopting this generalised framework from the outset, we automatically encompass Lie algebras as special cases, since their algebraic and geometric properties naturally fulfil the required criteria.

The sufficient (though not necessary) criteria required for the generalised phase-space approximations are: the existence of an overcomplete basis of coherent states with continuous labels that satisfy the resolution of identity; the existence of a quantum phase space with a well-defined classical counterpart in the appropriate limit; the factorisation property whereby the expectation value of the product of two operators can be approximated by the product of their individual expectation values; and the existence of well-defined limits of the commutator and anti-commutator that yield the Poisson bracket and metric bracket, respectively, on the classical phase space.

In Chapter 4, we addressed the $\mathfrak{su}_2$ Lie algebra as a familiar example to which our generalised framework could be applied. As with the Heisenberg-Weyl case, we established the essential background material and then examined a set of analogous examples to those presented in Chapter 2. For the $\mathfrak{su}_2$ algebra, both linear Hermitian and nonlinear Hermitian cases were addressed, demonstrating exact quantum-classical correspondence. We subsequently considered the two-mode Bose-Hubbard model adapted to the $\mathfrak{su}_2$ structure as an analogue to the Kerr Hamiltonian examined in Chapter 2. Similar features emerged: the superiority of the semiclassical Husimi approximation over the coherent-state approximation at short times, and the failure of both methods to replicate quantum state revival phenomena over longer time scales.

The chapter concluded with an analysis of non-Hermitian extensions of the two-mode Bose-Hubbard model, providing examples of PT-symmetric Hamiltonians where both broken and unbroken PT-symmetry regimes were explored. The classical counterpart to these systems exhibited three distinct parameter regions: two regions containing fixed points that corresponded to parameters yielding broken PT-symmetry, and a third region without fixed points corresponding to parameters that result in unbroken PT-symmetry for the quantum system.

In Chapter 5, we examined two-mode bosonic conversion systems, which give rise to polynomially deformed $\mathfrak{su}_2$ algebras. This represented the first example of a non-Lie algebra to which our framework could be applied. The semiclassical Husimi approximation for these deformed algebras

represents new and original work for both Hermitian and non-Hermitian systems. For the bosonic conversion systems, the non-Lie algebraic structure required a more careful and detailed analysis, revealing interesting features such as quantum phase spaces whose geometry depended on the chosen representation and classical phase spaces that were no longer manifolds but contained geometric features such as cusps.

Unlike the standard $\mathfrak{su}_2$ case, the exact quantum-classical correspondence broke down even for linear cases in the deformed algebra, highlighting the impact of the non-Lie algebraic structure on quantum-classical relationships. The reduction of symmetry in the deformed $\mathfrak{su}_2$ system meant that tunnelling was no longer a feature of the dynamics, even in the Hermitian case. Furthermore, this reduced symmetry precluded the construction of a PT-symmetric version of the Bose-Hubbard model. Additionally, the classical phase space contained cusps that led to interesting and distinct classical dynamics not seen in the Lie algebra cases.

Several key themes emerged consistently across all algebraic structures examined (Heisenberg-Weyl, $\mathfrak{su}_2$, and deformed $\mathfrak{su}_2$): the semiclassical Husimi approximation consistently outperformed the coherent-state approximation at short times, successfully capturing quantum effects such as state deformation. Across all systems studied, the semiclassical Husimi distributions characteristically developed finer structures over time, exhibiting detailed spiral patterns, filamentary features, and sharp boundaries, while quantum Husimi distributions remained broader and smoother due to fundamental quantum resolution limits. However, longer-term quantum phenomena such as interference and revival remained beyond the scope of both approximation methods. Crucially, for complex eigenvalued non-Hermitian systems, the non-Hermiticity dampens quantum effects and introduces a dominant eigenstate behaviour that the semiclassical Husimi method models effectively, enabling accurate approximation of the long-term asymptotic evolution.

These results demonstrate the promising potential and versatility of the generalised phase-space approximation framework across diverse algebraic structures, from Lie algebras to non-Lie deformed systems. The framework successfully captures the essential physics of quantum-classical correspondence in both Hermitian and non-Hermitian regimes, while revealing the crucial role of the norm landscape in determining long-term behaviour for non-Hermitian systems. However, there remain interesting and important areas for further extension and improvement of these methods, which warrant continued investigation and development. These opportunities and future directions will be discussed in detail in the following section.

6.2 Future Work

The theoretical framework developed in this thesis opens several promising avenues for future research and development. These directions range from fundamental theoretical questions about the scope and limitations of quantum-classical correspondence to practical improvements in approximation methods and their application to important physical systems widely used in quantum mechanics, alongside deeper mathematical understanding of the key mathematical objects and their properties.

A fundamental question arising from this work concerns the extent to which exact quantum-classical correspondence for linear non-Hermitian systems can be generalised across different Lie algebraic structures. While we have demonstrated this correspondence for both Heisenberg-Weyl and $\mathfrak{su}_2$ algebras, the broader applicability remains an open question. Recent work by Brody [107] has shown that in state space, non-Hermitian quantum evolution corresponds to symplectic motion combined with gradient flow, referred to as metriplectic flow in certain literature [122]. The key question is whether such metriplectic flows on state space can be reduced to phase space through coadjoint orbit structures, building on Souriau's symplectic foliation model where coadjoint orbits form entropy level sets with dynamics along orbits being conservative and transverse dynamics being dissipative. This reduction could explain why coherent states remain coherent for certain algebraic systems when extended to non-Hermitian cases, and we would like to further investigate for which cases this holds, all Lie algebras that admit the Kirillov orbit method or a subset of these.

Another promising area involves the four-dimensional phase-space approximations for Jacobi coherent states, developed in Appendix C, which represents a potential avenue for improving the accuracy of Gaussian approximation methods. These Gaussian approximation methods are vital and important in a wide range of applications throughout quantum mechanics, including the modelling of qubit systems and other fundamental quantum technologies. Future work could focus on applying this enhanced method to practical examples to quantify the improvements over the standard two-dimensional approach for both Hermitian and non-Hermitian systems. Ohsawa's recent work demonstrated significant improvements in Hermitian systems using symplectic reduction and a more consistent treatment of $\hbar$ for Gaussian states compared to traditional approaches. Building upon these foundations, extending these improvements to non-Hermitian cases and comparing the performance with existing methods represents a natural progression. This investigation could examine whether the four-dimensional approach can capture quantum effects that are missed by lower-dimensional approximations. Furthermore, exploring the integration of Ohsawa's improvements with the non-Hermitian methodological advances developed by Graefe et al. could potentially create hybrid approaches that combine the strengths of multiple approximation schemes.

A particularly important theoretical challenge involves analysing the long-term behaviour of the norm landscape for complex-valued non-Hermitian Hamiltonians and determining whether a long-term asymptotic analysis exists that avoids the computational burden of numerical simulations for each individual phase-space trajectory, which is required in most cases as analytical solutions are rarely available. Developing such analytical techniques would provide significant computational efficiency gains and make the methods more practical for large-scale applications. Additionally, understanding how this asymptotic behaviour relates to the dominant eigenvalue set and whether an analytic relationship can be established between the norm landscape's final form and the final quantum state would provide deeper theoretical insight into the mechanisms governing non-Hermitian quantum evolution and could lead to predictive tools for determining final states without full numerical integration.

A key theoretical question concerns whether the sufficient conditions identified for the generalised phase-space approximations can be refined to necessary conditions, thereby establishing the minimal requirements for these methods to be applicable. This investigation would examine whether

the Klauder generalised coherent state construction is enough to guarantee the required geometric and factorisation properties, or whether additional constraints are necessary. Understanding the minimal theoretical requirements would have significant practical implications, as it would provide clear criteria for determining when these approximation methods can be expected to work effectively.

The ultimate test of these theoretical developments lies in their application to realistic physical systems of current experimental and technological interest, including quantum optical systems with dissipation, many-body open quantum systems, and other platforms where non-Hermitian effects play a crucial role. Establishing clear connections between theoretical predictions and experimentally measurable quantities would complete the bridge between fundamental theory and experimental practice, providing experimentalists with powerful new tools to predict, control, and optimise the behaviour of realistic open quantum systems

Bibliography

[1] S. Adachi, "A numerical evaluation of the semiclassical coherent state path integral," *Ann. Phys. (N.Y.)*, vol. 195, no. 1, pp. 45–93, 1989.

[2] M. Combescure and D. Robert, "A semiclassical trace formula using coherent states methods," *C. R. Acad. Sci. Ser. IIB*, vol. 326, no. 9, pp. 569–574, 1998.

[3] M. Baranger, M. A. M. de Aguiar, F. Keck, H. J. Korsch, and B. Schellhaass, "Semiclassical approximations in phase space with coherent states," *J. Phys. A*, vol. 34, p. 7227, Aug. 2001.

[4] M. Novaes and M. A. M. D. Aguiar, "Semiclassical Husimi functions for spin systems," *Phys. Rev. A*, vol. 71, p. 012104, 2005.

[5] M. V. Berry and K. E. Mount, "Semiclassical approximations in wave mechanics," *Rep. Prog. Phys.*, vol. 35, p. 315, Jan. 1972.

[6] G. A. Hagedorn, "Semiclassical quantum mechanics," *Commun. Math. Phys.*, vol. 71, pp. 77–93, Feb. 1980. ISBN: 1432-0916.

[7] R. Gilmore, "Lie groups, Lie algebras and some of their applications," *Wiley, New York*, 1974.

[8] A. M. Perelomov, "Coherent–States for arbitrary Lie–Groups," *Commun. Math. Phys.*, vol. 26, p. 222, 1972.

[9] A. A. Kirillov, "Unitary Representations of Nilpotent Lie Groups," *Russian Mathematical Surveys*, vol. 17, p. 53, Aug. 1962.

[10] B. Kostant, "Quantization and unitary representations," in *Lectures in Modern Analysis and Applications III* (R. M. Dudley, J. Feldman, B. Kostant, R. P. Langlands, E. M. Stein, and C. T. Taam, eds.), (Berlin, Heidelberg), pp. 87–208, Springer, 1970.

[11] J. Souriau, "Quantification géométrique. Applications," *Annales de l'institut Henri Poincaré. Section A, Physique Théorique*, vol. 6, no. 4, pp. 311–341, 1967.

[12] I. Schafer and M. Kuś, "Constructing the classical limit for quantum systems on compact semisimple lie algebras," *J. Phys. A*, vol. 39, no. 31, pp. 9779–9796, 2006.

[13] S. Gnutzmann, "Klassischer Grenzfall, Semiklassik und Quantenchaos bei kollektiv gekoppelten n-Niveau-Atomen," *PhD Thesis, University Duisberg-Essen*, 2000.

[14] T. Ohsawa and M. Leok, "Symplectic Semiclassical Wave Packet Dynamics," *J. Phys. A*, vol. 46, 2013.

[15] S. Berceanu and A. Gheorghe, "Applications of the Jacobi group to Quantum Mechanics," *arXiv:0812.0448*, 2008. arXiv: 0812.0448.

[16] C. M. Bender, "Making sense of non-hermitian hamiltonians," *Rep. Prog. Phys.*, vol. 70, p. 947, 2007.

[17] G. Lindblad, "On the generators of quantum dynamical semigroups," *Commun. Math. Phys.*, vol. 48, pp. 119–130, June 1976.

[18] M. V. Berry, "Physics of nonhermitian degeneracies," *Czech. J. Phys.*, vol. 54, p. 1039, 2004.

[19] G. Gamow, "Zur Quantentheorie des Atomkernes," *Z. Phys. A*, vol. 51, p. 204, 1928.

[20] E. Narevicius, P. Serra, and N. Moiseyev, "Critical phenomena associatied with self-orthogonality in non-Hermitian quantum mechanics," *Europhys. Lett.*, vol. 62, p. 789, 2003.

[21] J. Okolowicz, M. Ploszajczak, and I. Rotter, "Dynamics of quantum systems embedded in a continuum," *Phys. Rep.*, vol. 374, p. 271, 2003.

[22] C. M. Bender and P. D. Mannheim, "PT-symmetry and necessary and sufficient conditions for the reality of energy eigenvalues," *Phys. Lett. A*, vol. 374, p. 1616, 2010.

[23] E. M. Graefe, "Stationary states of a PT-symmetric two-mode Bose-Einstein condensate," *J. Phys. A*, vol. 45, p. 444015, 2012.

[24] R. El-Ganainy, K. G. Makris, D. N. Christodoulides, and Z. H. Musslimani, "Theory of coupled optical PT-symmetric structures," *Opt. Lett.*, vol. 32, no. 17, pp. 2632–2634, 2007.

[25] A. Guo, G. J. Salamo, D. Duchesne, R. Morandotti, M. Volatier-ravat, V. Aimez, G. A. Siviloglou, and D. N. Christodoulides, "Observation of PT-symmetry breaking in complex optical potentials," *Phys. Rev. Lett.*, vol. 103, no. 9, p. 093902, 2009.

[26] K. G. Makris, R. El-Ganainy, D. N. Christodoulides, and Z. H. Musslimani, "Beam dynamics in PT symmetric optical lattices," *Phys. Rev. Lett.*, vol. 100, no. 10, p. 103904, 2008.

[27] C. E. Rüter, K. G. Makris, R. El-Ganainy, D. N. Christodoulides, M. Segev, and D. Kip, "Observation of parity-time symmetry in optics," *Nat. Phys.*, vol. 6, p. 192, 2010.

[28] H. Hodaei, M. A. Miri, M. Heinrich, D. N. Christodoulides, and M. Khajavikhan, "Enhanced sensitivity at higher-order exceptional points," *Nature (London)*, vol. 548, pp. 187–191, 2017.

[29] B. Peng, S. K. Özdemir, F. Lei, F. Monifi, M. Gianfreda, G. L. Long, S. Fan, F. Nori, C. M. Bender, and L. Yang, "Parity–time-symmetric whispering-gallery microcavities," *Nat. Phys.*, vol. 10, no. 5, pp. 394–398, 2014.

[30] A. J. Daley, "Quantum trajectories and open many-body quantum systems," *Advances in Physics*, vol. 63, no. 2, pp. 77–149, 2014.

[31] I. Rotter, "Dynamics of quantum systems," *Phys. Rev. E*, vol. 64, p. 036213, 2001.

[32] E. Schrödinger, "Quantisierung als Eigenwertproblem, (Dritte Mitteilung:Storungstheorie, mit Anwendung auf den Strakeffekt der Balmerlinien," *Ann.Phys.*, vol. 79, no. 4, pp. 470–471, 1926.

[33] W. C. Henneberger, "Perturbation Method for Atoms in Intense Light Beams," *Phys. Rev. Lett.*, vol. 21, p. 838, 1968.

[34] P. Buonsante and V. Penna, "Some remarks on the coherent-state variational approach to nonlinear boson models," *J. Phys. A*, vol. 41, p. 17530, 2008.

[35] R. L. H. S. N., "Variational analysis for a generalized spiked harmonic oscillator," *J. Phys. A*, vol. 33, p. 569, 2000.

[36] K. F. Freed, "Path integrals and semiclassical tunneling, wavefunctions, and energies," *J. Chem. Phys.*, vol. 56, no. 2, pp. 692–697, 1972.

[37] J. R. Klauder, "Path integrals and stationary–phase approximations," *Phys. Rev. D*, vol. 19, p. 2349, 1979.

[38] H. Kleinert, *Path Integrals in Quantum Mechanics Statistics and Polymer Physics*. Singapore: World Scientific, 2. ed. ed., 1995.

[39] D. M. Ceperley and B. J. Alder, "Ground State of the Electron Gas by a Stochastic Method," *Phys. Rev. Lett.*, vol. 45, pp. 566–569, Aug. 1980.

[40] P. M. Morse and H. Feshbach, *Methods of Theoretical Physics*. New York: McGraw Hill, 1953.

[41] M. D. Feit, J. A. F. Jr, and A. Steiger, "Solution of the Schrödinger Equation by a Spectral Method," *CoP*, vol. 47, p. 412, 1982.

[42] G. Friesecke and M. Koppen, "On the Ehrenfest theorem of quantum mechanics," *J. Math. Phys. (N.Y.)*, vol. 50, p. 082102, Aug. 2009.

[43] K. Hepp, "The classical limit for quantum mechanical correlation functions," *Commun. Math. Phys.*, vol. 35, pp. 265–277, Dec. 1974. ISBN: 1432-0916.

[44] E. Bonet-luz and C. Tronci, "Hamiltonian approach to Ehrenfest expectation values and Gaussian quantum states," *Proc. Roy. Soc. Lond. A*, vol. 472, no. 2189, p. 20150777, 2016.

[45] E. M. Graefe, M. Höning, and H. J. Korsch, "Classical limit of non-Hermitian quantum dynamics – a generalised canonical structure," *J. Phys. A*, vol. 43, p. 075306, 2010.

[46] S. Gnutzmann and M. Kus, "Coherent states and the classical limit on irreducible representations," *J. Phys. A*, vol. 31, no. 49, p. 9871, 1998.

[47] D. Bonatsos, C. Daskaloyannis, P. Kolokotronis, A. Ludu, and C. Quesne, "Nonlinear deformed su(2) algebras involving two deforming functions," *Czech. J. Phys.*, vol. 46, pp. 1189–1196, Dec. 1996.

[48] C. Daskaloyannis, "Generalized deformed oscillator and nonlinear algebras," *J. Phys. A*, vol. 34, no. 48, p. 10245, 2001.

[49] V. Sunilkumar, B. A. Bambah, R. Jagannathan, P. K. Panigrahi, and V. Srinivasan, "Coherent states of nonlinear algebras: applications to quantum optics," *J. Opt. B*, vol. 2, p. 126, Apr. 2000.

[50] J. R. Klauder, "Continuous-Representation Theory. I. Postulates of Continuous-Representation Theory," *J. Math. Phys. (N.Y.)*, vol. 4, pp. 1055–1058, Aug. 1963.

[51] J. R. Klauder, "Continuous-Representation Theory II. Generalized Relation between Quantum and Classical Dynamics," *Rev. Mod. Phys.*, vol. 4, p. 1058, 1963.

[52] J. P. Gazeau and J. R. Klauder, "Coherent states for systems with discrete and continuous spectrum," *J. Phys. A*, vol. 32, pp. 123–132, Jan. 1999.

[53] D. Ojeda-guillén, M. Salazar-ram\'ırez, V. D. Granados, and R. D. Mota, "su(1,1) and SU(2) Perelomov number coherent states: algebraic approach for general systems," *J. Nonlin. Math,Phys.*, vol. 23, no. 4, pp. 607–619, 2016.

[54] K. Fujii, "Introduction to coherent states and quantum information theory," in *10th Numazu Meeting on Integrable System, Noncommutative Geometry and Quantum Theory*, Dec. 2001.

[55] M. N. Sergeenko, "Semiclassical wave equation and exactness of the WKB method," *Phys. Rev. A*, vol. 53, pp. 3798–3804, June 1996.

[56] C. A. A. D. Carvalho and R. M. Cavalcanti, "Semiclassical series from path integrals," *AIP Conf. Proc.*, vol. 484, no. 1, pp. 256–269, 1999.

[57] D. Huber and E. J. Heller, "Hybrid mechanics: A combination of classical and quantum mechanics," *J. Chem. Phys.*, vol. 89, p. 4752, 1988.

[58] E. J. Heller, "Frozen Gaussians: A very simple semiclassical approximation," *J. Chem. Phys.*, vol. 75, p. 2923, 1981.

[59] R. G. Littlejohn, "The semiclassical evolution of wave packets," *Phys. Rep.*, vol. 138, p. 193, 1986.

[60] E. M. Graefe and R. Schubert, "Wave packet evolution in non-Hermitian quantum systems," *Phys. Rev. A*, vol. 83, p. 060101(R), 2011.

[61] T. Ohsawa and C. Tronci, "Geometry and dynamics of Gaussian wave packets and their Wigner transforms," *J. Phys. A*, vol. 58, no. 9, p. 092105, 2017.

[62] E. Wigner, "On the quantum correction for thermodynamic equilibrium," *Phys. Rev.*, vol. 40, p. 749, 1932.

[63] R. J. Glauber, "Coherent and incoherent states of the radiation field," *Phys. Rev.*, vol. 131, p. 2766, 1963.

[64] E. C. G. Sudarshan, "Equivalence of Semiclassical and Quantum Mechanical Descriptions of Statistical Light Beams," *Phys. Rev. Lett.*, vol. 10, p. 277, 1963.

[65] K. Husimi, "Some formal properties of the density matrix," *Proc. Phys. Math. Soc. Japan*, vol. 22, p. 264, 1940.

[66] G. J. Milburn, "Quantum and classical Liouville dynamics of the anharmonic oscillator," *Phys. Rev. A*, vol. 33, p. 674, 1986.

[67] A. Polkovnikov, "Phase space representation of quantum dynamics," *Ann. Phys.*, vol. 325, p. 1790, 2010.

[68] M. J. Steel, M. K. Olsen, R. L. de Matos Filho, M. J. Davis, P. D. Drummond, and D. F. Walls, "Dynamical quantum noise in trapped bose-einstein condensates," *Phys. Rev. A*, vol. 58, p. 4824, 1998.

[69] K. Holmes, W. Rehman, S. Malzard, and E. Graefe, "Husimi Dynamics Generated by non-Hermitian Hamiltonians," *Phys. Rev. Lett.*, vol. 130, p. 157202, Apr. 2023.

[70] E. Graefe, H. J. Korsch, and A. Rush, "Classical-quantum correspondence in bosonic two-mode conversion systems: Polynomial algebras and Kummer shapes," *Phys. Rev. A*, vol. 93, p. 042102, Apr. 2016.

[71] M. Orozco-ruiz, W. Rehman, and F. Mintert, "Generally noise-resilient quantum gates for trapped-ions," Apr. 2024. arXiv:2404.12961 [quant-ph].

[72] T. Guaita, L. Hackl, T. Shi, E. Demler, and J. I. Cirac, "Generalization of group-theoretic coherent states for variational calculations," *Phys. Rev. Res.*, vol. 3, p. 023090, May 2021.

[73] E. Schrödinger, "Der stetige übergang von der mikro- zur makrophysik," *Naturwissenschaften*, vol. 14, p. 664, 1926.

[74] V. Fock, "Verallgemeinerung und lösung der diracschen statistischen gleichung," *Z. Phys.*, vol. 49, p. 339, 1928.

[75] B. Hall, *Lie groups, Lie algebras, and representations*. Heidelberg: Springer, 2003.

[76] W. Zhang, D. H. Feng, and R. Gilmore, "Coherent states: Theory and some applications," *Rev. Mod. Phys.*, vol. 62, no. 4, p. 867, 1990.

[77] J. R. Klauder and E. C. G. Sudarshan, *Fundamentals of Quantum Optics*. New York Amsterdam: W. A. Benjamin, 1968.

[78] V. Bargmann, "On a hilbert space of analytic functions and an associated integral transform, part i," *Commun. Pure Appl. Math.*, vol. 14, p. 187, 1961.

[79] S. Berceanu and A. Gheorghe, "Differential operators on orbits of coherent states," Nov. 2002. arXiv:math/0211054.

[80] S. T. Ali, *Coherent states, wavelets, and their generalizations*. Theoretical and mathematical physics, New York ; Heidelberg: Springer, 2nd ed., [fully updated] ed., 2014.

[81] S. Berceanu, "Realization of coherent state Lie algebras by differential operators," Apr. 2005. arXiv:math/0504053.

[82] G. P. Berman, E. N. Bulgakov, and D. D. Holm, *Crossover-Time in Quantum Boson and Spin Systems*. Berlin Heidelberg: Springer, 1994.

[83] P. Ehrenfest, "Bemerkung über die angenäherte gültigkeit der klassischen mechanik innerhalb der quantenmechanik," *Z. Phys.*, vol. 45.

[84] B. Yurke and D. Stoler, "The dynamic generation of Schrödinger cats and their detection," *Physica B+C*, vol. 151, pp. 298–301, July 1988.

[85] R. W. Boyd, *Nonlinear Optics*. London: Academic Press, 1992.

[86] M. H. Anderson, J. R. Ensher, M. R. Matthews, C. E. Wieman, and E. A. Cornell, "Observation of Bose–Einstein condensation in a dilute atomic vapor," *Science*, vol. 269, pp. 198–201, July 1995.

[87] M. Arndt, O. Nairz, J. Vos-Andreae, C. Keller, G. vanderZouw, and A. Zeilinger, "Wave–particle duality of C_60 molecules," *Nature*, vol. 401, no. 6754, pp. 680–682, 1999.

[88] A. Aspect, J. Dalibard, and G. Roger, "Experimental Realization of Einstein-Podolsky-Rosen-Bohm Gedankenexperiment: A New Violation of Bell's Inequalities," *Phys. Rev. Lett.*, vol. 49, no. 2, pp. 91–94, 1982.

[89] M. A. Nielsen and I. L. Chuang, *Quantum Computation and Quantum Information*. Cambridge: Cambridge University Press, 2000.

[90] J. Preskill, "Quantum computing in the nisq era and beyond," *Quantum*, vol. 2, p. 79, Aug. 2018.

[91] Rivas and S. F. Huelga, *Open Quantum Systems: An Introduction*. SpringerBriefs in Physics, Berlin, Heidelberg: Springer, 2012.

[92] M. Sameti, J. Lishman, and F. Mintert, "Strong-coupling quantum logic of trapped ions," *Phys. Rev. A*, vol. 103, p. 052603, May 2021.

[93] C. Gardiner and P. Zoller, *Quantum Noise*. Berlin Heidelberg New York: Springer Series in Synergetics, 2004.

[94] D. C. Brody, "Biorthogonal quantum mechanics," *J. Phys. A*, vol. 47, p. 035305, 2014.

[95] C. M. Bender, "Introduction to PT-symmetric quantum theory," *Contemporary Physics*, vol. 46, p. 277, 2005.

[96] A. Mostafazadeh, "Pseudo-Hermiticity versus PT symmetry: The necessary condition for the reality of the spectrum of a non-Hermitian Hamiltonian," *J. Math. Phys. (N.Y.)*, vol. 43, p. 205, 2002.

[97] H. Dekker, "Classical and quantum mechanics of the damped harmonic oscillator," *Phys. Rep.*, vol. 80, pp. 1–110, Dec. 1981.

[98] J. Hall, S. Malzard, and E. Graefe, "Semiclassical Husimi Distributions of Schur Vectors in Non-Hermitian Quantum Systems," *Phys. Rev. Lett.*, vol. 131, p. 040402, July 2023.

[99] A. Odzijewicz, M. Horowski, and A. Tereszkiewicz, "Integrable multi-boson systems and orthogonal polynomials," *Journal of Physics A: Mathematical and General*, vol. 34, pp. 4353–4370, May 2001.

[100] A. Odzijewicz and E. Wawreniuk, "Classical and quantum Kummer shape algebras," *J. Phys. A: Math. Theor.*, vol. 49, p. 265202, July 2016.

[101] J. Schwinger, "On angular momentum, USAEC Report NYO-3071," in *Quantum theory of angular momentum* (L. C. Biedenharn and H. v. Dam, eds.), New York: Academic Press Inc, 1966.

[102] A. A. Kirillov, *Lectures on the Orbit Method*, vol. 64 of *Graduate Studies in Mathematics*. Providence, RI: American Mathematical Society, 2004.

[103] J. J. Sakurai and J. Napolitano, "Modern Quantum Mechanics," Sept. 2017. ISBN: 9781108499996 Publisher: Cambridge University Press.

[104] E. M. Graefe, H. J. Korsch, and A. E. Niederle, "Mean-field dynamics of a non-hermitian Bose-Hubbard dimer," *Phys. Rev. Lett.*, vol. 101, p. 150408, 2008.

[105] G. J. Milburn, J. Corney, E. M. Wright, and D. F. Walls, "Quantum dynamics of an atomic Bose-Einstein condensate in a double-well potential," *Phys. Rev. A*, vol. 55, pp. 4318–4324, June 1997. Publisher: American Physical Society.

[106] R. Gilmore, C. M. Bowden, and L. M. Narducci, "Classical-quantum correspondence for multilevel systems," *Phys. Rev. A*, vol. 12, no. 3, p. p1019, 1975.

[107] D. C. Brody, "Complex extension of wigner's theorem," *J. Phys. A: Math. Theor.*, vol. 46, p. 395301, Oct. 2013.

[108] D. Burns, E. Lupercio, and A. Uribe, "The exponential map of the complexification of Ham in the real-analytic case," *arXiv: 1307.0493*, 2013.

[109] B. D. Josephson, "Possible new effects in superconductive tunnelling," *Physics Letters*, vol. 1, pp. 251–253, July 1962.

[110] A. Vardi and J. R. Anglin, "Bose-Einstein condensates beyond mean field theory: Quantum backreaction as decoherence," *Phys. Rev. Lett.*, vol. 86, p. 568, 2001.

[111] G. Santos, A. Tonel, A. Foerster, and J. Links, "Classical and quantum dynamics of a model for atomic-molecular Bose-Einstein condensates," *Phys. Rev. A*, vol. 73, p. 023609, Feb. 2006.

[112] J. Liu, B. Liu, and L. Fu, "Many-body effects on nonadiabatic Feshbach conversion in bosonic systems," *Phys. Rev. A*, vol. 78, p. 013618, 2008.

[113] M. Kummer, "On the construction of the reduced phase space of a hamiltonian system with symmetry," *Indiana Univ. Math. J.*, vol. 30, no. 2, pp. 281–291, 1981.

[114] M. Kummer, "Lecture 1: On resonant hamiltonian systems with finitely many degrees of freedom.," in *Local and Global Methods of Nonlinear Dynamics* (A. W. Sáenz, W. W. Zachary, and R. Cawley, eds.), vol. 252, pp. 19–31, Berlin/Heidelberg: Springer-Verlag, 1986.

[115] Y. Lee, W. Yang, and Y. Zhang, "Polynomial algebras and exact solutions of general quantum nonlinear optical models I: two-mode boson systems," *J. Phys. A*, vol. 43, no. 18, p. 185204, 2010.

[116] F. Pan, "Generalized deformed algebras F(A1) and their applications," *J. Math. Phys. (N.Y.)*, vol. 35, pp. 5065–5073, Sept. 1994.

[117] P. Shanta, S. Chaturvedi, V. Srinivasan, and R. Jagannathan, "Unified approach to the analogues of single-photon and multiphoton coherent states for generalized bosonic oscillators," *J. Phys. A: Math. Gen.*, vol. 27, p. 6433, Oct. 1994.

[118] J. R. Klauder, "Enhanced Quantization."

[119] R. Abraham and J. E. Marsden, *Foundations of Mechanics*. Reading: Benjamin, 1978.

[120] T. Ohsawa, "Dual pairs and regularization of kummer shapes in resonances," *J. Geom. Mech.*, vol. 11, no. 2, pp. 225–238, 2019.

[121] E. M. Graefe, H. J. Korsch, A. Rush, and R. Schubert, "Classical and quantum dynamics in the (non-Hermitian) Swanson oscillator," *J. Phys. A*, vol. 48, no. 5, p. 055301, 2015.

[122] P. J. Morrison, "A paradigm for joined hamiltonian and dissipative systems," *Physica D*, vol. 18, p. 410, 1986.

[123] A. K. Pattanayak and W. C. Schieve, "Gaussian wave-packet dynamics: Semiquantal and semiclassical phase-space formalism," *Phys. Rev. E*, vol. 50, no. 5, p. p3601, 1994.

[124] S. Berceanu, "Coherent states associated to the jacobi group—a variation on a theme by erich kähler," *J. Geom. Symmetry Phys.*, vol. 9, pp. 1–8, 2007.

[125] T. Ohsawa, "Approximation of Semiclassical Expectation Values by Symplectic Gaussian Wave Packet Dynamics," *arXiv:2012.05464*, 2020.

[126] S. Berceanu, "A holomorphic representation of the Jacobi algebra," *Rev. Math. Phys.*, vol. 18, no. 02, p. 163, 2006. Publisher: World Scientific Publishing Co.

Appendix A

Generally noise-resilient quantum gates for trapped-ions

This appendix contains the paper ‘Generally noise-resilient quantum gates for trapped-ions. which is available as a preprint on arXiv (arXiv:2404.12961) and has been is under review at Physics Review A.

Generally noise-resilient quantum gates for trapped-ions

Modesto Orozco-Ruiz,[1] Wasim Rehman,[2] and Florian Mintert[1,3]

[1] *Blackett Laboratory, Imperial College London, SW7 2AZ, United Kingdom*
[2] *Department of Mathematics, Imperial College London, London, SW7 2AZ, United Kingdom*
[3] *Helmholtz-Zentrum Dresden-Rossendorf, Bautzner Landstraße 400, 01328 Dresden, Germany*

(Dated: April 22, 2024)

We present an entangling gate scheme for trapped-ion chains that achieves high-fidelity operations with excited motional states despite multiple error sources. Our approach incorporates all relevant motional modes and exhibits enhanced robustness against both motional heating effects and detuning errors, critical features for building robust and scalable trapped-ion quantum computers.

arXiv:2404.12961v1 [quant-ph] 19 Apr 2024

I. INTRODUCTION

Trapped-ion quantum computing holds promise for building scalable and fault-tolerant quantum computers due to the exceptional control that can be exerted over individual qubits and their collective interactions [1]. This exquisite control enables the implementation of the two-qubit entangling gate – a fundamental building block for quantum algorithms. Relying on the Coulomb interaction between ions, this gate utilizes the shared motion of the ions to generate entanglement in their electronic states [2].

The Mølmer-Sørensen gate [3] has emerged as one of the most promising implementations in trapped-ion quantum computing, with fidelities exceeding 99% in both optical and hyperfine qubits [4–7]. Exploiting precisely tuned bichromatic laser fields that couple internal and motional states, the Mølmer-Sørensen gate proves to be insensitive to the initial motional state, offering substantial advantages for scalability and error correction [8–12].

However, despite robustness to initial motional state, current entangling gates remain vulnerable to various experimental imperfections, due to their inherent coupling with the environment [3, 8, 9], as well as to systematic errors resulting from imperfect calibration of system parameters. The complex interplay of error mechanisms in entangling gates presents a significant obstacle to the development of a robust scheme against multiple errors. While some approaches have demonstrably enhanced resilience against specific noise sources, optimizing resilience against one mechanism typically compromises resilience against another. For example, increasing laser power for faster gates can alleviate detuning errors but exacerbate off-resonant coupling to undesired carrier transitions [13]. Similarly, suppressing motional mode cross-talk in many-ion systems by slowing down the gate operation can lead to reduced coherence time and imperfect coupling [14, 15]. These conflicting effects highlight the need for control protocols capable of simultaneously addressing diverse error sources.

Motional heating is arguably a primary source of errors in current implementations, with electric and magnetic field noise leading to unwanted phonon exchange that disrupts the motional states of the trapped ions [13]. Similarly, frequency fluctuations of the vibrational modes induce dephasing, ultimately compromising the gate fidelity. To address these challenges, several schemes have been proposed to enhance the motional robustness of entangling gates by engineering optimal ion trajectories in phase space. One approach involves modulating sideband field parameters (phase, frequency or amplitude [16, 17]) to create phase-space trajectories with minimal susceptibility to heating. Alternatively, a multi-tone driving strategy employs a combination of detuned fields with varying amplitudes for each ion sideband, achieving comparable robustness gains [18]. However, despite their demonstrated success [11], these techniques are inherently limited by the constraints of the Lamb-Dicke regime within which entangling gates operate [18]. This regime, characterized by weak laser-ion interactions, requires low laser power for high-fidelity operations, leading to slower gate times. Additionally, shared motional states must be cooled close to their ground state, posing a scalability bottleneck for proposals involving active ion shuttling [19, 20], as such movements inherently excite these states. Deviations from these conditions, such as using stronger laser fields or excited motional states, result in compromised fidelities.

Logic gates beyond the Lamb-Dicke regime offer significant improvements, including high fidelities with high motional states and significantly faster quantum operations. One approach employs a series of complex pulses inducing state-dependent kicks exceeding the motional frequencies [21]. While this method demonstrably enhances speed, current fidelities remain moderate due to experimental complexity and unwanted coupling to additional motional modes.

An alternative strategy employs simpler driving fields and higher-order sideband transitions that are designed to cancel undesired contributions from the non-linear spin-motion coupling beyond the Lamb-Dicke regime [18]. This approach holds promise for achieving high fidelities in the strong-coupling regime, but relying on driving more sideband transtions is more vulnerable to motional heating.

Another significant challenge faced by current entangling gates involves scaling to larger ion chains with a complex multi-mode structure [22–24]. This not only amplifies noise sensitivity due to increased crosstalk between

ions [15] but also significantly complicates control protocols, specially far from the Lamb-Dicke regime. This occurs because the coupling strength corresponding to each motional mode becomes comparable in magnitude and it varies across different ions in the chain. Selectively driving a single mode in such systems inevitably triggers higher-order phonon exchange processes, unintentionally coupling non-targeted spectator modes to the qubit states. This presents a significant challenge in achieving high-fidelity gates, requiring control strategies distinct from those employed in paradigms with fewer modes, where precise control over individual modes is sufficient.

This manuscript introduces a gate scheme that integrates multiple strategies to combat diverse error sources in trapped-ion quantum computing. Our control framework achieves high-fidelity entanglement in hot trapped-ions within a multi-mode system, demonstrating inherent resilience against motional heating and increased robustness against fluctuations in both qubit frequency and normal-mode frequencies.

II. HAMILTONIAN MODEL

The dynamics of a system comprised of the internal degrees of freedom of N ions and M collective motional degrees of freedom is induced by the Hamiltonian

$$H_0 = \sum_{j=1}^{N} \frac{\omega_j}{2} \sigma_z^{(j)} + \sum_{l=1}^{M} \nu_l a_l^\dagger a_l \ , \tag{1}$$

where $\sigma_z^{(j)}$ is the Pauli-Z operator for ion j with resonance frequency ω_j, and $a_l^\dagger(a_l)$ are the creation (annihilation) operators for the collective motional degree of freedom l with resonant frequency $\nu_l = \kappa_l \nu$ in terms of the trapping frequency ν.

The interaction with an external light field, such as a laser field, can excite both internal and motional degrees of freedom of the ions. The respective interaction Hamiltonian reads

$$H(t) = \sum_{j=1}^{N} f_j(t) \sigma_+^{(j)} \prod_{l=1}^{M} e^{i\eta_{jl}\left(a_l + a_l^\dagger\right)} + h.c. \ , \tag{2}$$

in terms of the raising operator $\sigma_+^{(j)}$ of the internal degree of freedom of ion j, and the driving functions $f_j(t)$ that encapsulate the generally time-dependent Rabi-frequency and a time-dependence due to carrier frequencies of the light field. The Lamb-Dicke parameters $\eta_{jl} = \chi_{jl}\Lambda$ characterize the coupling between the state transition in ion j and each motional state transition in mode l due to light field interaction. They depend on the expansion coefficients χ_{jl} and the coupling factor $\Lambda = \frac{2\pi}{\lambda}\sqrt{\frac{\hbar}{2m\nu}}$ defined in terms of the wavelength of the light field λ and the mass m.

Since entangling gates are realized via the exchange of virtual phonons in the collective motion of the ions, it is instructive to express the interaction Hamiltonian as

$$H(t) = \sum_{j=1}^{N} \tilde{f}_j(t) \sigma_+^{(j)} \prod_{l=1}^{M} \sum_{k=-\infty}^{\infty} \mathcal{D}_{l,k}(\eta_{jl}) + h.c. \ , \tag{3}$$

in terms of the operators

$$\mathcal{D}_{l,k}(\eta) = \sum_{n=0}^{\infty} (i\eta)^{2n+k} \frac{a_l^{\dagger n+k} a_l^n}{(n+k)!n!} \ , \tag{4}$$

and

$$\mathcal{D}_{l,-k}(\eta) = (-1)^k \mathcal{D}_{l,k}^\dagger(\eta) \ , \tag{5}$$

for $k \geq 0$, that encapsulate all processes resulting in the creation (of $k > 0$) and annihilation ($k < 0$) of k phonons in a given mode, and a renormalised driving function

$$\tilde{f}_j(t) = f_j(t) \ e^{-\frac{1}{2}\sum_{l=1}^{M} \eta_{jl}^2} \ . \tag{6}$$

The operators $\mathcal{D}_{l,k}$ capture the k-th order sideband transitions of the motional mode l. A generic driving pattern $\tilde{f}_j(t)$ can have spectral components that are close to resonance with each of these (red and blue) sideband transitions. In standard rotating wave approximation, each spectral component needs to be considered in the Hamiltonian only in close-to-resonant terms, but it can be neglected in any far-off-resonant term. A general parametrization of driving patterns is thus given by

$$\tilde{f}_j = -i \sum_l \frac{1}{\eta_{jl}} \sum_k F_{l,k}^{(j)}(t) \ e^{-i(k\nu_l + \omega_j)t} \ , \tag{7}$$

where the factors $e^{-i(k\nu_l+\omega_j)t}$ capture the time-dependence necessary for resonance with a given sideband transition, as demonstrated by expressing $H(t)$ (Eq. (3)) in the interaction picture with respect the free Hamiltonian $H_0(t)$ (Eq. (1)). The factors $F_{l,k}^{(j)}(t)$ have a slow time-dependence compared to ν_l and account for finite detuning and temporal modulation that can be used to achieve the desired robustness. Finally, the factor η_{jl}^{-1} reflects the fact that weaker interaction (smaller η_{jl}) requires proportionally stronger driving fields to maintain constant interaction strength.

A coherent gate requires that there are no changes to the motional state that depend on the internal state of the ions, and achieving this is facilitated in terms of driving patterns in which the driving amplitude $F_{l,-k}^{(j)}$ for any blue sideband transition ($k > 0$) is given by the driving amplitude $F_{l,k}^{(j)}$ for the corresponding red sideband transition following the relation

$$F_{l,-k}^{(j)} = (-1)^k \left(F_{l,k}^{(j)}\right)^* \ , \tag{8}$$

where the factor $(-1)^k$ has its origin in Eq. (5).

With any such driving pattern, the interaction Hamiltonian reduces to

$$H(t) = \sum_{j=1}^{N} \sigma_y^{(j)} \sum_{l,k>0} \frac{F_{l,k}^{(j)}(t)}{\eta_{jl}} \mathcal{D}_{l,k} \prod_{l' \neq l} \mathcal{D}_{l',0} + h.c. \,, \quad (9)$$

with $\sigma_y = i(\sigma_- - \sigma_+)$, and with factors

$$\mathcal{D}_{l,0} = \sum_{n=0}^{\infty} \frac{(i\eta)^{2n}}{n!^2} a_l^{\dagger n} a_l^n \quad (10)$$

that describe phonon-conserving, but phonon-number-dependent energy shifts.

III. DRIVING PATTERNS

A light field modulated as described in Eq. (7) allows the engineering of a time-dependent Hamiltonian (Eq. (9)) with desired dynamics. By carefully choosing the driving functions $F_{l,k}^{(j)}(t)$, the interaction with ions can be tailored to induce specific processes necessary for entangling state generation.

Crucially, not all motional modes of the ion chain are required for entanglement generation. Only a subset of these modes, along with a finite number of their sideband transitions, play a crucial role. The Mølmer-Sørensen (MS) entangling gate [3, 25] exemplifies this principle, where entanglement is achieved by driving solely the first sideband of a chosen set of motional modes.

This specific solution to Eq. (9) requires the weak coupling regime or motional states near their ground states as this allows approximating the displacement operators for the driven modes d in Eq. (9) to the lowest order in η as $\mathcal{D}_{d,1} \approx i\eta_d a_d^\dagger$, while those for the spectator modes reduce to the identity $\mathcal{D}_{l',0} \approx \mathbb{1}$. This first-order simplification implies that spectator modes do not couple with the driven modes (see Eq. (9)) and can therefore be safely neglected, thus resulting in the simplified Hamiltonian $H_{MS}(t) = iS_y \sum_d \left(F_d(t) a_d^\dagger - F_d^*(t) a_d\right)$, with the collective spin operator $S_y = \sum_j \sigma_y^{(j)}$. With this simplified Hamiltonian, a carefully chosen set of driving functions $F_d(t)$ enables the implementation of the entangling gate $U = e^{i\phi_T \sum_{j\neq k} \sigma_y^{(j)} \sigma_y^{(k)}}$ acting on all ion pairs.

A. Non-identical ion species and multi-mode systems

Although the Hamiltonian H_{MS} offers a straightforward approach for creating entangled states, it comes with certain limitations. While a global driving field ($f_j(t) = F(t)$ for all ions j) works for identical ion species, two key challenges arise when dealing with non-identical ions. Firstly, their differing resonance frequencies ω_j lead to the acquisition of distinct phase factors $e^{i\omega_j t}$ during their dynamics. Secondly, non-identical ions couple to the mediating modes with varying strengths $|\eta_{j,l}|$. This dependence on the specific ion j results in different scaling factors $e^{\frac{1}{2}\eta_{j,l}^2}$ arising in the expansion of the interaction Hamiltonian in Eq. (2).

These challenges related to non-identical ions can be addressed using a more sophisticated individual addressing approach instead of a single, global field. However, a more fundamental limitation lies with the Lamb-Dicke approximation used to obtain the simplified first-order Hamiltonian H_{MS}. This approximation restricts the applicability of H_{MS} to systems operating within the weak coupling regime or with motional states close to their ground states, as dictated by the inequality $\frac{\eta_l^2}{2} n_l \ll 1$ [18, 25]. Systems that do not satisfy this constraint necessitate alternative approaches to obtain high-fidelity operations.

B. Beyond the Lamb-Dicke approximation

Moving beyond the Lamb-Dicke approximation, either due to stronger ion-motion interactions or higher motional states, necessitates considering higher-order phonon-exchange processes within the displacement operators Eq. (4). This leads to more complex spin-motion interactions for driven modes ($\mathcal{D}_{l,k} \approx \frac{(i\eta)^k}{k!} a_l^{\dagger k} + \frac{(i\eta)^{k+2}}{(k+1)!} a_l^{\dagger(k+1)} a_l + \cdots$) and, crucially, indirect coupling between driven and spectator modes via the non-trivial products $\mathcal{D}_{l,k} \prod_{l' \neq l} (\mathbb{1} - \eta_{l'}^2 a_{l'}^\dagger a_{l'} + \cdots)$ in Eq. (9).

Consequently, control schemes beyond the Lamb-Dicke regime must account not only for higher-order phonon processes in the driven modes but also for the phonon exchange processes in the remaining non-addressed collective vibrational modes. To illustrate this phenomenon, consider a two-ion system where driving the first sideband of the center-of-mass mode induces phonon exchanges like $(\eta_1^3/2) a_1^{\dagger 2} a_1$ beyond the first-order term $\eta_1 a_1$. Similarly, even though the stretch mode is not directly addressed, it couples through this driving and contributes to dynamics with processes like $\eta_2^2 a_2^\dagger a_2$.

Therefore, capturing these inter-mode dependencies and designing high-fidelity entangling gates for many-mode ion chains beyond the Lamb-Dicke regime necessitates a higher-order expansion of the interaction Hamiltonian $H(t)$. This expansion reveals exchange processes neglected in the standard treatment, requiring the development of a new control strategy that eliminates their unwanted contributions at the gate time.

Following this crucial first step, designing a robust two-qubit entangling gate involves selecting a suitable set of driven motional modes L and the specific sidebands for each of those modes $K(l)$. These choices determine which processes are driven resonantly. The temporal modulation of the driving functions, $F_{l,k}^{(j)}$ is then tailored to

achieve entanglement at the desired gate time T while actively suppressing the unwanted processes and maximizing the gate's overall robustness.

C. Driven sidebands

The specific construction presented here enables the implementation of an entangling gate in a multi-mode system of N trapped ions with high motional states and offers enhanced resilience against both motional heating and combined errors in qubit and vibrational frequencies. While alternative choices exist, the proposed configuration minimizes the number of driven sidebands required for achieving the desired robustness, offering a practical advantage for experimental implementation.

In a system with M motional modes, the proposed gate implementation involves simultaneous driving of all modes ($L = M$). The first-order sideband ($k = 1$) of a designated central mode, typically chosen for its stronger spin-motion coupling, acts as the primary bus mode of the entangling process. Meanwhile, other modes (together with the central one) contribute through second-order sidebands ($k = 2$) to actively suppress unwanted contributions arising from higher-order terms in the Hamiltonian.

With such choice, the Hamiltonian Eq. (9) simplifies to

$$H_c(t) = \sum_{j=1}^{N} \sigma_y^{(j)} \left(\frac{F_{1,1}^{(j)}}{\eta_{j1}} \mathcal{D}_{1,1} D_1 + \sum_{l=1}^{M} \frac{F_{l,2}^{(j)}}{\eta_{jl}} \mathcal{D}_{l,2} D_l \right) + h.c., \tag{11}$$

with $D_k = \prod_{l' \neq k} \mathcal{D}_{l',0}$ being the product of phonon-conserving operators in the spectator modes.

Building upon Eq. (11), one can derive time-dependent functions $F_{1,1}^{(j)}$ and $F_{l,2}^{(j)}$ specifically to achieve an exact solution of the driven dynamics up to a particular order of η. Although higher-order solutions are theoretically feasible, the present solution results from an expansion to order $\mathcal{O}(\eta^3)$, significantly enhancing first-order expansions while minimizing the number of sidebands required for achieving the desired robustness. With their detailed derivation available in Sec. V, these functions are given by

$$F_{1,1}^{(1)} = F_{1,1}^{(2)} = \Omega \left(e^{2i\delta t} - \frac{3}{2} e^{3i\delta t} \right) \tag{12a}$$

$$F_{l,2}^{(1)} = s_{1l} \Omega \frac{\tilde{\eta}_l}{\eta_{1l}} e^{i\delta t} \tag{12b}$$

$$F_{l,2}^{(2)} = s_{1l} \Omega \frac{\tilde{\eta}_l}{\eta_{2l}} e^{i\delta t} \tag{12c}$$

where $l = 1, \cdots, M$ refers to the motional mode, $s_{jl} = \text{sign}(\eta_{jl})$ and $\tilde{\eta}_l := \frac{\sqrt{5}}{2} \sqrt{\eta_{1l}^2 + \eta_{2l}^2}$.

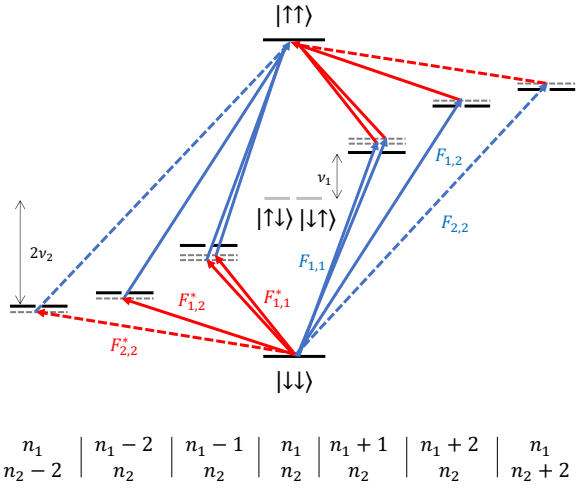
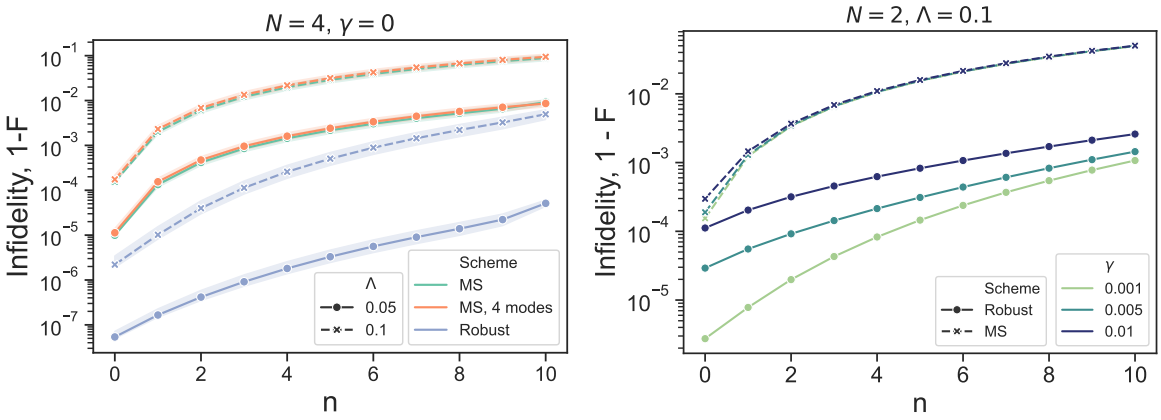


FIG. 1: Energy level diagram for two identical ions and two motional modes. Note that only energy levels involved in the driving process are shown for simplicity. Solid blue (red) sidebands represent transitions with a phonon gain (loss) in motional mode 1. Dashed blue (red) sidebands represent similar processes for motional mode 2.

Consider a specific pair of ions selected for entanglement generation within the N-ion chain. According to Eq. (12a), both ions receive identical bichromatic modulation with detunings 2δ and 3δ ions targeting the first sideband of the primary motional mode (see Fig. 1 for the case of two identical ions). With such a modulation, resilience against motional heating is enhanced, while the specific detuning ratio optimizes gate speed. Eqs. (12b) and (12c), in turn, specify different drivings for each ion in the pair targeting second order sidebands of all vibrational modes (see Fig. 1). These suppress unwanted processes that emerge as higher-order (in η) contributions to the system's dynamics and include mode-dependent amplitudes to compensate for the different coupling strengths across the different modes. Finally, the Rabi amplitude Ω is specified in terms of the detuning δ as a solution to the equation

$$-6 \frac{\Omega^4}{\delta^4} \left(\sum_j \eta_{j1}^2 \right) + \frac{\Omega^2}{\delta^2} \left(2 + \sum_{l,j} \eta_{jl}^2 \right) = \frac{2\phi_T}{5\pi} , \tag{13}$$

defined in terms of the entangling phase ϕ_T in the unitary gate U. In the weak-coupling regime, where $\eta_{jl} \approx 0$, the higher-order terms in the equation become negligible and the entangling condition reduces to the standard MS case with a bichromatic driving of the form Eq. (12b), *i.e.*, $\Omega^2/\delta^2 = \phi_T/5\pi$.



(a) (b)

FIG. 2: Infidelity $1-F$ of the entangling gate as a function of the initial Fock state occupation n for a 4-qubit (left panel) and 2-qubit (right panel) systems. In the left panel, each data point represents the average infidelity across all qubit pairs, with the shaded area showing the range of values found across different pairs. The infidelity corresponds to the standard MS gate (green), the MS gate applied to all four modes (orange), and the present gate (blue). No motional heating ($\gamma = 0$) is assumed and different values of the coupling strength Λ are shown with different markers. In the right panel, the impact of motional heating is evaluated for a fixed spin-motion coupling $\Lambda = 0.1$. Decay rates are represented by colors ranging from light green (low) to purple (high) and marker styles differentiate the standard MS gate (crosses) from the proposed robust scheme (circles). In all simulations, the amplitude of the driving fields in the present scheme is limited to match the amplitude of the MS gate, ensuring a fair comparison.

IV. RESULTS

The proposed control strategy enables the implementation of high-fidelity entangling gates for trapped-ions in noisy environments, even when the ions share multiple collective vibrational modes and are in high motional states. Gate performance can be quantified using the gate fidelity, which is given by

$$F(\rho_M) = \frac{1}{d^2} \sum_{\alpha,\beta=1}^{d} \langle\alpha|U^\dagger \,\mathrm{Tr}_M\left(\mathcal{E}(|\alpha\rangle\langle\beta| \otimes \rho_M)\right) U|\beta\rangle\,, \tag{14}$$

where the states $|\alpha\rangle\,, |\beta\rangle$ span the d-dimensional Hilbert space of spin states (with $d = 2^N$), ρ_M is the initial density matrix of motional states, U represents the target unitary and $\mathcal{E}(\cdot)$ the actual (potentially non-unitary) channel corresponding to the implemented gate. Evaluating the fidelity $F(\rho_{th})$ for thermal states ($\rho_{th} = \sum_{\mathbf{n}} P(\mathbf{n})\,|\mathbf{n}\rangle\langle\mathbf{n}|$, with $|\mathbf{n}\rangle = |n_1, n_2, \cdots n_M\rangle$) is crucial, as these states are commonly encountered in real experiments. By exploiting the linearity of the trace, one can avoid the construction of the density matrix and instead compute the fidelity for a sufficiently large set of Fock states. Averaging these individual fidelities yields the thermal state fidelity $F(\rho_{th}) = \sum_{\mathbf{n}} P(\mathbf{n}) F(|\mathbf{n}\rangle\langle\mathbf{n}|)$.

The following discussion delves into the dependence of the fidelity F on several key parameters relevant to an experimental implementation, including chain size N, initial motional occupations $|\mathbf{n}\rangle$, and the impact of non-idealities like motional heating and frequency errors in the vibrational modes ϵ_ν and spin transition frequencies ϵ_ω.

A. Multi-mode systems with no dissipation or frequency errors

Unlike simpler two-ion systems, designing entangling gates for larger, multi-mode, systems requires accounting for variations in coupling strengths η_{jl} across ion pairs. This key challenge is directly addressed by the proposed control scheme. Fig. 2a exemplifies this point by depicting the infidelity $1-F$ of the present gate in a 4-ion system under ideal conditions (no dissipation or frequency errors). The x-axis represents the initial motional Fock state $|n\rangle^{\otimes 4}$, and the shaded area shows the range of infidelities across all ion pairs, with marker points indicating the average value. Colors distinguish the present gate (in blue), the standard MS gate applied to the center-off-mass mode (in green), and the MS gate applied to all four motional modes [26] (in orange); while different marker styles represent varying coupling strengths Λ.

Crucially, under ideal conditions, the present gate consistently outperforms both MS variants across all initial states and coupling strengths. This advantage is par-

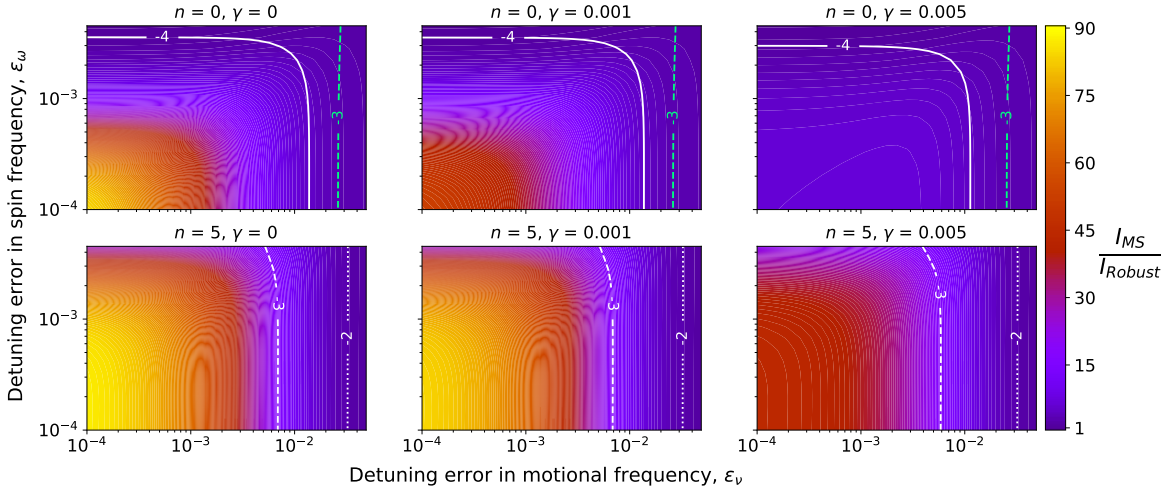


FIG. 3: Combined impact of vibrational and spin frequency errors on the performance of the present entangling scheme (Robust) compared to the standard MS gate in a two-ion system. Each panel shows the ratio of MS gate infidelity to SC gate infidelity I_{MS}/I_{Robust} for a specific initial motional state $|n\rangle$ and decay rate γ, with fixed coupling strength $\Lambda = 0.1$. The x-axis represents (in log scale) errors in vibrational frequency ϵ_ν; while the y-axis depicts symmetric errors in spin frequencies ϵ_ω. Contour lines reveal actual fidelities achievable by each method. Solid lines enclose regions where infidelities remain below 10^{-4}, dashed lines correspond to 10^{-3} and dotted lines to 10^{-2}. Green lines represent the MS gate, while white ones represent the robust scheme.

ticularly evident in weak-coupling regimes ($\Lambda = 0.05$, circles). Even with high motional states ($n = 10$), it achieves infidelities below 10^{-4}, a remarkable two orders of magnitude lower than any MS variant. Notably, this performance is independent of the specific ion pair within the four-ion system, demonstrating its robustness across various configurations, a crucial feature for practical applications.

While the current analysis is limited to Fock states with $n = 10$ for a four-ion system, numerical evidence suggests this trend persists for significantly higher levels of motional excitation, indicating the gate's high performance even under substantial thermal noise. Indeed, fidelities exceeding 99% are still achievable even at mean phonon occupations as high as $\bar{n} \sim 100$, as shown in Supp. Mat. B for a two-ion system.

B. Motional heating

The previous results suggest that the present entangling protocol allows high-fidelity entanglement without near-ground-state motional cooling, particularly advantageous for systems with weak spin-phonon coupling. However, a critical consideration is whether this benefit comes at the cost of increased susceptibility to motional decoherence due to the additional side-band driving. Crucially though, the temporal modulation of the driving fields, as defined in Eq. (12), strategically mitigates heating effects, thereby enabling robust entanglement generation even in the presence of thermal noise. This protection, as detailed in Sec. V, stems from the bichromatic driving in $F^{(1)}_{1,1}$ and $F^{(2)}_{1,1}$, which minimizes the impact of incoherent processes arising from motional heating to first order in η. Further enhanced robustness can be achieved by implementing a polychromatic version for all drivings in Eq. (12), although at the cost of a more intricate driving scheme.

Fig. 2b illustrates the performance of the proposed gate in the presence of motional heating for a two-ion system of identical species. In contrast to the prior scenario, the coupling strength remains uniform across all motional modes and ions (*i.e.* $|\eta_{jl}|$ is independent of j and l) and, therefore, local drivings can be relaxed to be global. The infidelity $1 - F$ is represented as a function of the motional occupation for a fixed coupling strength $\Lambda = 0.1$ and different heating decay rates γ (see Eq. (19)). The crosses correspond to the performance of the MS gate applied to the center-off-mass mode, while circles represent solutions derived from the parametrization in Eq. (12). The results demonstrate a significant performance advantage of the present scheme over the MS approach across all decay rates, particularly in low-dissipative environments. This enhanced robustness achieved with bichromatic driving enables fidelities close to 10^{-3} for motional occupations of up to $n = 10$ in low and medium dissipative environments ($\gamma \leq 0.01$), compared to an infidelity close to 10^{-1} for the MS gate.

C. Detuning errors

Even minimal errors in vibrational and spin frequencies can significantly affect the gate fidelity. These errors, typically small compared to the resonant frequencies (*i.e.*, $\epsilon \ll \omega$), can be modeled as shifts of the form $\omega \to \omega + \epsilon$. Specifically, errors in motional frequencies manifest as shifts for each motional mode l, $\nu_l \to \nu_l + \epsilon_{\nu_l}$, whereas (symmetric) spin frequency errors are modeled as $\omega_j \to \omega_j + \epsilon_\omega$, affecting the resonant frequencies of the spin transitions. These small frequency drifts in vibrational and spin transitions lead to a crucial mismatch between the actual transition frequencies and the driving frequencies defined in Eq. (7), introducing an undesired detuning error that modifies the actual dynamics and may lead to potential performance degradation.

Crucially, the properties that enhance resilience to motional heating (mainly closed phase-space trajectories and vanishing time-integral, as detailed in Supp. Mat. A) are also relevant for mitigating the impact of motional detuning errors [8]. Therefore, the proposed gate exhibits robustness against these errors by design. On the other hand, while not explicitly designed to address spin frequency detuning errors, the proposed gate still exhibits a relevant degree of robustness to them, as shown in Fig. 3.

Fig. 3 depicts the combined impact of detuning errors in vibrational and spin frequencies for a two-ion system also experiencing motional heating. Each panel represents the ratio in infidelities between the MS gate (applied to the center-off-mass mode) and the present robust protocol, I_{MS}/I_{Robust}, using a color code ranging from purple (similar performance) to yellow (significant improvement). The panels vary across different initial motional states $|\mathbf{n}\rangle$ and decay rates γ; and the x and y axes correspond to errors in the vibrational ϵ_ν (assumed to be the same across all modes for simplicity) and spin frequencies ϵ_ω, respectively.

The first row of panels shows the infidelity ratio for the initial motional ground state ($n = 0$) with increasing decay rates from left to right. Here, the present scheme (robust) exhibits substantial improvement over the MS gate for small and moderate errors in motional frequencies ($\epsilon_\nu < 0.5\%$), even with spin frequency shifts of up to $\epsilon_\nu < 0.1\%$. Notably, reductions in infidelity of up to two orders of magnitude are achieved in the case with no motional heating and small frequency errors (yellow region in leftmost panel). While this advantage diminishes with increasing motional heating (moving right within the first row), the present scheme maintains superior performance across all decay rates depicted, within the studied range of frequency errors.

Overall, when restricting motional frequency errors to a maximum of 1.5%, the proposed gate achieves fidelities exceeding 99.99% (as delimited by the green contour line), which represents an improvement of at least a factor of five, and up to two orders of magnitude, over the standard MS approach.

Moving to higher motional states ($n = 5$), the present scheme demonstrates a more significant advantage. The region with very substantial improvement (in red and yellow tones) expands to encompass larger errors across both axes. This improvement also decays more gradually with higher decay rates compared to the case with motional ground states (first row). Importantly, the MS gate fails to achieve fidelities exceeding 99% for any frequency error within the studied range. In contrast, the robust scheme maintains high fidelities exceeding 99% within a broad range of errors (up to $\epsilon_\nu < 3\%$ and $\epsilon_\omega < 2\%$) and even achieves exceptional fidelities exceeding 99.9% with frequency errors of any type of up to 0.7%. This advantage persists even for high motional occupations ($n \sim 100$), where the robust scheme still maintains fidelities exceeding 99% with moderate frequency errors.

V. METHODS

This section details the derivation of the driving protocol in Eq. (12) that implements a robust entangling gate operation. The approach involves first designing the general driving pattern for the desired operation and then refining it to enhance robustness against noise and imperfections.

A. Entangling gate

While Eq. (9) describes the ion-laser interaction Hamiltonian with a driving pattern $\tilde{f}_j(t)$ near-resonant with all sideband transitions, only a finite subset of those sidebands is needed for the implementation of the entangling gate. This selection process involves specifying the time-dependent functions $F_{l,k}^{(j)}(t)$ for specific side-bands (k) of specific motional modes (l). Crucially, achieving a successful implementation relies on both a well-designed set of functions $F_{l,k}^{(j)}(t)$ and an appropriate choice of sidebands. If the chosen set of sidebands is inadequate, there may not exist a modulation strategy (i.e., a choice of $F_{l,k}^{(j)}(t)$) that fulfills both requirements at the gate time: (i) eliminating undesired spin-motion coupling terms and (ii) reaching the desired Rabi angle ϕ_T for the entangling term.

Once a sideband set and modulation strategy are chosen, one can analyze the system's evolution. An initial spin-motion state $\rho = \rho_S \otimes \rho_M$ evolves under the influence of the time-dependent Hamiltonian $H(t)$ in Eq. (9) to a final state $\rho(T) = U(T)\rho U^\dagger(T)$, with the unitary evolution operator $U(T) = \mathcal{T}\exp\left(-i\int_0^T dt H(t)\right)$. Constructing $U(T)$ for a chosen modulation strategy thus reveals the effective operators present at the gate time and therefore the final state $\rho(T)$. The Magnus expansion [27] provides an approximation of $U(T)$ using a finite number of terms, effectively acting as an exact solution up to a specific order in the Lamb-Dicke parameter η.

This work employs a third-order solution in η, surpassing the standard first-order approach, which leads to a more accurate model of the system's dynamics.

Specifically, the interaction Hamiltonian to order η^3 is given by

$$H(t) = \sum_j \left[iF_{1,1}^{(j)}\sigma_y^{(j)}a_1^\dagger \left(\mathbb{1} - \frac{1}{2}\eta_{j1}^2 a_1^\dagger a_1 - \sum_{l=2}^{M} \eta_{jl}^2 a_l^\dagger a_l \right) - \frac{1}{2}\sum_{l=1}^{M} \eta_{jl} F_{l,2}^{(j)} \sigma_y^{(j)} a_l^{\dagger 2} \right] + h.c.\ , \tag{15}$$

with the creation and annihilation operators $a_1^\dagger$ and a_1 referring to the designated central motional mode. Accordingly, the unitary evolution operator induced by this Hamiltonian can be found analytically with the Magnus expansion truncated to fourth order, *i.e.*, $U(t) = \exp\left(\sum_{i=1}^{4} \mathfrak{H}_i(t)\right)$, where

$$\mathfrak{H}_1 = -i \int \mathbf{dt}_1\, H_1 \tag{16a}$$

$$\mathfrak{H}_2 = \frac{-1}{2} \iint \mathbf{dt}_2\, [H_1, H_2] \tag{16b}$$

$$\mathfrak{H}_3 = \frac{i}{6} \iiint \mathbf{dt}_3 \left([H_1, [H_2, H_3]] + [H_3, [H_2, H_1]] \right) \tag{16c}$$

$$\begin{aligned} \mathfrak{H}_4 = \frac{1}{12} \iiiint \mathbf{dt}_4 \Big(& [[[H_1, H_2], H_3], H_4] \\ & + [H_1, [[H_2, H_3], H_4]] \\ & + [H_1, [H_2, [H_3, H_4]]] \\ & + [H_2, [H_3, [H_4, H_1]]] \Big)\ , \end{aligned} \tag{16d}$$

with the short-hand notations $H_i \equiv H(t_i)$ and $\mathbf{dt}_j \equiv dt_1 \cdots dt_j$. This expansion reveals that $U(T)$ becomes an exponential of a sum of operators of the form $g(T)\left(\prod_l a_l^{\dagger p_l} a_l^{q_l}\right)\left(\sigma_y^{(1)}\right)^r \left(\sigma_y^{(2)}\right)^s$ for some integers p_l, q_l, r, s and function $g(T)$ dependent on the integrals over the driving functions $F_{l,k}^{(j)}(t)$.

Crucially, not all these terms contribute to the desired entangling operation. To achieve pure entanglement at the gate time T, the driving functions $F_{l,k}^{(j)}$ need to be carefully designed to eliminate all terms except for the one responsible for the entangling operation $i\phi_T \sigma_y^{(1)}\sigma_y^{(2)}$. This selective elimination translates to a set of constraints on the driving functions, that have been provided in electronic format for convenience [28].

One can then verify that the monochromatic driving functions

$$\begin{aligned} F_{1,1}^{(1)} &= F_{1,1}^{(2)} = \Omega e^{2i\delta t} \\ F_{l,2}^{(1)} &= s_{1l}\Omega \frac{\tilde{\eta}_l}{\eta_{1l}} e^{i\delta t} \\ F_{l,2}^{(2)} &= s_{1l}\Omega \frac{\tilde{\eta}_l}{\eta_{2l}} e^{i\delta t}, \end{aligned} \tag{17}$$

with $\tilde{\eta}_l := \frac{\sqrt{2}}{2}\sqrt{\eta_{1l}^2 + \eta_{2l}^2}$ and the entangling condition $-3\frac{\Omega^4}{\delta^4}\left(\sum_j \eta_{j1}^2\right) + \frac{\Omega^2}{\delta^2}\left(2 + \sum_{l,j}\eta_{jl}^2\right) = \frac{\phi_T}{\pi}$ are sufficient to satisfy all those constraints and, therefore, to eliminate undesired contributions, as well as to achieve entanglement at the gate time T. Notably, while the driving scheme based on Eq. (17) achieves entanglement, it offers limited robustness compared to the solution presented in Eq. (12).

B. Robustness to motional heating

Motional heating, caused by interaction with the environment, significantly degrades gate fidelity by introducing correlations between qubits and motional degrees of freedom. Thermalisation and dephasing, the leading sources of error, can be modeled by the master equation [29]

$$\frac{d}{dt}\rho = -i[H(t), \rho] + \sum_{l=1}^{M} \mathcal{L}^{(l)}(\rho)\ , \tag{18}$$

with the density matrix $\rho = \rho_S \otimes \rho_M$, the Hamiltonian $H(t)$ in Eq. (9) and the Lindbladian $\mathcal{L}^{(l)}(\rho)$ that includes the jump operators $C_-^{(l)} = a_l$ and $C_+^{(l)} = a_l^\dagger$ for thermalization in the l-th mode and $C_n^{(l)} = a_l^\dagger a_l$ for dephasing:

$$\mathcal{L}^{(l)}(\rho) = \sum_{j=-,+,n} \gamma_j^{(l)} \left(C_j^{(l)} \rho C_j^{(l)\dagger} - \frac{1}{2}\{C_j^{(l)\dagger} C_j^{(l)}, \rho\} \right). \tag{19}$$

Here, $\gamma_j^{(l)}$ are the decay rates associated to the j-th operator of the l-th motional mode and $\{\cdot,\cdot\}$ the anticommutator.

In the absence of dissipation, the target gate U is perfectly implemented, *i.e.* $\rho(T) = U\rho(0)U^\dagger$, but the presence of dissipating processes $\mathcal{L}^{(l)}(\rho)$ introduces noise, resulting in an imperfect (potentially non-unitary) gate $\tilde{\mathcal{E}} : \rho \to \tilde{\mathcal{E}}(\rho)$. Since this distortion depends on the evolution of the motional state, the choice of the driving functions $f(t)$ in $H(t)$ significantly impacts the susceptibility of U to these dissipative effects. The Mølmer-Sørensen gate is particularly vulnerable to motional heating due to its non-centered phase-space trajectories, but alternative choices of the driving functions $F_{l,k}(t)$ can significantly enhance gate's resilience to heating [9].

In the time-dependent frame defined by the non-dissipative unitary $U(t)$ (defined before Eq. (15)), as long as the entangling conditions on the functions $F_{l,k}^{(j)}(t)$ are met, the coherent evolution reduces to the identity $\mathbb{1}$, and the the master equation in Eq. (18) becomes purely dissipative $\frac{d}{dt}\rho = \sum_l \tilde{\mathcal{L}}^{(l)}(\rho)$ with

$$\tilde{\mathcal{L}}^{(l)}(\rho) = \sum_{j=-,+,n} \gamma_j^{(l)} \left(\tilde{C}_j^{(l)} \rho \tilde{C}_j^{(l)\dagger} - \frac{1}{2}\{\tilde{C}_j^{(l)\dagger} \tilde{C}_j^{(l)}, \rho\} \right), \tag{20}$$

where the time-dependent jump operators are now expressed in the rotated frame $\tilde{C}_j(t) = U^\dagger(t) C_j U(t)$, and their explicit expressions up to order η^3 can be found in electronic format in [28]. Given that the decay rates satisfy $\gamma_j T \ll 1$, the dynamics of $\rho(t)$ can be described at first order by the propagator $e^{\tilde{\mathcal{L}}t} \approx \mathbb{1} + \sum_l \int_0^t dt' \tilde{\mathcal{L}}(t')$. Specifically, the spin state evolves to a final state at the gate time $\rho_S(T) = \rho_S(0) + \Delta\rho_S$, with

$$\Delta\rho_S = \mathrm{tr}_M \int_0^T dt' \tilde{\mathcal{L}}(t')[\rho_S \otimes \rho_M] \ , \tag{21}$$

and tr_M denotes trace over the motion. While in the absence of dissipation Eq. (21) vanishes, thermalization and dissipation result in a non-zero $\Delta\rho_S$, which can be generally expressed as

$$\Delta\rho_S = \sum_{m,n} \chi_{mn} A_m \rho_S(0) A_n^\dagger \ , \tag{22}$$

with the operators $A_m \in \{ \mathbb{1}, \sigma_y^{(1)}, \sigma_y^{(2)}, \sigma_y^{(1)}\sigma_y^{(2)} \}$. Here, χ_{mn} are the process matrix elements whose norm characterizes the infidelity of the gate and depend on the motional properties of the state through elements of the form $\mathrm{tr}_M \left(\rho_M \prod_l a_l^{\dagger p_l} a_l^{q_l} \right)$ (for some integers p_l, q_l) as well as on the temporal shaping of the driving functions $F_{l,k}^{(j)}(t)$. Therefore, since each element χ_{mn} is weighted with a factor of η, it is possible to devise schemes that are robust to a particular order of η. Formulated as an optimisation problem, this entails determining the form of the drivings $F_{l,k}^{(j)}(t)$ that minimize a set of contraints, as shown in Supp. Mat. A.

While the parametrization in Eq. (17) offers limited opportunities to improve its robustness, a bichromatic drive with minimal modifications to the protocol of Eq. (17), which results in Eq. (12), can significantly improve robustness to the leading order $\mathcal{O}(\eta^0)$ by minimizing the functionals in Eq. (A1) of the Supp. Mat. A.

VI. CONCLUSIONS

Achieving high-fidelity entangling gates is a critical bottleneck for trapped-ion quantum computation. Current gate implementations, while often tailored to address specific error sources, struggle when confronted with the combined effects of thermal excitations, control field imperfections, and environmental coupling. These factors lead to unwanted spin-motion couplings, detuning errors, and motional heating, ultimately degrading gate performance. Consequently, high-fidelity operations often require highly controlled environments and sophisticated control techniques, even to achieve moderate entanglement fidelities with small ion chains.

This work presents an entangling gate scheme that tackles the fundamental challenge of mitigating diverse error sources simultaneously. Our proposed gate utilizes a specifically designed driving protocol that addresses multiple sidebands of each motional mode. This approach effectively suppresses inhomogeneous spin-motion couplings, leading to significant improvements in gate fidelity, even for large ion chains with numerous motional modes. Furthermore, the driving patterns enable high-fidelity operations even under substantial thermal excitations, a crucial factor for scalability.

The proposed scheme demonstrates remarkable robustness against motional heating, vibrational frequency fluctuations, and detuning errors. This combined robustness and scalability pave the way for significant advancements in trapped-ion quantum computation. By enabling high-fidelity entanglement under noisy conditions, this work brings us closer to the realization of practical quantum computers.

VII. ACKNOWLEDGEMENTS

We gratefully acknowledge stimulating discussions with Jake Lishman, Nguyen Le, Winfried K. Hensinger and Samuel J. Hile. This work was supported by the U.K. Engineering and Physical Sciences Research Council via the EPSRC Hub in Quantum Computing and Simulation (EP/T001062/1).

[1] T. D. Ladd, F. Jelezko, R. Laflamme, Y. Nakamura, C. Monroe, and J. L. O'Brien, Quantum computers, Nature **464**, 45 (2010).
[2] C. D. Bruzewicz, J. Chiaverini, R. McConnell, and J. M. Sage, Trapped-ion quantum computing: Progress and challenges, Applied Physics Reviews **6** (2019).
[3] A. Sørensen and K. Mølmer, Quantum computation with ions in thermal motion, Physical Review Letters **82**, 1971 (1999).
[4] J. P. Gaebler, T. R. Tan, Y. Lin, Y. Wan, R. Bowler, A. C. Keith, S. Glancy, K. Coakley, E. Knill, D. Leibfried, *et al.*, High-fidelity universal gate set for be 9+ ion qubits, Physical Review Letters **117**, 060505 (2016).
[5] T. Harty, M. Sepiol, D. Allcock, C. Ballance, J. Tarlton, and D. Lucas, High-fidelity trapped-ion quantum logic using near-field microwaves, Physical Review Letters **117**, 140501 (2016).
[6] S. Weidt, J. Randall, S. Webster, K. Lake, A. Webb, I. Cohen, T. Navickas, B. Lekitsch, A. Retzker, and W. Hensinger, Trapped-ion quantum logic with global radiation fields, Physical Review Letters **117**, 220501 (2016).
[7] J. Benhelm, G. Kirchmair, C. F. Roos, and R. Blatt, Towards fault-tolerant quantum computing with trapped

ions, Nature Physics **4**, 463 (2008).
[8] C. Valahu, I. Apostolatos, S. Weidt, and W. Hensinger, Quantum control methods for robust entanglement of trapped ions, Journal of Physics B: Atomic, Molecular and Optical Physics **55**, 204003 (2022).
[9] F. Haddadfarshi and F. Mintert, High fidelity quantum gates of trapped ions in the presence of motional heating, New Journal of Physics **18**, 123007 (2016).
[10] J. Lishman and F. Mintert, Trapped-ion entangling gates robust against qubit frequency errors, Physical Review Research **2**, 033117 (2020).
[11] A. E. Webb, S. C. Webster, S. Collingbourne, D. Bretaud, A. M. Lawrence, S. Weidt, F. Mintert, and W. K. Hensinger, Resilient entangling gates for trapped ions, Physical Review Letters **121**, 180501 (2018).
[12] D. Hayes, S. M. Clark, S. Debnath, D. Hucul, I. V. Inlek, K. W. Lee, Q. Quraishi, and C. Monroe, Coherent error suppression in multiqubit entangling gates, Physical Review Letters **109**, 020503 (2012).
[13] J. A. D. Randall, *High-fidelity entanglement of trapped ions using long-wavelength radiation*, Ph.D. thesis, Imperial College London (2015).
[14] T. Choi, S. Debnath, T. Manning, C. Figgatt, Z.-X. Gong, L.-M. Duan, and C. Monroe, Optimal quantum control of multimode couplings between trapped ion qubits for scalable entanglement, Physical Review Letters **112**, 190502 (2014).
[15] Y. Lu, S. Zhang, K. Zhang, W. Chen, Y. Shen, J. Zhang, J.-N. Zhang, and K. Kim, Global entangling gates on arbitrary ion qubits, Nature **572**, 363 (2019).
[16] G. Zarantonello, H. Hahn, J. Morgner, M. Schulte, A. Bautista-Salvador, R. Werner, K. Hammerer, and C. Ospelkaus, Robust and resource-efficient microwave near-field entangling be+ 9 gate, Physical Review Letters **123**, 260503 (2019).
[17] A. R. Milne, C. L. Edmunds, C. Hempel, F. Roy, S. Mavadia, and M. J. Biercuk, Phase-modulated entangling gates robust to static and time-varying errors, Physical Review Applied **13**, 024022 (2020).
[18] M. Sameti, J. Lishman, and F. Mintert, Strong-coupling quantum logic of trapped ions, Physical Review A **103**, 052603 (2021).
[19] B. Lekitsch, S. Weidt, A. G. Fowler, K. Mølmer, S. J. Devitt, C. Wunderlich, and W. K. Hensinger, Blueprint for a microwave trapped ion quantum computer, Science Advances **3**, e1601540 (2017).
[20] M. Orozco-Ruiz, S. Simsek, S. A. Kulmiya, S. J. Hile, W. K. Hensinger, and F. Mintert, Optimal control with a multidimensional quantum invariant, Physical Review A **108**, 022601 (2023).
[21] J. D. Wong-Campos, S. A. Moses, K. G. Johnson, and C. Monroe, Demonstration of two-atom entanglement with ultrafast optical pulses, Physical Review Letters **119**, 230501 (2017).
[22] H. Häffner, W. Hänsel, C. Roos, J. Benhelm, D. Chekal Kar, M. Chwalla, T. Körber, U. Rapol, M. Riebe, P. Schmidt, *et al.*, Scalable multiparticle entanglement of trapped ions, Nature **438**, 643 (2005).
[23] K. Kim, M.-S. Chang, R. Islam, S. Korenblit, L.-M. Duan, and C. Monroe, Entanglement and tunable spin-spin couplings between trapped ions using multiple transverse modes, Physical Review Letters **103**, 120502 (2009).
[24] K. A. Landsman, Y. Wu, P. H. Leung, D. Zhu, N. M. Linke, K. R. Brown, L. Duan, and C. Monroe, Two-qubit entangling gates within arbitrarily long chains of trapped ions, Physical Review A **100**, 022332 (2019).
[25] A. Sørensen and K. Mølmer, Entanglement and quantum computation with ions in thermal motion, Physical Review A **62**, 022311 (2000).
[26] C. A. Sackett, D. Kielpinski, B. E. King, C. Langer, V. Meyer, C. J. Myatt, M. Rowe, Q. Turchette, W. M. Itano, D. J. Wineland, *et al.*, Experimental entanglement of four particles, Nature **404**, 256 (2000).
[27] S. Blanes, F. Casas, J.-A. Oteo, and J. Ros, The magnus expansion and some of its applications, Physics reports **470**, 151 (2009).
[28] Data for Orozco-Ruiz et al. "robust entangling gates for trapped-ion chains with high motional states" (2024), DOI:10.5281/zenodo.10908290.
[29] H.-P. Breuer and F. Petruccione, *The theory of open quantum systems* (OUP Oxford, 2002).

SUPPLEMENTARY MATERIAL

Appendix A: Functionals for resilience against motional heating

The gate fidelity F (Eq. (14)) in the presence of motional heating depends on the temporal modulation of the driving functions $F_{l,k}^{(j)}$. Specifically, the fidelity F can be maximized by selecting these functions $F_{l,k}^{(j)}$ to minimize the matrix elements $\chi_{m,n}$ in Eq. (22), or equivalently, a set of cost functions $\{c_i\}$ evaluated at the gate time $t = T$, which naturally arise at various orders in the Lamb-Dicke parameter η.

Order η^1 The first-order-in-η contributions to the motional heating are functionals of the driving functions corresponding to the central motional mode, $F_{1,1}^{(j)}$, with $j = \{1, 2\}$. Specifically, the cost functions read

$$\begin{aligned} &c_1 = \{\alpha_i\}\ , && c_2 = \{\alpha_i^2\}\ , && c_3 = \{\alpha_i\alpha_j\}\ , \\ &c_4 = \{|\alpha_i|^2\alpha_j\}\ , && c_5 = \{\alpha_i^2\alpha_j^{*2}\}\ , && c_6 = \{|\alpha_i|^2\}\ , \\ &c_7 = \{\alpha_i\alpha_j^*\}\ , && c_8 = \{|\alpha_i|^2|\alpha_j|^2\}\ , && c_9 = \{\alpha_i^2\alpha_j^*\}\ , \end{aligned} \tag{A1}$$

with $i \neq j$, $\alpha_j := \{F_{1,1}^{(j)}\}$ and with the short-hand notation $\{f\} = \int_0^t dt' f(t')$.

Crucially, a Fourier series parametrization of the form $f = \sum_m A_m e^{ia_m t}$ with the constraint $\sum_m \left(A_m \prod_{k\neq m} a_k\right) = 0$ for the functions $F_{1,1}^{(j)}$ ensures that all conditions vanish $c_i = 0$, except for $i = \{6, 8\}$. Consequently, optimal motional heating resilience at first order in η can be achieved through the minimization of the functional $C = \max(c_6, c_8)$.

Orders η^2 *and* η^3 Second and third-order contributions to motional resilience involve numerous functionals, becoming significant only in the regime of large Lamb-Dicke parameters. For 2 ions, there are 186 and 2543 independent elements for the respective orders, available conveniently in electronic format in [28].

Appendix B: Highly excited thermal states

While Figure 2 in the Main text showcases the performance of the proposed gate for various ion chain sizes and scenarios including ideal conditions or motional heating, the results are limited to motional Fock states $|\mathbf{n}\rangle$ with occupation numbers of up to $n = 10$.

Fig. 4 depicts the infidelity of a two-ion system for thermal states with average phonon occupations (thermal excitation) of up to $\bar{n} = 100$ and different spin-motion coupling strengths Λ. The figure demonstrates that the proposed scheme outperforms the standard MS approach for any value of $\bar{n}$ and Λ. Remarkably, fidelities exceeding 99% are achieved with spin-motion couplings Λ of 0.05, a value commonly encountered in experiments, which represents more than an order of magnitude improvement compared to the standard MS approach.

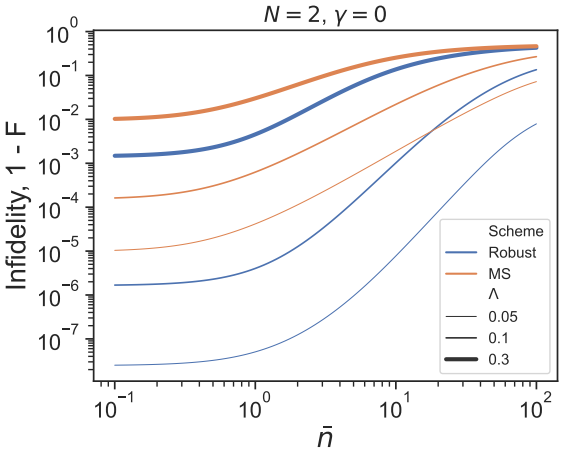


FIG. 4: Infidelity $1 - F$ for $N = 2$ qubits as a function of the mean occupation $\bar{n}$ of a thermal state (on log scale). Increasing line thickness represents increasing values of the coupling parameter Λ (defined in the main text), while the color line distinguishes between the conventional MS approach (orange) and the present robust gate scheme (blue). No motional heating or detuning errors are considered.

Appendix B

Coordinate Systems for the Sphere and the $(2,1)$ Classical Kummer Shape - the Teardrop

In this Appendix we provide relevant definitions of some of the different coordinate systems that can be used to the parametrise the sphere and $(2,1)$ classical Kummer shape. For each coordinate system we provide expressions for the Poisson and metric brackets where appropriate.

Sphere

Cartesian Coordinates: s_x, s_y, s_z

$$s_x = \frac{\zeta + \zeta^*}{1 + \zeta\zeta^*} = \sqrt{(1 - s_z^2)}\cos\phi, \tag{6.1}$$

$$s_y = \mathrm{i}\frac{\zeta^* - \zeta}{1 + \zeta\zeta^*} = \sqrt{(1 - s_z^2)}\sin\phi, \tag{6.2}$$

$$s_z = \frac{1 - \zeta\zeta^*}{1 + \zeta\zeta^*}, \tag{6.3}$$

with Poisson and metric brackets

$$\{s_i, s_j\} = \epsilon_{ijk}s_k, \qquad \{\!\{s_i, s_j\}\!\} = \delta_{ij} - s_i s_j. \tag{6.4}$$

Stereographic Projection: ζ

$$\zeta = \frac{s_x + is_y}{1 + s_z} = \sqrt{\left(\frac{1 - s_z}{1 + s_z}\right)}e^{i\phi}, \tag{6.5}$$

with Poisson and metric brackets

$$\{\zeta, \zeta^*\} = -\frac{i}{2}(1 + |\zeta|^2)^2, \qquad \{\!\{\zeta, \zeta^*\}\!\} = \frac{1}{2}(1 + |\zeta|^2)^2. \tag{6.6}$$

Canonical Coordinates ϕ, s_z

$$\phi = \tan^{-1}\left(\frac{i\left(\zeta^* - \zeta\right)}{\zeta + \zeta^*}\right) = \tan^{-1}\left(\frac{s_y}{s_x}\right), \tag{6.7}$$

$$s_z = \frac{1 - \zeta\zeta^*}{1 + \zeta\zeta^*} \tag{6.8}$$

with Poisson and metric brackets

$$\{\phi, s_z\} = 1, \qquad \{\!\{\phi, \phi\}\!\} = \frac{1}{1 - s_z^2}, \qquad \{\!\{s_z, s_z\}\!\} = 1 - s_z^2. \tag{6.9}$$

$(2,1)$ Classical Kummer Shape

Cartesian Coordinates: s_x, s_y, s_z

$$s_x = \sqrt{2}\frac{(\zeta + \zeta^*)}{(1 + \zeta\zeta^*)^{\frac{3}{2}}} = \sqrt{(1 + s_z)^2(1 - s_z)}\cos\phi, \tag{6.10}$$

$$s_y = \mathrm{i}\sqrt{2}\frac{(\zeta^* - \zeta)}{(1 + \zeta\zeta^*)^{\frac{3}{2}}} = \sqrt{(1 + s_z)^2(1 - s_z)}\sin\phi, \tag{6.11}$$

$$s_z = \frac{1 - \zeta\zeta^*}{1 + \zeta\zeta^*}, \tag{6.12}$$

with Poisson brackets

$$\{s_x, s_y\} = \frac{1}{2}(1 + s_z)^{k_1 - 1}(1 - s_z)^{k_2 - 1}(k_1(1 - s_z) - k_2(1 + s_z)) \tag{6.13}$$

$$\{s_y, s_z\} = s_x, \tag{6.14}$$

$$\{s_z, s_x\} = s_y, \tag{6.15}$$

and metric brackets

$$\{\!\{s_x, s_x\}\!\} = \frac{1}{4\left(1 - s_z^2\right)}\Big[4\left(1 - s_z\right)^{k_2}\left(1 + s_z\right)^{k_1} + s_x^2\left(-4 + k_1^2\left(1 - s_z\right)^2 + k_2^2\left(1 + s_z\right)^2 + 2k_1k_2\left(1 - s_z^2\right)\right)\Big], \tag{6.16}$$

$$\{\!\{s_x, s_y\}\!\} = \frac{s_x s_y}{4\left(1 - s_z^2\right)}\left[-4 + k_1^2\left(1 - s_z\right)^2 + k_2^2\left(1 + s_z\right)^2 + 2k_1k_2\left(1 - s_z^2\right)\right], \tag{6.17}$$

$$\{\!\{s_x, s_z\}\!\} = \frac{s_x}{2}\left[k_1\left(1 - s_z\right) - k_2\left(1 + s_z\right)\right], \tag{6.18}$$

$$\{\!\{s_y, s_y\}\!\} = \frac{1}{4\left(1 - s_z^2\right)}\Big[4\left(1 - s_z\right)^{k_2}\left(1 + s_z\right)^{k_1} \tag{6.19}$$

$$+ s_y^2\left(-4 + k_1^2\left(1 - s_z\right)^2 + k_2^2\left(1 + s_z\right)^2 + 2k_1k_2\left(1 - s_z^2\right)\right)\Big], \tag{6.20}$$

$$\{\!\{s_y, s_z\}\!\} = \frac{s_y}{2}\left[k_1\left(1 - s_z\right) - k_2\left(1 + s_z\right)\right], \tag{6.21}$$

$$\{\!\{s_z, s_z\}\!\} = 1 - s_z^2. \tag{6.22}$$

Stereographic Projection: ζ

$$\zeta = \frac{s_x + i s_y}{(1+s_z)^{\frac{3}{2}}} = \sqrt{\left(\frac{1-s_z}{1+s_z}\right)} e^{i\phi}, \tag{6.23}$$

with Poisson and metric brackets

$$\{\zeta, \zeta^*\} = -\frac{i}{2}(1+|\zeta|^2)^2, \qquad \{\!\{\zeta, \zeta^*\}\!\} = \frac{1}{2}(1+|\zeta|^2)^2. \tag{6.24}$$

where

Canonical Coordinates: ϕ, s_z

$$\phi = \tan^{-1}\left(\frac{\mathrm{i}\,(\zeta^* - \zeta)}{\zeta + \zeta^*}\right) = \tan^{-1}\left(\frac{s_y}{s_x}\right), \tag{6.25}$$

$$s_z = \frac{1-\zeta\zeta^*}{1+\zeta\zeta^*}. \tag{6.26}$$

Appendix C

Non-Hermitian Coherent-State Approximation for Gaussian wave packet dynamics

The Jacobi Group and its Algebra: A Symplectic Approach to Gaussian Wave Packet Dynamics

Ohsawa and Leok [14] develop a symplectic-geometric account of Gaussian wave-packet evolution and illustrate an approach for evaluating approximations of quantum dynamics. In later work, Ohsawa [61] noted that Gaussian wave packets are coherent states of the Schrödinger group, which is equivalent to those generated from the Jacobi algebra, a semi-direct sum of the symplectic and Heisenberg algebras [59, 123, 124], and noted their connection to squeezed states. We interpret their approach as equivalent to the coherent-state approximation applied to the Jacobi algebra.

Furthermore, Ohsawa [125] showed that this symplectic Gaussian wave packet technique provides an $O(\hbar^{3/2})$ approximation for semiclassical expectation values, demonstrating significant enhanced accuracy compared to the $O(\hbar)$ precision of Heller's classical approximations in the semiclassical regime [58].

In this Appendix, we demonstrate this equivalence between Gaussian wave packet dynamics and the coherent-state approximation, which enables us to extend their approach to non-Hermitian systems and apply the semiclassical Husimi approximation developed in previous chapters.

We begin by constructing coherent states for the Jacobi algebra using the Perelomov group-theoretic method [8] discussed by Ohsawa. We then establish the factorisation property, phase space, Poisson brackets, and metric brackets, allowing us to formulate the coherent state approximation for the Jacobi algebra.

We complete this section by demonstrating that this coherent-state approximation is equivalent to the approximation technique employed by Ohsawa et al. Although the authors use the nomenclature

'semiclassical', we interpret this as a 'classical' approximation of a Gaussian state, as their approach approximates the trajectories of a point in four-dimensional phase space. An extension of this approach would be the semiclassical Husimi approximation, which would result in four-dimensional Husimi distributions that, while mathematically well-defined, are more intricate to visualise.

Through our lens, we identify four forms of approximations for systems in the universal enveloping algebra of the Heisenberg-Weyl algebra: the Glauber coherent-state approximation, the Glauber semiclassical Husimi approximation, the Jacobi coherent-state approximation (equivalent to Ohsawa's method), and the Jacobi semiclassical Husimi approximation. While beyond the scope of the current work, it would be interesting to compare these four approaches, building upon Ohsawa's work, which can be interpreted as comparing the accuracy of the Glauber coherent-state approximation to the Jacobi coherent-state approximation.

Coherent States of the Jacobi Group

Gaussian states can be viewed as coherent states of the Jacobi group, whose Lie algebra is the semidirect sum $\mathfrak{g}_1^J = \mathfrak{su}(1,1) \ltimes \mathfrak{h}_1^o$ of the symplectic algebra $\mathfrak{su}(1,1)$ and the ordinary Heisenberg algebra $\mathfrak{h}_1^o$. The ordinary Heisenberg algebra $\mathfrak{h}_1^o$ has three generators $\{\hat{q}, \hat{p}, \mathbf{1}\}$ satisfying the canonical commutation relation $[\hat{q}, \hat{p}] = i\hbar\mathbf{1}$. When represented in Fock space using ladder operators $\hat{a} = \frac{1}{\sqrt{2\hbar}}(\hat{q} + i\hat{p})$ and $\hat{a}^\dagger = \frac{1}{\sqrt{2\hbar}}(\hat{q} - i\hat{p})$, the Jacobi algebra contains the oscillator operators $\{\hat{a}, \hat{a}^\dagger, \hat{I}\}$ from the Heisenberg subalgebra and the squeezing generators $\hat{K}_+ = \frac{1}{2}(\hat{a}^\dagger)^2$, $\hat{K}_- = \frac{1}{2}\hat{a}^2$, $\hat{K}_0 = \frac{1}{2}(\hat{a}^\dagger\hat{a} + \frac{1}{2})$ from the $\mathfrak{su}(1,1)$ subalgebra.

To construct the coherent states, we use the same Hilbert space and extremal state as for the Heisenberg-Weyl algebra. The stability group is generated by the elements $\hat{n}, \hat{I}$, resulting in $I = U(1) \otimes U(1)$. The coset space is $H_1 \rtimes Mp(2)/U(1) \otimes U(1)$.

The coherent state orbit is obtained via the generalised displacement operator

$$\hat{B}_1(\alpha, \beta) = \exp(\alpha\hat{a}^\dagger - \alpha^*\hat{a} + \beta(\hat{a}^\dagger)^2 - \beta^*\hat{a}^2), \tag{6.27}$$

with $\alpha, \beta \in \mathbb{C}$. Using the Baker-Campbell-Hausdorff formula and a change of variables from β to ε, we can factorise this expression as

$$\hat{B}_2(\alpha, \varepsilon) = \exp(\alpha\hat{a}^\dagger - \alpha^*\hat{a}) \exp\left(\frac{1}{2}(\varepsilon\hat{a}^2 - \varepsilon^*(\hat{a}^\dagger)^2)\right). \tag{6.28}$$

This has the form $\hat{B}_2 = \hat{D}\hat{S}$ where $\hat{D}$ is the Heisenberg displacement operator and

$$\hat{S} = \exp\left(\frac{1}{2}(\varepsilon\hat{a}^2 - \varepsilon^*(\hat{a}^\dagger)^2)\right) \tag{6.29}$$

is commonly referred to as the "squeezing operator." The coherent states can then be written as

$$|\alpha, \varepsilon\rangle = N(\varepsilon)\hat{D}(\alpha)\hat{S}(\varepsilon)|0\rangle, \tag{6.30}$$

where $N(\varepsilon)$ is a normalisation factor. These expressions are recognised as 'squeezed states' from

quantum optics.

These coherent states are equivalent to the Gaussian states discussed by Ohsawa [14],

$$\psi(x) = N(b) \exp\left\{ \frac{i}{\hbar} \left[\frac{1}{2}(a+ib)(x-q)^2 + p(x-q) \right] \right\}. \tag{6.31}$$

Here $N(b)$ is a normalisation factor and q, p, a, b determine the expectation values and uncertainties of position and momentum as

$$\langle \hat{q} \rangle = q, \quad \langle \hat{p} \rangle = p, \tag{6.32}$$

$$(\Delta \hat{q})^2 = \langle \hat{q}^2 \rangle - \langle \hat{q} \rangle^2 = \frac{\hbar}{2b}, \tag{6.33}$$

$$(\Delta \hat{p})^2 = \langle \hat{p}^2 \rangle - \langle \hat{p} \rangle^2 = \frac{\hbar(a^2+b^2)}{2b}. \tag{6.34}$$

These parameters are related to α, ε as follows:

$$\alpha = \frac{1}{\sqrt{2\hbar}}(q+ip), \tag{6.35}$$

and

$$\varepsilon = \frac{1}{2} \ln \left(\frac{\sqrt{a^2+b^2}+a}{b} \right) \cdot \frac{a+ib}{\sqrt{a^2+b^2}}. \tag{6.36}$$

For future calculations, it is helpful to define the coordinate system:

$$r = \frac{1}{2} \ln \left[\frac{\sqrt{a^2+b^2}+a}{b} \right] \tag{6.37}$$

$$\phi = \frac{1}{2} \arctan\left(\frac{b}{a} \right) \tag{6.38}$$

Factorisation Property

We now establish the factorisation property for the Jacobi coherent states. For the $\mathcal{D}$-algebra approach, it is important to work in coordinates z, w which are $\hbar$-independent and related to α, r, ϕ as

$$\alpha = \frac{z + z^* w}{1 - ww^*}, \quad w = \tanh\left(\frac{|r|}{2} \right) e^{2i\phi}. \tag{6.39}$$

The normalisation function for these coherent states is given by [126]

$$\mathcal{M}(z,w) = (1-ww^*)^{-\frac{1}{2}} \exp\left(\frac{2zz^* + z^2 w + z^{*2} w^*}{2(1-ww^*)} \right), \tag{6.40}$$

with $z, w \in \mathbb{C}$, and the $\mathcal{D}$-algebra operators of the Jacobi algebra are given by

$$\hat{a} = \frac{\partial}{\partial z^*} \tag{6.41}$$

$$\hat{a}^\dagger = z^* + w^* \frac{\partial}{\partial z^*} \tag{6.42}$$

$$\hat{K}_- = \frac{\partial}{\partial w^*} \tag{6.43}$$

$$\hat{K}_0 = \frac{1}{4} + \frac{1}{2} z^* \frac{\partial}{\partial z^*} + w^* \frac{\partial}{\partial w^*} \tag{6.44}$$

$$\hat{K}_+ = \frac{1}{2} z^{*2} + \frac{1}{2} w^* + z^* w^* \frac{\partial}{\partial z^*} + w^{*2} \frac{\partial}{\partial w^*} \tag{6.45}$$

To illustrate that the factorisation property holds, we explicitly calculate $\langle \hat{q}\hat{f} \rangle$ where $\hat{f}$ is an analytic function of $\hat{q}, \hat{p}$. Through detailed calculation involving the chain rule and analysis of $\hbar$-dependence, we find:

$$\langle \hat{q}\hat{f} \rangle = qf + O(\hbar), \tag{6.46}$$

establishing the factorisation property as required. Results for the remaining operators can be calculated in a similar manner.

Coherent-State Approximation

Having established the coherent states and the factorisation property, we now present the final properties required for our coherent-state approximation.

The phase space is the 4-dimensional manifold $\mathbb{R}^2 \times \Sigma_1$, parametrised by (q, p, a, b) with $b > 0$. The Poisson and metric brackets expressed in matrix form are [14]:

$$\omega = \begin{pmatrix} 0 & 1 & 0 & 0 \\ -1 & 0 & 0 & 0 \\ 0 & 0 & 0 & \frac{4b^2}{\hbar} \\ 0 & 0 & -\frac{4b^2}{\hbar} & 0 \end{pmatrix}, \tag{6.47}$$

$$g = \begin{pmatrix} \frac{1}{b} & \frac{a}{b} & 0 & 0 \\ \frac{a}{b} & \frac{a^2+b^2}{b} & 0 & 0 \\ 0 & 0 & \frac{4b^2}{\hbar} & 0 \\ 0 & 0 & 0 & \frac{4b^2}{\hbar} \end{pmatrix}. \tag{6.48}$$

We now have all the key components for the non-Hermitian coherent state approximation for Gaussian states:

$$\frac{\mathrm{d}x_i}{dt} = \{x_i, h\} + \{\!\{x_i, \gamma\}\!\}, \tag{6.49}$$

where $x_i \in \{q, p, a, b\}$, and the associated semiclassical Husimi approximation:

$$Q_{\psi(t)}(\chi) = Q_{\psi_0}\left(\Phi_{-t}(\chi)\right) w(\chi, t), \tag{6.50}$$

where $\chi = (q, p, a, b)$. This completes the formulation of the coherent-state approximation framework for Gaussian wave packet dynamics.

Applications and Extensions

With the conditions for coherent-state approximations established, we can now use this framework to consider phase-space approximations for the evolution of Gaussian states under non-linear, non-Hermitian Heisenberg-Weyl systems. The natural extension to semiclassical Husimi distributions

in the four-dimensional parameter space (q, p, a, b) is possible, though quite intricate as we are providing a semiclassical approximation to the evolution of Jacobi group coherent states, which are themselves often used as semiclassical approximation tools.

Through our lens, we identify four forms of approximations for systems in the universal enveloping algebra of the Heisenberg-Weyl algebra: the Glauber coherent-state approximation, the Glauber semiclassical Husimi approximation, the Jacobi coherent-state approximation (equivalent to Ohsawa's method), and the Jacobi semiclassical Husimi approximation. Ohsawa has demonstrated that his symplectic formulation gives an $O(\hbar^{3/2})$ approximation to expectation value dynamics, improving upon the conventional Glauber $O(\hbar)$ methods. It would be interesting to investigate whether these $O(\hbar^{3/2})$ improvements persist when extended to non-Hermitian systems, and whether the four-dimensional semiclassical Husimi approximation via symplectic reduction provides further enhancement beyond the $O(\hbar^{3/2})$ accuracy achieved by Ohsawa's approach.